January 2013

Application and Characterization of Self-Assembled Monolayers In Hybrid Electronic Systems

Michael Enoch Celesin
University of South Florida, mail@michaelcelestin.com

Application and Characterization of Self-Assembled Monolayers In Hybrid Electronic Systems

by

Michael E. Celestin

A dissertation submitted in partial fulfillment
of the requirements for the degree of
Doctor of Philosophy in Chemical Engineering
Department of Chemical and Biomedical Engineering
College of Engineering
University of South Florida

Co-Major Professor: D. Yogi Goswami, Ph.D.
Co-Major Professor: Lee Stefanakos, Ph.D.
Shekhar Bhansali, Ph.D.
Babu Joseph, Ph.D.
Norma Alcantar, Ph.D.

Date of Approval:
November 26, 2013

Keywords: SAM, rectenna, energy harvesting, tunnel diode, printable electronics

DEDICATION

I would like to dedicate this dissertation to my wife, Carolina, and parents, Gabriel and Raisa, who have supported me in immeasurable ways. The emotional, physical, and financial needs of undertaking such a task practically mandate an excellent support group—and I have nothing to complain about. I really cannot imagine how I could have achieved this without your love and care. I would attempt to list all the individual contributions and kind acts however the thought of writing an additional hundred pages to this document seems unattractive at this time. Thank you.

ACKNOWLEDGMENTS

I would also like to take a moment to thank a number of special groups and individuals who had a most memorable impact on my progress including (but not limited to): All the staff at the Nanotechnology Research and Education Center (NREC)—especially Rob Tufts, Dr. Yusef Emirov, Jay Bieber, and Richard Everly. I wanted to take a moment to thank my PhD committee, countless influential professors, and amazing support staff including: Michael Konrad, Tom Gage, Chuck Garretson, Barbara Graham, Ginny Cosmides, Sebnem Thiel, Dr. Scott Campbell, Dr. Richard Gilbert, and the late Dr. John Wolan. I would like to express warm thanks to the students and postdocs of the USF BioMEMS research group, especially Dr. "Subbu" Subramanian Krishnan, Dr. "Super" Supriya Ketkar, and Dr. "Shank" Shankar Koiry (sorry your name was never spelled correctly while in the US). You have been through all the nomadic laboratory moves, dark conference meetings, presentations, travels, and frustrating lab moments by my side.

From my time at Sandia National Labs, all the amazing support staff—especially Dr. Regan Stinnett, Dr. Steven Wix, and Dr. Phil Campbell. Next door at the Center for Integrated Nanotechnology (CINT), I could not have gotten very far without the help of John Nogan, Denise Webb, and Catherine Mombourquette.

I must also make mention of my family and friends who acted as role models to help me become who I am, especially: Vladislav Slep, Veronika Slep, and Alex Slep; Samuel Sanker, Aditya Joshi, Nat Kaplan, Daniel Miller, Bret Galbraith, Katie Satterlee, and Gopal Patel.

TABLE OF CONTENTS

LIST OF TABLES

LIST OF FIGURES

ABSTRACT

In this study, we explore ultra-thin insulators of organic and inorganic composition and their potential role as high-speed rectifiers. Typical applications for these structures include IR sensing, chemical detection, high speed logic circuits, and MEMS enhancements. While there are many elements in the functional group required to create a rectifying antenna (rectenna), the primary thrust of this work is on the rectifier element itself.

To achieve these research goals, a very good understanding of quantum tunneling was required to model the underlying phenomenon of charge conduction. The development of a multi-variable optimization routine for tunneling prediction was required. MATLAB was selected as the programming language for this application because of its flexibility and relative ease of use for simulation purposes. Modeling of physical processes, control of electromechanical systems, and simulation of ion implantation were also to be undertaken.

To advance the process science, a lithographic mask set was made which utilized the information gleaned from the theoretical simulations and initial basic experiments to create a number of diode test structures. This came to include the creation of generations of mask sets—each optimizing various parameters including testability, alignment, contact area, device density, and process ease. Following this work, a complete toolset for the creation of "soft" contact top metals was required and needed to be developed. Ultra-flat substrates were needed to improve device reliability and measurement consistency.

The final phase of research included measurement and characterization of the resultant structures. Basic DC electrical characterization of the organic monolayers would be accomplished using metal probes. Statistical studies of reliability and process yield could then easily be carried out. The rectification ratio (ratio of forward over reverse current at a given voltage magnitude) was found to be a reliable indicator of diode performance in the low frequency ranges. This would mean writing additional code in MATLAB to assist in the automatic analysis for the acquired IV curves. Progression to AC / RF measurements of tunneling performance was to be accomplished using relatively low frequencies (below 100 MHz). Finally, the organic films themselves would be studied for consistency, impedance characteristics, incidence of defects, and thickness by a variety of metrology techniques.

This project resulted in a number of advances to the state-of-the-art in nanofabrication using organic monolayers. A very detailed review of the state of alkanethiol research was presented and submitted for publication. A single pot technique was developed to softly deposit metal nanoparticles onto a charged surface with a high degree of control. A temporary contact method using pure, sub-cooled gallium liquid metal was used to probe organic monolayers and plot IV curves with better understanding of surface states than before. An inkjet printer solution was devised for top contact printing which involved the development and production of a work-up free insulator ink which is water soluble and printable to resolutions of about 25 μm. Localized selective chemical crosslinking was found to reduce printed ink solubility following deposition. Future work will likely include additional exploration of crosslinkable Langmuir-Blodgett films as MIM insulators. Stability and testing will hinge on the fabrication of enclosures or packages for environmental isolation.

CHAPTER 1:

INTRODUCTION

Tunnel diodes have been proposed for a variety of sensing and energy harvesting applications. In this study, we explore ultra-thin insulators of organic and inorganic composition for their potential role as high-speed rectifiers. The concept, while not a new one, has significant challenges when applied to the terahertz (THz) frequency range which includes mid and far infrared light. Military and commercial interest in sensing has spawned many products which operate in both the infrared and hyperspectral response regions. Overcoming some of the technical challenges will result in a device with far superior response range and refresh rate. With a more academic focus in mind, basic research exploration of these films is thoroughly discussed here. This study will begin with an explanation of existing tunnel diode technologies and theory of operation. Modeling of performance, characterization of film quality, self-assembly optimization, and patterning and functionalization of the resultant films will also be covered. Finally, an analysis of experimental data using these organic monolayers will be covered in great depth in addition to design reasoning.

1.1 Brief Background Overview

It is important to understand the very basics of what the research goals were originally for this project. While there are many elements in the functional group required to create a rectifying antenna, the primary thrust of this work is on the rectifier element, itself. In a short

while, the overall structure of the system will be explained. At the most fundamental level, the rectifier is a diode—an electronic device which allows flow of current primarily in only one direction. There are many mechanical analogs to this such as one-way check valves for fluid flow or a ratchet gear and pawl for mechanical motion. In an ideal diode, there would be no resistance to electrical current flow in the forward bias direction starting at any infinitesimally small positive bias voltage. In the reverse direction (negative bias), there would be an infinitely high resistance and thus no current would flow. It is important to understand that with our current maturity and understanding of electronics, this type of response is simply not possible. It is important, when we are about to consider the performance of some tunnel diodes, that we also consider characteristics which exhibit diodic behavior which may not otherwise pass for a diode.

Commercial silicon diodes perform well for many common electronics applications. They exhibit relatively low reverse current leakage, fast turn-on, and high forward bias current handling capabilities. Unfortunately, the specific application of a terahertz rectifier requires very exotic performance characteristics. Silicon diodes, based on a purely semiconductor PN junction, cannot operate far beyond about 10 GHz. Carrier recombination delays are responsible for the slower operation speeds. Schottky diodes have a metal-semiconductor interface and operate much more quickly. Because Schottky diodes only operate using majority carriers (electrons, not holes), they do not suffer from some of the slow recombination delays seen in similar sized silicon diodes. (Hole propagation is much slower than electron propagation in a semiconductor.) Still, once operating in the hundreds of gigahertz, their performance trails off. Both of these diodes have performance characteristics which are relatively close to ideal but are not suitable for this application.

Tunnel diodes are proposed for this ultra-high speed rectifier application. Also known as Esaki diodes, these devices exploit the property of quantum mechanical tunneling. By comparison, a tunnel diode might be described as a very poor performer. The diodes typically exhibit very low current handling, high reverse leakage current, poor electrostatic discharge (ESD) tolerance, and non-ideal diode response. Specifically, classic tunnel diodes have a negative resistance region in the forward bias direction where increased voltage results in decreased current. These limitations have rarely been enough to suggest their disuse as they are incredibly stable, more resistant to radiation, and tremendously fast. The physics behind their operation will be covered in great detail.

1.2 Research Objectives

The overall objective of this research thrust is to develop the technology required for the fabrication of a rectenna (rectifying antenna) which can operate in the terahertz (THz) frequency range. Naturally, this was broken down in to a number of specific tasks to advance the state-of-the-art in these areas.

A very good understanding of quantum tunneling was required to understand the underlying phenomenon of charge conduction. The development of a multivariable optimization routine for tunneling prediction was required. The MATLAB programming language was selected for this application because of its flexibility and relative ease of use for simulation purposes. Modeling of physical processes, control of electromechanical systems, and simulation of ion implantation were also to be undertaken.

To advance the process science, I was to develop a lithographic mask set which utilized the information gleaned from the theoretical simulations and initial basic experiments to create

diode test structures. This would include the creation of generations of mask sets—each optimizing various parameters including testability, alignment, contact area, device density, and process ease. Following this research, additional requirements of "soft" top metal contact methods needed to be further developed. Additionally, ultra-flat substrates were needed to improve device reliability.

The final phase of research was measurement and characterization of the resultant structures. The first task was to determine whether the current approach could yield any results. Following this, DC electrical characterization of the organic monolayers would be accomplished using tungsten probes and a liquid metal probe setup. Statistical studies of reliability and process yield could then easily be completed. The rectification ratio was found to be a reliable indicator of diode performance and applied to the study. This would mean writing additional code in MATLAB to assist in the automatic analysis for the measured IV curves. Progression to AC / RF measurements of tunneling performance was to be accomplished using relatively low frequencies (below 100 MHz). Finally, the organic films, themselves, would be studied for consistency, impedance characteristics, incidence of defects, and thickness by a variety of metrology techniques.

1.3 Dissertation Structure

While clearly visible in the Table of Contents, I wanted to take a moment to discuss the ordering of information presented in this dissertation. Due to the highly interdisciplinary nature of the research outlined in this work, it is very difficult to start at a basic point and advance forward without crossing into a topic which must be discussed at further time. This unfortunately means some brief explanations of specific terms may be found repeated through

the document. This writing style allows the reader to skip sections they feel technically confident in without the risk of becoming lost in the deeper found jargon and technical aspects of foreign topics.

With this philosophy of writing in mind, the most pertinent and esoteric topic to discuss would be that of quantum tunneling itself. For this reason, after the brief introduction and motivation for work, Chapter 3 starts the technical discussion of tunnel diode physics and modeling of tunneling performance. After this, the reader is more readied to read about the formation of the organic monolayers which are the key element in all the devices which will be discussed in the remainder of the research. Chapter 5 presents a research section which describes methods of optimizing and expanding the monolayers learned about in the prior chapter. At this point in the document, the reader is ready to follow the review of the existing technological systems for testing MIM organic diode structures.

The primary research thrust is presented in Chapter 7 where almost all the experimental aspects of the work are discussed. This includes optimizing the smoothness of the substrate, soft top-contact techniques, optimizing contact area, and packaging for final purpose. The logical next step is to describe the performance characteristics of these resultant devices. Wrapping up the topic, applications and future uses are presented and the conclusions are drawn.

CHAPTER 2:

MOTIVATION

Before delving into the specifics of the project, it is important to give some specific backing to the motivation of an energy harvesting device. At the most basic level, an energy harvester is a device which captures energy from a variety of sources and converts it into a more useful form. This clearly describes a multitude of devices. There is an important difference between energy production, as seen in electrical power plants, and energy harvesting, such as a hydroelectric dam. In energy harvesting, the energy source is typically a cost-free entity such as wind, geothermal, or water flow which occurs naturally and will continue to occur with or without the presence of the harvesting device. This is in sharp contrast to a power plant where perhaps most of the operating cost goes to providing the consumable fuel which is used to generate heat. We can think of the first use of this energy harvesting to be the capture of solar energy for heating and photosynthesis in nature. As for human history, wind power was said to have been utilized as early as 17^{th} century BC where Hammurabi of Babylon purportedly harnessed it for irrigation [1]. Since then, there have been many examples of windmills and water wheels which utilize wind to produce mechanical energy and, in-turn, power some mechanism.

Most of the time, energy harvesting will refer to the generation of small scale power for relatively localized applications. In the energy community, this distribution technique is known as microgeneration. While a solar concentrator powering a Stirling engine is indeed an example

of energy harvesting, this research will focus on much smaller scale examples where power production is less than 10 watts and device size is generally less than 1 m^3. In these systems, an energy harvester can utilize sources not only from nature, but also man-made. A common example is waste heat from an industrial process. The goal is typically to achieve a symbiosis (harvester produces power and improves existing process) or commensalism (harvester produces power and has no effect on existing process) in the applied area. For a symbiotic case study, we can observe a system such as an internal combustion engine which has some undesirable mechanical vibration which can be captured and converted into useful electrical energy to power remote sensors. Here the existing process needed improvement and this was accomplished in addition to power generation. Most natural energy harvesting tends to be an example of commensalism where the energy harvesting devices has no effect, positive or negative, on the outcome of the process. An area of heated debate is truly how little effect a system may have in the wild. Environmental concerns are great as the device would otherwise be useless if it caused more harm than benefit.

2.1 Current Trends in Energy Harvesting

The marketing of energy harvesting solutions has exploded in recent years [2]. Systems come packaged as turn-key solutions to typically power remote sensors or controls, maintain operation of small systems, or work together to generate significant sums of power. Most of these technologies focus on the accumulation of energy for the intended application. Also of importance is the storage and transmission of this power if needed in the application. In the case of a remote solar powered sensor, all three elements may be needed in the design of a complete system. A photovoltaic (PV) array can be used to harvest solar energy which is fed to a

rechargeable battery. From here, the power is used for the sensing application and wireless signals are transmitted to a base station.

2.2 Radiation and Thermal Harvesters

The first group of harvesters we will discuss is radiation harvesters. These will be made to broadly include all types of electromagnetic radiation from battery-less AM radios to ultraviolet (UV) sensitized PV panels. Implementation of radio frequency identification (RFID) systems is an example of short-range communication made possible by energy harvesting. For energy applications, stray radio waves offer very low power margins often barely able to power significant electronics. A special type of radio wave harvester which is optimized for the upper MHz through GHz range called the rectenna will be discussed separately in the following section. Photovoltaics (PVs) are semiconducting structures which generate DC electricity through the photovoltaic effect. When the PV structure is exposed to light, electrons in the valence band absorb the photon and jump into the conduction band. The fine conductive circuitry around the PV panel directs these free electrons to the intended circuit. There are many different types of PV technologies in place today [3]. The most popular are crystalline silicon-based junctions. A p-n junction is formed near the surface of the silicon where the power generation takes place. An illustration of this process is seen in Figure 2.1. For most commercial photovoltaic installations, only around 20% of the incident light energy is converted into electricity. Much of the energy is emitted as heat either from the face or back of the PV panel.

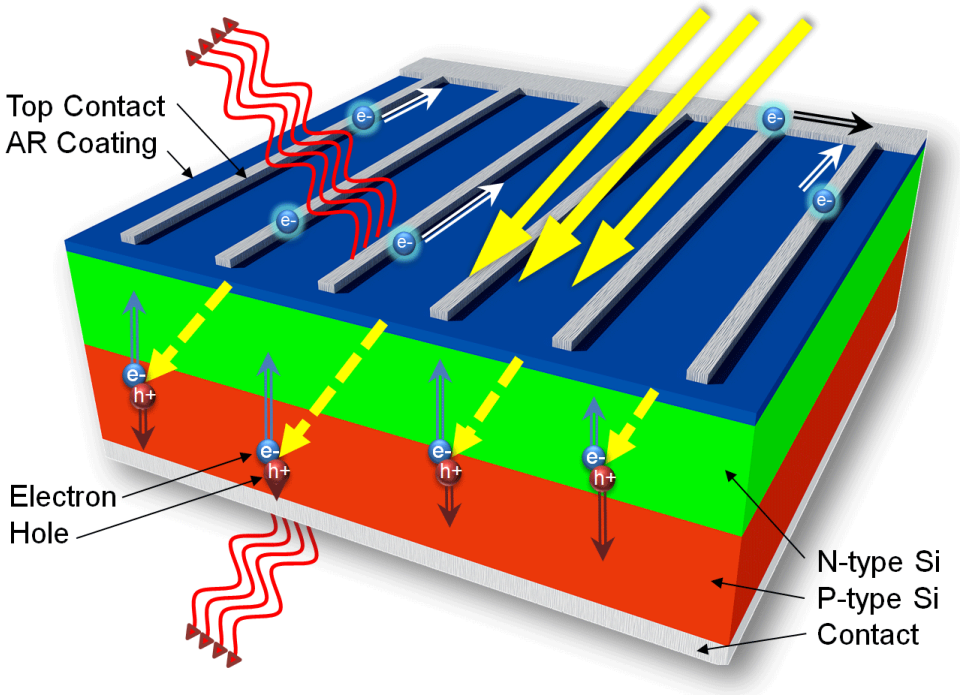

Figure 2.1: An illustration of a photovoltaic solar panel in operation. Light, incident from top right, generates pushes valence electrons into the conduction band and down the top conductors. Waste heat is largely generated due to photons which are either above or below the semiconductor bandgap.

In practice, there are a number of losses which makes this conversion quite inefficient. Efficiency in PV elements is calculated by the following equation:

$$\eta = \frac{P_{PVCell}[W]/Area[m^2]}{P_{Light}[W/m^2]} \tag{2.1}$$

Single junction PV elements face quantum efficiency problems. The bandgap of the semiconductor is a minimum energy level which the incident photon must overcome to excite the electron sufficiently to raise it to the conduction band. Any photons which have less energy (below-bandgap photons) than this are typically absorbed and re-emitted as heat. Photons with energies higher than that of the semiconductor result in surplus energy being wasted. At lower bandgaps, there is significant relaxation to the band edges. Collectively, these parameters are described by the Shockley-Queisser limit which predicts a maximum theoretical efficiency of

around 33.7% for a single junction solar cell [4]. The workaround to this was found by creating multi-junction panels with varying bandgaps. In these structures, the junctions are applied in increasing energy order resulting in preferential capture of blue-shifted photons at the top layer(s) and red-shifted photons in the lower layers(s). This is made possible because the thinner top layers do not interact significantly with the longer wavelength light which is to be absorbed by a lower layer [5]. Efficiency and practicality limitations are still present in these complex structures. Cost is a major inhibitor of multi-junction panels. Still, in applications where solar energy is concentrated (for example through the use of Fresnel lenses) reduced system cost and increased efficiency can be realized. As of the writing of this document, the most efficient single junction systems top out at around 25% with multi-junctions demonstrating up to 44% under concentrated light [6].

Additionally, but not directly related, are thermal energy harvesters. Sources of waste and natural thermal energy are ubiquitous [7]. Here, we make the distinction between thermal energy and thermal radiation in the form of how it is captured. Radiation of infrared light (heat) through a vacuum or low density fluid (e.g. air) constitutes thermal radiation. Thermal energy which is conducted through direct contact with the thermal source can be described as thermal energy. Both sources can, within reason, can be converted for ease of energy harvesting. This is commonly seen through industrial solar thermal power stations which use mirrors to concentrate the radiation energy of the sun onto a blackbody surface to facilitate conduction with the heat transfer fluid (HTF). The HTF, typically a low vapor pressure liquid or low melting temperature salt, is circulated at the rear of the absorber and utilized at a nearby turbine. Examples of natural thermal energy are geothermal and solar thermal. Of course, solar thermal is actually thermal radiation which has been absorbed for ease of use. In addition to turbines, thermal energy can be

converted to motion and electricity through the use of a Stirling engine. Because these systems can be made very small, micro generators based on parabolic dish collectors and absorbers are possible [8].

Besides mechanical motion, heat can be directly converted to electricity though exploitation of the Seebeck effect. Known as Peltier heat pumps, multiple p-n semiconductor junctions are arranged in a 2D plane resulting in a reversible heat pumping surface. Through the application of current, thermal energy can be forcibly driven up or down through the Peltier plane. Furthermore, if a temperature gradient is established between the two sides of the heat pump, electricity will be generated [9]. This electricity is conveniently direct current and can be used directly or stored simply in a capacitor or battery. These systems can be manufactured using microfabrication onto single chip thermal harvesting devices. In turn, these small, thin harvesters could be used to generate power using heat sources as low-grade as human body heat in a cool ambient environment. When rigorous calculations are explored, it would seem that these systems prove to be poor cost values for their generation capability. The low efficiency and low power output of human body thermal harvesting is clearly visible when we consider the Carnot cycle efficiency expression and factor in the average human body temperature (≈37°C) and the average surface temperature of Earth (≈16°C):

$$\eta_{max} = 1 - \frac{T_{cool}}{T_{hot}} \tag{2.2}$$

This gives a maximum system efficiency of 6.88%. For thermoelectric harvesters, a more realistic upper limit is shown by the following equation:

$$\eta_{max} = \frac{T_{hot} - T_{cool}}{T_{hot}} \frac{\sqrt{1 + Z\overline{T}} - 1}{\sqrt{1 + Z\overline{T}} + \frac{T_{cool}}{T_{hot}}} \tag{2.3}$$

Here $Z\overline{T}$ is a figure of merit which is simply expressed as:

$$Z\overline{T} = \frac{\sigma T S^2}{\lambda} \tag{2.4}$$

where σ is electrical conductivity, T is temperature, S is the Seebeck coefficient, and λ is thermal conductivity. This equation is modified to take thermoelectric capacity for both materials into consideration and becomes:

$$Z\overline{T} = \frac{\left(S_p - S_n\right)^2 \overline{T}}{\left(\sqrt{\rho_n \kappa_n} + \sqrt{\rho_p \kappa_p}\right)^2} \tag{2.5}$$

where ρ is electrical resistivity, $\overline{T}$ is the average temperature, and the subscripts p and n describe which semiconductor properties are being described.

It should be noted that average indoor temperatures are considerably warmer than this. Under normal waking conditions, the average human body produces 100 – 200 W of heat through the entire skin surface [10]. All these factored together, the maximum theoretical power we could expect to extract from a 100 cm^2 thermal harvester of human heat is 77.4mW. (Assuming average human body surface area (BSA) of 1.75 m^2 [11].) Practical Peltier-based systems which take into account more average ambient temperatures, realistic coefficient of performance, and conservative human thermal output are likely to see generation closer to 15mW.

2.3 The Rectenna

Until now, we have been carefully working around the key subject which must be discussed—the rectenna. The word rectenna is a portmanteau of the words "*rec*tifying an*tenna*." At the simplest level, it is an antenna tuned to couple some RF energy into traces or wires where it is rectified from AC to DC power. These devices will operate as long as the turn-on voltage of the rectifying element is below the amplitude of the coupled RF signal. One of the earliest

examples of this technology in application was the crystal radio. In this application, the radio wave is coupled into a simple wire antenna and rectified by a cat whisker diode made typically of a Galena (Lead (II) Sulfide) crystal. For the purpose of simplicity, the tunable capacitor and inductor typically accompanying these devices are omitted. At these low frequencies, there is barely enough energy to drive a highly efficient piezo earphone. Still, the entire operation is powered from the harvested RF energy.

The rectenna as it will be known for the rest of this document was invented in 1964 by William C. Brown [12]. He used a dipole antenna rectified by a Schottky diode to convert microwaves into DC power (Figure 2.2). In a very popular demonstration, a toy helicopter achieved wireless powered flight by converting the incident 2.45GHz radar emitter feed below to useful DC power which spun the rotor. The Schottky diode was selected for this application because of its high switching speed and low forward voltage drop. This meant more of the power coupled into the antenna would be converted form AC to DC and thus more was available to power the intended application. There have been successful industrial implementations of wireless power transfer in the microwave region using this technology. It was proposed that this technology could be extended into high frequencies approaching that of visible light [13]. If the antenna, impedance matching circuitry, and rectifier could all be built to an appropriate size and operational speed, the system could, in theory, be used to rectify light—which is an electromagnetic wave. This was a very attractive proposition because it opened up the possibility of direct harvesting of solar radiation and remote harvesting of waste heat from industrial and possibly even animal sources.

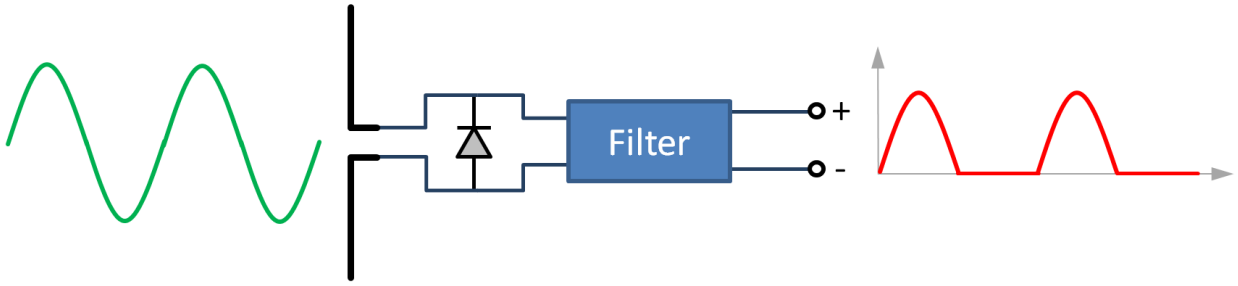

Figure 2.2: An illustration of the operation of a single diode rectenna system. The incident electromagnetic radiation is coupled into the antenna and a clamp diode serves to restrict AC flow resulting in DC power after filtering.

2.3.1 Incident Radiation and Concentrators

Before we can talk about the classical rectenna, we must first discuss the source of power. The incident radiation, for most applications, is presumed to be of solar nature. There have been many studies which have debated whether or not coherent light would be necessary to achieve power output. It is now generally accepted that the light does indeed need to exhibit coherence to achieve efficient output. Two proposed methods are commonly seen in literature as a solution. The first takes advantage of the observation that sunlight is spatially coherent over small area domains. This means that if a small enough area can be used for the purpose of harvesting, the light will be sufficiently coherent to allow for rectification. For a circle with a diameter of 38 μm, incident light will be 90% coherent [14]. This value drops to 50% for a diameter of 120 μm and 9% for 400 μm. Any antennas or antenna arrays must be designed keeping these rules in mind. Alternatively, some type of emitter-concentrator may be fashioned over the rectenna. This may be able to serve multiple functions which would prove beneficial for energy conversion. (1) The generation of coherent energy from randomly oriented energy. (2) The emitter-concentrator may serve to concentrate weak sources of electromagnetic energy to achieve greater efficiency. This concept is subject to interpretation dependent on the operating

regime. For classical rectenna models, this concentration proves functional but when semi-classical quantization of photon packets is considered, this may not hold true. (3) The cover can serve to protect the delicate rectenna system from environmental damage. This may include corrosion, abrasion, oxidation, etc. (4) The emitter may be able to shift the frequency of the incoming radiation to produce a more monochromatic source for rectification. Because antennas can be made most efficient for narrowband applications, this would improve antenna efficiency.

2.3.2 Antenna Design

The rectenna requires four major functional groups for successful operation. While especially true when attempting high frequency rectification, these additional components benefit energy conversion at all frequencies. An appropriate antenna must be selected to couple the incident RF energy. In the research environment, simple planar etched antennas are often selected for ease of experimentation. Since a very small antenna size is needed as incident radiation approaches that of IR light, nanofabricated antennas and carbon nanotubes have been demonstrated as antenna candidates [15]. When considering harvesting, an array of antennas will be required to capture a large field of incident RF energy. Optimization of radiation pattern, effective aperture, antenna gain, size, bandwidth, and pattern arrangement must all be addressed. Fractal patterns have been proposed as an efficient topography for antenna arrangement [16].

For experimentation, dipole antennas have received the most attention because of the straightforward fabrication process. Within this family is the bow tie antenna with a diode located at the connection point of the two terminals. The bow tie antenna exhibits better broadband performance and is more attractive for harvesting. To couple more efficiently to

varying polarizations of incoming energy, spiral antennas have been implemented with junctions at the center where the spirals meet.

Next, the antenna must be impedance matched to the rectification element. The matching network of lower frequency rectennas is typically comprised of discreet inductors and capacitors which serve to minimize reflections prior to rectification. In smaller applications, surface structures which approximate these functions are microfabricated onto the same die which carries all the other components. Further still into the upper gigahertz regime, tuning the antenna impedance comes in the form of structural design changes. It should be noted that each design choice here must attempt to minimize losses at all processing stages. While attempting to match the impedance of free space (376.73Ω) might seem attractive, most transmission techniques are lower impedance (50 to 75Ω) [17]. This means losses in the form of reflection would be higher. Most antennas are in the range of 100Ω.

For a receiving antenna couple to some load, we can express the voltage between the dipole terminals as:

$$I_L = \frac{V_{oc}}{Z_A + Z_L} \tag{2.6}$$

where V_{oc} is the open circuit voltage, I_L is the current through the load, Z_A is the antenna impedance, and Z_L is the impedance of the load. Looking at Equation 2.6, it is clear that a very large rectifier impedance will significantly limit the current flow possible at the rectifier. In addition, RF reflection due to a significant mismatch can be expressed by the reflection coefficient:

$$\Gamma_{12} = \frac{Z_R + Z_A}{Z_R + Z_A} \tag{2.7}$$

where Z_R is the rectifier impedance and Z_A is the antenna impedance. The aforementioned expressions hold true for classical frequencies only. As rectification approaches the THz regime, a semi-classical approach is required to estimate antenna voltage. This approach is discussed around equation 2.10 in the section to follow.

2.3.3 The Diode

The primary challenge in the quest for a high speed rectenna (often touted: nantenna—due to its scale requirements) is the rectifier. As we have read earlier in the background, the harvesting rectifier requires a very high speed diode. Schottky diodes which were used in microwave harvesting will not be capable of operating far into the hundreds of terahertz required to approach the near-IR operating regime [18]. Tunnel diodes which operate on quantum mechanical principles can function near the required frequencies. A summary of the different diode characteristics are given in Table 2.1. Unfortunately, there are still a number of challenges when considering the fabrication of a diode which operates in the hundreds of THz.

Table 2.1: Comparison of various diode technologies as rectifiers and their respective strengths and weaknesses.

	Silicon Diode	Schottky Diode	Tunnel Diode
Rectification Principle	P-N Junction	Majority Carrier	Quantum Tunneling
Turn-on Voltage	0.6 – 1.7 V	0.15 – 0.45 V	Varies
Recovery Time	3.5 ns	100 ps	n/a
Reverse Leakage	Very Low	Low	High
Frequency Limiting Factor	Recombination	Mostly RC	RC

First is parasitic capacitance. The contact area required is determined in part by the roll-off frequency for the capacitor-like structure of the MIM diode:

$$f_c = \frac{1}{2\Pi R_a C_a} \tag{2.8}$$

where R_a is antenna resistance and C_d is the capacitance of the diode. For this nano-scale parallel plate capacitor, operation is primary quantum tunneling. Still, we must consider the capacitive effects of placing two planar conductors in a structure separated by an insulator. We have a simple expression for capacitance:

$$C_d = \frac{\varepsilon_o \varepsilon_r A}{d} \tag{2.8}$$

where ε_o is the permittivity of empty space, ε_r is the permittivity between the plate materials, A is the contact area, and d is the separation of the conductors. An example of the incredibly small contact area required is seen when we consider rectification of far-infrared light of 20 THz. With a reasonable polymeric permittivity assumption of 2.5, the diode should be a square with sides smaller than 147nm. A full example set of diode dimensions are seen in Table 2.2.

Table 2.2: Example electromagnetic energy comparing frequency, photon energy, and MIM contact size. An organic insulator of 3nm is assumed to have an εr of 2.5 in these calculations.

Electromagnetic Region	**Wavelength λ**	**Frequency Hz**	**Photon Energy**	**Square Contact Side Length**	**Photon Voltage**
Microwave	1 mm	300 GHz	1.24 meV	1.20 μm	1.24 mV
Far IR	25 μm	12 THz	49.6 meV	190 nm	49.6 mV
Far IR	15 μm	20 THz	82.7 meV	147 nm	82.7 mV
Long IR	10 μm	30 THz	124 meV	120 nm	124 mV
Mid IR	5 μm	60 THz	248 meV	85 nm	248 mV
Short IR	1.5 μm	200 THz	827 meV	46 nm	827 mV
Visible Red	750 nm	400 THz	1.65 eV	33 nm	1.65 V

This scale of fabrication is now possible using advanced photolithography techniques but is typically reserved for production facilities rather than research experimentation. For the research community, e-beam lithography is commonly used to achieve these small geometries at the

expense of very slow write times and small field which can be processed. Recently, advances in roll-to-roll manufacturing have demonstrated success in duplicating patterns cheaply and to great fidelity. Micro-gravure and nano-imprint lithography have been the subject of a technical revival. Application of fluid mechanical modeling to these old forms of duplications have resulted in highly predictable prints [19].

Besides fabrication and geometry limitations, there is the aspect of rectification mechanisms. While this will be discussed in greater detail in the quantum mechanical section to follow, at these tremendously high frequencies, rectification is no longer classical. As the voltage equivalent of the incident photon:

$$V_{photon} = \frac{\hbar\omega}{e} \tag{2.10}$$

approaches or exceeds the turn-on voltage of the diode, a semi-classical approach is needed for analysis. This is often described as photon assisted tunneling (PAT) [20]. Diode performance can be given by rectification ratio or (more usefully) diode responsivity, β_d, where:

$$\beta_{diode} = \frac{I''}{2I''} \tag{2.11}$$

Qualitatively, the diode needs four key characteristics to operate correctly in a THz rectenna system. First, the diode resistance needs to be as low as possible. An impedance match is critical in the rectenna system to achieve efficient power transfer. As the antenna operating frequency is pushed towards the visible range, antenna resistance will rise to the low hundreds of ohms [21]. Most MIM tunnel diodes exhibit resistance which is orders of magnitude larger. This will be a source of system crippling loss if implemented without a matching solution. From a quantum mechanical point of view, resistance is lowered with barrier height. This translates

into a thinner insulator and a larger contact area. Unfortunately, as we are about to see, this causes problems with the subsequent characteristics.

Capacitance is the next hurdle to overcome. As detailed clearly above, the roll-off frequency (or time constant if considering semi-classical operation) is highly dependent on the capacitance. Because the diode resistance, ideally, should be tailored to achieve the best power transfer and impedance match, this leaves capacitance as a key variable. When considering very low resistances (100Ω) which might operate well in theory, we find the required contact area drops to a 100 nm^2 [22].

Turn-on voltage is still a point of controversy. Some argue that a sharp I(V) curve inflection is all that is required to achieve small signal rectification. The diode can be external or self-biased in such a design which can allow the "turn-on" voltage to be located anywhere. In practice, there are losses associated with biasing. These losses are often far outweighed by the improved performance of the diode in application. The concept of diode turn-on is perhaps a misnomer as it transfers the label of a phenomenon which occurs within semiconductor-based diodes and reappropriates it to tunnel junctions. Instead, tunnel diodes typically have softer inflections where ever greater amounts of current are able to tunnel through the barrier. Sharper inflections in the I(V) characteristics of the tunnel diode are desirable but typically come at the price of a thicker dielectric layer. As the barrier thickness increases, so does the resistance of the diode. Immediately, it is evident that balancing one parameter of the diode causes significant upsets in other areas.

Reverse-bias leakage current will be a familiar parameter to all who regularly work with diodes. When biased in the negative voltage region, the ideal diode will exhibit practically no current flow. Tunnel diodes are based on a barrier and despite how trapezoidal the barrier shape

can be made, some current will be able to flow in the reverse direction. It is therefore common to describe the difference in forward and reverse current in terms of asymmetry. A highly symmetrical diode with similar metals and a rectangular barrier will exhibit identical reverse and forward bias characteristics. The techniques which reduce reverse leakage current typically increase the forward-bias resistance. A simple measure of diode operability is rectification ratio where the quotient of the forward current and the reverse current are taken at a given voltage. This is normally expressed in an absolute value plot for positive voltage values. Looking at this plot can help determine the optimum point of bias based on the amplitude of the incident signal.

2.3.4 Topographies

The layout or topography of the rectenna system is an important design aspect of a successful system. Research has focused on fractal antenna systems in the past to realize gains for multi-band communication applications [23]. These multi-band advantages can be translated into broadband energy conversion in the area of the rectenna. In addition to frequency selectivity, the coherence, intensity, and polarization of radiation entering the rectenna system direct how system architecture must be constructed. It is for this reason that research focus on emitter-concentrators was deemed necessary. By producing a consistent and predictable radiation profile, a higher efficiency rectenna system could be designed—tailored for the output under the expected conditions. Independent of the rectifier, one can combine either the RF or DC signals in the rectenna array. Topology using DC combiners are best for networks with very high number of antennas while RF combiners are best with fewer elements. An example of these can clearly be seen in Figure 2.3.

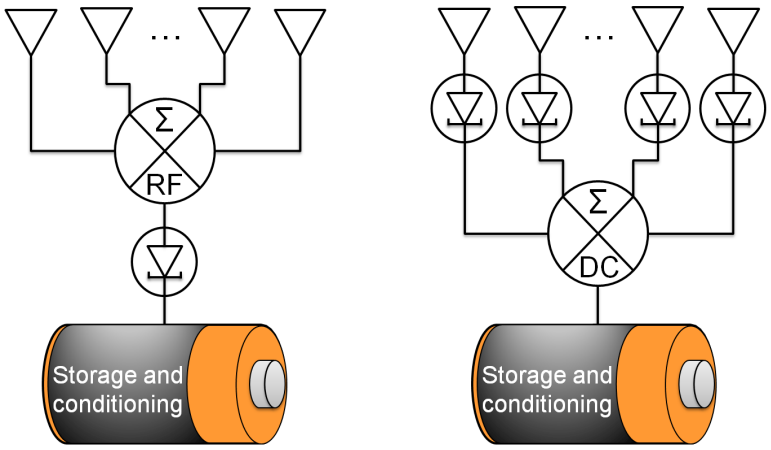

Figure 2.3: A schematic of different antenna-rectifier topologies. In the first example, RF power is mixed from nearby antennas and fed into a common rectifier diode. Higher signal amplitude here results in less diode turn-on losses. At right, each diode rectifies the signal from its respective antenna and the DC signals are combined.

There is not a universally better system among the two. The RF combiner topology is superior for systems with very weak signal input. Because the amplitudes are summed, the diode operates well above its turn-on voltage and a greater percentage of power is allowed to flow into the DC backend. It is important to note that the RF combiner will results in greater losses than a DC combiner and will be more complex to design. On the other hand, when signal amplitude is high (and assuming diodes are not expensive to manufacture), the second scenario offer a familiar layout of discreet rectenna elements which are combined at the DC stage. This type of combination topology is the most often attempted due to the simple connectivity required.

The final step in the conversion is power conditioning and storage. Very little consideration in research is placed on this final step. Despite the straightforward nature of DC power conditioning, the development of filters comprised of THz inductors and capacitors may not be trivial. Pulsed DC power at these high frequencies must be conditioned to permit use in semiconductor and logic applications. In scenarios where excess power is being generated, the conditioning system may be employed to charge a battery or supercapacitor (SC). The power

storage will likely be staged to take advantage of downstream semiconductors which are more efficient at handling larger currents. An example of a staged power distribution may involve an on-die supercapacitor which is drained in pulses to charge a conventional battery.

2.3.5 Efficiency

System efficiency is of utmost important for a harvesting system. The sources of waste heat are typically very low grade and thus are intrinsically low energy. In the rectenna, each component is dependent on the output of the previous for operation. This series nature quickly diminishes outputs of working devices. Optical rectification has been reported but there is often argument as to whether it is indeed rectification or simply the formation of a thermocouple and response from radiation heating.

The rectification equation which describes the overall system efficiency appears to be reported incorrectly in most texts. Overall rectenna efficiency can be given by:

$$\eta_{system} = \eta_a \eta_s \eta_c \eta_r \tag{2.12}$$

where η_a is the coupling efficiency of the electromagnetic radiation of interest to the antenna. As we have seen, there are many different antenna designs which seek to improve broadband and varied polarizations. The efficiency term, η_s, describes the efficiency of energy propagation (phonon conduction) within the antenna leading through the rectifier. The coupling efficiency, η_c, is governed by the impedance match of the diode to the antenna. Lastly, the efficiency of the rectifier is given by η_r. As recently as late 2013, the diode responsivity, β_d, was described as being equal to that of the rectifier efficiency, η_r, by a number of authors. This assumption ignores the rectenna layout which is almost always described in terms of clamp diode across a dipole antenna as depicted in Figure 2.2. In this half-wave rectifier setup, the maximum η_r

possible is 0.5 for cases where $\beta_d = 1$. Of course this is not a realistic assumption as a diode with a β_d of unity (Figure 2.4b) would exhibit: (1) a reverse-current leakage of nearly 0nA, (2) a turn-on voltage at some infinitesimally positive voltage above 0V, and (3) a near infinite forward current handling capability. In Figure 2.4, we see the effect of varying β_d efficiency values and the resultant η_r. A full wave bridge rectifier consisting of tunnel diodes will provide greater rectification efficiency at lower frequencies (provided diodes exhibit a $\beta_d > 1$). However, the added component load and circuitry will likely make this solution impractical for rectification at very high frequencies. There are other ideas being circulated on how rectenna efficiency can be improved. Because narrowband antennas tend to have very high gain, and thus high efficiency, a beam splitting concentrator might be able to break a continuous radiation spectrum into two or more notch tuned sources. These can be channeled, respectively, to well-tuned rectenna systems. While the use of a beam splitter is practical in the laboratory, it is not immediately evident how such a device can be deployed in practice.

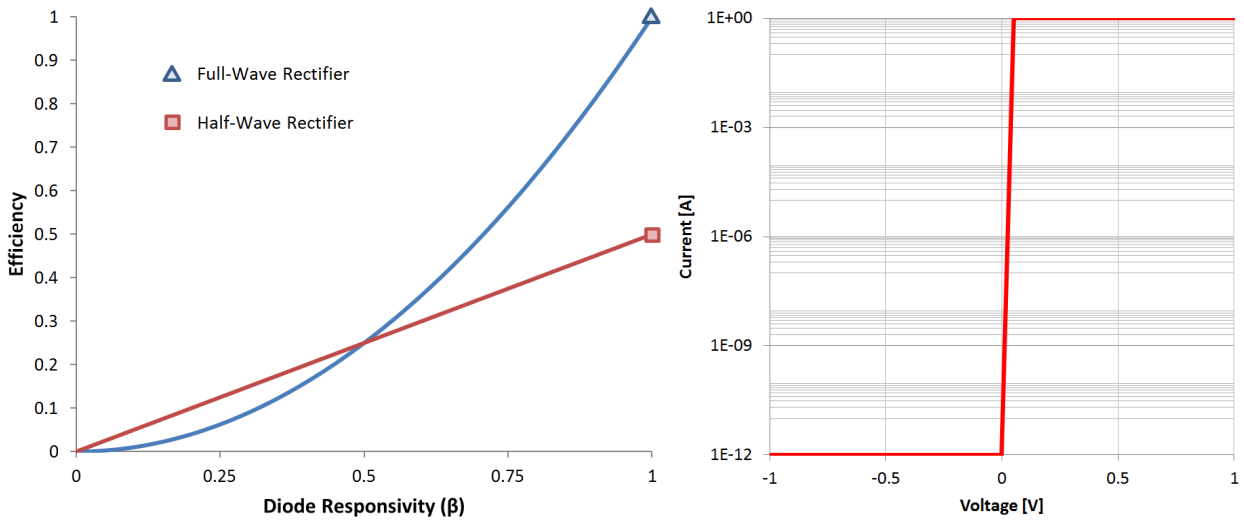

Figure 2.4: Graph of efficiency comparison of two different rectifier schemes. For diode responsivities >0.5, it is advantageous to consider the full wave bridge rectifier if extra components and traces do not introduce excessive impedance and capacitance. At right (b), the I(V) curve of a near-ideal diode which might produce a β_d approaching unity.

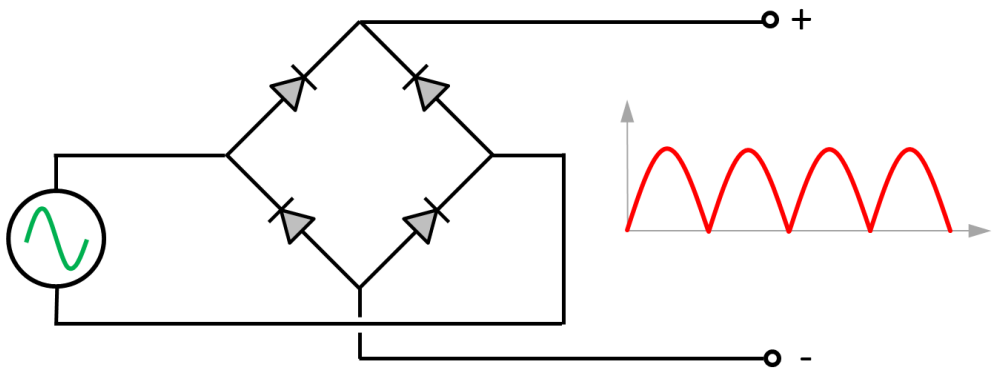

Figure 2.5: An illustration of a full-wave bridge rectifier and the pulsed DC output. For cases where the AC source (left) is replace with a dipole antenna, evaluation of the two rectifier topographies must be evaluated to select the most appropriate. Despite being more efficient for lower frequencies, the added parasitic inductance, capacitance, and resistance of the more complicated setup may prove to be not advantageous at higher frequencies.

2.4 Motion Harvesters

Commonly deployed energy harvesters capture motion energy (both microscopic and macroscopic) for the purpose of energy production. We have already seen capture of linear motion in the original example presented at the start of this chapter—the windmill. The laminar wind flow was mechanically converted into rotational energy which turned the alternator/generator which generates electricity. On a much smaller scale, vibrational energy can be harvested by devices down to near atomic length scales.

Vibrations can manifest in a variety of modes depending on the shape and size of the harvesting source. Vibrations are a common source of nuisance energy loss which typically has detrimental effects on the machine or structure within which they manifest. There have been multiple demonstrations of chip-scale energy harvesters which utilize proof masses on beams [24], masses which slide freely, torsion springs [25], and pressure differential membranes to name a few.

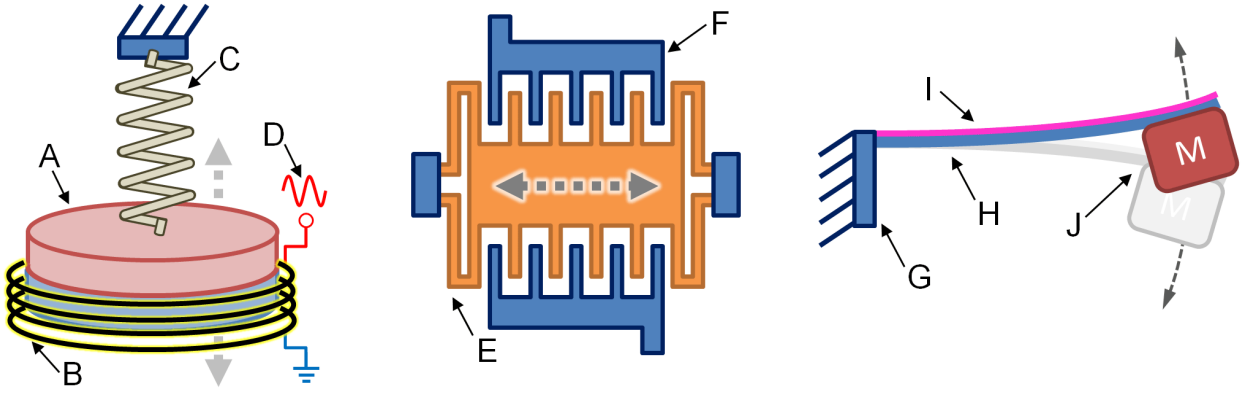

Figure 2.6: A set of illustrations depicting the operation of various vibration energy harvesting devices. At left, an electrodynamic energy harvester fixes a permanent magnet (A) to a spring (C) which is allowed to freely swing within a coil (B) which generates an AC signal (D). At center, an electrostatic harvester contains a set of fixed electrodes (F) and moving electrodes (E) where MEMS springs allow predominantly 1-axis movement and field generation at the combs. At right, a piezoelectric material (I) is applied to a flexible beam (H). The vibration forces at fixed point (G) result in oscillation of the proof mass (M) generating voltage within the piezo material.

Within these physical collection configurations, the backing technology enabling harvesting can be through electrodynamic, piezo electric, magnetostrictive, or electrostatic (Figure 2.6) [26, 27]. The intermittent nature of typical power sources require advanced power conditioning and optimization to make practical power for use by an electronic system. Moreover, each back-end transduction technology has advantages and disadvantages which must be weighed carefully with the intended application and nature of waste vibration. A brief presentation of the strengths and weaknesses of some of these various methods can be seen in Table 2.3.

Table 2.3: A table comparing the advantages and disadvantages of various mechanical vibration transduction methods.

Transduction Method	Advantages	Disadvantages
Electrodynamic	▪ Simple construction ▪ No start voltage	▪ Large size ▪ Low voltage generation
Piezoelectric	▪ High voltage output ▪ Direct MEMS fabrication	▪ Low Durability ▪ High output impedance ▪ Charge leakage
Electrostatic	▪ High voltage output ▪ Direct MEMS fabrication	▪ Start voltage needed ▪ Narrow bandwidth
Magnetostrictive	▪ High frequency response ▪ High coupling coefficient	▪ Non-linear response ▪ Complex inductor

Adapted from Wang, L and F. Yuan 2007.

CHAPTER 3:

TUNNEL DIODE PHYSICS

The tunnel diode is also known as an Esaki diode—named after Japanese researcher Reona Esaki who shared the Nobel Prize in Physics for his discovery of electron tunneling [28]. Quantum tunneling is a somewhat strange concept which seems to break many classic laws of physics. The fact of the matter is that at these atomic length scales, classic physics as we know it breaks down and leads into quantum mechanics. The treatment here is to begin with a study of quantum mechanics and progress to the device structure which may be useful in application. Finally, a review of the theoretical models and MATLAB analysis software will be given.

3.1 Quantum Mechanics

Quantum mechanics (QM) is the study of the physics of events at microscopic and smaller scales. The laws which govern this invisible world would make no sense at our scale. In QM, we see objects that are able to pass through barriers, seemly random events which cannot be predicted on a single event basis, and uncertainties in velocity and position relationships. These are just some of the strange characteristics of this branch of physics. Fortunately, the study is not relegated to chance as there are a number of rigorous equations which can be used to describe the phenomena seen at the atomic scale.

The name of the science is formed from the observation that some measured values change by discreet amounts. For example, we can move in any direction in space and it would

appear as though we can be located at an infinite number of positions. At the extremely small scale on the order of a Planck length (10^{-35} m), it is believed that you can approach the granularity of space itself. On this length scale, motion would perhaps resemble the illumination of pixels on a display—an adjacent cell turning on just its nearest neighbor turns off. It is important to consider how incredibly small this length scale is tiny subatomic particles such as electrons are still 17 orders of magnitude larger.

When trying to understand how these laws in any way relate to our world, we must consider the immense number of events which occur at the quantum scale. If we consider the humble coin toss, we know that that there is a 0.5 probability of the coin landing on "heads". What that means is that for an infinite number of trials, the coin should land half the time on heads and half the time on tails. While we can predict this with great certainty, it is impossible to know what the next flipped state of the coin will be. Quantum events occur in a seemly random manner in the same way; while it is impossible to predict individual events, the trends through countless trials collapse into very regular and predictable patterns.

One of the first important concepts to understand within QM is that of particle-wave duality. The understanding is that objects traveling at some velocity exhibit properties of both particles (as we would expect) and that of waves [29]. There have been numerous experiments which have demonstrated this strange phenomenon with very consistent reproducibility. While not the first, the most popular of such experiments was Thomas Young's double slit experiment [30]. The setup consisted of a coherent light source passing through two parallel slits. The light transmitted on the screen behind the slits exhibits bright and dark bands which would result from interference of waves.

Similar results would occur for hydrodynamic fluid experiments. This seems unremarkable until we consider the same setup where only single photos (packets of light energy) are allowed to reach the slit at any given time. Because only one light packet (photon) reaches the slit, one would assume that it must go through one slit or the other and evenly disperse on the screen. However, even in this scenario, we still observe bright and dark bands when the photon landing locations are summed over time [31]. This diffraction in the absence of direct interference is observed not only for tiny particles such as electrons but has also been seen in larger molecules such as C_{60} Fullerenes [32]. It is not necessary to discuss the equations behind this phenomenon however, it is important to note that the only logical conclusion as to how this may happen is that the particle going through both slits at once. Even though it is possible to predict with great accuracy what the overall probability of an event is, it is impossible to determine where the next particle will strike on the screen. Put another way, the appearance of the screen at the conclusion of the experiment can be predicted with great accuracy while the determination of the landing site of a single photon is impossible.

3.2 Barriers and Thickness

One of the appealing applications for two-terminal organic devices is a molecular rectifier. The principle of operation is quantum mechanical tunneling through the dielectric. This rectifier promises speed which is not possible in conventional or Schottky diodes. These devices are quite simply composed of a metal-insulator-metal (MIM) stack. Tunneling is not seen in the macroscopic world and involves a particle at some energy passing through a potential barrier which is at a higher energy [33]. Because there are no carrier recombination delays as in the prior two examples, the primary factor affecting maximum operating frequency is parasitic

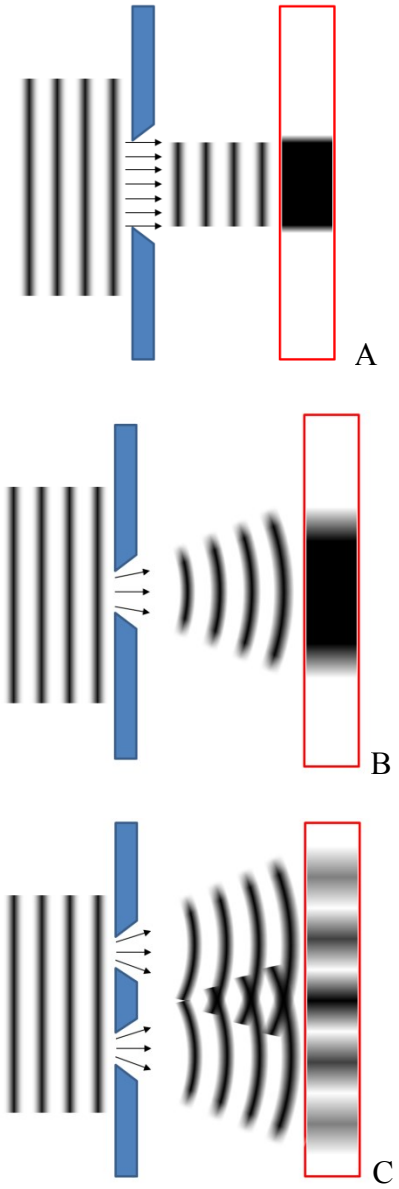

Figure 3.1: An illustration of Young's double-slit experiment. Coherent light appears incident at left which passes through a slit and is allowed to illuminate a screen at right. In (a) where the slit separation $d >> \lambda$ (wavelength of incident light), there is minimal diffraction observed. In (b), we have a slit separation, d, on the order of the wavelength, λ, and observe diffraction. In (c), two slits cause the wave nature of the photos to interfere and result in dark and bright bands on the opposite screen (boxed in red). For print clarity, the light and dark regions are inverted (black indicates a bright band).

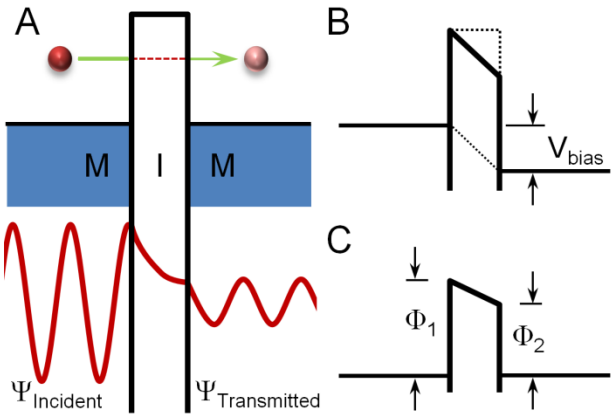

Figure 3.2: An illustration of a barrier and the statistical response of an incident electron. In (A), we see the wave function attenuated after passing the barrier with a higher energy than the incident packet. The effects of bias voltage and work function of boundary metals is seen in (B) and (C), respectively.

capacitance [34]. In the case of SAMs, non-resonant tunneling is seen most often [35]. Typically, metal oxides are used as the insulating layer in the stack [36]. From a particle point of view, the tunneling through the barrier can be understood by imaging the electron as a cloud of probability. When the center of the probability cloud reaches the barrier, if the barrier is sufficiently thin, a significant portion of the cloud may exist on other side of the barrier. This phenomenon was originally described by Heisenberg in terms of the uncertainty principle [37]. Put plainly, it asserts a fundament limit to how well certain property pairs can be known. For the case of many quantum mechanical systems, such complementary variables as position and momentum cannot be both simultaneously known with great accuracy.

There are numerous benefits to incorporating a SAM as the dielectric including: low cost, consistent thickness, ease of application, and fewer through-film metallic defects. Imperfect deposition conditions of metallic oxides typically leads to stoichiometric variations within the dielectric. These affect operation and are preferential sites for device failure. As barrier thickness increases, tunneling probability decreases exponentially. Modeling and experimental

data suggest that barrier thicknesses of about 3 nm are optimal for functional rectifiers. Significantly thicker barriers require a very high voltage for operation and enter into a different operating regime called Fowler-Nordheim tunneling.

3.3 Descriptive Models

There are a variety of descriptive models which are used to predict quantum tunneling in one dimension through one or more barriers, surrounded by two or more conductors. In literature, there is inconsistent reporting of correlation to these models. Because tunneling depends heavily on the surface conditions around the insulating barrier, there is wide variability observed in tunneling characteristics—even those measurements taken within the same lab. Here, we will discuss some of the commonly applied models and finally present a solution to the parameter extraction challenge.

3.3.1 Schrödinger's Equation

Modeling of the tunneling behavior, in the simplest case, describes a finite potential barrier which electrons travel through. This, at the basic level, is described by Schrodinger's time-independent equation for particle travel in one dimension. Due to the complexity of calculation, tunneling is almost always just considered in the one dimensional axis normal to the plane of the device stack. The equation is expressed as:

$$E\Psi(x) = -\frac{\hbar^2}{2m}\frac{d^2}{dx^2}\Psi(x) + V(x)\Psi(x) \tag{3.1}$$

where the Hamiltonian operator acts on the wave function, Ψ. The mass of the particle (an electron in this case) is m, the reduced Planck constant is ħ, x is the distance the particle traveled in the tunneling, the potential energy of the particle is V, the Schrödinger wave function is Ψ,

and the energy level of the particle relative to V is given by E. The solution to this equation comes in the form of wave transmission probabilities. While interesting from a QM perspective, a more useful value is desired. Current density can directly be approximated from these transmission probabilities but an approximation is typically employed.

3.3.2 Wentzel-Kramers-Brillouin (WKB) Approximation

The WKB approximation method was named after three physicists (Wentzel, Kramers, and Brillouin) who devised a mathematical method for finding an approximate solution to linear PDEs (Partial Differential Equations) with spatially varying coefficients [38]. It takes advantage of approximations of slowly changing parameters within the PDE and thus can be expressed as an exponential function and expanded. For the case of Schrodinger's equation we are able to rewrite Equation 3.1 as:

$$\frac{d^2}{dx^2}\Psi(x) = \frac{2m}{\hbar^2}(V(x) - E)\Psi(x) \tag{3.2}$$

where now we can replace the wave function term with:

$$\Psi(x) = \exp(\phi(x)) \tag{3.3}$$

Significant treatment of the resultant equation is needed due to the formation of imaginary components from the derivation of ϕ. For the sake of breivity, these intermediate steps are omitted and the final result of

$$\mathrm{T} = \frac{\exp\left(-2\int_{x1}^{x2} dx \sqrt{\frac{2m}{\hbar}(V(x) - E)}\right)}{\left(1 + \frac{1}{4}\exp(-2\int_{x1}^{x2} dx \sqrt{\frac{2m}{\hbar}(V(x) - E)}\right)^2} \tag{3.4}$$

While this does not immediately seem better than the starting point, does have terms which can be readily entered and a simple output of transmission coefficient for the tunneling particle.

3.3.3 Simmons Model

In the early 1960's, John Simmons [39] set out to derive a theory to model current flow through a generalized barrier. Simmons described this relation which relates the probability of transport (in one dimension) to give current density (J_{DT})

$$J_{DT} = \frac{q^2 V}{h^2}\sqrt{(2m\phi)}exp\left(\frac{-4\pi d}{h}\sqrt{2m\phi}\right) \tag{3.5}$$

from dielectric thickness (d), barrier height (ϕ), electron charge (q), voltage applied (V), electron mass (m), and Planck's constant (h) [40]. This phenomenon can be seen graphically in Figure 17 where the barrier limits electrons traveling to the opposing metal layer. One issue with this simple form of the equation is it does not natively allow for dissimilar work functions to be input. Instead, and average value must be input with some correction factors. For cases where high voltage tunneling is occurring, barrier shape narrows at the top and is said to be in the Fowler-Nordheim regime seen in Equation 3.6 [41]. Specifically, for cases where the bias voltage eV > ϕ_2, the following equation must be employed:

$$J_{FN} = \frac{q^3 E^2}{8\pi h\phi_{FN}}exp\left(\frac{-4\sqrt{2m^*}}{3qhE}(q\phi_{FN})^{3/2}\right) \tag{3.6}$$

Here the tunneling current is calculated with electric field (E) and electron reduced mass m^*. In this regime, voltage is the primary control variable. The reduced mass term is introduced to simplify the otherwise two equations necessary to describe the interaction of the wave packets with the barrier. The electron behaves as if its mass was the product of the reflected and transmitted components divided by their sum.

3.3.4 Brinkman Dynes Rowel (BDR) Model

A more complete description of tunneling through organic films that accounts for asymmetric barriers and was described by the BDR model [42]. The trapezoidal barrier shape more accurately describes the effects the chemisorbed monolayer has on even similar metal electrodes. The BDR model can be expanded to include additional parameters but it is seen that random inconsistencies in devices significantly affect measured results [43]. The equation settled on to compute current is:

$$J = \frac{2e}{h}\iint exp\left(-\frac{2}{\hbar}\int_0^s \sqrt{2m\phi(x,V,E)}dx \times \left[f\big(E(k)\big) - f(E(k) - |e|V)\right]\right)dEdk \quad (3.7)$$

where s is the barrier thickness, ϕ(x, V, E) is the barrier height as a function of position at bias V with an electron incident energy of E, m is the free electron mass, f is the Fermi function, e is the elementary charge, and k are wave vectors which run in the same direction as the junction.

When considering application performance, these very thin barriers are still easily destroyed with very high voltage despite having a very high breakdown strength (E_b > 50MV cm^{-1}) [44]. Still, for most applications which call for small signal rectification, they are a very appealing candidate. This high performance rectification unlocks the capability to directly rectify high frequency electromagnetic radiation [36].

$$f_c = \frac{1}{2\pi R_a C_d} \quad (3.8)$$

In equation 5, f_c is the cutoff frequency, R_a is the antenna resistance, and C_d is the capacitance of the diode. The MIM diode capacitance is a function the junction area, A, and dielectric thickness, d, as shown in the following relationship

$$C_d = \frac{\varepsilon_0 \varepsilon_r A}{d} \quad (3.9)$$

Organic dielectrics open up additional possibilities for tunneling control with variable chain length, dipole moment, and termination chemistries. Metal work function modification unlocks additional materials options while accomplishing asymmetry control [45]. Combining these properties, devices of high rectification ratio have been reported [46]. As the frequency of operation approaches the THz range, additional concerns of molecular interactions materialize. For these high frequency cases, asymmetric dielectric dispersion may prove a superior rectification principle [47].

3.3.5 Other Considerations and Expansion

Besides tunneling, thermionic emission is often included in complete equations to describe electron flow over the barrier. This happens in scenarios where the barrier is sufficiently low and temperature is sufficiently high to allow some upper tail portion of the Gaussian distribution curve of electrons to be sufficiently energetic to overcome the barrier. Thermionic current can be given by:

$$J = \frac{4\pi me(kT)^2}{h^3} \exp\left(-\frac{\phi}{kT}\right) \tag{3.10}$$

There is thermionic emission current in both directions which will compete and be slightly different for barriers $\Phi_1 \neq \Phi_2$. The contribution to measured tunneling current from thermionic emission is very miniscule at most normal testing conditions. Simulation results confirm that for measured I(V) data, thermionic emission is several orders of magnitude lower than tunneling current.

Different tunneling regimes demand the use of their respective move accurate governing equations. From a modeling perspective, this is accomplished through a piecewise expression

which evaluates the conditions prior to equation selection. This coupled with thermionic emission forms the basis of the customized model selected for MATLAB analysis.

3.4 Model to Experimental Fitting

At this point, the motivation for modeling may not be entirely clear. As we saw, work functions of the conductive layers surrounding the insulator play a large part in determining conduction characteristics. Highly polarized, aromatic, and organometallic insulators affect the work function of the adjoining metal by modifying the Fermi level. In doing so, the work function changes but due to the stacked nature of the device, cannot be directly measured. If we carefully select pure metals whose work functions are well known, we can introduce these values into the model as initial conditions. In addition to this, the barrier thickness, contact area, and experimental I(V) characteristics can be included. From these parameters, it is possible to deduce the work functions required to produce that unique I(V) curve.

Matlab was selected to perform the calculations and automated data manipulation required for this study. A GUI Matlab code was written which prompts the user to select the file to analyze and input all the required variables. At the conclusion, the computer begins an optimized 5D variable search to produce an I(V) with the lowest least-squares value as compared to the experimental one imported. Least squares was selected as a basic and fast measure of quality of fit. The program performs a course mesh with the input parameters and iteratively refines the mesh local to the minima (Figure 3.4) until the convergence tolerances are met. The result is the program reporting the new calculated work function values for the metals in addition to a refined area and barrier thickness value (Figure 3.3). The two I(V) curves are overlaid to demonstrate the variance. Modeling also confirmed that the primary observed mechanism of

conduction is tunneling. Contributions from thermionic emission proved to be several orders of magnitude less.

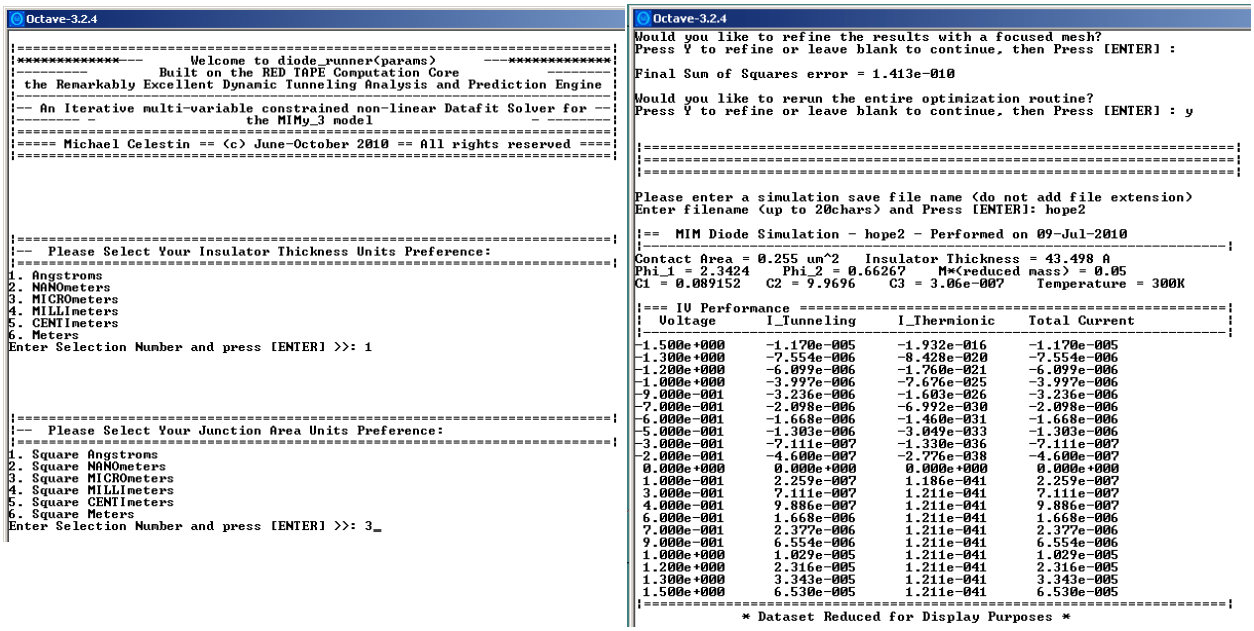

Figure 3.3: A screen shot of the first input and final output screen of the MATLAB simulation. At left, the GUI allows for simplified data entry. At right, the extracted parameters are reported, tabulated, and graphed for user study.

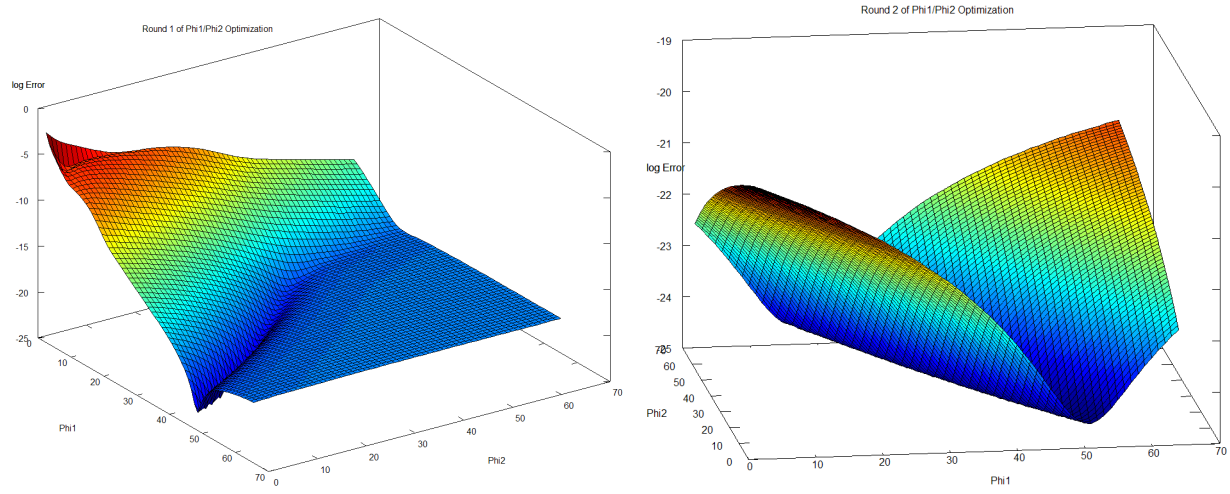

Figure 3.4: A MATLAB simulation output which is optimizing the barrier heights given an initial guess. The routine computes the log of the error and determines the 3D minima.

CHAPTER 4:

FORMATION OF ORGANIC MONOLAYERS

Now that a basic motivation for research and understanding of tunneling has been established, it is useful to understand how an organic monolayer is formed. The focus of this research is on alkanethiol self-assembled monolayers but others will be briefly discussed as well.

To paint a brief picture of the assembly process (in solution) we start with a noble metal coated substrate. For the purpose of this example, we will be using a square 10mm chip of silicon which is e-beam evaporated with a chromium tie layer followed by 100nm of gold. The sample is prepared fresh and immediately placed into a solution containing a millimolar concentration of alkanethiol species in high purity ethanol. Protected from heat, light, and oxygen, the sample is allowed to rest for up to 24 hours (<100kiloseconds) upon which it is removed, rinsed with solvent, and dried in a high purity inert gas stream. At this point, the gold layer will have been modified and exhibit very high surface coverage by the monolayer species.

In the prior example, there were very specific chemicals and materials used to achieve this result. The reality is there are a multitude of different conditions, substrate materials, assembly molecules, and assembly methods and solvents which may achieve similar results. In the interest of clarity, these process steps have been broken up into modules with each one receive due attention. The approach is to talk about these both chronologically and from the ground-up. The discussion begins with the fabrication and selection of the assembly electrode

and material. After the assembly of the monolayer and optimization of film quality, film modification options and real-world considerations are presented.

4.1 Assembly Electrode

The assembly, or bottom, electrode of the two-terminal junction is typically a noble metal. The surface metal and underlying support structure (often glass or silicon) make up what is referred to in some texts as the "substrate." Gold [48-53] has been the most frequently studied material for use as the substrate; however, assembly is also possible on silver [54-57], platinum [58-61], palladium [62, 63], and copper [53, 64, 65]. In addition, semiconductor surfaces such as CdS [66], GaAs [67], and InP [68]. This is not an exhaustive list but simply some common examples. Noble metals tend to be preferred for these studies because they do not form native oxides in ambient environments. These oxide layers will inhibit proper growth of the monolayer given the weaker thiol interaction. It will be shown later that Mercury also serves as an excellent assembly metal and is often leveraged for its featureless, amorphous surface (due its physical state at room temperature) [69-72]. Analysis by electrochemistry of SAMs on Hg shows a low incidence of pin-holes at the expense of a more amorphous packing order as compared to those on solid, crystalline metals [73].

4.1.1 Metal Deposition Methods

From the above outlined materials, metals of interest are deposited by one of a number of thin film techniques onto an insulating substrate of silicon, glass, polyamide, or mica. Because the organic layer is not yet involved, the techniques for this are less constrained and include e-beam evaporation, thermal evaporation, sputtering, electrodeposition, and electroless deposition

[74, 75]. For high noble metals such as gold, platinum, and palladium, which do not readily form oxides, a thin adhesion or tie layer is used to prevent delamination from the underlying substrate. The adhesion layer, commonly between 1-10 nm, is deposited in a high vacuum, oxygen-free environment, and is blanketed with a thicker film of the metal of interest [75]. Common tie layers are chromium and titanium. It is also possible to use these physical vapor deposition techniques to deposit semiconducting materials. Most experiments take advantage of the crystalline wafers commonly available to the semiconductor industry as a ready-to-use substrate. As will be later seen, the order of the monolayer is highly influences by the surface structure of the assembly material.

4.1.2 Metal Selection

One reason Gold has been so frequently studied, as compared to other materials, is its prevalence and ease of application. Gold is very common in the lab and is found in forms such as colloidal, electroplate solution, and evaporation material. Experimentation with SAM coated nanoparticles is explored and will be described in greater detail for the case of non-planar surfaces. For now, we will only consider planar surfaces which are near atomically flat. High purity metal sources should be used since impurities can lead to SAM film defects. A nice feature of noble metals is that they do not readily undergo changes when exposed to atmospheric conditions for short periods of time. While this simplifies handling with respect to oxidation concerns, bare surfaces adsorb adventitious hydrocarbons and other atmospheric contaminants [76]. These surface adsorbates change the interface properties and have the ability to block or hinder the assembly of thiols on the metal surface. The contaminants are not consistent in nature and may have unique properties which can attack the surface and change the electrical, chemical,

or physical properties [77, 78]. Aggressive chemical and physical treatments can be applied to Gold and other noble metals to remove these adventitious organic compounds. Care should be taken as some of these increase the roughness of the film surface and thus reduce the quality of the resultant adsorbed film. Because metals like copper and silver cannot withstand acid attack or aggressive oxygen plasmas, fewer alternatives exist for cleaning these surfaces after contamination and it is generally preferred to work in a high vacuum or inert environments (such as a glovebox). Furthermore, these environments are not perfect and so assembly and subsequent study of thiol species often quickly follows the metal deposition without disrupting the high vacuum environment. It has been suggested that fresh metal depositions be used regardless of the metal in question to reduce the poorly characterized effects of contamination and treatment [77]. Storage of samples in solvent is seen in some reports but can also contamination and represents the problem of cleaning in some cases.

4.2 Roughness and Film Quality

The process of metal deposition leaves a number of surface imperfections which present problems for SAM growth. SAM growth is most often described for (111) metal faces; face centered cubic (FCC) metals tend to have a hexagonal atomic configuration at the surface [53, 79]. The atomic range of order is highly variable and dependent on the deposition techniques and conditions. In general, continuous grains will be smaller than 1 micron in size. High temperature deposition and thermal annealing can used to alter the surface morphology to be favorable to SAM growth.

Film quality on these metals can be evidenced through contact angles and electrochemical impedance spectroscopy measurements which are then related to metal

roughness and grain size [80]. Depending on the desired application, smaller grain size may be desirable to reduce lithographic edge roughness. Unfortunately, this directly contradicts the conditions (large grain size) which produce densely packed SAMs that are suitable for charge conduction experiments. One solution to the grain problem is the use of unique metallic alloys which result in amorphous films; these relatively featureless films reduce the incidence of defects in SAM formation [81]. These "metallic glasses" have evolved from initially requiring very rapid cooling rates (to avoid crystallization) to modern formulations which can be cooled at rates of less than one Kelvin per second [82, 83]. Mercury is amorphous in its common liquid state; however for the purpose of creating a permanent device, the utility of liquid contacts is limited. What is clear is that some improvement of surface conditions is needed and so this became a large area of experimentation in this research. A full treatment of the proposed, implemented, and successful solutions is presented in Chapter 7.

The straightforward nature of assembly has encouraged researchers to seek the boundaries of SAM applications. With the original intent of a fully encapsulated metal particle, we find that for non-planar substrates, SAM growth is not uniform [84]. Initially with experimentation and observation by AFM, NMR, IR, and TEM analysis, it was discovered that aliphatic carbon chains group together due to Van der Waals attraction rather than remain disperse as we might expect in solution. Later, molecular dynamics (MD) simulation was able to confirm this and describe specific temperatures at which molecules would break free from their order ($\approx>$ 200 K) [85]. Greater disorder and more exposed metal sites are seen for smaller particles. One common application of thiol encapsulated metallic particles is to facilitate dispersal in a liquid medium and to prevent agglomeration [86].

In the simple case of an aliphatic long chain SAM, the space-filled structure can be approximated to that of a cylinder. For large substrates with small surface non-uniformities, the difference in area at the surface location of the head-group and at the tail is minimal. For highly curved nanoparticles such as Au_{140}, we find the volume which the SAM can occupy approximates a frustum of a cone whose point originates at the center of the nanoparticle. Moving further from the metallic surface yields a larger space and greater volume which cannot be filled by the SAM [87].

For simple visualization, we can approximate these volumes as shown in Figure 4.1 left by:

$$V_{cyl} = \pi {r_{site}}^2 h \tag{4.1}$$

$$V_{cone} = \frac{\pi h}{3}({r_{site}}^2 + r_{site} r_{cone} + {r_{cone}}^2) \tag{4.2}$$

For $R_{substrate} \approx h$, the volume difference is such that chain-chain interactions are reduced and thus disorder or clustering of the chains results. In addition, for very small nanocrystals, the surface becomes increasingly populated by vertices and edges which are not ideal for SAM growth. For example, in the case of a 1.1 nm cuboctahedron gold nanoparticle, there is a defect rate of 52% [88]. Theoretical results from MD models give us a clear picture beyond the lower limit of physical imaging technique (Figure 4.1 right).

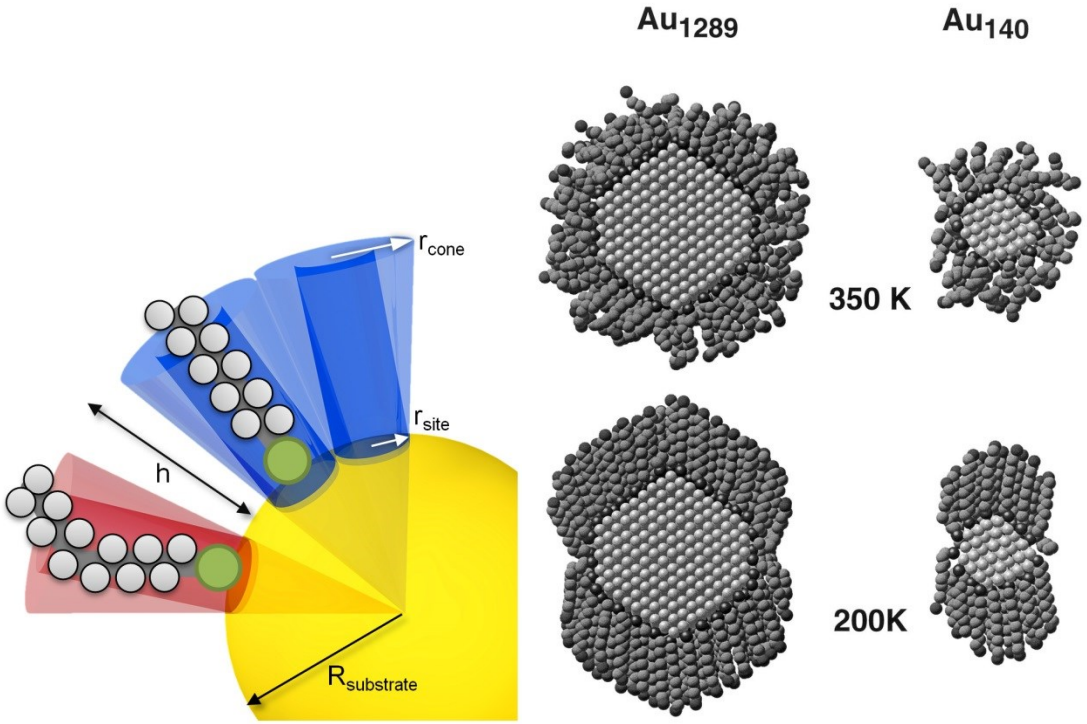

Figure 4.1: Illustration and atomistic model of a SAM decorated gold nanocluster. At left, an illustration which explains the non-intuitive morphology of the self-assembled monolayer on the highly curved surface. At right, is an atomistic model at both room and low temperatures demonstrating effect of nearest neighbor interactions in strengthening the monolayer. (Reprinted with permission from Luedtke. Copyright 1998 American Chemical Society.)

4.3 Surface Chemisorption

The procedure for creating SAM films in solution on compatible substrates involves immersion into millimolar dilute solutions of the alkanethiol in solvent. The duration of this immersion depends of the quality of film desired. Many groups allow 12-24 h at room temperature for satisfactory results. In spectroscopic studies and microbalance studies, the bulk of surface coverage occurs within the first 10 minutes of SAM exposure [89, 90],[90]. The added time allows reordering of the surface species to minimize defects and pinholes. The nature of the film is highly dynamic with extended immersions maintaining a continuous cycle of

desorption and adsorption around grain boundary sites. The most common liquid solvents used are alkanes and alcohols where the concentration of the SAM is typically ≈1-10 mM [91]. In addition to alkanethiol assembly, alkylsiloxanes and alkylsilanes can coordinate on substrates such a mica, glass, and metal oxides and phosphonates with Zirconium [92-94]. Factors that affect SAM growth include solvent, precursor concentration, immersion time, purity of chemicals, temperature, cleanliness of the setup, flatness of the substrate, length of chain, and terminal chemistry of the desired SAM.

The assembly of the organic layer onto the surface is directed by surface interaction (metal-thiol) along with molecule to molecule interactions. The activation energy of the S-H head group in the alkanethiol was studied to determine the binding energy to the metal surface [95]. End groups sometimes create significant steric hindrances which can reduce the density of packing at the substrate surface. Organic monolayers organize to maximize van der Waals interactions and to reduce the free energy of the metal surface with respect to the environment [77, 96]. Hydrogen bonding also plays a role for some molecules. On planar surfaces, even at the relatively warm room temperature, aliphatic chains are typically in the all-trans configuration. Order in chemisorbed SAMs is described primarily by three parameters which define the tilt, twist, and azimuth (tilt direction) angles of the chain with respect to the metal lattice [53, 97]. There seems to be some inconsistency with variable assignment and nomenclature of these various angles in reporting. Adoption of the Euler Angle standard may improve the uniformity of reporting. This would come with some added complexity due to the reference axis for each rotation being based on the new projected axis system from the last rotation (Z-X'-Z''). The most common current rotation scheme involves static axis rotations (rotation about z-y-z) which can be seen in Figure 4.2 [52, 98, 99]. Molecule tilt (θ) is the tilt

(w.r.t. z-axis from the origin) of the carbon chain in a fully-trans configuration from the normal of the surface. In the case of aliphatic thiols, values range from about 0 – 60° [100, 101]. Tilt angle tends to decrease (a more vertical stance) as the chain length increases [102]. The twist angle (ψ) is the rotation about the axis of the molecule and the azimuth angle (χ) is the tilt direction with respect to the substrate about the Z axis. These parameters vary for the head group, termination chemistry, chain length, and solvent; the values represent optimized orientations which maximize the molecule-molecule interactions and surface bonding to create the lowest energy, highest density film. A brief collection of values for commonly used substrates is shown in Table 4.1.

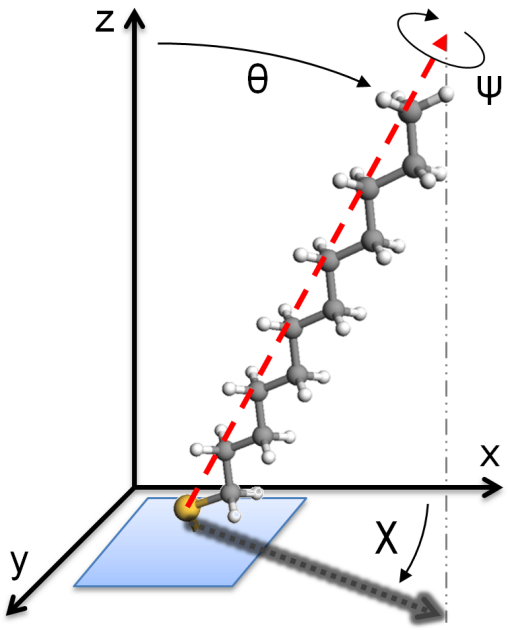

Figure 4.2: An illustration of variable parameters used to describe SAM organization with respect to the assembly surface. The variable notation varies throughout literature but the most common convention is presented here.

Table 4.1: Tilt and twist angles for fully saturated alkanethiol SAMs on various substrates. (Adapted from Love 2005.)

Substrate	Tilt Angle θ	Twist Angle ψ	Method	Ref.
Ag	11-14°	45°	RAIRS	[53]
Au(100)	14°	70°	RAIRS	[103]
Au(111)	28°	53°	RAIRS	[53]
Cu	12°	45°	RAIRS	[53]
GaAs(100)	57±3°	45±5°	RAIRS	[100]
Hg	0°	n/a	X-ray	[101]
InP(100)	55±6°	n/a	XPS	[104]
Pd	16±2°	45°	RAIRS	[79]
Pt	< 15°	n/a	RAIRS	[61]

Extensive studies of the bonding of alkanethiols on Au(111) have been performed and are mostly in agreement regarding the $(\sqrt{3}\times\sqrt{3})R30^\circ$ hexagonal packing structure [67, 99]. In addition, there are a number of secondary ordering superlattices, such as c(4 × 2), which are commonly accepted [105]. Visible in Figure 4.3, we can see additional proposed superlattice and assembly configurations. Theoretical atomistic modeling is often used in conjunction with STM, AFM, TEM, and spectroscopic analyses for validation of the proposed structures [103]. The discussion of binding site location has been a hot topic of debate. Different groups using atomistic modeling predicted conflicting energetically favorable binding sites for the thiol group [106, 107][106]. These early models were in disagreement with grazing incidence X-ray studies which saw population of top and FCC sites—that which was earlier predicted to be less favorable. Further models incorporated a gold surface which would undergo reconstruction to produce Au-thiol complexes [108]. These adatoms are lifted from the surface to yield a lower energy confirmation for the thiol molecules. A consequence of the displacement is the formation of vacancy islands (which appear as holes) in the gold surface. Adatoms can from either bridged $(RS)_2$-Au supporting only the c(4 × 2) lattice or single RS-Au contributing to the $(\sqrt{3}\times\sqrt{3})R30$ and c(4 × 2) lattices [109].

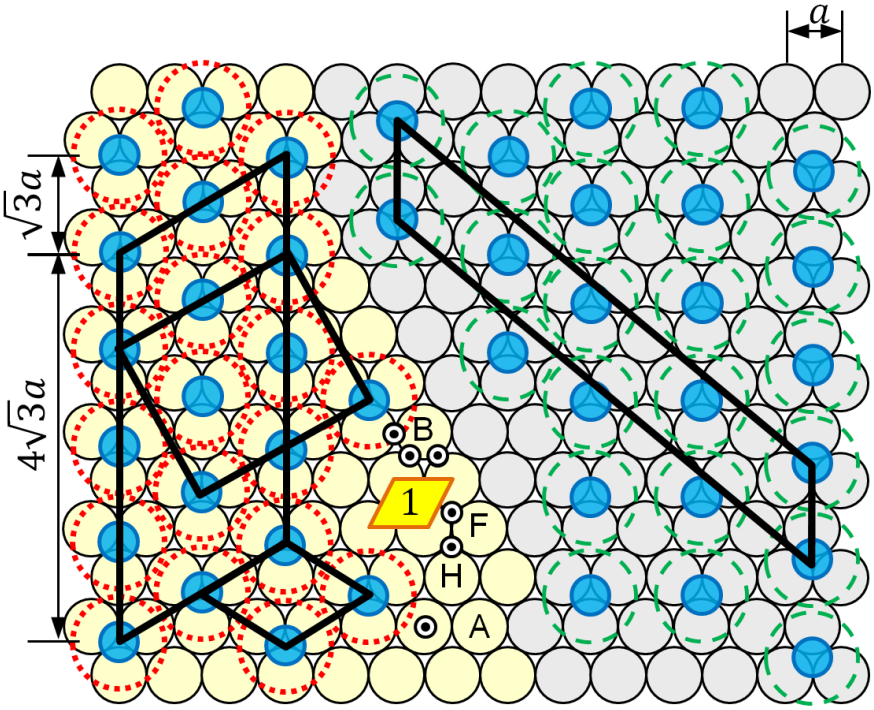

Figure 4.3: An illustration of common assembly sites and surface packing configuration of SAM films on Au(111). In this figure, the gold atoms are portrayed as the base layer of circles, and the site names include (B) bridge, (F) FCC site, (A) atop site, and (H) HCP site.

4.4 Surface Physisorption

An alternative method of monolayer deposition is the Langmuir-Blodgett method. Unlike the surface assembly seen in SAM films, Langmuir-Blodgett (LB) films self-assemble on the surface of a liquid [110]. One or more amphiphilic monolayer species (which may be dissolved in a co-solvent for ease of surface spreading and delivery) are deposited onto a liquid surface whose surface tension is being monitored. The liquid used for deposition is typically water. The hydrophilic head of the monomer species orients towards the water while the hydrophobic tail points outwards into the air. This operation is performed in an inert trough typically fashioned out of a single block of PTFE (Teflon™). A barrier is located at the end of the shallow trough which is used to slowly compress the surface species while the surface

tension is being monitored. The result is the tight packing of the surface species such that Van der Waals interactions between nearest neighbors improve the film strength and cohesion. Further compression once an isotherm is reached will result in breaking of the monolayer as sheets of loosely attracted monolayer run on top of one another. In Figure 4.4, we can see one of the processes by which the film can be transferred to a substrate.

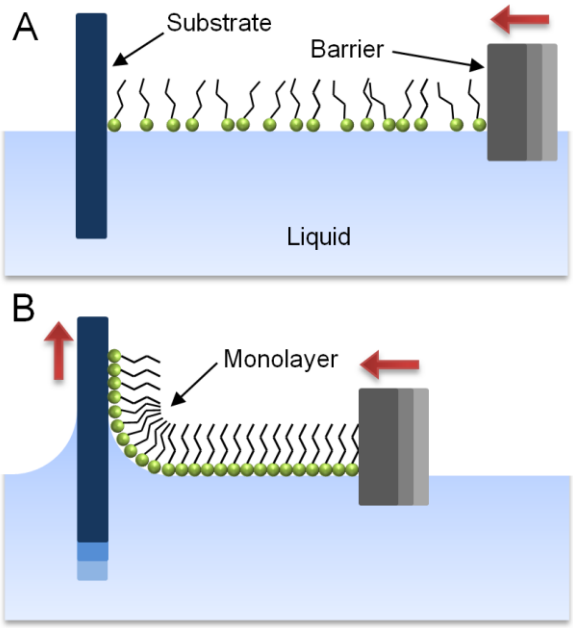

Figure 4.4: An illustration of the Langmuir-Blodgett film deposition process. An amphiphilic molecule is dispersed on a liquid surface and compressed using a barrier until a monolayer is achieved on the liquid surface. At that point, the substrate is withdrawn from the water at the same rate as the barrier compression resulting in the transfer of the film.

Throughout the initial compression stage, the surface pressure (really surface tension) is monitored by a Wilhelmy plate. This is typically a calibrated plate of paper, glass, or platinum which has a predictable wetting characteristic and is attached to a microbalance. When dipped into the water, the hydrophilic nature of the plate will cause it to be drawn into the water body and register some related force through the microbalance. The relationship between the force experienced by the Wilhelmy plate and the surface tension of the liquid is given by:

$$\gamma = \frac{F}{l \cdot Cos(\theta)} \tag{4.3}$$

where l is the wetted perimeter of the plate, θ is the contact angle of the liquid with the plate, and F is the downwards forced measured by the microbalance from the plate (after initial tare of gravity force).

As the compression reaches a critical point, an isotherm is achieved. This is the surface pressure at which the fractional surface coverage approaches unity. A target pressure approximately 80% to the value of monolayer failure is selected for the deposition. Depending on the surface characteristics, the sample is either already immersed in the sub-phase or suspended just above the liquid surface. With the barriers moving in coordinated manner with the dipping of the sample substrate, the film is transfer as depicted in Figure 4.4. Because of the self-attractive nature of the film, multi-layer coatings are easily accomplished by repetitive dipping. Unlike the in the SAM films where the film is chemisorbed onto the surface, adhesion in LB films is by physisorption.

4.5 Solvents and Kinetics

Assembly can be carried out in a solvent medium or in the vapor phase under high vacuum. The most straightforward method of assembly is in ethanol or hexane solution [111]. Ethanol has been shown to result in greater number of defects and slower assembly time than short chain alkanes. It is, however, a more universal solvent permitting assembly on substrate materials which are not possible in non-polar media [112]. Contributing factors to the selection of ethanol as a solvent are its low toxicity, low cost, ubiquity, and high available purity. While toxicity of the solvent may be low, alkanethiols tend to be, at the very least, strong irritants with a potent stench. Assembly kinetics are affected by solvent selection with speed favoring lower

viscosity liquids [113]. Beyond the viscosity, interactions between the solvent and the surface, along with the potential self-interactions of the solvent such as hydrogen bonding, contribute to the assembly kinetics [114]. Chain length and termination chemistry also play an important role in the diffusion of the assembly species to the surface boundary. Of course, these are general trends which have been shown to have many exceptions. These experiments have been carried out by many teams and through many different conditions have confirmed these non-intuitive trends such as C_{18} assembling more quickly than C_8 in hexane [115]. Alternative solvents for alkanethiol assembly include tetrahydrofuran (THF), toluene, heptane, hexadecane, and dimethylformamide. Higher concentration of the SAM species in the solvent also positively affect the initial surface population however this has the later effect of disturbing ordering for extended immersions. It is believed small pinhole defects can entrap micelles of ionic or non-ionic surfactants hindering reorder and tighter packing [116].

Vacuum assembly, or vapor deposition, of thiols has been used to study the initial order mechanism of the films. While useful for shorter chain alkanethiols, kinetic bottlenecks and vapor pressure limitations constrain the degree of experimentation possible [117]. The prospect of in situ studies of films under very clean growing conditions makes this deposition technique appealing for kinetics and growth studies. It is especially useful for the assembly of silanes where small amounts of water can cause undue crosslinking defeating the monolayer topology. This sensitivity to –OH groups can be utilized to selectively pattern bi-layers over regions of alcohol terminated SAMs [118]. Explanation of assembly mechanisms using vapor deposited revealed a two-step assembly process in which nucleation and growth of striped phase SAMs fill the surface. Striped phase packing is seen when the tail of the assembly species lies on the assembly surface. In these cases, the molecules arrange adjacent in head-to-head or head-to-tail

configurations. Once this phase dominates, and grains reach the next striped island, surface pin-holes act as nucleation points for the proper standing SAM orientation as conversion of the surface molecules takes place [117, 119].

4.6 Environmental Factors

Substrate cleanliness problems, along with the introduction of other contamination, will degrade the quality of the self-assembled films. Because adventitious hydrocarbons quickly coat free surfaces in atmosphere, every effort must be made to quickly transition the sample following cleaning or metal deposition. While thiols have a high affinity for surface sites, adsorbed contaminants slow down the assembly process and break apart larger domains of order [77]. In some cases, the binding energy of the contamination is greater than that of the SAM and no additional immersion time will permit displacement. Besides fresh metal samples used immediately after deposition, cleaning in strong oxidizing solutions (such as piranha etch) or in an oxygen plasma can restore surface quality [75]. Hydrogen flame annealing of the surface is also reported to reduce surface contamination and increase terrace size [120].

The concentration of the precursor in solvent relates to the immersion time. Concentration is typically around 1 mM with an acceptably short immersion time. The lower limit for proper film formation is ≈1 μM [90]. While this time to concentration relationship can be scaled, there are differences in the resultant films. Very high concentration solutions cause continued disruption of the thiol film and introduce a greater quantities of contaminants along with the desired materials. Because these contaminants may have stronger affinity for gold than the desired species, it is recommended to use the minimum amount of assembly materials to mitigate this problem. Groups occasionally seek to further purify obtained precursor chemicals

by percolation over activated neutral alumina [121]. Standards for purity vary by author with most accepting that low concentrations of contaminants (< 5%) do not significantly affect assembly. It is for this reason, along with the difficulty of purifying small quantities of material for more costly precursors, that most chemicals are used as received [122].

Opinions regarding the effect of Oxygen dissolved in solution during assembly vary. While experimentation has only offered qualitative results on the matter, because SAMs oxidize in atmosphere, it follows that oxygen likely plays a negative role in solution as well. Solution preparation in an inert gas purged glove box has showed improved film quality [121]. Often, the solvents used are allowed sufficient time to outgas trapped O_2 through extended storage under Argon prior to use. It has also been suggested that the presence of O_2 gas can lead to the formation of O_3 which would more readily oxidize or react with the surface species.

Most SAMs are kept at room temperature during deposition but elevated temperatures can improve kinetics, speed up formation, and allow displacement of more surface contaminants. As we saw earlier, kinetics are highly dependent on the solvent and deposition molecule used. The temperature range for assembly varies from -20 °C to around 80 °C with the best film order seen at the upper end of the scale [123]. Because most of the assembly occurs within the first minutes of immersion, all the conditions mentioned are particularly important during this time. The remaining immersion time allows tighter polycrystalline packing and reorder of the surface adsorbates [123, 124]. There have not been too many studies addressing the dynamic variation of these conditions during assembly.

4.7 Molecule Termination and Functionalization

Monolayers offer the interesting characteristic of choosing surface interface properties. The creation of a hydrophobic/hydrophilic, acid, polar, amine, anhydride, aromatic, and quinone terminated films are all possible. In addition to terminal groups, functional elements can also be placed at the interior of the chain permitting additional possibilities such as crosslinking with neighboring molecules [125, 126]. Bio-active terminations can be used to selectively bond markers to proteins, peptides, viruses, or cells for fast detection and diagnosis sensors [127]. Modification of terminal groups after assembly unlocks the potential of: (1) attaching larger terminations than possible during assembly (while maintaining film order), (2) use of chemicals not compatible with unbound thiol groups, (3) ease of synthesis where chemistry restrictions prevent the creation of the assembly molecule, (4) control of functional element spacing, order, and steric hindrance interference [128]. In addition to attracting select groups, protein-resistant surfaces can be created which help direct the desired species to the bonding site.

The additions and modification to the terminal chemistry can be carried out by nucleophilic addition and substitution, acylation, esterification, and oxidation [129]. These surface modifications are among the first to achieve mainstream commercial success in applications of DNA detection [130]. Graft polymerization has been demonstrated to attach a conductive polymer (PANI) to a SAM modified surface [131]. In addition to the capability of lithographically directed grafting, this technique enables a conductive contact to be formed above the monolayer without causing damage [132]. This film can then be more freely processed with less risk of damage during metal evaporation.

4.8 Defects

Defects in organic films can be broken down into intrinsic and extrinsic defects. Extrinsic defects are those which can conceivably be remedied through better handling, cleaning of the substrate, reduction of contaminants, and smoothing of the assembly surface. Beyond the parameters of temperature, solvent, and immersion time that are used to direct the assembly, there are still defects that occur which are intrinsic to the self-assembly process. That is not to say that there will never be a method to correct these inconsistencies, but currently, the defects are representations of the SAM behavior.

As hinted above, major sources of surface defects are grain boundaries, lattice steps, and impurities (both in and on, the assembly substrate). These cause defects beyond merely the height differences in the end film because thiols have a high rate of coverage on the (111) plane (Figure 4.5). As is the case in non-planar substrates, vertices and edges are not well suited for growth [103, 117]. These sites have been shown to be nucleation points for adsorption and desorption. Some grain boundaries can sometimes be healed given extended assembly time however terraces tend to remain small even with indefinite immersion times. The dynamic nature of the SAMs permits reordering and exchange of the molecules at defect sites during adsorption. Thermal annealing of the SAM can reduce the number of grain boundaries through reorientation of the SAMs [92]. Dry annealing can increase the coherence length of the deposited SAM to >100 nm but also facilitates desorption [133]. In-solution annealing is often performed to mitigate these effects. Additionally, the vacancies and defects can be backfilled with shorter chain alkanethiol molecules. These smaller molecules have greater mobility to overcome steric hindrance and assist in the desorption of weakly bound, heavier species.

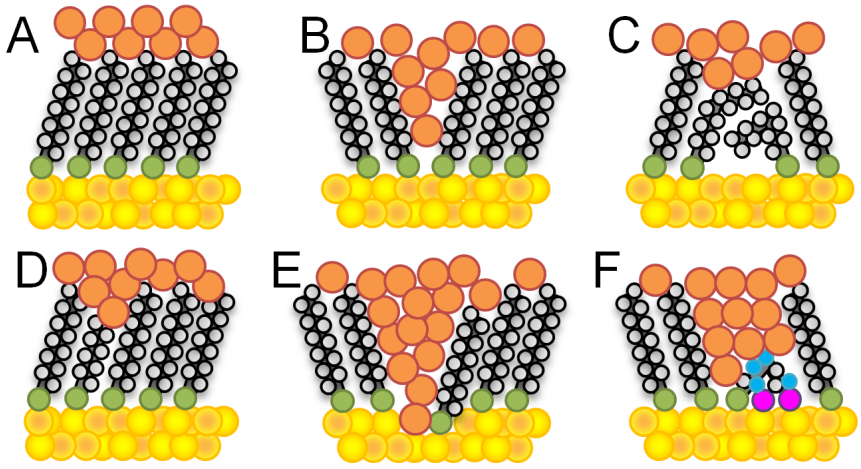

Figure 4.5: An illustration of common defects in SAM-based MIM junctions. Depicted is (A) a normal idealized junction, (B) grain boundary defect which caused some of the top metal (orange) to come closer to the assembly electrode, (C) chain folding resulting in barrier gap defect, (D) metallic punch through due to high temperature or reactive metal evaporation, (E) grain boundary defect coupled with a gold lattice step defect, (F) impurity contamination which has preferentially adhered to the surface blocking further assembly.

We spoke just earlier about the presence of adatoms and the creation of RS-Au complexes which permit observed lattice structures. The surface rearrangement studies seek to understand the stoichiometric relationship between adatoms and the thiolates which cause their displacement. The island vacancies which occur are not limited to step edges (though these sites are more favorable for reorientation). In addition, these vacancies are not always monoatomic in depth making models and measurement more challenging. Through extended adsorption/desorption experiments, aggregation of the gold atoms are seen on the surface which are sourced from these vacancy islands [134]. This process feedback process is one of the challenges in the creation of a uniform SAM film—reconstruction of the underlying surface increases roughness which in-turn reduces SAM order and permits further attack and reorientation of the assembly surface. Originally, it was suggested that the density of these defects increased with alkanethiol concentration and decreased as longer chain assembly

molecules were used [135]. More recent reports suggest an independent relationship between chain length and vacancy formation with the exception of methanethiol [136].

CHAPTER 5:

MODIFICATION OF THE ORGANIC LAYER

One of the benefits of designing electronic devices around SAMs is the diversity and variability of the insulating layer itself. One method for unlocking a greater degree of experimentation is to transcend beyond designed devices on planar, featureless insulators. Because of their ease of application, SAMs can be selectively added or removed through a variety of nanolithographic techniques. Because of the application potential in the field of chemical and bio detection, this has significant implications for ultra-fast response testing platforms. Current technology limits the methods of modification to mostly top-down (subtractive) techniques. There has been an emergence of more techniques, such as Dip-Pen nanolithography (DPN), which do adhere to the bottom-up fabrication principle.

5.1 Photolithographic Modification and Limitations

Alkanethiol films can be patterned directly simply through exposure to UV light [137]. A straight chain monolayer typically acts as a positive-tone photoresist being selectively removed in the exposed areas [138]. This technique uses the same exposure equipment as conventional photolithography, produces high resolution patterns (< 100 nm) due to, in part, the thickness of the monolayer, and is compatible with additional substrates (such as Ag and GaAs) [138-140]. Exposure times for the alkanethiol films are longer than that of common photoresists ranging from a few minutes to several hours depending on the substrate, intensity of the UV

source, chain length [141, 142], and terminal chemistry [139]. Because the primary pathway for photooxidation with conventional UV sources is photocatalytic O_3 generation [143], the mercury lamp used must be broadband as not to block the 184 nm line. It is still possible to pattern at wavelengths above this (demonstrated with a 488 nm Argon laser) but the mechanism becomes localized heat assisted desorption [144]. This technique has the benefit of high patterning speed but very poor resolution because of thermal gradients away from the beam center.

Following the exposure, samples are typically rinsed in a polar solvent (ethanol or water) to remove any oxidized species from the patterned surface. Longer chain alkanethiols protect select regions enabling etching or directed growth in the exposed regions [145, 146]. In addition, the exposed metal regions can be utilized for the assembly of a different functional SAM thus creating a region functionalized surface [140].

5.2 Particle Beam Lithography

Beams of energetic neutral atoms, electrons, and ions can induce changes in SAMs [147-149]. While not a particle beam, X-rays are a source of energy which is sufficient to chase changes within the film [150]. The pathway by which X-ray damage occurs is typically similar to that of electrons due to secondary electron generation under the incident source [150]. Particle beam patterning has enabled features on the 10 nm scale. Limitations in resolution are similar to those found for imaging applications such as backscatter of particles. Functioning as resists, these films are described as self-developing because the incident beam results in the final desired state of the surface. Low energy electrons (< 100 eV) break C-S, C-C, and C-H bonds within the alkanethiol molecule resulting in tail fragmentation, desorption, crosslinking, and double bonding [151]. The resulting damage creates lower energy pathways to desorption resulting in

film damage. Negative-tone performance is also possible through the use of SAMs which contain aryl groups within the chain [132]. Ring-opening metathesis polymerization and other random crosslinking with neighboring molecules strengthen the monolayer resulting in better etch resistance and more difficult removal [126]. This also permits the addition of functional groups to the tail groups giving additional functionality or a thicker monolayer for more versatile etching. In the case of atomic beam patterning, the neutral atoms used are typically those of a noble/rare earth gas which has been excited to 8-20 eV above the ground state [149]. Due to the low energy of these particles, a large flux is required to perform significant changes. Despite the high dose required for patterning, the edge resolution of this technique is very sharp due to the highly localized surface damage and insensitivity to Coulombic forces [152].

5.3 Assembly Fluid Transfer

A family of techniques which typically result in high speed and high resolution patterning is assembly fluid transfer. In this method, the SAM is dispersed in a fluid medium which is transferred onto the surface through contact, spraying, or controlled deposition. In the process, the assembly takes place in the domain of the highly surface tensioned droplet. Because of the relatively short time before evaporation and constrained liquid volume, these deposition techniques typically see reduced quality of deposited films.

5.3.1 Microcontact Printing

In a similar manner to that described in section 6.9, patterning can occur by direct transfer from an elastomeric (typically PDMS) stamp. A master is etched from a hard material and PDMS is cast onto the surface which captures the negative relief of the surface. The SAM

solution (sometimes referred to as an "ink") is prepared and allowed to wet the stamp [153]. The solvent is largely allowed to evaporate which prevents "bleeding" of the ink. Solvent selection is important in ink formulation because PDMS does absorb solvents; uptake of ethanol results in a 2.5% swell of the stamp which is generally acceptable [91]. The stamp is then pressed in contact with the substrate for a number of seconds and then removed [153, 154]. Mole fraction of thiol species present on the stamp is critical to the quality of the resultant film. Packing density and order of adsorbates from microcontact printed patterns are not as good as those of films made in solution. Because monolayers offer no contingencies for defects in etching, use of this method for protection of the substrate is limited.

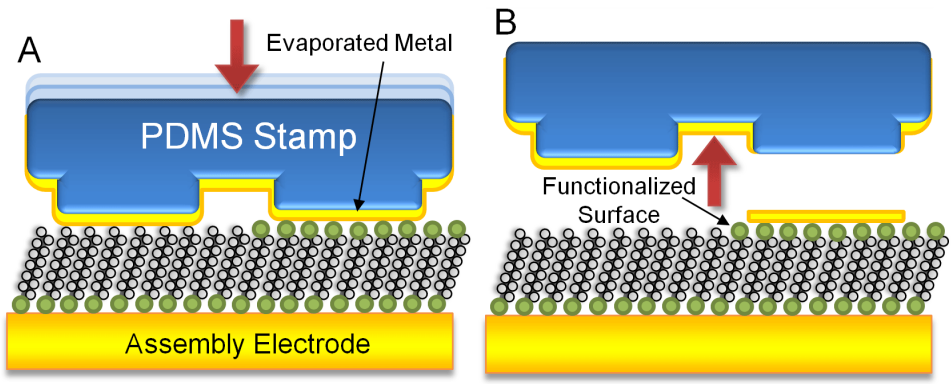

Figure 5.1: An illustration of the PDMS transfer printing process. A PDMS (poly (dimethyl siloxane)) stamp is fashioned and used to transfer an evaporated film onto a SAM modified surface. An alternative use of the stamp is the direct transfer of SAMs onto an unpopulated surface by "inking" the stamp with a SAM loaded solution. (Adapted from Haick 2008)

5.3.2 InkJet Localized Assembly

Simple commercial ink-jet printers have the capability of depositing nanoliter volumes of liquid to very specific areas on large substrates. Here, the conventional pigment ink tank is replaced with a SAM solution and assembly is carried out in tiny surface droplets. Reproducible resolution is below 100 µm in size however examples below 10 µm have been shown [155, 156].

Customization of ink-jet printing systems, surfaces, fluids, and deposition conditions can favor enhanced surface films. SAM films printed in this manner are not as well ordered as those grown in solution. Still, an exciting opportunity is the capability of creating a complete device through ink-jet printing alone [155]. Conductive and semi-conductive polymers can be printed which form the basis of polymeric transistor devices [157]. Faster printing is possible with micro gravure techniques. There has been a renewed interest in the basic research of fluid mechanics in printing permitting even higher resolution with significantly faster patterning speeds than inkjet [19]. Still, inkjet offers highly flexible, zero-cost design changes which are very useful in research. This field is one of extensive personal interest and will be covered in much greater detail in future chapters.

5.4 Dip-Pen Nanolithography

Dip-Pen Nanolithography (DPN) provides bottom-up patterning on the 1-100 nm scale. The principle of operation is somewhat analogous to that of a fountain pen—here using an AFM tip to selective delivery functional molecules (called “nano inks”) to the substrate [158, 159]. A wide variety of materials have been deposited such as self-assembly molecules, polymers, DNA, and colloidal particles to name a new. Piner et al. first reported on this novel deposition technique in 1999 and it has received much attention since [160]. From first demonstration, the technology has evolved to using massively parallel patterning through 50 000 AFM cantilever heads [161]. Parallel technology allows areas on the order of square centimeters to be with sub-100 nm resolution. One major drawback to this technology is patterning time. Parallel patterning largely resolves this but limits experimentation to repeated patterns over the write head. Still, the field of metamaterials study can greatly benefit from high resolution repeated

patterning over large areas. AFM-based technologies offer the benefit of in situ imaging along with surface modification through (in this case) deposition, oxidation, shaving, replacement, and grafting. To assist in extended deposition without re-inking, a "volcano" tip was developed which employed a shell, microchannel, and ink reservoir to greatly extend writing area [158].

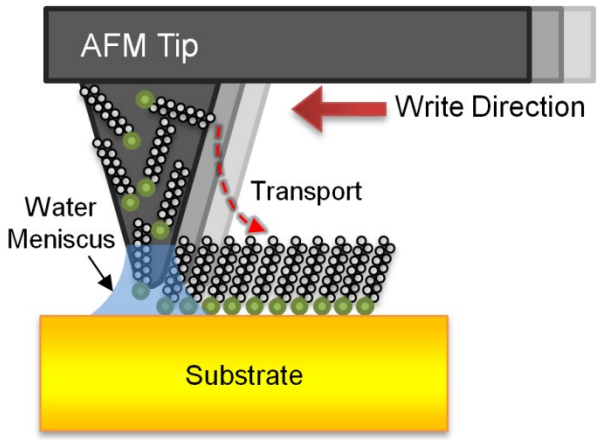

Figure 5.2: An illustration of Dip-Pen nanolithography. This write technique utilizes AFM tips to deposit "nano inks" onto the desired substrate. Because of the slow write speed, massively parallel heads were developed with thousands of tips. (Adapted from Piner 1999)

5.5 Removal and Damage

Complete or selective removal of organic monolayers is essential for their eventual incorporation into functional devices. At the same time, their delicate nature means a better understanding of damage mechanisms is critical to produce reliable molecular electronics. For example, current state-of-the-art work in molecular research boasts results with 90% yield of individual devices while commercial products demand failures rates of 6 or 7 sigma for complete products [162].

5.5.1 Photooxidation

SAMs undergo photooxidation during exposure to UV light in air. The pathway typically results in the alkanesulfonate (RSO_3^{-1}) for straight chain molecules. In this case of chemically mediated photooxidation, the UV radiation is believed to generate a more reactive oxygen species which results in oxidation [143]. The photosynthesized O_3 requires sufficient sub-200 nm light in addition to an O_2 atmosphere. The rate determining step in the formation of the sulfonate is the migration of O_2 to the S-Au interface where it will be converted into the reactive species. An alternative pathway has been demonstrated with high intensity laser desorption which, as in the case of short wavelength (193nm) UV, results in desorption of an alkanethiolate negative ion [137]. Following desorption, the site is studied (typically XPS or other spectroscopy) to not only determine the degree of change but also the mechanism of removal. Additional desorption studies have been carried out on GaAs [139, 140] substrates and also with focus on different termination chemistries [163, 164].

5.5.2 Desorption

Thermally assisted desorption of the surface species is one of the two primary means of SAM aging. The dynamic properties of the film mean that molecules can migrate and reorder—this movement is kinetic energy limited. Studies have been performed on the stability and oxidation of SAMs in atmosphere; Raman and XPS spectra show that the majority of surface loss is due to oxidation rather than thermal effects, at room temperature [165, 166]. As the temperature is allowed to rise (≈ 80°C), greater reordering is facilitated and well covered regions can be annealed to a greater density of packing [167]. Final stability of monolayers for short temperature excursions are still relatively low compared to normal microfabrication processing

conditions. Straight chain alkanethiol SAMs degrade around 110 °C while perfluorinated molecules were stable to 145 °C [168]. Stability depends not only on chain length and substrate but also the environment during heating (water, air, solvent, etc.) [169]. An established SAM film can be removed by exchange with a thermodynamically favorable surface adsorbate [169]. The exchange process is described as incomplete—arriving at some equilibrium thus creating a heterogeneous surface modification. Grain boundaries and defects typically serve as the exchange sites as molecules are more weakly packed receiving more solvent contact than those in more densely packed regions [170]. Bonding between thiols and gold is quite strong and can weaken Au-Au bonds; desorption has been found to dissolve gold in solution [117].

5.5.3 Oxidation

Atmospheric stability of SAMs is often a challenge for reliable electronic use. Studies typically involve XPS and Raman analysis following exposure to test conditions [166, 169]. As in the case of photooxidation, the rate limiting step is the migration of O_2 to the film interface. This is evidenced in studies where oxidation is significantly faster for short chain (3 carbon) alkanethiol films as opposed to longer (18 carbon) films [165]. Oxygen plasma and flame annealing have been used to prepare substrates for SAM assembly. This same technique can be applied to the removal of alkanethiol adsorbates restoring the clean surface. Masked oxidation or ion etching of organic films has also been demonstrated [171]. Substrate metals must not be easily corroded in an oxygen environment or risk being damaged in the cleaning process [172].

Chemical treatment of substrates can also be an effective way of removing stubborn contaminants or adsorbates. A “piranha solution” (concentrated H_2SO_4 and H_2O_2) is often used as a preparation step prior to SAM immersion [173]. For the case of silane chemistry assembly,

a surface treatment which leaves a hydrophilic surface and removes all organics is desired [174]. Because flame annealing of the substrate can produce inconsistent results, Campiña et al. report an electrochemical method for SAM removal [175].

CHAPTER 6:

REVIEW OF EXISTING DESIGN SOLUTIONS

An extensive literature review was conducted to determine the state of the art in organic junction devices. This search focused on electronic test structures for the purpose of charge transport studies. There are numerous other structures which were proposed and developed which were for applications other than electronic devices—these were not included in this review. The variety of electronic test beds needed to be grouped by some broad categories. The most frequently seen were selected and grouped accordingly. This is in no way an exhaustive list but it does cover the vast majority of structures. The review will begin with a look at implementations employing temporary junctions and then continue to more permanent device structures. Because the goal of this project is to arrive at a diode-like device, additional emphasis will be given to structures which exhibit or promote promising rectification ratios.

6.1 Liquid Metal Contacts

Liquid metal contacts were among the first used to study tunneling through organic monolayers [70]. Mercury was used because of the quality SAM that could quickly grow on the smooth, featureless liquid surface. As stated above, this results in less crystalline packing of the SAM but also a lower incidence of pinholes, thus proving acceptable for electrical conduction studies [73]. The soft surface also made surface contact very easy since there was lower risk of abrasion or compression of the film. The configuration is optimized by having SAMs on both

electrodes and bringing them into contact thus forming a metal-SAM-SAM-mercury junction. The contact area is normally calculated by video microscopy. Together with a simple goniometer, consistent experimental data can be produced [176-179]. In addition to mercury-gold metal combinations, mercury-mercury metal contacts are possible by allowing two SAM coated droplets to meet inside a capillary. The area constrained nature of the capillary coupled with the non-wetting properties of mercury in glass form very consistent junctions separated by their respective monolayers. Surface tension will also tend this interface to be completely flat resulting in more accurate contact area measurement. In cases where the bottom electrode is an evaporated metal film, there is a chance that a large surface feature can disrupt the SAM film and come in direct contact with the mercury top electrode. Metal compatibility is again a concern as mercury will quickly form an amalgam with the exposed gold, and diffuse and embrittle aluminium, if used [180-182].

Beyond mercury, there are a number of other metals and metal alloys which are liquid at or near room temperature. Gallium has a melting point of around 29.8 °C however there are a number of eutectic alloys which exhibit lower melting points for liquid use at room temperature [183]. Most common are eutectic gallium-indium (EGaIn) which has a melting point of 15.7 °C and Galinstan which is a eutectic alloy of Ga-In-Sn that lowers the melting point to -19 °C [184, 185]. Though not often mentioned, gallium can be readily supercooled following a prolonged and elevated melting of the liquid thus facilitating supercooled work at room temperature [186, 187]. One potential benefit of using pure metallic electrodes rather than alloys is the ability to study the effects of work function on tunneling. These liquid metals are preferred due to the significantly reduced toxicity and vapor pressure (as compared to Hg). There is still the concern with liquid metal embrittlement as gallium and its alloys readily attack aluminium and steel by

diffusing into their metal lattice. The wetting characteristics and surface tension of these alloys allow the formation of liquid metal "tips" which can be used to accurately probe the substrate with contacts of relatively low area [185]. The use of gallium alloy metals in atmosphere introduces a semiconducting Ga_2O_3 film around the bulk metal. This additional tunneling barrier of unknown or discontinuous thickness is not well defined [188]. As a technique of improving the consistency of data, template stripping is utilized on the substrate to greatly reduce the incidence of junction failure. Recently, there have been some novel implementations which utilized template stripped metal and constant area liquid metal contacts achieved through microfluidic channels in a PDMS bonded structure [46].

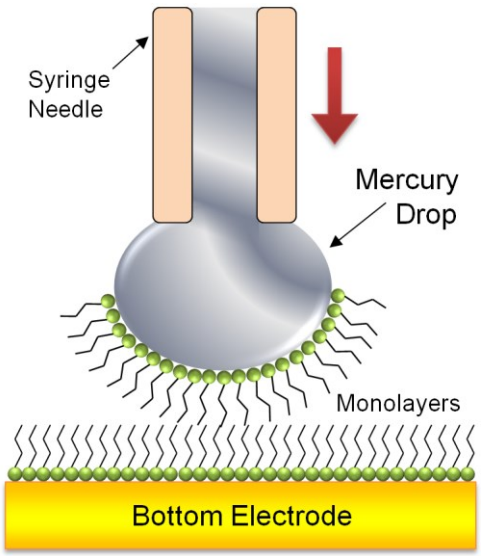

Figure 6.1: An illustration of a mercury drop contact on a SAM decorated substrate. A syringe containing the liquid metal (mercury in this case) is brought into contact with the surface in a SAM loaded solution.

6.2 Conducting Probe AFM

Conducting probe AFM is an evolution of conventional atomic force microscopy. In conventional AFM imaging, the tip is brought into atomic contact with the surface. At the basic level, AFM offers imaging data only by measuring the deflection of the cantilever due to Van der Waals interactions with the tip and the sample surface. This deflection is monitored optically and translated into height data. This data is extremely useful for the visualization of individual molecules which comprise the SAM film. In a conductive probe (CP-AFM) setup, the tip is coated with a conductive metal which permits it to act as the top metal electrode [189].

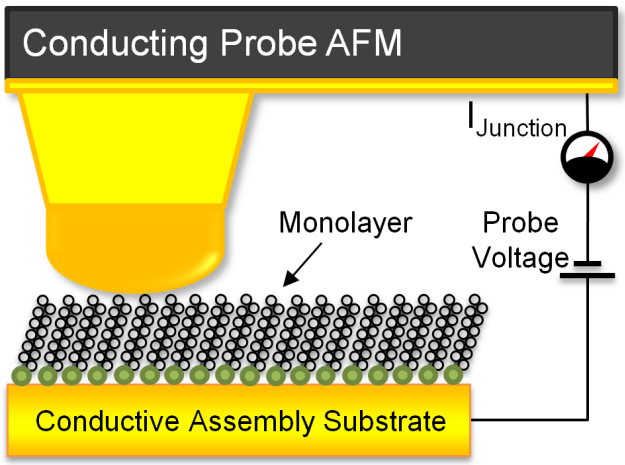

Figure 6.2: An illustration of a conducting probe AFM electrical measurement on a SAM film. Because the conductive coating on the AFM tip makes it large relative to the SAM molecule size, this technique averages electrical signals over many adsorbed species.

The metal coating process results in enlargement or dulling of the tip and thus contacting of more than one molecule. Additionally, with a likely lower conical slope at the tip, there will be additional tunneling contribution through a vacuum gap immediately near the point of contact. Bilayer junctions can be created by growing a SAM on an Au tip; SAM formation on these surfaces will not be as dense as desired due to the high curvature near the tip (See 4.2, Non-Planar Substrates). This conclusion can be evidenced by the unusually high tunneling current

seen when the SAM is only present on the probe and not on the substrate. All these factors make difficult to deduce the actual number of molecular junctions being measured. One solution is to intentionally blunt the CP tip to create a more sharp transition from the sidewalls and the contact surface [190, 191]. An additional concern is the compression of the film by the tip/cantilever force. It is not clear whether the presence of this force causes changes in the film geometry [192, 193].

6.3 Scanning Tunneling Microscope

The scanning tunneling microscope (STM) is used to study a number of aspects regarding self-assembled films. It offers the great utility of direct study of individual molecules which make up the film and also probe the electrical characteristics on a single molecule basis. A sharp STM tip acts as the top electrode approaching the area of interest (without contacting it) and some bias voltage is applied between the tip and the substrate. Tunneling current is monitored along with height revealing surface morphology and electrical characteristics [194]. Problems can arise because under constant height mode, it is not always clear what the distance between the tip and the surface is. The current changes being recorded can be due to either changes in height or changes in molecular conduction. Morphology contrast depends strongly on the atomic sharpness of the tip and the termination chemistry of the SAM. Alkane-dithiols (double sulfur terminated SAMs) have the risk of interaction with the tip [195]. Even equipped with a very sharp tip, the dense packing found in SAMs coupled with the real life multi-dimensional tunneling potential will skew the results. It is also important to consider the vacuum or air gap between the tip and the SAM in question. Still, this property offers an opportunity to investigate

the metal-SAM-air/vacuum interface [194, 196]. The end result is a lower than actual measured current [191].

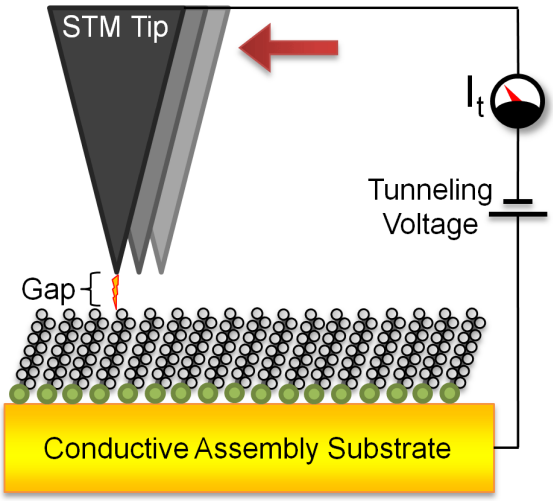

Figure 6.3: An illustration depicting a STM tip probing a SAM coated surface. The sharp tip is scanned over the SAM surface and the small tunneling current is amplified and analyzed.

6.4 Break Junction

Break junctions are formed by either mechanical elongation or electrical migration of a thin metal bridge. In the mechanically controllable break (MCB) junction, a wire or thin lithographically defined bridge is suspended above a bending beam which provides rigidity from in-plane motion while offering compliance in the Z-direction [197]. A piezoelectric pushing element flexes the substrate at the site of the bridge thus elongating the gap between the two pinned ends of the metal link. A highly ductile metal, such as gold, is a good candidate for this study because it forms a sharp point on either side following tensile stress and does not experience fracture. This setup offers very high positioning accuracy and very low positioning drift over time [198-201]. In the case of electro-migration formed junctions, a common electronic failure mode is levered by passing a high current through a metal nanowire causing

localized heating and migration away from a central point. The resultant gap is consistently around 1 nm due to the self-limiting current conduction [202, 203]. Both techniques offer the ability to measure current through single molecules physisorbed to both contacts. The MCB technique offers more fine control and the ability to contact single molecules more reliably while electro-migration tends to create gaps which are more irregular and less defined [204].

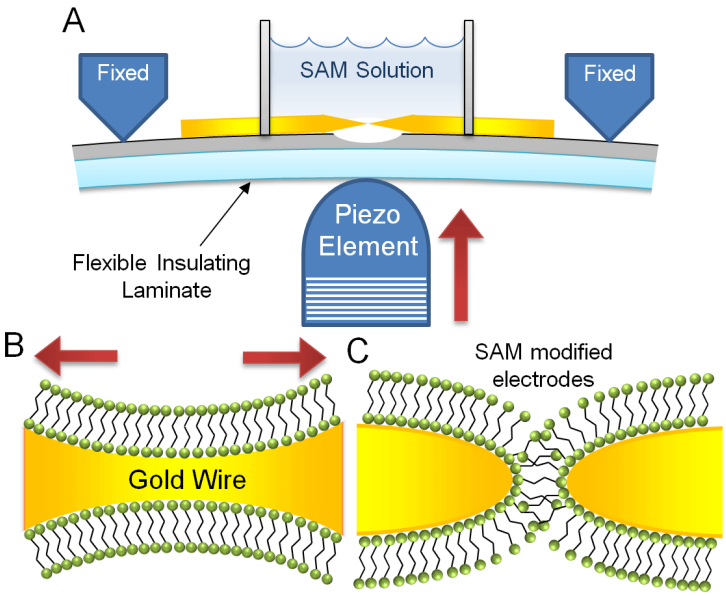

Figure 6.4: An illustration of a mechanically controllable break junction (MCB). A ductile metal wire is attached to opposite ends of a flexible substrate which is accurate deflected using a Piezo element perpendicular to the setup. As ductile failure occurs, the wires are allowed to return to gentile contact after SAMs have populated the newly formed surfaces.

6.5 Crossed Wire Junction

Crossed wire junctions have been used to study dithiol molecular transport on relatively low number of molecules ($\approx 10^3$). Two gold wires, one decorated with the SAM molecule to be studied, are mounted in a test chamber and brought perpendicularly near each other. Lorentz force is used to magnetically position one of the wires carrying a deflection current to soft contact with the other wire [205]. The experimental setup can be varied to accommodate

different metals and wire diameters. Initially, the contact area was estimated, and so produced results which were only qualitative in nature. Due to the relatively low number of contact molecules, it is possible to calculate the area of the junction through current correlation given a statistical performance basis. In comparison to STM analysis of the SAMs, it was cited that the chemical connection between the wires through the SAM created a more stable and well defined contact than that of the hovering STM tip [206]. Concern regarding curvature of the substrate was brought up by [207], and suggested the relatively large diameter of the wire likely had a minimal effect on the quality of the SAM.

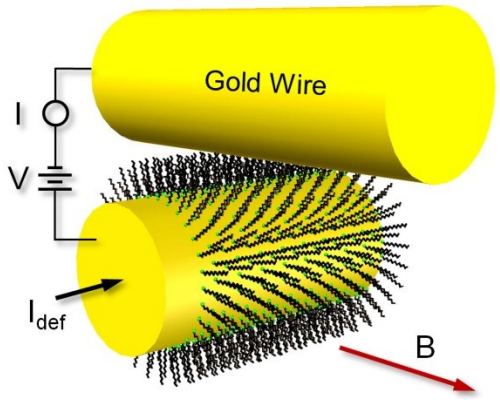

Figure 6.5: An illustration of a crossed wire junction directed with magnetic fields. The setup starts with a SAM modified wire which is magnetically positioned (using electrical current) into proximity with another wire.

6.6 Evaporation and Nanopores

Electrical contact of the top electrode in inorganic devices is generally made using conventional fabrication techniques such as metal evaporation. A problem arises in the case of an organic dielectric because of the delicate nature of the film [208]. In addition to the punch through and heat damage caused during evaporation, filamentary growth due to condensation of metallic gasses on the surface is believed to be another failure pathway [209]. In the organic

films, pinholes, grain boundaries, and contaminants lead to top metal migration towards the bottom electrode often resulting in shorts.

Solutions to counteract these effects include using cooled substrates, indirect evaporation, small contact areas [210, 211], inert gas back-filled evaporation [212], and e-beam evaporation [213]. Each of these techniques presents their own merits and shortcomings. Reported device yield varies greatly from ≈ 1% to > 90% [211, 214]. Use of a coldfinger to cool the substrate to around 150 K and evaporation at very low rates (< 0.05 nm s^{-1}) reduces the thermal damage. The high energy of gas phase metal often still causes damage to the tail end of the SAM at the very least [215]. Reactivity of the top metal with the end group of the SAM can determine the extent of penetration into the monolayer. For high melting point, unreactive metals, evaporated clusters can more easily migrate towards the bottom electrode forming shorts. Metals which react more actively with the terminal group of the SAM will likely remain on top of the film but can cause intermediate surface compounds which lead to an ill-defined interface [210, 216]. In the case of metals which can oxidize, these thin filaments can become oxidized leading to a hybrid insulating layer—thus defeating the purpose of having the pure organic dielectric.

Introduction of an inert gas such as Argon into the evaporation chamber during deposition serves to create a more indirect path for metal transport onto the substrate. Typically, the chamber is pumped to a base pressure to remove undesirable contaminants. Following this, Argon is introduced which increases the deposition pressure to the low 10^{-3} Torr range [213]. Here, the inert gas acts to block some of the direct radiation from the evaporation source and reduces the energy of the metal clusters traveling towards the substrate. This technique greatly increases the anisotropy of the deposition and requires a much greater (≈10^2 times) amount of material to be evaporated to achieve the desired end thickness on the sample [217].

E-Beam evaporation has been used to minimize because of the lower incidence of large atomic clusters. Techniques such as cooling of the sample, inert gas depositions, and e-beam evaporation can all be used together to further improve yield. Additionally, samples can be positioned at some low incidence angle thus reducing the heat exposure, or in a completely indirect location near an additional coldfinger to accumulate chamber impurities. This technique results in the least damage at the expense of the greatest amount of wasted evaporation material.[218] Because the initial metal deposition is the most critical, after appreciable metal has been deposited onto the SAM surface, the sample can be processed to final top metal thickness through other means. Conventional evaporation can follow or the metal seed layer can be used to permit electrodeposition of the desired top metal. It is important to consider the effects of incomplete penetration of the top metal into the organic layer when reviewing test results [207].

Rather than targeting the evaporation conditions, the test bed which holds the SAM can be improved to result in better yield. The use of nanometer-size wells serves to improve yields in multiple ways. Intrinsic defects from grain boundaries in both the assembly electrode and the SAM are all potential points of failure. As contact area increases, so does the probability of the formation of a short with one of these defects [211, 219]. When device area approaches that of a single molecule, the electrical response tends to be mostly bimodal consisting of electrical shorts and functional junctions. Larger well contacts can be fabricated with conventional UV lithography and result in single micron-sized contacts. Alternatively, the wells can be defined by e-beam lithography and etched by RIE or milled directly with an FIB in SiN_x or SiO_2 [219-221]. The contact is clearly defined prior to application of the organic layer; inspection by AFM or

SEM can provide useful information about the exact contact area and assembly electrode roughness.

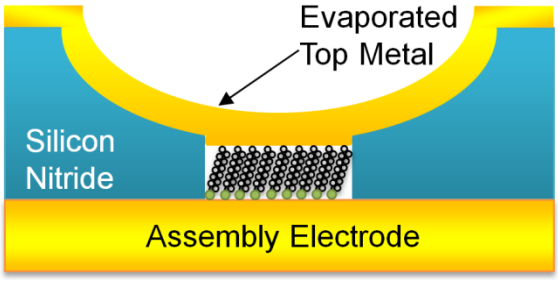

Figure 6.6: An illustration of a nanopore junction using nitride as an insulator. These junctions exhibit higher consistency due to the small contact area.

6.7 Polymer Protected Junctions

An exciting experiment was described by Akkerman, et al. in 2007 where junctions were demonstrated with contact areas of hundreds of square microns. Conductive polymers are utilized to shield the underlying SAM film from the harsh conditions of metal evaporation. Through this technique, large area junctions of 100 μm in diameter were able to achieve yields of > 95% [171]. Devices were fabricated by first defining the bottom metal contact on Silicon. Photoresist was patterned defining a small well in which SAM growth would take place. In these devices, the photoresist was retained as a mechanical support and electrical insulator. Water-based SAM assembly was carried out followed by a spin-casting of the conductive polymer. Poly(3,4-ethylenedioxythiophene) stabilized with poly(4-styrenesulfonic acid), or PEDOT:PSS (used here) is a common conductive polymer with a number of unique electrical and physical properties [222]. The final step in the process was evaporation of a top metal contact. Because the PEDOT:PSS is relatively thick as applied, it offers excellent protection from metallic punch through during metal deposition. The comparatively large cross-linked

molecules which make up the hydrophilic conductive polymer do not interfere with the hydrophobic terminal and aliphatic body of the SAM. One of the remarkable aspects of these devices is their stability in atmosphere over a period of 75 days [171, 223].

There are a number of factors which complicate the electrical transport study in these conductive polymer topped devices. The nature of the contact between the PEDOT:PSS layer and the SAM is not well understood. Cross-linked sections of the polymer are not in perfect intimate contact with the SAM. Despite drying in vacuum and monitoring of the solvent weight loss, it is expected that some solvent remains. To negate these effects, measurements were conducted in vacuum [171, 223]. In addition to PEDOT, there are a number of other conductive polymers which could function similarly, such as, polyaniline, polypyrrole, polyacetylene, and poly[(m-phenylenevinylene)-co-(2,5-dioctoxy-p-phenylenevinylene)] (PmPV) [224, 225].

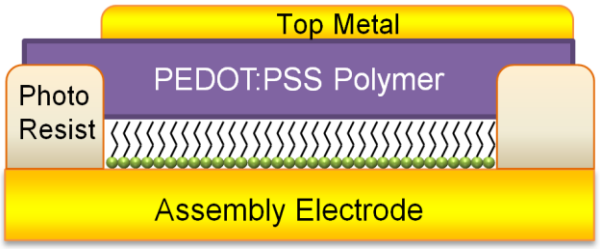

Figure 6.7: An illustration of a polymer protected SAM junction with an evaporated top metal contact. The conductive polymer PEDOT:PSS is used to make a soft contact against the delicate monolayer. (Adapted from Akkerman 2006)

6.8 Metal Transfer

One of the methods of applying the top electrode in a non-damaging way is lift-off-float-on (LOFO) [226]. This technique is not just limited to gold; however, there are oxidation concerns for reactive free floating films. In this process, a thin film metal is lifted off of its substrate and floated in a solvent medium [227]. As a part of this process, the metal film, or leaf,

can be modified by growth of a SAM film. The metal is then transferred to the target SAM coated substrate. Because the metal is prepared away from the device, harsh chemical processes for etching and lithography can be performed. Wrinkling of the metal film does occur but can be minimized by ensuring the solvent has a high vapor pressure and is hydrophobic to the metal surface [227]. Additional concerns center on liquid capture and repulsive interaction at the SAM-metal interface. An extension of this technique is known as PALO or polymer assisted lift-off. PALO uses a polymer layer on top of the sacrificial substrate. The lift-off process separates the metal contacts and polymer together such that they can be simultaneously positioned on the desired device sites. In addition to minimizing tearing and wrinkling, more aggressive geometries can be attempted [228, 229]. Solvent evaporation is accelerated by 2 hour vacuum chamber drying. Using these techniques, metal diffusion into the organic layer is unlikely and a high device yield is seen (> 90%).

6.9 Transfer Printing

The transfer printing technique uses an elastomeric stamp (often polydimethylsiloxane (PDMS)) which is cast and cured on a Silicon wafer [230]. Features which are patterned as valleys appear as hills on the PDMS stamp (negative relief of the pattern). Metal film is evaporated onto the bottom of the stamp and it is brought into contact with the SAM modified substrate [231, 232]. The chemical bond between the thin metal film and the dithiol is greater than that of the metal and the stamp and thus metal in contact with the modified substrate strips the metallic layer from the stamp. Because the adhesion of the metal layer must be preferential on the sample, the end group of the SAM must interact with the metal film on the stamp. If this is not satisfied, the stamp will likely lift off retaining the metal layer or if transfer does occur,

contact resistance will be relatively high [195]. The print results in well-defined structures, nanometer resolution, and step-and-repeat capability by reuse of the stamp [74, 232]. As in the case of lift-off, edge resolution is partially limited by the grain size of the metal in use. Edge roughness can be reduced by increasing the aspect ratio of the stamp, achieving resolutions of 5-15nm [233]. Stamps can be made of more rigid materials such as GaAs or Si but the flexible PDMS stamp is preferred as it will conform to small surface inconsistencies. The consequence of rigidity is higher contact pressure and greater chance of shorted devices; flexible stamps can possibly cause local deformations and changes in the final device size.

6.10 Nanoparticle Junctions

SAM decorated nanoparticles can be utilized to bridge small gaps (typically 40-50 nm). Contacts can be defined using e-beam lithography, electromigration [234], or oblique angle evaporation [235] creating the required contact gap. Because of lithographic limits, this technique often employs more than one encapsulated nanoparticle to complete the electric connection. This technique can also be used to create three-terminal devices, as a gate electrode can be patterned underneath the nanoparticle bed. Alternating current electric fields are used to trap the nanoparticles in the gap for further DC testing [236]. It is important to note that unlike the crossed wire, break junction, and STM techniques, the molecules are under compression in this setup. In the base of magnetically susceptible particles, an externally applied magnetic field can be used to trap the particles within the gap. Such a setup was described by Long et al. where silica microspheres where partially coated with gold, decorated with SAMs, and positioned on an electrode assembly [237]. Also demonstrated are 2D nanoparticle arrays with the powerful potential of being printed, coordinated, or creating a self-assembled “nano-breadboard” [238].

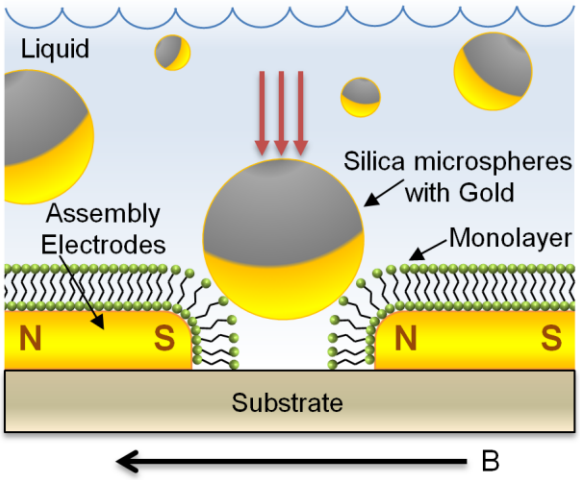

Figure 6.8: An illustration depicting magnetic assembly of coated silica microspheres onto a SAM decorated junction site.

6.11 Electrochemical Deposition

Electrochemical deposition of metal on thiols is carried out in solution to protect the organic monolayer and forms the electrical top contact of the two-junction device. The steps leading to this growth are nucleation, cluster growth, and agglomeration of the clusters to form a continuous film. In the case of nucleation on the thiol, growth clusters occur in three dimensions while nucleation of Copper on bare Gold is flat and homogeneous. Monolayer films require an over-potential to permit nucleation on the Gold assembly electrode [239]. Electrochemical deposition occurs preferentially at defect sites such as scratches, SAM boundaries, and rough patches on the bottom electrode. Free metal ions in solution can penetrate the SAM layer and become a pathway to failure. When nucleation does occur at these defect sites, an electrical short is formed through the monolayer; as the cluster continues to grow, a mushroom-shaped particle is formed [240]. It is for this reason that successful formation of the top metal can be challenging. A solution to this problem is to carry out the deposition very slowly and at very low

voltage [241]. Alternatively, the SAM surface can be coated with metallic nanoparticles which provide nucleation sites and be fused together in the electroplating process [242].

The promotion of solution deposition with nanoparticles can also be performed in the absence of electrical potentials. It is possible to carry out electroless deposition by promoting the reduction of metal ions through the use of a catalyst. The metal catalysis (Pd or Sn for example) will be seeded to the surface in the form of transfer printing or nanoparticle dispersion [243, 244]. In the case of alkane-dithiol, the end group will bind these particles which will form the nucleation sites for metal growth. Additionally, it is possible to select alkanethiols with terminal groups which interact with the electroless solution. In the case of Copper, elevated temperatures and a region of 16-mercaptohexadecanoic acid permitted the preferential copper plating [245]. The non-acid terminated SAMS acted to protect the underlying Gold substrate. An extension of the electroless plating is the formation of nanowires in small channels through subsequent electroplating [246]. It is possible to combine these techniques and leverage the benefits of each in device creation.

6.12 Review Commentary

Now that we have seen the breadth of device contact solutions, we should look back at the options to select those which are most suitable for permanent device applications. Permanent devices, in this context, will be defined as stable, self-contained junctions based on SAMs whose functionality is not reliant on bulky lab equipment. Permanent devices should also exhibit some shelf-stability after manufacture (i.e. not undergo rapid degradation of electrical characteristics). Other characteristics which are important in consideration are the possible device dimension. Because cutoff frequency rolls off with contact area, we want a structure which permits a very

small contact area. Based on data reported in the published papers, the polymer protected devices seem to exhibit the best long-term stability. It is important to note that packaging can be used to create a hermetically sealed inert environment for devices which might be more unstable due to atmospheric/environmental aging factors.

Table 6.1: A table comparing commonly used test structures with their characteristics.

Technique	Yield	Molecules	Permanent Structure	Resistance per Molecule (C12)	Ref
Liquid Metal	High	10^{11}	No	10^{8}	[176, 247]
Conducting Probe	High	10^{2} - 10^{3}	No	10^{4} - 10^{7}	[248]
STM	High	1	No	10^{4}	[195, 249]
Evaporation	Low	10^{3} - 10^{10}	Yes	10^{6}	[250]
Nanopore	Moderate	7300	Yes	10^{6}	[221]
Polymer Protected	High	10^{8} - 10^{10}	Yes	10^{8} - 10^{12}	[223]
Nanoparticle	Moderate	10^{2}	Yes	10^{8}	[251]

CHAPTER 7:

ORGANIC TUNNEL DIODE DEVELOPMENT

This section will introduce the bulk of experimentation presented in the scope of this research work. Because of this, it is broken into a number of very large sections. The rectenna research project began with a study and replication of prior experimentation of tunnel diodes based largely on inorganic dielectric materials. Optimizations were performed on these structures resulting in vastly improved diode performance. Encountering a limit in the electrical characteristics that could be achieved with the available process equipment, evolution to an organic dielectric layer was attempted. This was not without problems due to the delicate nature of the films. Each section of the design is discussed in detail and includes smoothening of the assembly electrode, cleaning the assembly surface to prepare for film assembly, development of a "soft" metal contact system, development of a photolithographic process for discreet SAM dielectric-based tunnel diodes, development of a set of permanent top metal contact solutions, and consideration of packaging and long term stability of the fabricated devices.

7.1 Inorganic MIM Structures

The first experimentation in this work was the duplication of Nickel-Nickel Oxide-Chromium diodes fabricated by a previous researcher here at the University of South Florida [36]. The diode design consisted of a hybrid fabrication process involving optical and e-beam lithography. To achieve these results, familiarization with all the microelectronic processing

equipment for fabrication was required. This proved to be a source of significant problems as will soon be discussed below. There were various design flaws with the existing fabrication attempts which were carefully studied, corrected, and re-evaluated for measurable improvement.

7.1.1 Conventional Process Equipment

The use of a microfabrication tools commonly found inside the cleanroom may not be familiar to all readers. In this section, we will briefly discuss the operation of some critical pieces of equipment in addition to commenting on some of the limitation and challenges of conventional fabrication equipment.

7.1.1.1 Cleanrooms

Because the final output of the research may be a molecular device, it is important to talk about purity and absolute cleanliness in process conditions. Ideally, it would be desirable to fabricate structures out of completely pure materials and to single atom critical dimensions. Realistically, there are a number of impurities, contamination, and geometric variations which plague process flows. Conventional lithography takes place almost entirely in the confines of a cleanroom. The cleanroom is a controlled environment utilizing HEPA filters on the ceiling and a complicated air return system to minimize the presence of dust particles in the air [252]. This laminar flow of air with the assist of gravity pushes dust particles out of the air column. Proper cleanroom protocols to minimize dust entry include a gowning room where cleanroom garb is worn to minimize human contamination. There are various standards and technical details concerning cleanrooms which are outside the scope of this discussion. It is sufficient to offer the following comparison: typical outdoor air contains on the order of tens of millions of dust

particles 0.5 μm (or larger) in size per cubic meter of air. The air in some state-of-the-art cleanrooms can contain fewer than 12 particles 0.3 μm in size per identical volume [253].

7.1.1.2 Thin-film Deposition

One of the first requirements in the process of creating a microelectronic circuit is that of depositing thin films of insulting, semiconducting, and conducting materials. At the research level, the most common technique for depositing conductive (metallic) materials is vacuum evaporation. This can be further broken down into thermal and e-beam evaporation. In the process of thermal evaporation, a durable tungsten filament or "boat" is heated by passing electrical current through two terminals resulting in the melting and subsequent evaporation of the material of interest in the vacuum environment. The vacuum environment permits a more pure film to be formed, allows the formation of films using reactive species, and reduces arcing dangers. An electron beam (e-beam) evaporator uses a filament to generate a flux of electrons which are magnetically steered into a crucible (typically graphite or some other refractory material) which contains the material to be deposited. Because the energy transfer occurs through electrons rather than thermal conduction, a much greater localized temperature is possible without damage of the container. In addition, this deposition technique typically allows evaporation of a broader range of materials including insulators and semiconductors.

Sputter deposition is a form of physical vapor deposition (PVD) and is used where a higher quality film is desired. Ionized inert gas is directed to a sputtering target. The energetic inert gas (typically argon) impacts the surface and dislodges many surface atoms on the target. The highly unstable argon ions reunite with their missing electrons and the vaporized target material float through the vacuum towards the substrate. Optimum kinetic energy transfer of the

plasma is achieved when the molecular weight of the inert gas is on the order of the target material. While gas selection is not often considered when changing targets, helium, argon, krypton, and xenon can be used. When depositing compounds, it is sometimes advantageous to include stoichiometric correction gasses. An example of this may be the sputtering of ZnO insulator. During target ablation, some of the bonds between zinc and oxygen molecules are broken and result in recombination of monoatomic O^0, O^-, O^{-2}, etc. oxygen radicals which form elemental oxygen. This gas is then pumped out of the deposition chamber by the vacuum system and results in a change in stoichiometry of the deposited material. The bleeding of supplemental oxygen gas along with the argon plasma corrects for these deficiencies by making surplus oxygen available at the reaction site.

Chemical vapor deposition (CVD) is a chemical, rather than physical, process where reactions happen in situ resulting in pure depositions. CVD allows greater control of film characteristics and can produce amorphous, polycrystalline, and monocrystalline materials. It is especially useful for deposition of compounds which tend to not retain stoichiometry well during other types of deposition. Nitrides, oxides, and even nanodiamond coatings can be deposited with this technique. Reactions are usually carried out in well characterized, purpose-built chambers that require conditioning due to ever-changing chamber conditions. Great care must be taken in process staging and gas control as the highly reactive precursor species used in CVD systems are usually highly volatile and very toxic [254].

These evaporation techniques are limited in producing highly planar films due to the bulk nature of the evaporation process. Random evaporation events may produce spalling, bulk voids, and large molecular clusters to be deposited onto the target substrate. Workup is sometimes performed to restore planarity by way of CMP (Chemical Mechanical Polishing). Certain soft

metals (such as gold) are not readily polished by CMP. Because the grit slurry is much harder than the metal being polished, it often becomes embedded into the metal surface. Steps to remove this grit simply reveal pitting on the soft metal surface.

7.1.1.3 Vacuum Technology

As stated earlier, vacuum systems are employed to minimize contamination in the ultra-pure world of microfabrication. A vacuum is simply the absence of gaseous phase material within an enclosed volume. In the laboratory, vacuums are achieved by means of pumping, moving, condensing, and/or absorbing free moving gaseous molecules. Different vacuum pumps operate offering specific strengths and weaknesses which are evaluated carefully prior to installation into a particular system.

Most systems employ a basic "roughing" pump, which is typically a rotary-vane pump, which is capable of pumping air down to the milliTorr vacuum range. These pumps are often also used to back a high vacuum system which operates efficiently at high vacuums but is sometimes incapable of dealing with pressures near atmosphere. In addition to rotary vane, piston, scroll, diaphragm, and booster pumps can be used.

For most application, high vacuum is what is actually needed to achieve quality results in experimentation. High vacuum is a subjective range of pressures typically encompassing from around 10^{-3} Torr to 10^{-8} Torr. Beyond this is the region of ultra-high vacuum. The ultra-high vacuum range requires very precise control of all conditions and is typically reserved for instruments which perform analyses such as electron microscopes. High vacuum pumps commonly seen on processing equipment include diffusion pumps, turbo pumps, cryo pumps, cold traps, and ion pumps. One of the oldest technologies in this family is the diffusion pump

which heats heavy oil that entrains the gas to be pumped at high velocity. This pump is extremely reliable due to the lack of moving parts. It is still used today where low vibration, low noise, and high reliability is required. Some of the primary downsides are the long warm-up time and risk of damage from air exposure while in operation.

Cryo(genic) pumps and cold traps operate under similar principles. Their primary mode of operation is to condense gas molecules onto cold surfaces effectively removing them from the operating volume for a period of time. While cold traps are generally simple insulated regions of plumbing with liquid nitrogen circulating through, cryo pumps are complicated heat pump systems with high surface area materials for adsorption of a large quantity of molecules. These systems use ultra-pure helium as a working (refrigeration) fluid. Both of these eventually will become saturated in operation and require regeneration.

The turbomolecular pump is reminiscent of a jet engine containing many stages of turbines with blades at varying pitch. The electrical motor within spins the assembly at high speed and imparts a change in direction and kinetic energy to any molecules which approach. This is a very fast and powerful pumping technology but is typically costly and can be destroyed by sudden exposure to atmosphere or small particles striking the turbines.

Lastly, we briefly consider the ion pump which will include consideration of titanium sublimation pumps (TSP). In both cases, these would perhaps be better called gas collectors than pumps. The pumps work by ionizing free gas with high voltage and accelerating the ions towards charged plates. The ions then become implanted into the plate surface removing them from the vacuum system. These pumps must be protected from exposure to atmospheric conditions at all costs—especially when in operation. A leak even can completely saturate the collection media of this type of pump in less than 60s.

Vacuum system limitations often present a variety of challenges for quality and reliability in the laboratory. As we have just seen, they tend to be fairly delicate regarding sudden failure and exposure to atmosphere. In addition to contributing to downtime, there is the topic of leaks. In Figure 7.1, we see an illustration of a variety of sources of gas leaks within a vacuum chamber. Many times, systems are inherited and designed by researchers long before our presence in a lab.

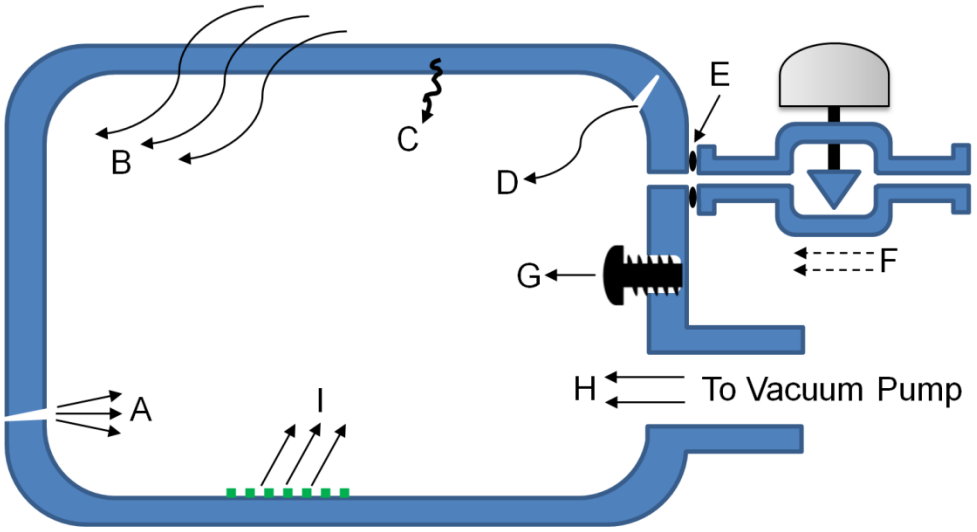

Figure 7.1: Common sources of leaks in process vacuum chambers. In a clockwise fashion starting with (a) actual leaks in the chamber wall, (b) permeation of gas through wall, (c) diffusion of gasses trapped in the wall, (d) virtual leaks from partially covered regions such as poor (or double) welds, (e) fitting seal leakage, (f) feed-through or gas valve leaks, (g) virtual leaks from screw/bolt enclosed volumes, (h) vacuum system backstreaming, (i) outgassing of surface species.

7.1.1.4 Micro-pattern Formation

Now that we have seen how to produce the thin films that are the backbone of so many structures, let us look at how the small planar features are defined. All these techniques fall under an umbrella term called lithography. Photolithography is the patterning of small features with light. Often shortened to photolitho, this technique begins with a yellow filtered light

cleanroom. Photoresist, a UV photo sensitive polymer, is spun at high speed onto the surface of the sample. The photoresist goes through a pre-baking step and is placed into a mask aligner. The mask aligner serves to expose select regions of this light sensitive polymer to UV light. The photomask is a plate of glass which has a reproduction of the desired features etched into a chrome reflective layer on the surface. When the mask and sample are put into contact by the mask aligner, the chrome regions reflect incident UV light and thus prevent exposure under these regions. Depending on the chemistry of the photoresist, light either crosslinks the polymer and causes the photoresist to stick (negative tone), or breaks bonds and results in the development process washing away the photoresist (positive tone). In either case, after development, the result is polymer protect regions reproduced with great fidelity from the original mask. From here, further chemical processing can selective target these exposed areas.

Photolithography is limited by the wavelength of light used. Most research mask aligners employ a mercury vapor lamp where the G-line (435.8 nm) or I-line (365.4 nm) are used in patterning [255]. As a general rule, it is difficult to produce features below 1.5 times these wavelengths. Through multiple exposures, deep UV, and modeling of advanced interference patterns, photolithography has been used by the semiconductor industry to achieve features down to the single nanometers. For most research applications, the volume and revenue which the semiconductor industry leverages in their technological investments are not warranted. If low throughput high resolution is desired, electron beam lithography can offer very high resolution at the expense of very slow writing speeds. In a manner very similar to that described for photolithography, an electron sensitive photoresist is spun onto the sample. This film is patterned using a highly focused beam of accelerated electrons whose de Broglie wavelength is far smaller than that of any mask aligner light [256]. Specialty machines are available which

offer acceptable patterning speed. Due to funding limitations, many researchers opt to retrofit an existing system many labs have which closely resembles the e-beam writer. An electron microscope is used to pattern the features by scanning the defection coils/plates to direct the beam of electrons to expose the photoresist.

7.1.1.5 Etching of Films

Up to now, we have studied the application of materials and patterning of polymers. The logical progression is to use the photoresist to protect certain regions of the underlying material during removal. Etching is the chemical reaction of a species for the purpose of removal. Photoresists are typically plastic-like in nature and thus resist chemical attack from the exact reagents which readily attack metals. Etchants are available for a variety of materials with very specialized etch characteristics. Etch rates and selective (or preferential rate) reagents are used to achieve almost all imaginable final geometries. For cases where feature are very small or fine detail is required, dry etching (gas or plasma) is possible. Reactive Ion Etching (RIE) and Deep Reactive Ion Etching (DRIE) use chemically reactive plasma to etch specific surface materials. DRIE, also known as the Bosch process, utilizes short succession cycles which etch and deposit a protective polymeric coating onto the etch sidewalls. Using these more advanced etch methods, nearly vertical sidewall etching is possible with very high aspect ratio features.

7.1.2 MIM Inorganic Materials and Process

The initial MIM structure was taken and advanced to the most mature state possible given the available equipment. The initial design (seen in Figure 7.2) consisted of optical lithography patterned contact pads upon which a small pad of nickel and nickel oxide was sputtered. From

there, e-beam lithography on the JEOL JSM-840 electron microscope outfitted with Joe Nabity's Nanometer Pattern Generation System (NPGS) was used to define the critical top-contact area.

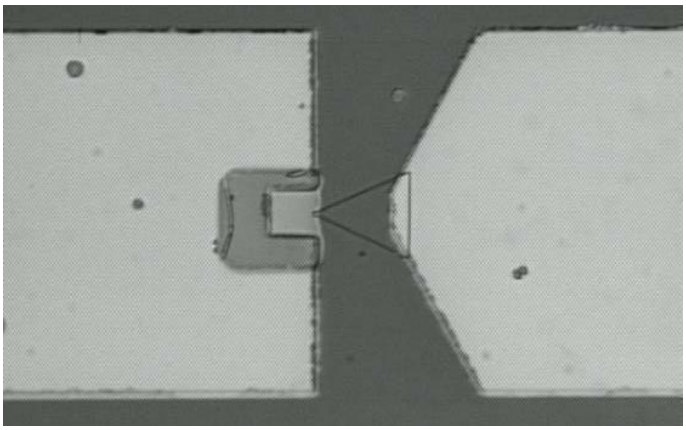

Figure 7.2: A SEM image of the e-beam lithography patterned top contact of the original inorganic MIM diode design. The base and intermediate layers were processed using optical lithography and the final step which constrained the contact area was performed using the NPGS system on the JEOL JSM-840 electron microscope.

Because the top contact was used to define the area and it was performed using e-beam lithography, contact areas below 1 μm^2 was routinely accomplished. While the layout was able to yield devices, there was great inconsistency in the contact area because (1) the prior step utilized optical lithography which introduced great variations in the alignment of the base and insulator elements, (2) the e-beam litho writing field was chosen by the user and did not incorporate and automatic fiducial marks to improve accuracy, (3) the triangular shaped top contact amplified any alignment error resulting greater inconsistency.

For our lift-off application, it would be desirable to have a negatively sloped sidewall such that there would be a region of discontinuous deposition near the edge resulting in much improved lift-off. Of course, this is provided that the photoresist is on the order of 3 times thicker than the deposition film. In the case of these thin films, this does not cause a problem but it does create a conflicting requirement for feature detail. Another common general rule is that

the photoresist should be less than twice as thick as the minimum feature is long [74]. So if our goal is to produce a very high resolution feature, we must weigh these conflicting parameters to result in an optimum recipe. The spinning of multiple layers of photoresist with varying sensitivity has been used in both optical and e-beam lithography to create positively or negatively sloping photoresist sidewalls. After much experimentation, optimum feature detail and lift-off performance was achieved with a 6000 rpm coating of MMA co-polymer for 60s followed by 5000 rpm coating of PMMA for 90s. The photoresist thickness was verified on a Dektak stylus profilometer and was found to be consistently between 280 and 290 nm. Following spin coating, the samples were pre-baked on a hotplate set at 150°C for 90s. A dose of 1-6 nC/cm^2 of electrons was used to pattern the resist. Lithographic dosing varies significantly for e-beam process (even within the same sample) and depends on (1) resist thickness (2) acceleration voltage (3) underlying material (4) feature proximity and density. A common example of some of the challenges of e-beam lithography is the reproduction of an array of parallel lines positioned less than 1 μm pitch. The center of the array will require a lower does in part due to the backscatter of electrons within the underlying material which will enhance the exposure in the area. Development of the e-beam defined pattern was done in a 3:1 solution of IPA:MIBK for 90s with mild agitation.

The large photo litho defined contact was thermally evaporated on a Denton vacuum deposition system. All critical layers were processed using an in-house built, 3 target sputtering machine. The first set of layers, nickel and nickel oxide, were obtained by first pumping down to a base pressure of $< 5 \times 10^{-6}$ Torr. Argon was selected as the sputtering gas with a deposition pressure of 1.5×10^{-2} Torr. Nickel deposition was performed at 100W plasma power for 8 minutes. Nickel oxide was deposited using the same pure nickel target while bleeding surplus

oxygen gas into the chamber (6:2 ratio with argon) for 2 additional minutes. For all these process steps, a shutter was used to ensure stable plasma and removal of surface target contamination prior to actual deposition. The chromium top contact area was defined using a similar e-beam lithography procedure and deposited using sputtering.

Realizing these problems a modified design was presented for consideration. This modification would seek to resolve as many of the limitations present without requiring a costly change of optical masks. The large contact pads which were processed with photo lithography could be preserved and instead of a triangle, the contact was changed to a crosshair pattern. Because the contact consisted of two intersecting lines, the area was constant even with the presence of significant alignment problems.

One benefit of the smaller contact areas was a lower incidence of failures. Because the insulator layer has pinholes, the smaller contact area is statistically less likely to include one of these defect sites which would result in shorting of the device. The e-beam patterning still did not completely resolve the issues with reliability which were later studied using atomic force microscopy (AFM) and SEM. After the AFM study, it became clear that the problem was the lift-off step for the removal of the nickel-nickel oxide layers. The lift-off process was selected due to difficulty in etching of the non-homogenous layers and the weak chemical resistance problems of the PMMA during the etch process. The AFM image (Figure 7.3) shows significant edge roughening which upturns non-oxidized metal to make contact with the following litho step. This shorts out the device along the step edges and this was seen after electrical testing in an SEM image in Figure 7.4. That was somewhat mitigated through the use of a bi-layer photoresist.

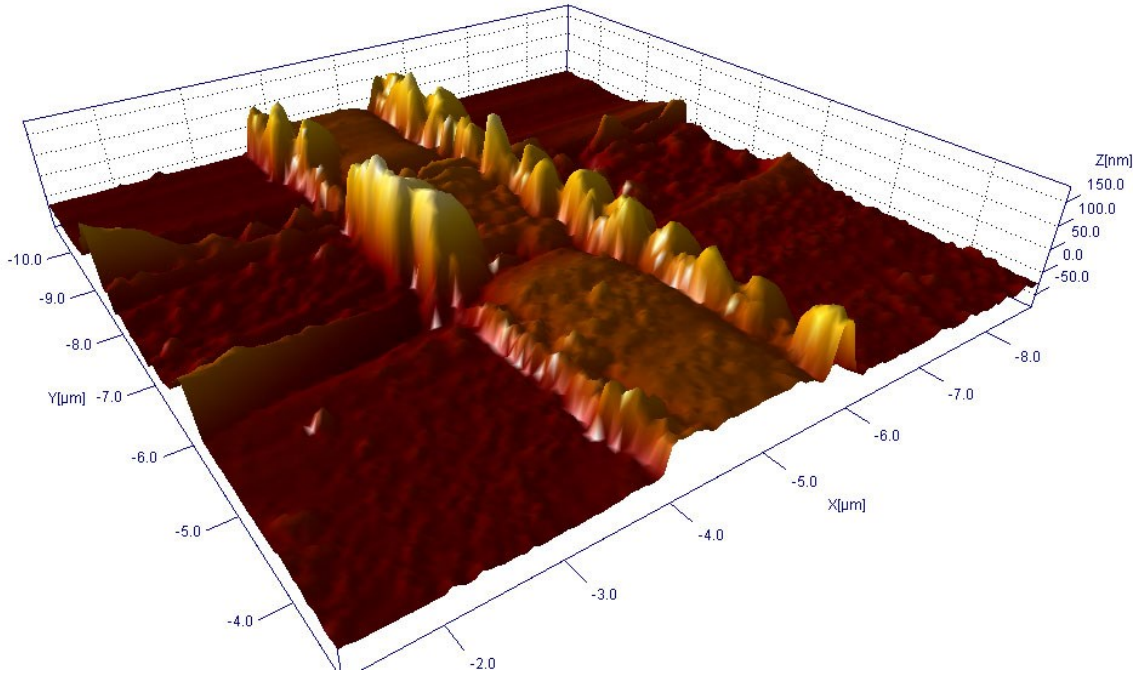

Figure 7.3: A 3D AFM reconstruction of an inorganic MIM junction showing rough sidewalls due to lift-off issues. The z-scale of this image is exaggerated by a factor of 5 to more clearly depict the edge roughness.

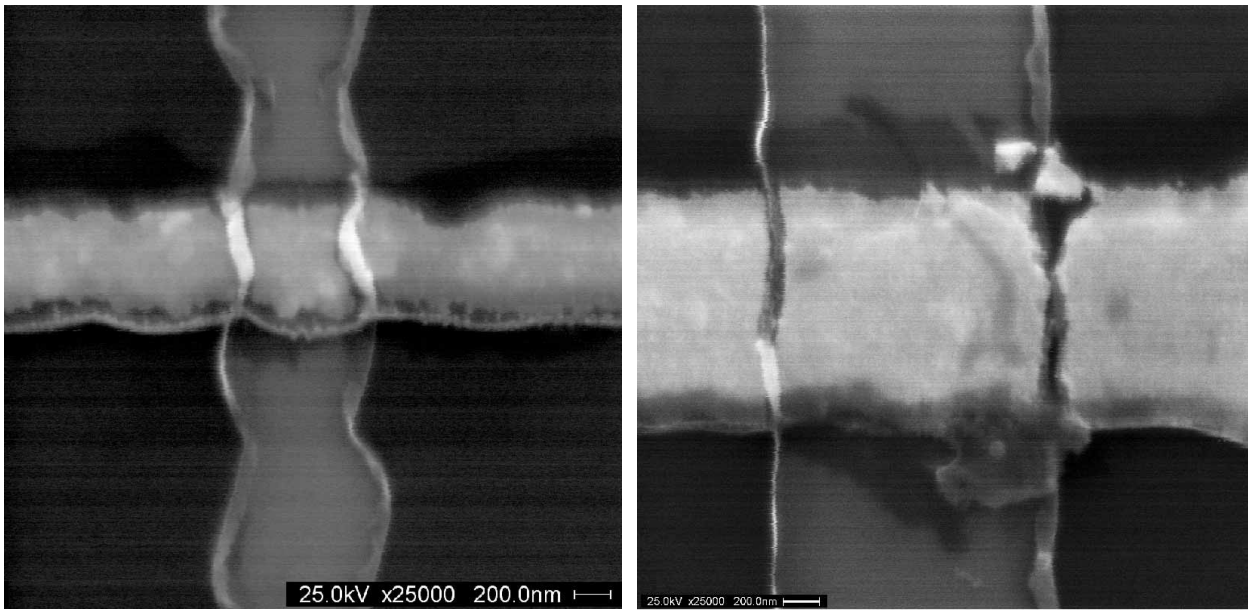

Figure 7.4: A set of SEM image of sub-micron cross bar MIM contacts patterned with e-beam lithography. The first is included to depict process control problems in the form of wavy lines from e-beam lithography problems. The second image shows failure after electrical testing which resulted in opening of circuit near the step region of the contact.

7.1.3 Process Optimization and Improvement

Device reliability was further enhanced by introduction of a (relatively) thick spacer insulating spacer which prevented edge contact. This spacer was originally designed to be patterned with e-beam lithography but it is possible to include with careful photolithography. The function of the spacer is illustrated in Figure 7.5 in a top view. To prevent damage to the delicate NiO_x dielectric layer, lift-off was selected to pattern the SiO_2 spacer. The spacer was e-beam evaporated from quartz evaporation fragments obtained from Kurt J. Lesker Company. Despite offering the potential to greater consistency, cracking and poor lift-off of the small contact pore feature resulted in a very high fraction of these devices to fail. Future implementation of improvements was ceased due to migration to organic dielectric technology. There were a number of promising results with the crosshair design diodes and performance is discussed in Section 8.2.2.

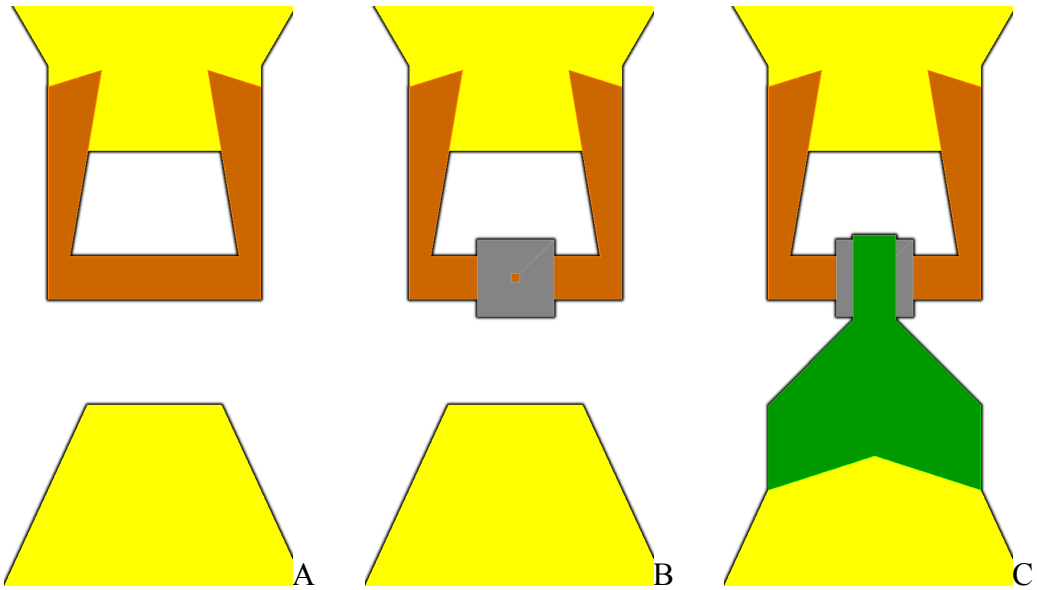

Figure 7.5: An illustration depicting the fabrication steps of an inorganic MIM junction with a spacer. The spacer acts to negate the effect of the rough edge resultant of the lift-off process. The system also tends to compensate very well for minor alignment errors.

7.2 Critical Substrate Smoothness

Reliability and packing density of self-assembled monolayers depends highly on environmental conditions and chemical purity of the precursors. Another factor which greatly affects the quality of the resultant film is the planarity and flatness of the assembly substrate [257]. This need manifests in an interesting study on simple, low-cost methods by which nearly atomic flat noble metals can be obtained. As we saw in Chapter 4, highly curved nanoparticles cause SAM to cluster at low temperatures revealing defects. These features will lead to shorted devices if metal is allowed to make contact with the tail end of the monolayer. Moreover, surface area calculations of tunneling can be affected by the disparity between actual surface area and dimensional area. Here, a novel system and technique are presented to demonstrate near atomically flat metal surfaces.

7.2.1 Design of Heating System

Highly controlled heated air flow has been used to clear the surface of contamination and improve metal surface quality [258]. Studies have reported the use of hydrogen flame annealing for this purpose. The high temperature flame reorders the surface structure to the desirable (111) assembly surface. Additionally, the hot plasma strips off any organic contamination leaving the monolayer with the minimum energy to overcome and bind to the surface. Due to lab safety concerns, open hydrogen flame is highly discouraged in most labs and definitely not an option in a cleanroom environment. For cases where the more dangerous gas is not available, personal experimentation has yielded acceptable results while using butane flames. Contamination is often touted as a significant concern when flame annealing. A number of authors have suggested a setup in which the flame is used to heat the metal coated substrate through a flask which is

continuously purged with a high purity noble gas. These experiments have been repeated yielding acceptable but unpredictable results. The problem I experienced is that it relies too much on individual operator skill and a simple variable like gas flow variations can mean the difference between an unmodified surface and a thermally damaged surface. The thermal processing is most suited for substrates which have been protected with a silicon nitride layer. Because gold readily diffuses into silicon, this technique is not only incompatible with CMOS process, it can even contribute to leakage currents where the silicon is simply an insulating carrier. A workaround to this problem is to deposit titanium as a tie layer between the silicon and gold. While chromium is more often used due to its greater prevalence and lower cost, it provides less of a diffusion barrier and often alloys with the gold [259].

To achieve better control, I explored the use of an electrically heated and electronically controlled annealing system. The system was named the Hydrodynamic Open-Ended Thermocouple-Based Inert Gas Heating and Temperature System (HOT NIGHTS). The system is outlined in Figure 7.6. The heart of the system consisted of a mica and ceramic insulating hot air gun core which was modified for use with laboratory gas and relay control. The heating coil was controlled by an Omega model CN77332-C2 PID controller. The power switching was done with a Crydom 25A solid state relay (SSR) with a sizable heat sink and fan attached. Temperature monitoring was accomplished with a K-type thermocouple located in the exhaust nozzle. The heating elements were found to be too reactive with air at the high temperatures necessary for processing so argon gas was flowed through a regulator and expanded in a laminar flow plenum just above the heating block. The system was mounted vertically and nozzle modeled in a multiphysics environment (AutoDesk Algor) to ensure even heating and ambient atmosphere isolation (Figure 7.7).

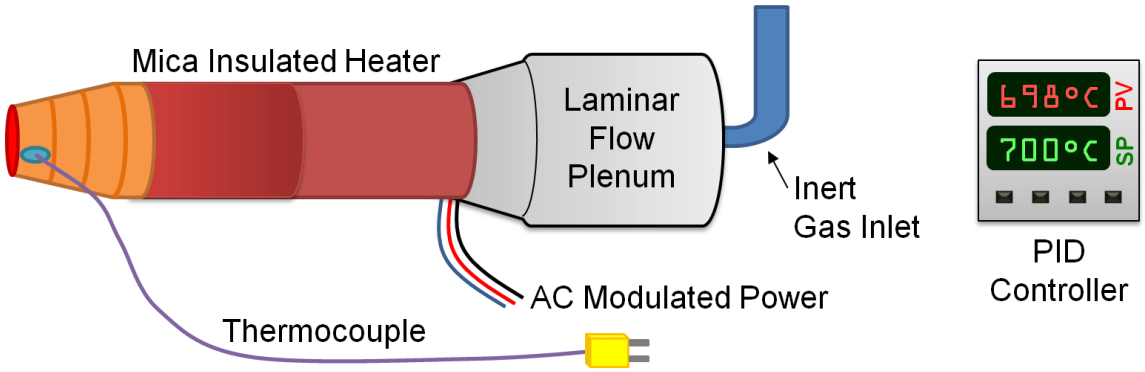

Figure 7.6: An overview illustration of the thermal annealing system for smooth substrates.

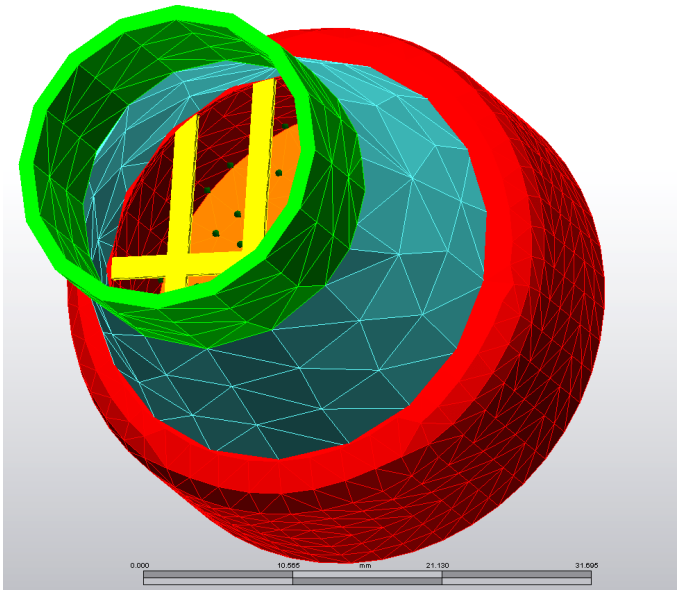

Figure 7.7: A meshed simulated solid model of the thermal nozzle of a substrate annealing system. The simulation was performed in AutoDesk Algor which provided important data to better control gas flow rates and heating power required to achieve uniform substrate heating.

Relatively small test coupons of gold e-beam evaporated on silicon were used to evaluate performance. The samples were placed on an alumina plate stand which allowed proper flow of gases around the sample (Figure 7.8). The results of this processing are further commented and compared with other solutions in Section 7.2.3. In Figure 7.9, we can clearly see the rough film surface giving way to "lakes" of annealed gold. Processing requires minimum disturbances and

variations. Surface contamination should be minimized as it tends to break the crystalline reordering at the surface. Temperature excursions resulted in cracking and were found to be the result of slow SSR switching in the original PID programming.

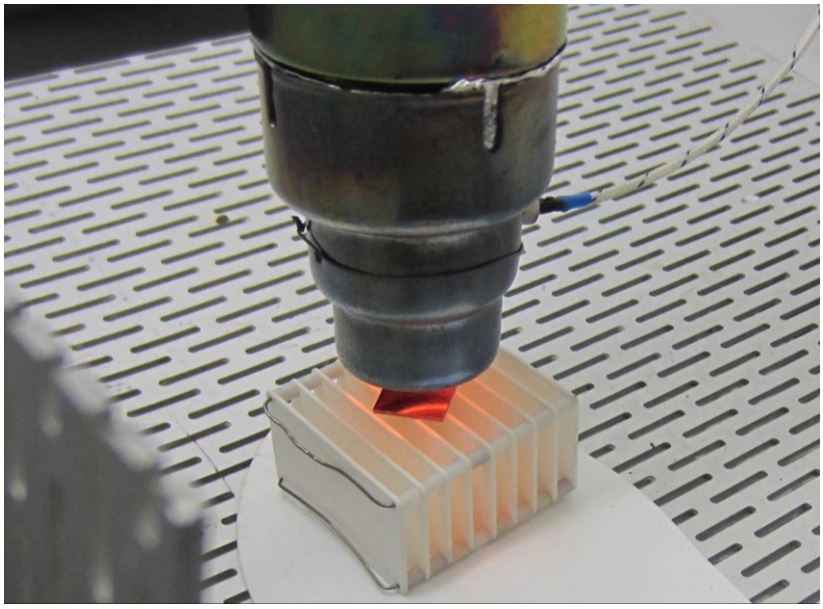

Figure 7.8: A photograph of the thermal annealing system processing a small sample. A thermocouple and lead are seen at right protected by ceramic beads. A substrate holder was crafted consisting of alumina plates spaced by alumina beads and strung together with molybdenum wire.

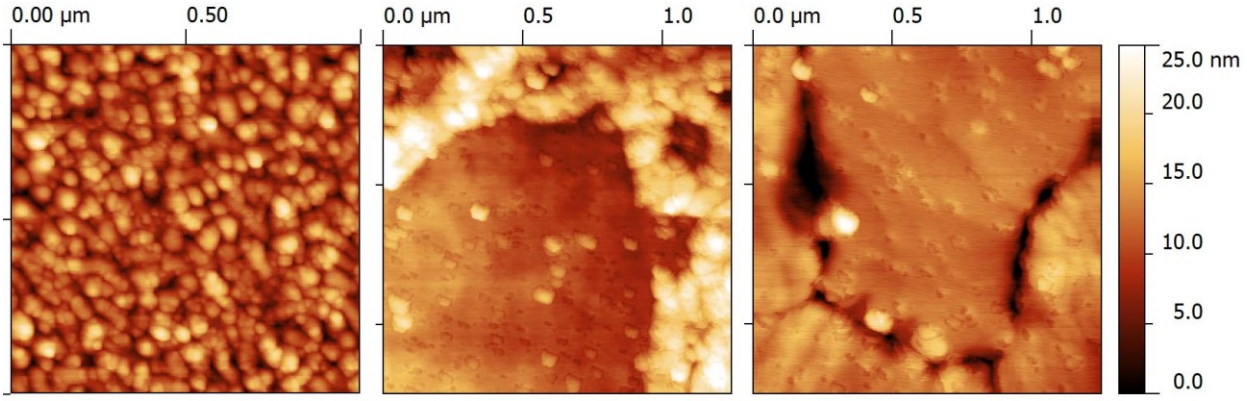

Figure 7.9: A set of AFM images depicting progressively smoother gold film after thermal processing. At left, a freshly evaporated surface. At center, is the in-progress smoothening using the HOT NIGHTS annealing system—notice the "lake" of smoothed gold. At right, film exhibits cracking as a result of a temperature excursion.

7.2.2 Template Stripping

One of the ways that smooth gold was achieved was through a process called template stripping. This technique was first described by Frey [260] in 2000 and saw immediate popularity among those in the microfabrication field. Template stripped gold (TSG) and silver have been extensively explored due to the material compatibility for self-assembly. Many groups studying electron transport through monolayers now exclusively test on template stripped platforms and have seen significant improvement in device yield and consistency [261].

The typical procedure involves the preparation of a template surface which is known to have an ultra-flat surface quality. Most often, a high quality, polished silicon wafer is used. Alternatively, many have reported success using V-1 grade freshly cleaved mica. Muscovite mica is a phyllosilicate crystal which exhibits nearly perfect basal cleavage. Through the use of a sharp implement such as a razor or needle, the near-atomically flat planes can be separated revealing a clean, uncontaminated surface which can act as a template for evaporation. Alternatively, this cleavage process is used in critical AFM studies where the subject to be investigated may be on the order of single nanometers and may not be readily visible on a more rough field.

After deciding upon the template surface, small silicon and glass samples were prepared by dicing and solvent cleaning. The template underwent a reverse evaporation of gold-then-chromium. The typical procedure during thin film evaporation of noble metals is to first deposit a “tie” or adhesion layer. Titanium or chromium is typically used as the adhesion layer. In this case, the gold is deposited first (typically 120 nm) and a high rate chromium deposition (approximately 80 nm) caps the film. The faster rate of the chromium deposition creates a rougher surface to enhance epoxy adhesion. A minimum of 120 nm of noble metal was used to

(1) provide good mechanical flexion resistance to the epoxy, (2) provide a sufficient barrier to any intermetallics and interdiffusion between it and the adhesion layer, and (3) ensure complete contact with the template was achieved with no pinholes exposing epoxy. The heat of the continued evaporation acts to reorder the molecules near the template resulting in a flatter, truer surface representation. For cases where the epoxy may have a small defect such as a bubble, the thicker metal film is more resistant to tearing during the delamination procedure. The samples are first primed using 3M Scotch-Weld 3901 primer and baked on a hotplate per the product instructions. The two-part epoxy chosen for the template stripping was Loctite Hysol E-30CL. This is a low cost, optical adhesive with very good solvent resistance. Still, the chemical resistance needed to be validated for this application. The epoxy was mixed in a small polypropylene cup, drawn up into a disposable syringe, and applied generously to the evaporated template surface. The samples were applied to the epoxy with the primed side facing the epoxy. After some experimentation, care was taken to avoid bubbles in the epoxy pour as they later manifested in tears or pits in the stripped surface. The best technique found for this was to "massage" the glass sample in small 1mm circles with a pair of tweezers until visual confirmation that all the bubbles were pushed to the outside of the bond area. A mass was placed over each sample and it was allowed to rest at room temperature (22°C) for 48 hours. To remove the sample and reveal the template stripped surface, a sharp implement was pushed into the edge of the epoxy where it met the template plane. With continuous pressure, the sample popped free revealing the pristine surface. A small blade or pair of scissors was used to cut excess epoxy or gold film from the edges of the TSG sample.

The procedure proved to be very reliable at creating relatively small samples for SAM immersion. Films grown on this more flat surface exhibit fewer defects and pinholes which

makes them more attractive for rectifier applications. While trick to remove, it is possible to create a 25 x 25mm sample by the technique outlined above. Thicker sources of sample glass (such as microscope slides) and silicon cut from larger wafers are recommended for samples larger than 10 x 10mm. The force required to dislodge larger samples may prove greater than the breaking force of the template or sample. An alternative tool or secondary epoxy may be required to remove and then release these larger samples. A full analysis of the surface quality is given in the next section.

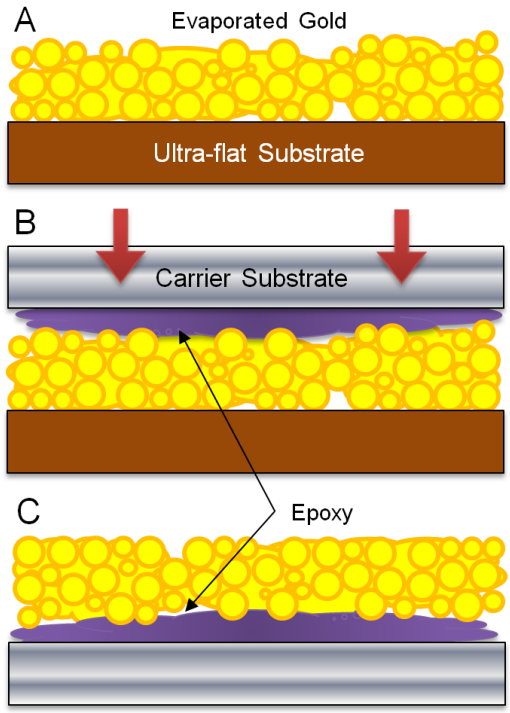

Figure 7.10: Illustration of template stripping process in cross-section perspective. In subset (a) gold is evaporated onto an ultra-smooth template substrate which will be sacrificed in the fabrication process. The top of the gold film is then epoxied to a carrier substrate (typically glass) (b). Finally, the ultra-flat template is stripped off (c) revealing a surface of enhanced smoothness.

7.2.3 Analysis of Smoothened Surfaces

Evaluation of the long term solvent tolerance of the samples was required to ensure that SAM assembly would not significantly warp the template stripped surface. The experiment began by creating several identical template stripped gold test coupons. These coupons were immersed in various solvents relevant to SAM assembly and wafer cleaning. The samples were maintained in darkness and at a temperature 22°C for 500 hours. At the conclusion of this immersion, the samples were removed from their respective solvents, dried with an N_2 stream, and immediately analyzed by a white light interferometer. The Wyko NT9100 was used to perform the surface analysis. Table 7.1 shows the results of the AFM and interferometer study which compares aged and new template stripped surfaces to freshly evaporated and thermally processed samples. Thermal processing using the HOT NIGHTS system did achieve impressive results but trouble with cracking and uniformity of process makes the template stripped surface more attractive. This immersion time for SAM assembly is 1 – 2 orders of magnitude shorter than tested for and so normal processing would likely not pose any problem. The most aggressive solvent was acetone and was found to disrupt the underlying bond structure so much that significant surface cracking of the stripped metal was visible (Figure 7.12). The surface deformations resulting from polymer distortion with all other solvents still preserved the smooth surface necessary for assembly. The full set of optical profile results is visible in Figures 7.12 to 7.16. Template stripping is recommended for all applications possible involving SAM assembly.

Table 7.1: Roughness measurements of template stripped and annealed gold.

	Acetone	Water	Hexane	Ethanol	Control	Evaporated	Annealed
R_a	40.30nm	31.25nm	20.45nm	11.36nm	0.69nm	2.61nm*	0.76nm*

* These roughness values were obtained by AFM while others by optical profiler.

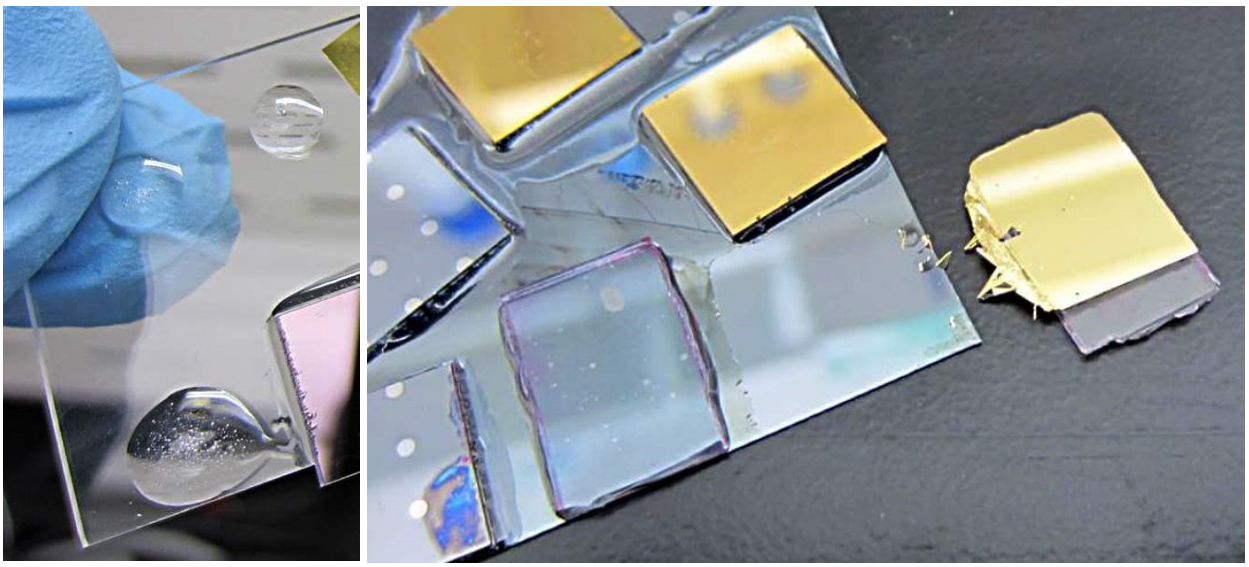

Figure 7.11: A photograph of the template stripping process detailing epoxying and freeing of sample. At left, epoxy droplets with high air void content which result in pitting on the final template stripped surface. At right, gold surface is revealed after prying off sample.

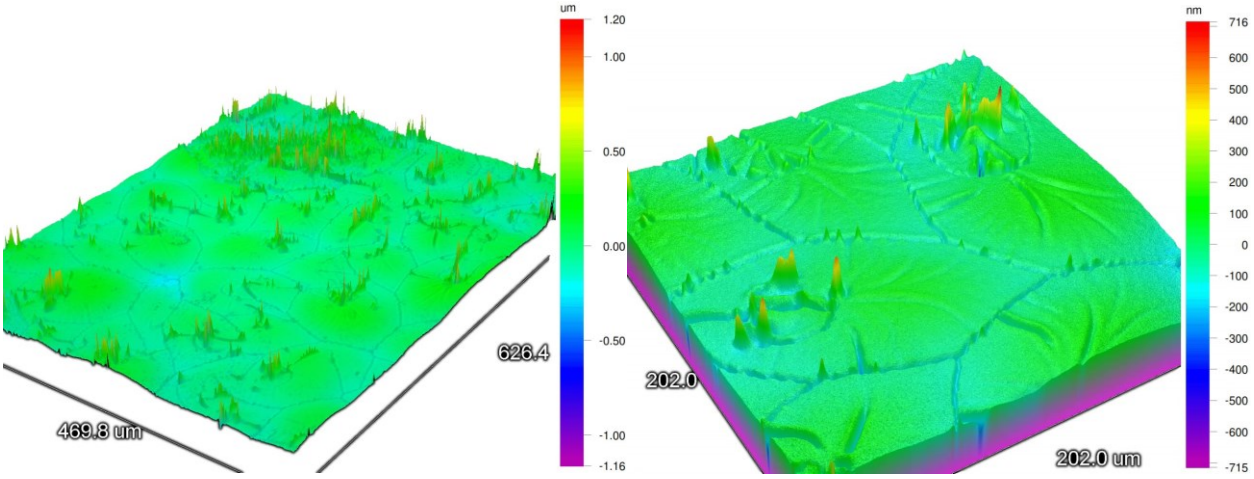

Figure 7.12: Optical profiler 3D reconstruction of surface damage of template stripped gold after 500 acetone soak. Left image is at 10x magnification and right image is at 50x showing details of cracking and wrinkling of gold film on swollen epoxy.

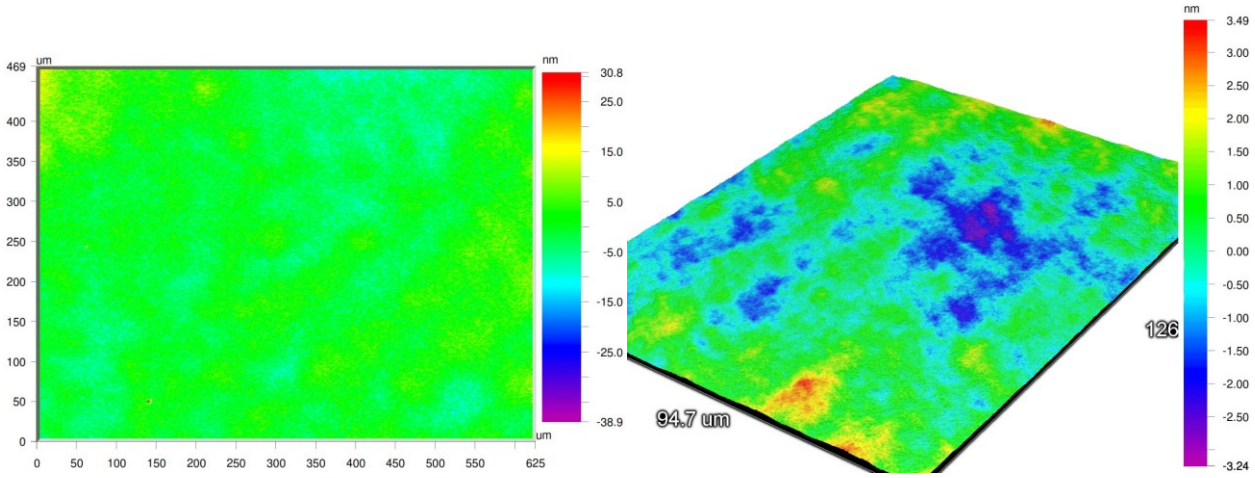

Figure 7.13: Optical profiler image of template stripped gold highlighting minimal damage on the control sample which was stored in atmosphere for 500 hours. The roughness was only slightly increased as compared to a freshly made sample and may have been aggravated by atmospheric moisture absorption. Left image magnification is 10x, right image is 50x.

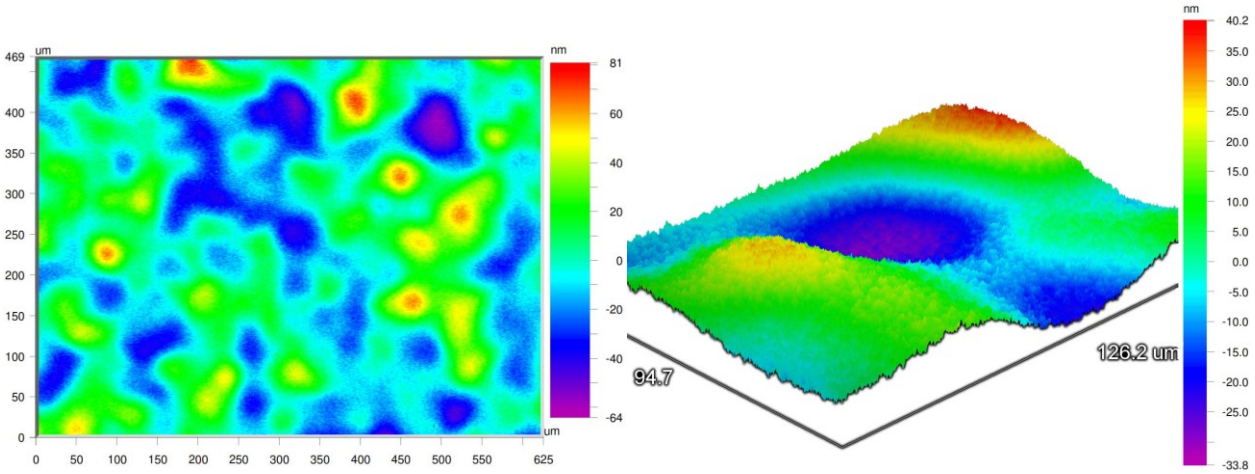

Figure 7.14: An optical profiler image of template stripped gold after 500 hour exposure to ethanol. While the underlying epoxy swelled and warped, the surface maintained its integrity with very minimal cracking. Left image magnification is 10x, right image is 50x.

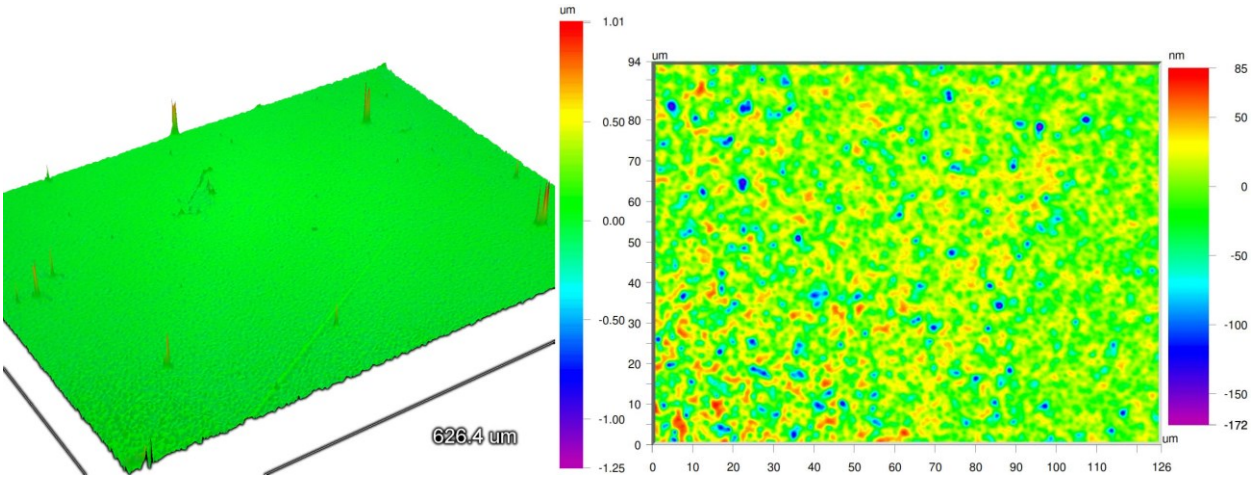

Figure 7.15: An optical profiler image of a template stripped gold surface after 500 hour immersion in hexane solvent. The highly volatile solvent attacked the epoxy and created numerous fine cracks on the surface. Left image magnification is 10x, right image is 50x.

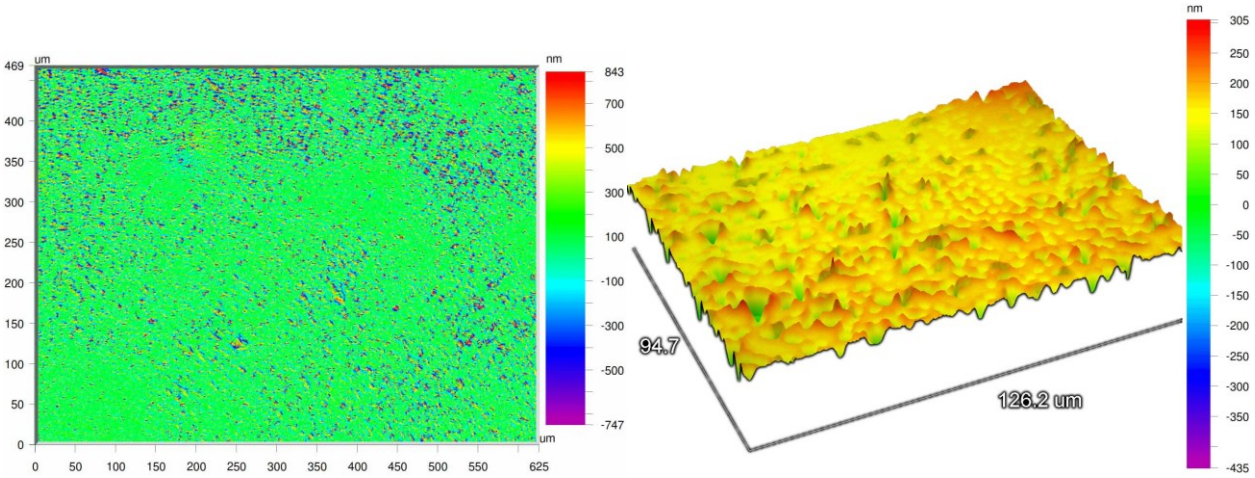

Figure 7.16: An optical profiler image of the surface of template stripped gold after 500 hour exposure to DI water. The sample exhibited significant texturing of the gold surface on the micron scale. Left image magnification is 10x, right image is 50x.

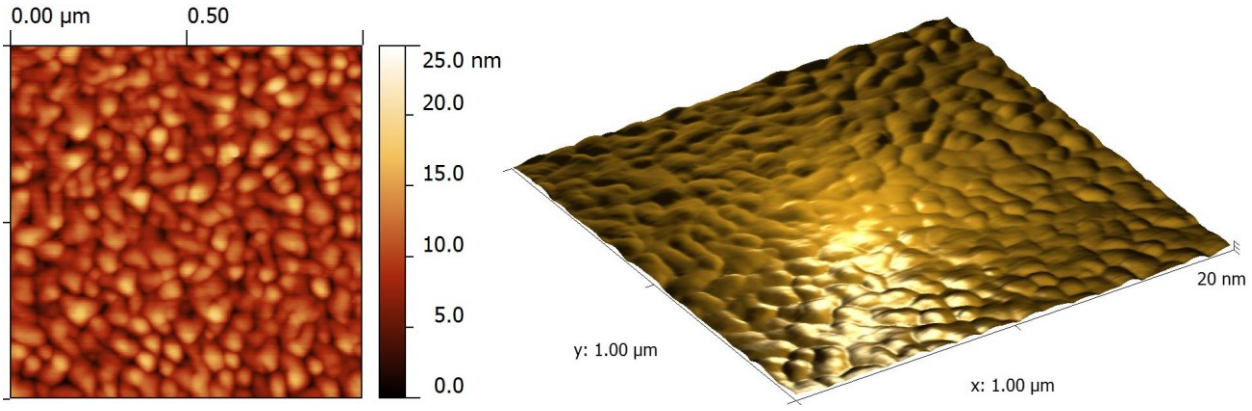

Figure 7.17: An AFM image and 3D reconstruction of a freshly evaporated gold film. At right, we see a false-color 3D reconstruction of the 1:1 scale roughness.

7.3 Monolayer Assembly

The laboratory process for SAM film formation on appropriate assembly surfaces was touched upon previously in Chapter 4. This section will elaborate further into the actual lab processes used for film growth. A list of insights and process improvement advice is shared as well. In addition, exact equations for solution calculation and a table for ratio determination are presented in Appendix E.

7.3.1 Critical Cleaning of Substrate

Cleaning of the samples just prior to processing is imperative to quality film synthesis. This is especially true in exceptionally humid regions (such as Florida, where this research is being conducted) because of the common requirement to take samples through un-air conditioned paths during transport from building to building. Even if enclosed and well protected from the environment, adventitious hydrocarbons will deposit onto all free surfaces requiring displacement prior to SAM deposition [262]. To counteract these effects, cleaning was performed by either UV/Ozone (UVO) or Oxygen Plasma chamber. Both systems are effective

at removing various types of organic contamination with the oxygen plasma being far more aggressive a cleaning solution.

The UVO cleaning was performed in a BioForce UV.TC.110 exposure unit with a minimum radiant emission of 12mW/cm^2 at the fixed gap between bulbs and sample. The bulbs consist of various mercury vapor bulbs with quartz envelopes. These bulbs have prominent peaks at 185, 254, 313, and 365nm. The lower wavelength peaks cleave the O-O bond in atmospheric oxygen which results in the formation of highly reactive ozone and oxygen radical species [263]. The advantages of this technique are that is fairly low cost and can be performed in atmospheric conditions. The disadvantages are that it is very slow (as compared to the oxygen plasma method, taking over 10 minutes to clear non-populated surfaces), it is ineffective on thick contamination or organic films, and it is not compatible with reactive metals as it will readily oxidize the metal surface.

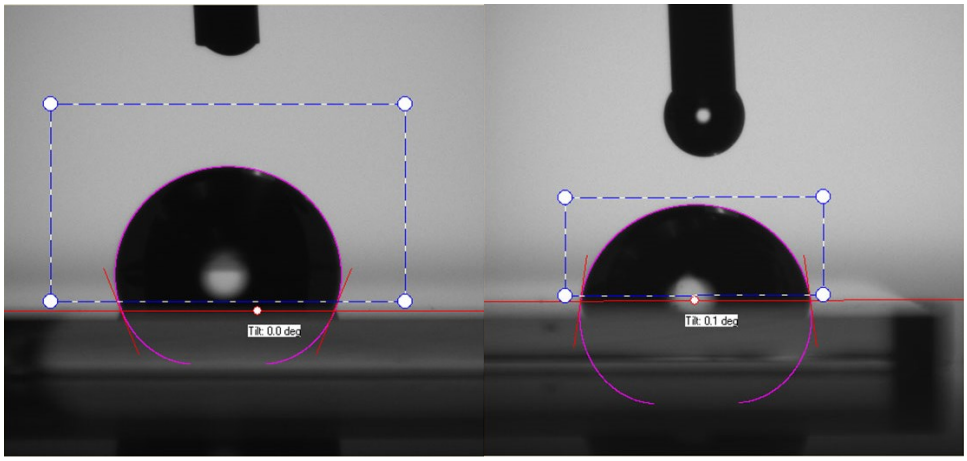

Figure 7.18: A software processed photograph of the contact angles of PFDT and the same sample after undergoing UVO cleaning. The 1H, 1H, 2H, 2H-Perfluorodecanethiol (PFDT) SAM was freshly deposited in the first panel then exposed to 10 minutes of UVO cleaning. The lower contact angle is an indication of reduced surface monolayer.

Oxygen plasma cleaning, also known as plasma ashing, is a process by which a low pressure atmosphere of oxygen is excited with an RF signal which ionizes the gas. The ionization of the gas, often held at under 1 mmHg, results in radical species of oxygen, free electrons, monoatomic species, and short wavelength photons—all of which are highly reactive and quickly strip contamination from the surface [264]. Varying the chamber pressure and RF power controls the characteristics of the plasma. It is important to select a recipe which provides the minimum plasma dose required to achieve the cleanliness goal. The process can effectively clean simple surface contamination in seconds and can also be used to remove photoresist scum over the course of a few minutes. The disadvantage of this technique is the harsh treatment of the sample. Not only is it held at relatively low pressure during the process, but it is subjected to species which will readily oxidize most materials which form thin native oxide layers [265]. It is for this reason that it is preferable to use high noble metals for SAM assembly. These materials are largely free of surface oxides and can be aggressively cleaned with minimal change in bulk structure or surface morphology. In some cases, it is appropriate to use plasmas of different gasses such as argon, helium, nitrogen, and hydrogen. Each gas has selectively and physical ablation concerns which need to be weighed carefully for process compatibility. In general, oxygen plasma is the most commonly used ashing/descum process gas.

7.3.2 Assembly Solution Preparation

This section will outline the techniques required to create quality, densely packed SAM films on noble metals. A number of molecules were used in experimentation (full list available in Appendix E). The different monolayers create different surface characteristics in addition to varying polarizations which affect adjoining metal work function. In agreement with published

observations, it is recommended that assembly be carried out in an inert atmosphere and stored in dark conditions.

Properly clean all glassware prior to initial use and designate glassware to particular chemical use. A piece of glassware used for assembly of one SAM should not be used with another. The entire procedure should be carried out in a fume hood due to the putrid smell of most of the thiol molecules. Great care should be exercised to avoid spillage or contamination. Using a micropipette, obtain the required quantity of SAM from the stock bottle using a disposable polypropylene pipette tip. Proper procedure is to immerse the tip approximately 3 mm below the liquid surface, draw up the liquid, and slide the pipette tip across the container wall while withdrawing. Place the pipette tip low besides the container wall where it needs to be dispensed. Carefully release the small volume onto the container sidewall and dispose of the pipette tip properly. Accurately measure the volume of solvent necessary to create the solution. A volumetric flask or burette can be used to ensure accuracy. Add the solution such that it washes the sidewall where the SAM was added. While correct processing procedure would include the volume of the SAM in the total solution volume, it is typically insignificantly minimal compared to the total solution volume and well within the measurement inaccuracy range of larger volume measuring vessels. Close the container and ultrasonicate for 5-10 minutes to ensure proper mixing of the SAM. SAMs that are highly viscous or solid at room temperature should be agitated in a heated bath to ensure proper solvation. For best results, only process one sample per assembly solution container. Following the cleaning procedure outlined in Section 7.3.1, the substrate is immersed in the solution and allowed to rest in a dark, inert environment for 8-24 hours. The longer assembly time is recommended for tighter packing of monolayer as the surface species are in a dynamic equilibrium of adsorption and desorption as

long as they are in solution. Also, molecules with longer or kinked chains should be allowed additional assembly time to allow for lowest energy packing. Following this period, the samples can be removed and rinsed carefully with reagent alcohol or the same pure solvent base used in solution mixing. A stream of argon or dry nitrogen can be used to dry the sample. If not to be used immediately, the samples can be stored in a dark, anaerobic environment held at a cool temperature. To minimize damage to the monolayer, care must be taken to avoid oxygen or ozone-rich environments, UV exposure, and abrasion.

7.3.3 Alternative Organic Films

The primary thrust of this work was the application and characterization of alkanethiol monolayers for use in electronic systems. This study would prove incomplete is a study of other monolayer and organic films was not presented as well. Langmuir-Blodgett (LB) films are physisorbed monolayers which are created on the surface of a liquid and transferred to the desired substrate. A more detailed explanation of the phenomenon behind these films was covered in Section 4.4. The LB process begins with a trough which is used to house the subphase assembly surface and compress the disperse species. The subphase used in most experiments is purified, DI water. The purity of this water is very important to the experiment and water with a resistance of > 1.8GΩ-m is recommended. Because the interface is marked by the liquid-gas interface, the air quality is also of great importance. To avoid air particulates and organics from introducing disturbances, a cleanroom or HEPA filtered cabinet is recommended to house the trough. Utmost care must be taken to avoid trough contamination. Careful cleaning of the trough (typically machined out of solid PTFE) should be performed regularly using chloroform or ethanol (per manufacturer's instructions).

For the formation of a successful MIM insulator, it was desired to achieve a lower incidence of defects in the deposited film. A amphiphillic molecule, 10, 12-Pentacosadiynoic Acid (Figure 7.19), was selected by a collaborator, Saumya Sharma, due to its ability to undergo crosslinking under UV light exposure [266]. The molecule was dissolved in a co-solvent of chloroform at a proportion of 0.2 mg/mL (534 μM). The co-solvent assists in the spreading of the molecule across the liquid surface. After the subphase was given some time to settle and sample substrate attached, 8 μL was deposited and allowed to spread and reorder for 40 minutes. Following this, compression began and the isotherm seen in Figure 7.20 was produced. During the dipping stage, a target pressure of 38 mN/m was maintained. For cases where the LB film was the only dielectric to be used, a 2 layer dip was performed to reduce the incidence of pinholes in the film. Alternatively, the LB process was used in conjunction with a conventional SAM assembling resulting in a hybrid organic film.

Further experimentation using naturally derived organic molecules was performed. Curcumin is the primary organic constituent of the spice turmeric. It was extracted by first obtaining freshly ground turmeric powder and wetting thoroughly with ethanol. The mixture was ultrasonicated and allowed to rest. The supernate was removed and the bulk liquid placed into a centrifuge vial where it was further separated of any particulates. The supernate was carefully extracted and placed into a small container where it was vacuum dried until only stable organic compounds remained. The curcumin was again dissolved in ethanol and spread in liquid solution using a spinner onto samples.

Experimentation with 5, 10, 15, 20 tetra(4-hydroxyphenyl)-porphyrin (THPP) was carried out due to interest in ferroelectric behavior in the molecule. The molecule was deposited as a film onto gold coated samples. THPP was obtained from Sigma-Aldrich and used as received.

A 1mM solution of THPP in ethanol was prepared and mixed with a 0.1M solution of $LiCLO_4$ in a 1:1 ratio. Surface polymerization was carried out by application of cyclic low voltage sweeps at 1V peak. The gold coated surface underwent a color change upon the endpoint of the polymerization being reached. These samples were studied by cyclic voltammetry, Raman spectroscopy, and ambient light controlled current-voltage measurement. The details of the findings are reported in Section 8.2 and 8.3.

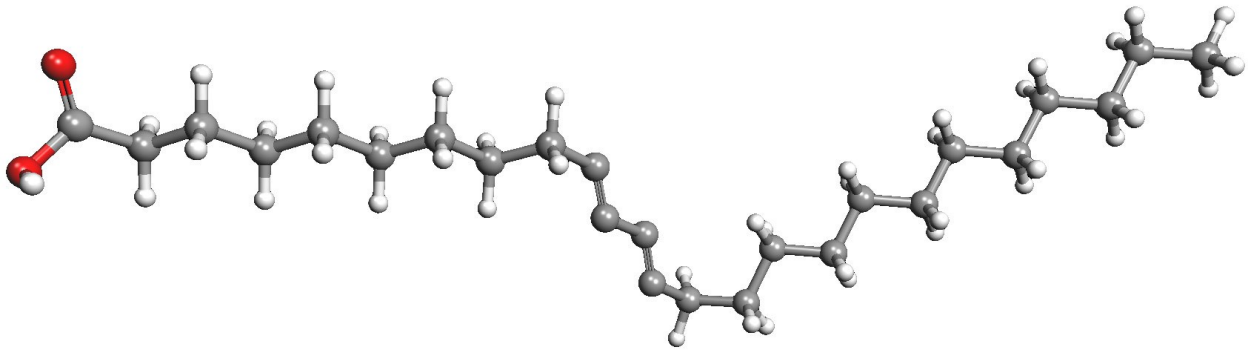

Figure 7.19: A ball-and-stick molecular model of 10, 12-Pentacosadiynoic Acid. This monomer is selected for its viability in UV-induced crosslinking resulting in a denser, more stable monolayer. Simulation results suggest a kinked molecule length of 26.9 Å or 31.1 Å unfolded.

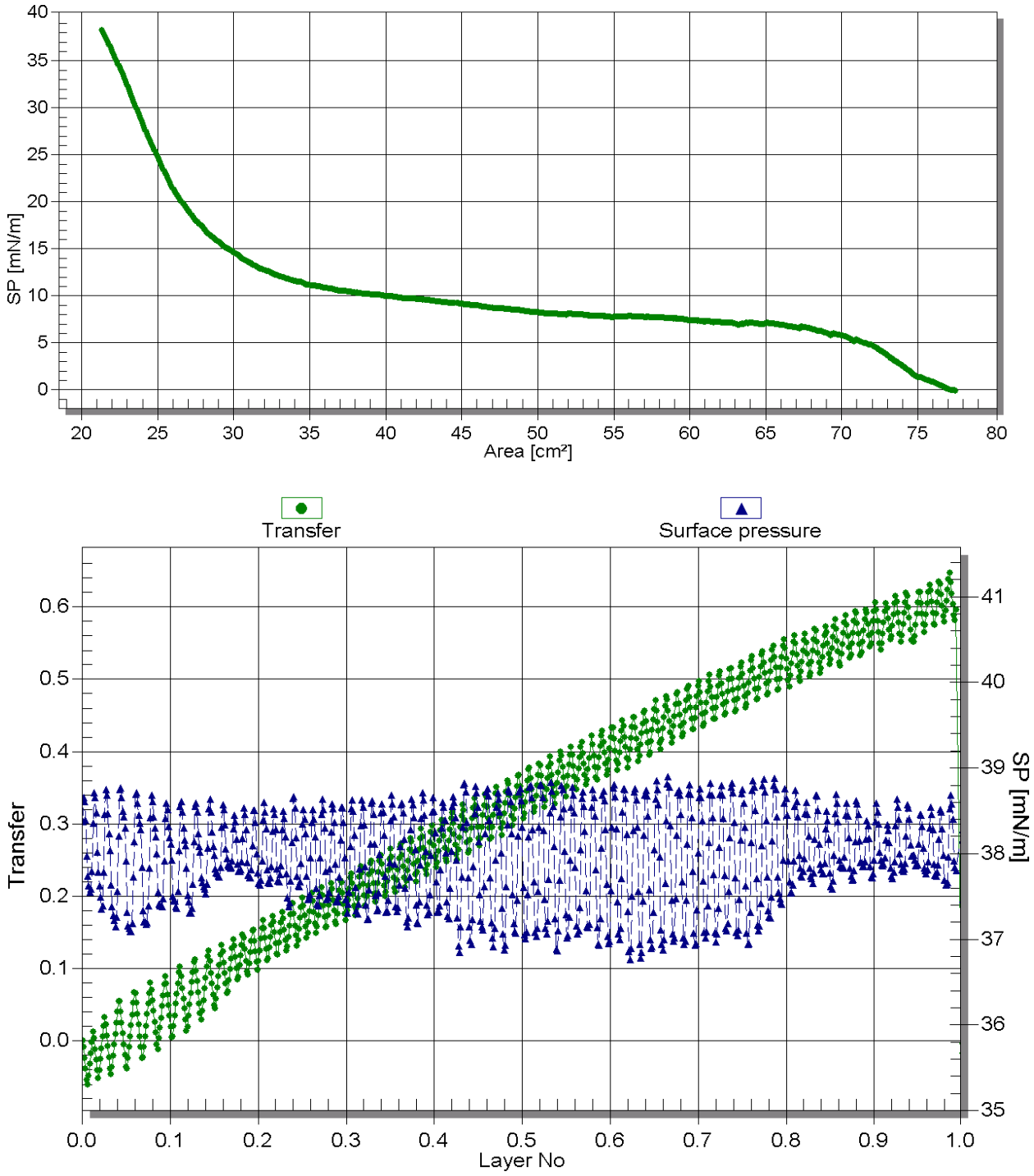

Figure 7.20: A set of graphs monitoring the compression and deposition pressure of a Langmuir-Blodgett monolayer. Here, 10, 12-Pentacosadiynoic acid is deposited with a target surface pressure of 38 mN/m. Note the top graph is best read from right to left, following the compression of the surface species.

7.4 Liquid Gallium Contacts

To evaluate different candidate materials quickly without the need for process optimization, a temporary contact solution was desired. In literature, mercury junctions are very popular and a common starting point in SAM junction research [69, 176, 267]. At times, different liquid metal contact materials were suggested and implemented including various galistan alloys [184]. These eutectic alloys employ varying amounts of gallium, tin, and indium to produce an alloy which is liquid at, or below, room temperature. There are other alloys which may work but in the interest of safety, we are not considering combinations like the highly dangerous NaK alloy. The push to use these alloys comes from the vapor toxicity of using mercury in a laboratory environment. As regulations tighten surrounding the RoHS initiative, the prospect of marketing any device which utilizes a forbidden material is troubled. The use of the galistan alloys has an intrinsic from an experimental perspective—the non-homogenous nature means precise work-function determination is deeply complicated. Following an extensive search, it was concluded that pure gallium could be used at room temperature despite a measured melting point of 29.8 °C [183]. This is made possible by a property of the metal which allows it to be supercooled if confined to a small space. These have been numerous studies which document the significant reduction in freezing when trapped inside carbon nanotubes. For our application, the syringe used to house the liquid metal has an approximate inner diameter of 150 μm. This is more than sufficient to give the syringe a working temperature range of 15 °C and above. The remaining problems are the concern over contact area inconsistency and native oxide formation. Gallium oxidizes in atmosphere forming a protective GaO_x film over the underlying pure metal. This gallium oxide layer acts as an insulating semiconductor adding to the complexity of the resultant electrical characterization. By chance, it was also discovered that

this produces superior asymmetry in the probed devices. The results of this electrical characterization are discussed in Chapter 8.

The experimental setup utilized to achieve these results began with the assembly of a square aluminum tube frame which firmly held a 3 axis goniometer. The sample was placed onto an aluminum block which had a Peltier device thermal epoxied to the metal mass. The Peltier cooler is a solid state thermoelectric device which allows the heating or cooling of a surface by the application of a forward or reverse bias to the electrical leads. This feature was implemented for future temperature dependent tunneling experiments but was rarely used. A syringe holder was crafted out of plastic and mounted to the goniometer (Figure 7.22). Initially, a commercially available micromanipulator was used to drive a tungsten probe into the assembly electrode material. After this was determined to be the source of some inconsistency in measurement and electrical noise, it was replaced in favor of a directly soldered silver plated, low oxygen Kynar 460 insulated wire (Figure 7.23). The syringe was filled from the back with gallium heated above its melting point and then excess air removed. To facilitate more accurate control of gallium feed rate, a screw drive was added to the syringe plunger. An electrical connection was made to the syringe tip and formed the basis of the measurement system (Figure 7.21). This system requires a minimum vibration due to the liquid nature of the contact. Disturbances due to electrical noise, air flow over liquid droplet, and vibration were all handled through the development of bench top, low cost solutions. The native oxide layer on the gallium droplet demanded additional tests to determine the contribution of the inorganic insulator in the now MIIM stack.

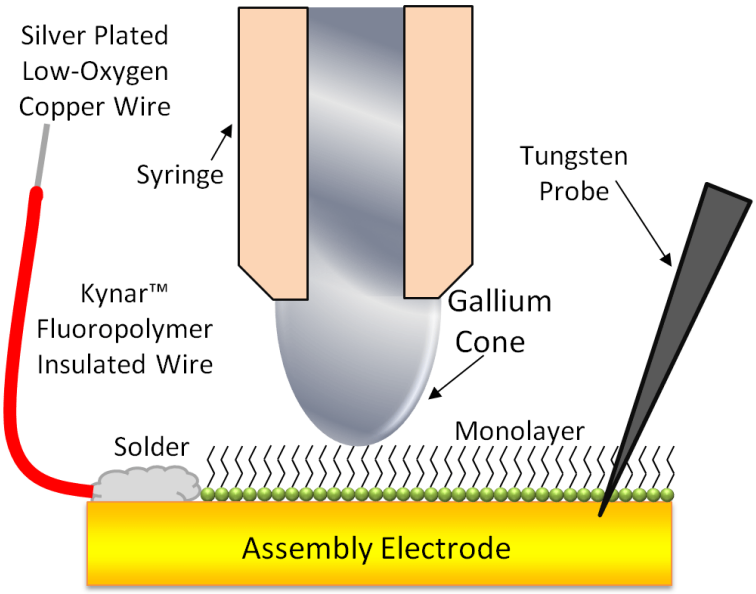

Figure 7.21: An illustration of the improved liquid metal contact test setup. By using a soldered electrical connection, electrical noise and measurement stability increased significantly.

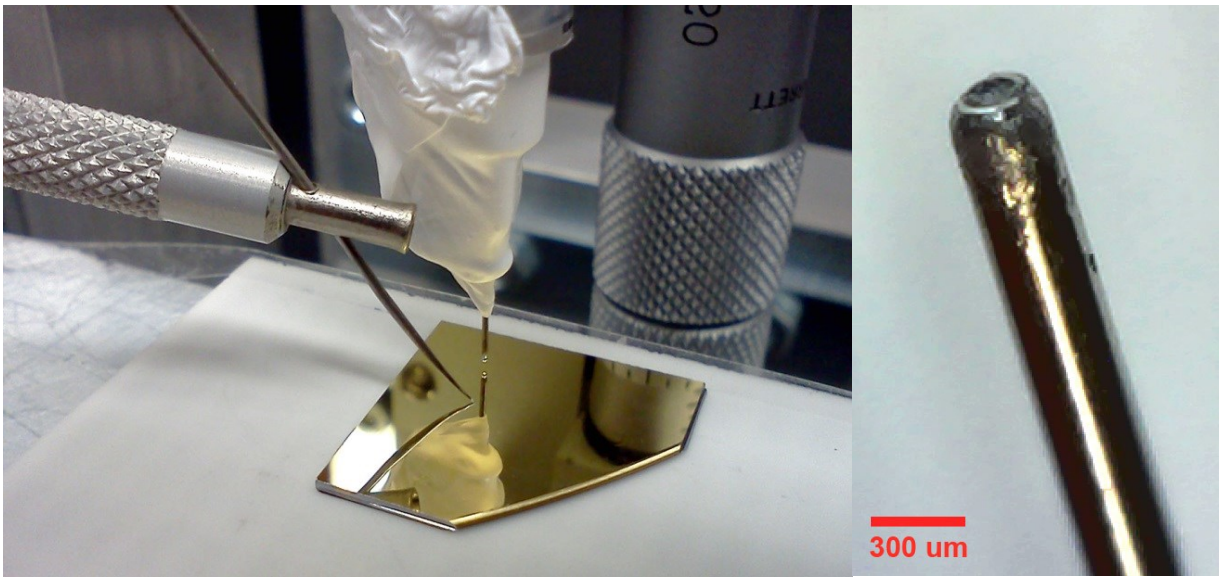

Figure 7.22: A sub-cooled liquid gallium contact syringe approaching the surface of a SAM coated gold sample. The counter electrode is simple a tungsten probe which breaks through the delicate organic layer and makes firm contact with the underlying gold layer. At right we see a microscope close-up of the manually rounded syringe needle.

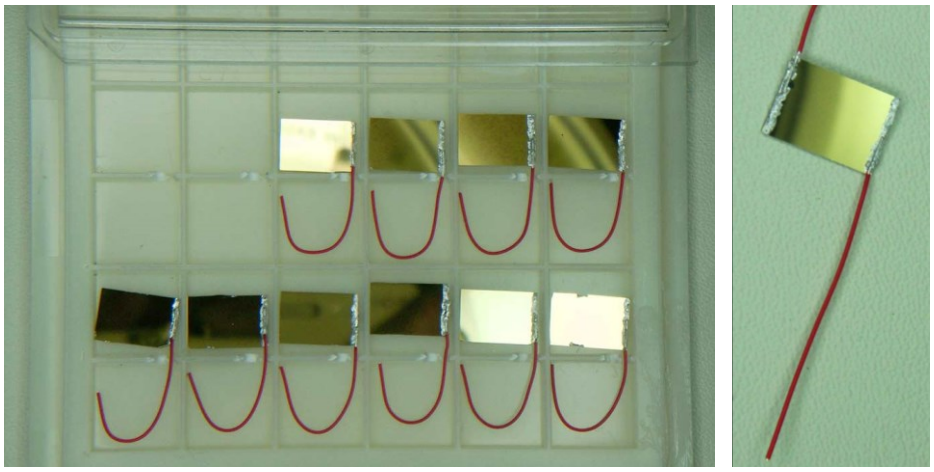

Figure 7.23: Images of soldered sample substrates coated with SAMs ready for testing. To achieve a more robust electrical connection with the substrate, silver plated oxygen free Kynar wires are soldered to the e-beam gold coated silicon samples. These are immersed in SAM solution for film formation and the wire insulation stripped just prior to testing.

7.5 E-beam Lithographic Process

After successful formation of monolayers on featureless metal coated samples, a permanent device structure was desired. The challenge of creating a metal contact over an organic monolayer is not a trivial one. Most depositions have poor adhesion to the tail end of the monolayer. In addition, it is well known that direct thermal evaporation of metals on SAM films causes significant damage [268]. There have been many solutions proposed and implemented toward this problem but contact area reduction then becomes a problem [171]. The solution I proposed was the use of a MEMS beam which would span three electrode contacts, fixed at the first and last while floating over the monolayer film on the middle electrode. Because this design would likely require significant experimentation to achieve success, the first step was to evaluate the feasibility of the design. The MEMS simulation software Coventor was used to create a solid model, apply material characteristics, and simulate deformation and durability of the beam.

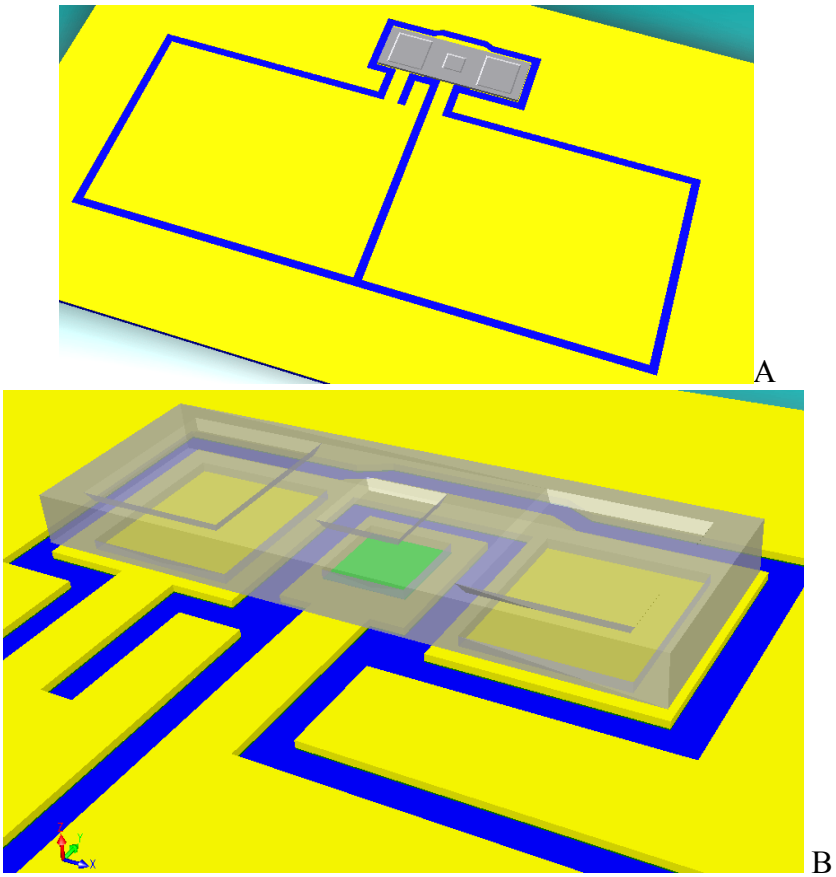

Figure 7.24: Rendering of MEMS beam for MIM contact in Coventor. In (A), an overview of the layout including the contact pads is given. In (B), the view is exaggerated 5x in the z-direction and the beam is made translucent to reveal the SAM contact site (green), gold electrodes (yellow), and insulating substrate (blue).

After evaluation of a number of deposition techniques, e-beam was chosen to be the ideal process. Sputtering released a high flux of UV light during plasma generation which would damage the SAM film. Thermal evaporation resulted in a broader distribution of heated metal particles which would cause more damage. In addition, the thermal evaporator available had a very small standoff range between the evaporation source and the sample. To minimize the punch-through of hot metallic particles, a large standoff range was required. Initially, the material selected for beam construction was aluminium. The material was selected for its relatively low melting point in e-beam evaporation of 660°C, low density, and high suitability

for evaporation by e-beam. After some experimentation, problems with adhesion of aluminium on the gold electrode layer were discovered. A literature investigation into the matter resulted in the discovery of a phenomenon called "purple plague." This is an intermetallic formed between the incompatible materials, gold and aluminium, which results in a brittle and unstable bond [269, 270]. Following this revelation, titanium was selected as the candidate material for evaporation. Simulations were re-run for the new material and the beam thickness was optimized to require the minimum material—this would result in reduced heating during deposition. Deformation of the beam was assumed to be worst case under the condition of vacuum under the beam with atmospheric pressure on the top side. The deformation was reduced to less than a nanometer under the SAM under those conditions. The results of the simulation also provided insight into the regions of stress and where failure was likely to occur.

To achieve the small geometries desired and allow for dynamically flexible design, e-beam lithography was selected for all steps. This would require additional design simulations to ensure that electron damage does not affect the reliability of the SAM films. For this, the simulation software SRIM (Stopping Range of Ions in Matter) was used to determine electron damage range [271]. An exact duplication of the material stack to be patterned was added to the simulation and run with the expected acceleration voltage of incident electrons. From the simulation, it was determined that a safe 99.99+% confidence of electron exclusion from the focal site was about 4 μm away. This gap ensured that no electron-induced polymer damage occurred.

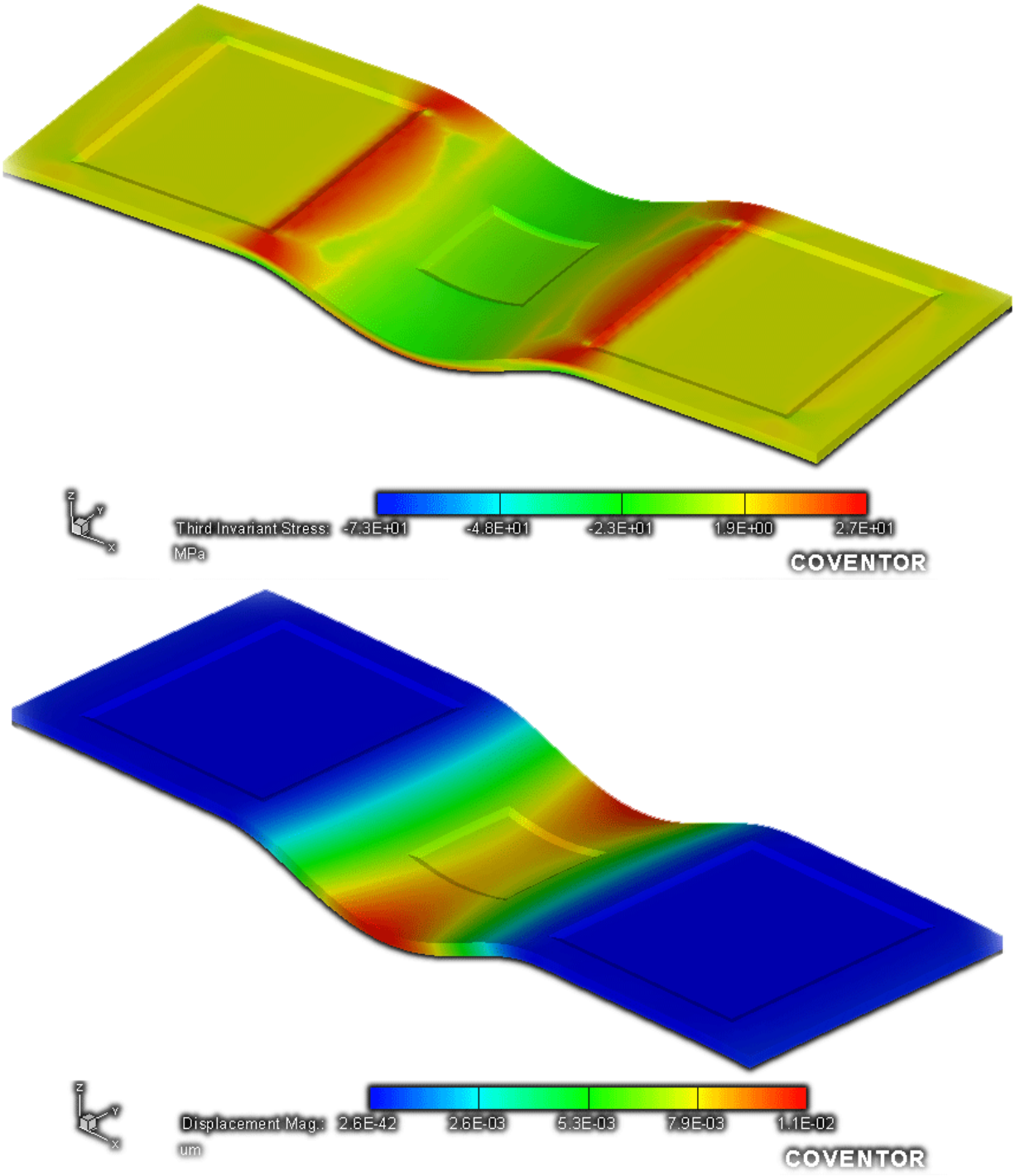

Figure 7.25: Simulation results of stress and beam deformation for MEMS cantilever contact. At top, the greatest stress is concentrated at the point near the base where the suspension begins. Lower, deformation under worst case scenario model with z-scale deformation exaggeration of 50x.

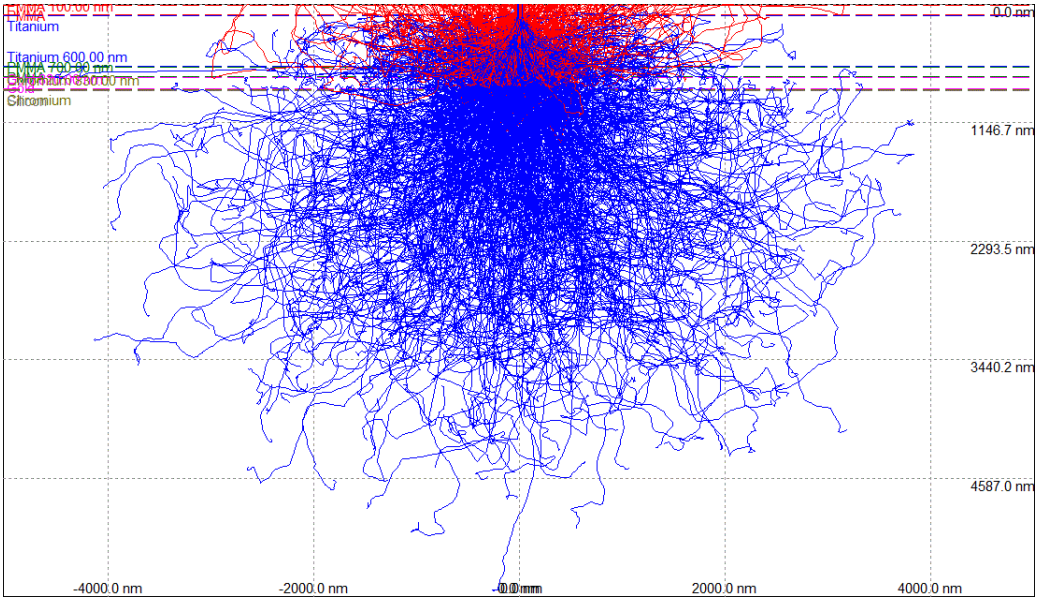

Figure 7.26: A simulation of electron scattering in a multi-stack material under SEM observation. The multi-stack structure is defined in SRIM simulation software and exposed to a beam of 25kV accelerated electrons. This simulation is used to determine the spatial gap required to minimize damage from these electrons.

E-beam lithography was carried out on a JEOL JSM-840 scanning electron microscope outfitted with an NPGS user interface. Because this is not an actual e-beam system but instead a retrofitted SEM, various problem workarounds needed to be developed. First, the write area was very small. This means finding and aligning to this very miniscule region (smaller than 1 mm in many tests) would prove challenging. Also, the patterning time needed to be reduced to accommodate for the relatively weak flux of electrons possible from the thermionic source in the SEM. Commercial e-beam writing systems employ electron sources which are much brighter and higher current to permit shorter write times with less thermal drift. The pattern was optimized by minimizing line width and avoiding large areas of full exposure. The result seen in Figure 7.27 is a routed PCB style layout which serves to electrically isolate the individual test pads and diode structures.

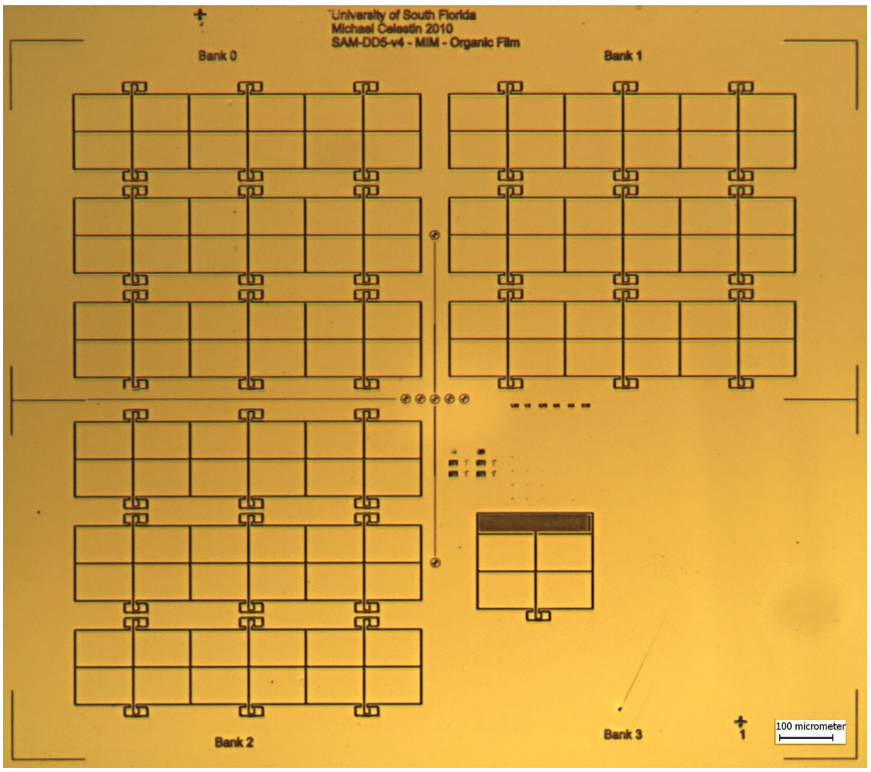

Figure 7.27: An optical image of an e-beam patterned large field of contacts for design X5v4. To save patterning time (already in hours), gold etching is performed in the same manner that a PCB would be routed—only removing enough material to isolate the desired circuit.

Poly(methyl methacrylate) was used as an electron sensitive photoresist for the litho process. To achieve better lift-off and sharper features, a two-step spin coating of the photo resist was adopted. A thin, low molecular weight coating at 6000 rpm of MMA was spun prior to the PMMA, which was applied at 5000 rpm for 1 minute. This dual-layer photoresist was characterized through a series of experiments and found to produce the best features in this pattern when dosed with 0.85 nC/cm^2 of electrons. Development of the photoresist was done by swirling the exposed sample in a 3:1 solution of IPA:MIBK (Isopropyl Alcohol and Methyl Isobutyl Ketone) for 30s and rinsing in DI water. Despite attempts to remove photoresist scum and erroneous lithography features, the edge roughness was very high.

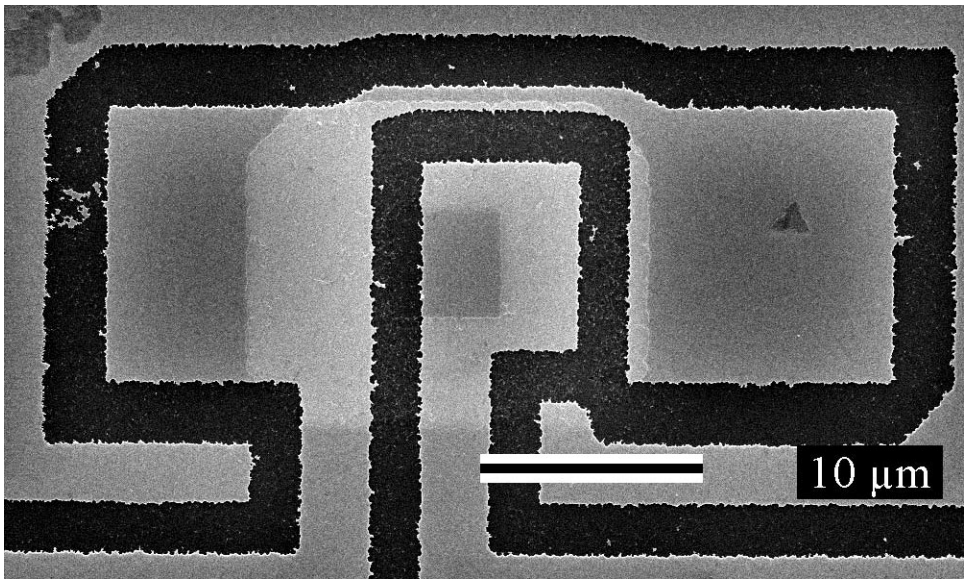

Figure 7.28: An SEM image of an e-beam lithography defined gold contact for an MIM structure with contact masking present. Careful observation will reveal a lightly colored region indicating masking photoresist present in a rectangular shape in the center of the image.

A study of the edges using SEM revealed a number of problems with alignment and edge roughness (Figure 7.28). It can be also noticed in the figures that many corrections through revisions had been applied to the digital "mask" file and each resolved an issue or improved patterning in some way. Initial e-beam writing times were nearly 4 hours. The final design used was coded SAM-DD5-v4 and represented the 4^{th} stepping level of the 5^{th} major design revision. The pattern features fiducial marks which assisted in automatic alignment, easy to probe contact, dosing and etching experiments, and a total of 54 diodes sites for testing.

The second lithography step involved the patterning of a scaffolding and spacer layer. This PMMA layer would direct the metal evaporation and provide "windows" to the underlying metal structure where the beam would join and make the intended electrical connection. Metal evaporation was carried out in an e-beam evaporator in accordance to the Coventor simulation results. The first problem encountered was thermal stress and cracking of the Titanium film. This occurred in part because of shifting and melting of the underlying PMMA layer during

deposition. Eventually, a thermal sink in the form of a metal block was included in evaporations to dissipate and absorb the heat generated and transferred during a deposition. While this did improve the cracking problem, the entire process became increasingly poor yield and unreliable. The final lithography step defined the region to be etched at the top level. Alignment to the previous step was extraordinarily difficult because of limitation in the SEM. Due to one problem or another, the available tools and equipment would not allow the fabrication of these MEMS beams for electrical test.

7.6 Photolithography Process

After an analysis of the failures associated with the e-beam lithography process, it was decided to return to a photolithographic process. This more conventional processing technology would likely face fewer equipment outages and technical limitations. The first task was to devise a process flow which allowed the use of UV exposure in the proximity of delicate SAM films. A full detailed process flow is presented in Appendix D which outlines how this was accomplished.

7.6.1 Overview of Lithographic Challenges

The number one goal of these new process sets was to minimize UV exposure to the monolayer. The way this was accomplished was by using a solvent tolerant photoresist which would be dipped in the assembly solution. This semi-permanent mask directs the assembly to windows defined by the photolithography step and can be mechanically stripped from the sample surface due to the Omnicoat release layer spun prior to the photoresist. Because SAM immersions can last up to 24 hours, a very durable photoresist was needed. After researching the

optimum thickness, solvent resistance, and surface adhesion, the selected photoresist was MicroChem SU-8 2015.

The first generation mask set produced a 25 x 25 mm die which contained a variety of test structures. The passivation layer was e-beam evaporated silicon dioxide which was pattered using a lift-off process. The completed die used for testing is seen in Figure 7.29.

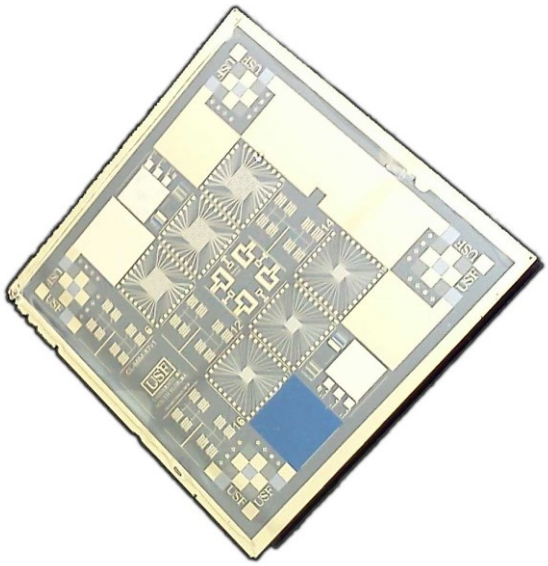

Figure 7.29: A photograph of a finished X7v1 die reading for testing. The features on the silicon substrate are 25mm on each side and were ordered such that all 4 layers fit on one 5 inch glass photomask.

While it did produce successful device structures, the junction yield was under 5%. Further inspection by SEM and AFM revealed the extent of the process problems which were responsible for the low device yield. In Figure 7.30, we see, at left, the brittle and rough edges due to lift-off damage causing the evaporated top metal to fail to make a connection at the junction site. Additionally, the probe pads were designed to be a 3 layer stack of metal-passivation-metal. This proved to be too delicate to probe reliably and chipped whenever a tungsten probe was landed (Figure 7.31). This flaking of gold coated SiO_2 not only made measurement taking very difficult but it also contaminated the wafer.

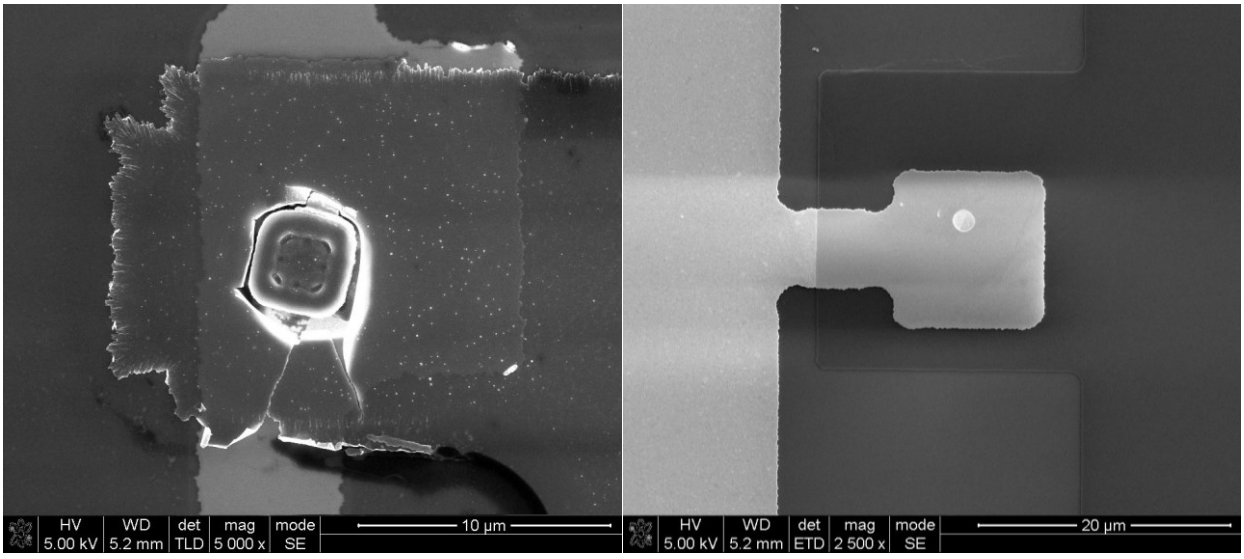

Figure 7.30: A set of SEM images comparing the insulator lift-off to insulator etching. At left, we clearly see significant cracking and defects of the insulator. At right, all these issues are rectified with an improved process of critically timed RIE etching using a custom chemistry.

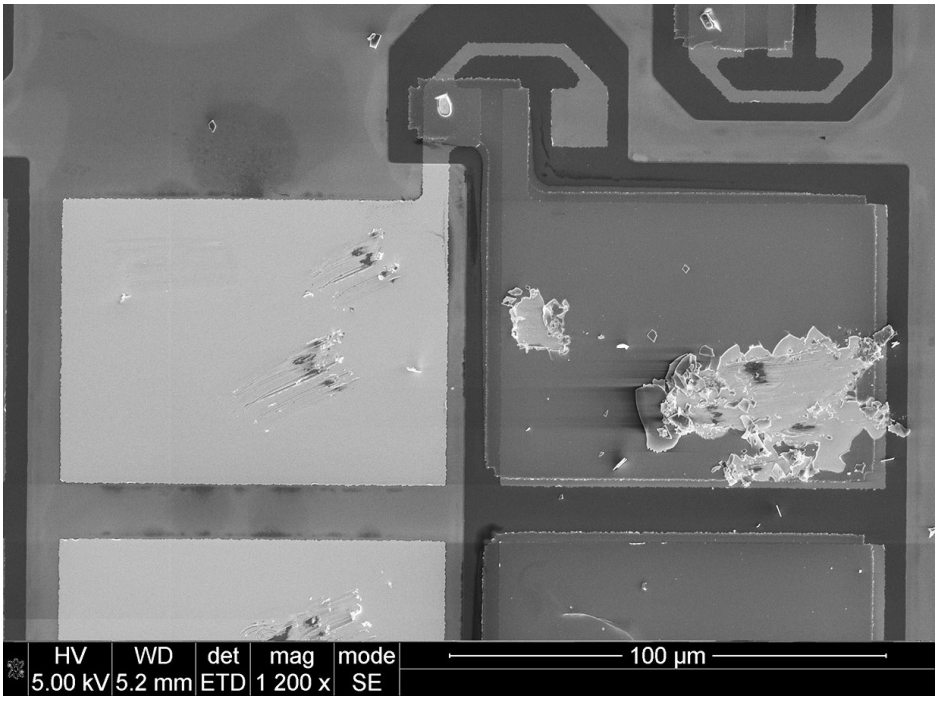

Figure 7.31: An SEM image of an X7V1 device being damaged after electrical measurement from probe scrubbing. The lateral sliding of contact probes (scrubbing) on contact pads is common but good film adhesion is critical in these applications. At left, we see the single layer gold film survives with only minor surface scratching. At right, the gold-insulator-metal stack produces weakness at the gold-insulator layer resulting in destruction of the pad and unreliable electrical contact.

7.6.2 Demonstrated Solutions

The final evolution of the photolithographic process was developed at Sandia National Laboratories. This updated process was the 8th evolution of the organic MIM test set and was designed to support a variety of experiments. The finished wafer is seen in Figure 7.32. This design revision incorporates coplanar waveguides for RF testing, e-beam lithography fiducial marks, process characterization tests, and a variety of photolithography 2-terminal junctions. The feature set was defined by a substrate floor plan which accommodated samples shaped from 25 x 25 mm to a 2 inch wafer. The floor plan was divided into 10 x 10 mm cells.

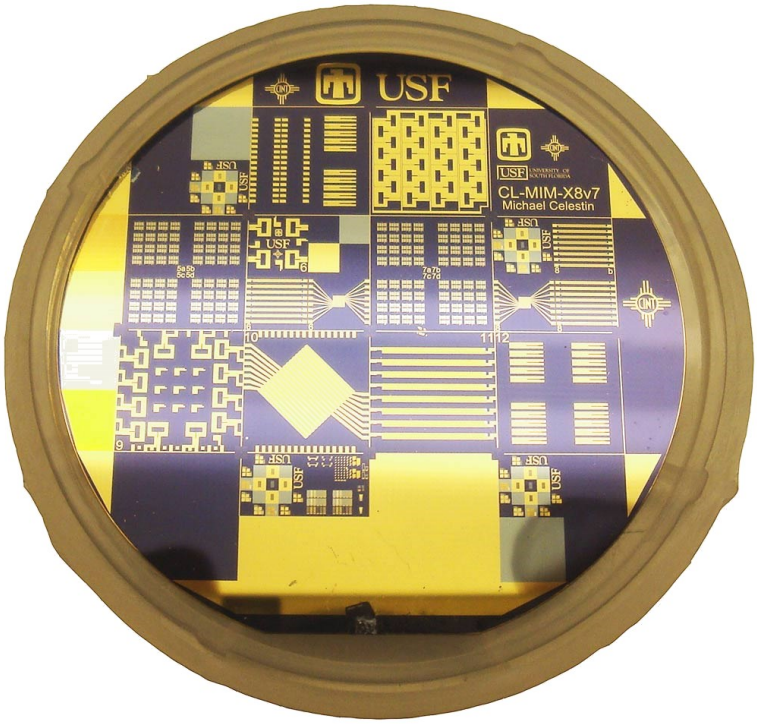

Figure 7.32: A photograph of a 50mm silicon wafer in open holder showing off the X8v7 lithography design.

The first challenge this design overcame was that of alignment. In photolithography, the alignment of successive processing steps ensures that passivation and electrical contacts function as designed. For cases of very poor alignment, a top metal electrode may never make contact

with the underlying electrode to complete a circuit. A Common workaround is to make features larger or design them to be more intrinsically alignment insensitive. This is exactly the solution implemented in the e-beam lithographically defined junctions detailed in Section 7.5. The consequence of larger features is greater parasitics which reduce the quality of measured data and characterization. Through experimentation, it was found that the common "cross-on-cross" alignment marks are very poor for use in visual alignment. Instead, an alignment system was developed which allowed for sub-micron alignment using a conventional optical microscope. The alignment cell contained features large enough to be seen by the naked eye. This initial alignment gave a rough precision of around 250 μm. From there, progressively smaller and varied alignment features allowed for alignment down to about 2 μm. These negative space alignment marks are insensitive to minor process and development errors. Below this limit, it becomes very difficult to resolve spatial positions accurately using an optical microscope. For further alignment, moiré patterns were included for X and Y alignment. Moiré patterns are interfering gratings which are slightly dissimilar (in this case, 39 and 40 lines) which amplify any small alignment errors as a mismatch in color shading within two bars. In Figure 7.33, alignment was intentionally skewed to demonstrate the phenomenon. In the X direction, alignment is off by almost exactly 1 period resulting in a near match. In the Y direction (lower right), we see the alignment features (crosshairs) suggest an accurate match but the moiré pattern reveals an error.

Using careful process optimization, the resolution limitations of prior patterning attempts were overcome. Sub-micron optical patterning is demonstrated in Figure 7.34 with the formation of nanowells in silicon nitride passivation. These wells bridge the gap between photolithographic patterning and e-beam patterning. The demonstrated nanowells could form the

basis of a diode which would operate all the way to the upper limits of the microwave band at 300 GHz. In addition, the top contact can be made using a variety of techniques which will be discussed in sections to follow.

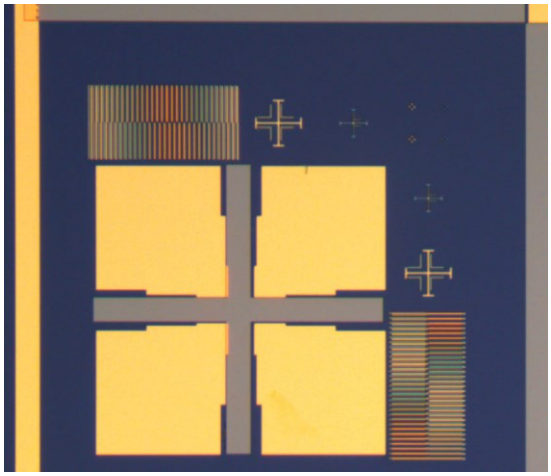

Figure 7.33: A microscope image of moiré alignment marks allowing sub-micron alignment through a lower powered optical microscope. The design consists of slightly mismatched gratings which create and interference pattern visible as large scale banding when aligned.

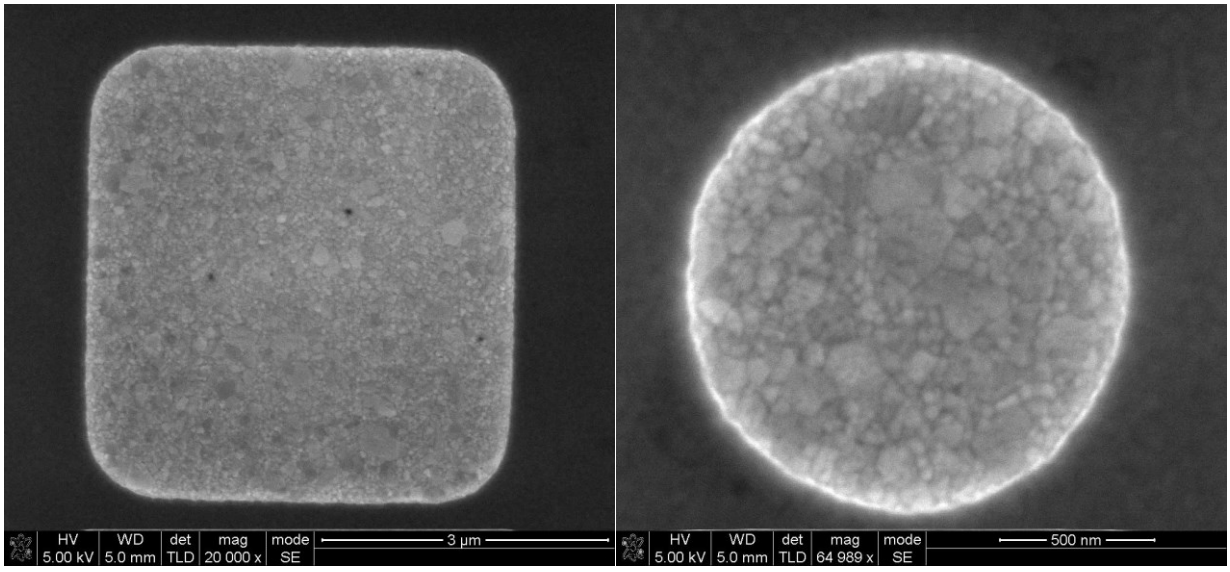

Figure 7.34: SEM images of small geometry contact holes patterned with optical lithography. At left, we see the limitation of vertex sharpness in the square feature due to the relatively large wavelength of patterning light. At right, a well formed circle approaching the limit of conventional broadband UV patterning.

7.6.3 Optimization of Process

This section will feature a few process and measurement problems which have been seen and how they were overcome. As we saw in Figure 7.34, the minimum feature size achieved was less than 1 μm. This was done by measuring process step times to less than a single second, introduction of process resolution tests in the photomask, and careful metrology after each step to glean optimization steps. A thinner photoresist (AZ 5214E) and recipe gave far superior pattern transfer. Solvent clean following development was found to be insufficient at removing photoresist scum from the wafer. The scum caused partial masking during etching steps which created image ghosts seen in Figure 7.38. After 300 s O_2 plasma clean at 50 W, the problem was resolved and edge sharpness improved. The low stress nitride was deposited at 16-18 Å/s on a Trion CVD machine. Process conditions were: SiH_4 at 16 sccm, Ar at 24 sccm, N_2 at 32 sccm, 100°C substrate temperature, and 650W power. The target deposition thickness was 600 Å. The passivation was thin to avoid contact failures between top metal and assembly surfaces. One of the challenges associated with the nitride etch was the small geometries of the thin layer. The ICP RIE etching proved to be too fast to control using a photo endpoint detector. The etch process was very well characterized using chamber conditioning and test coupons of various thicknesses. The etch rate was tuned to 18.75 Å/s by turning off running at the lowest stable power with which the plasma would strike: 35W. Furthermore, the etch rate needed to be extended to at least 30s to allow for consistent etching. This was accomplished by diluting gaseous etchants with He. The custom RIE recipe had very high selectivity for nitride and the low molecular weight He had very little PVD effect on the underlying Au layer at the low etch power selected.

Gold used for patterning overall features was etching using a custom mixed KI-based etchant. The etchant was made by dissolving 4g of KI and 1 g of I_2 into 40mL of DI H_2O. After proper mixing using ultrasonication and agitation, a surfactant was added to improve feature resolution. The etch rate was characterized to be 167 Å/s using this custom formula. The result was very sharp features as seen in Figure 7.35 and 7.36. Large block arrays of test junctions were patterned, each with slightly different contact dimensions including controls. A rectenna tuned for 94GHz was patterned (Figure 7.37). This can be simply probed with a high precision multimeter to measure voltage output under RF test conditions. Alternatively, the CPW can be connected to a power analyzer or high performance oscilloscope to determine rectenna efficiency. The rectifier junction is located within the CPW strip.

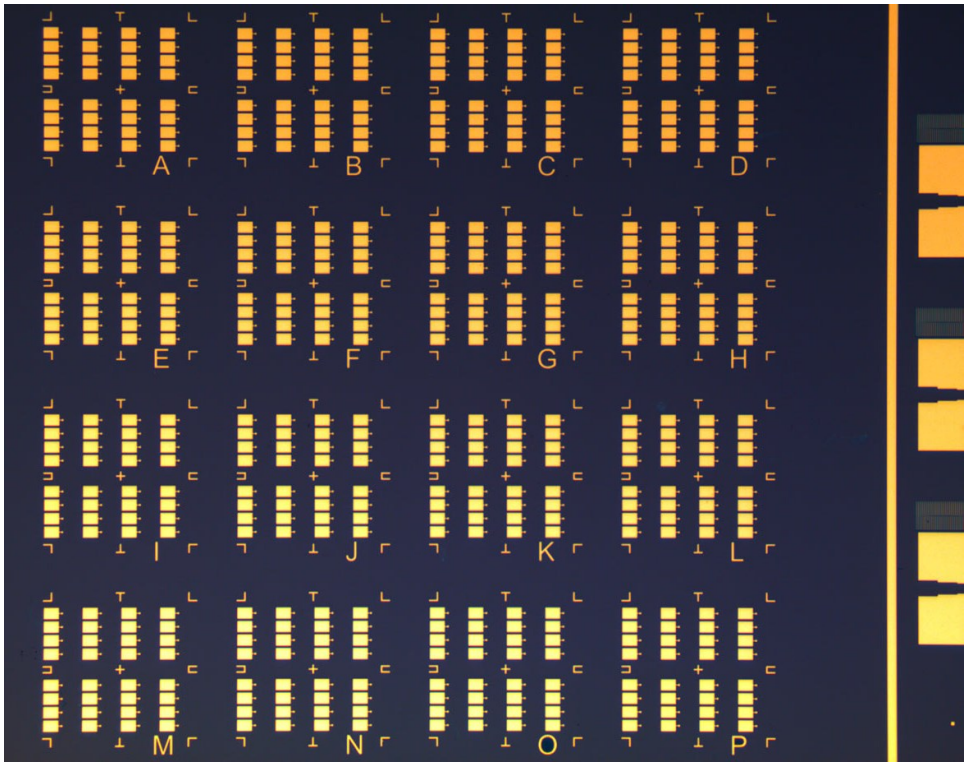

Figure 7.35: An optical microscope image of a 512 block array of contact pads for the X8v7 litho process. The deep blue substrate is oxidized silicon with etched gold evaporated contacts.

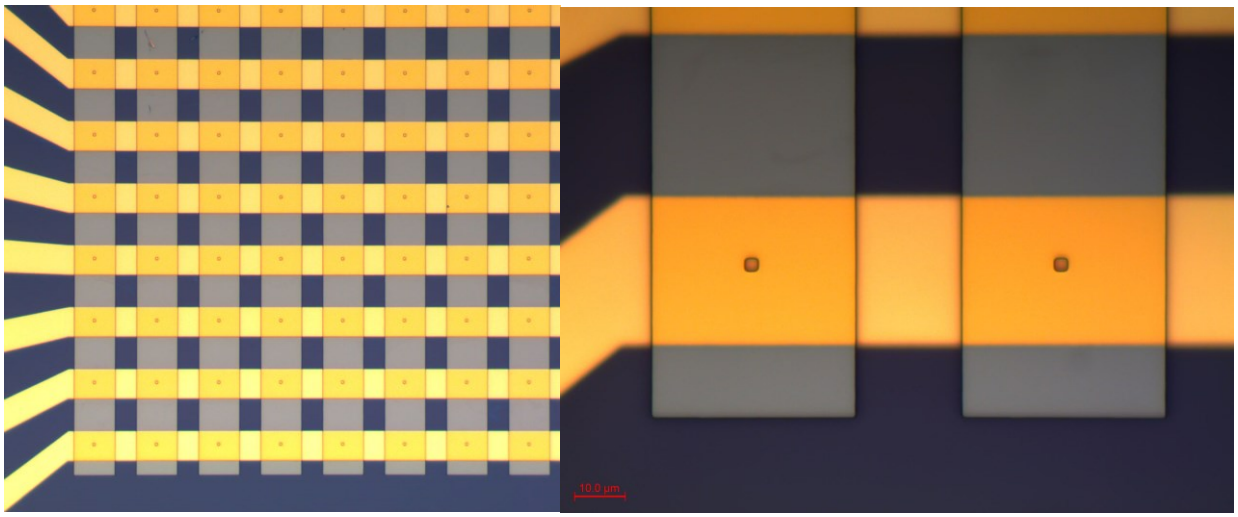

Figure 7.36: A set of optical images showing crossbar contacts and insulators patterned with optical lithography. At right, we see a detail of the bottom left region of the first image.

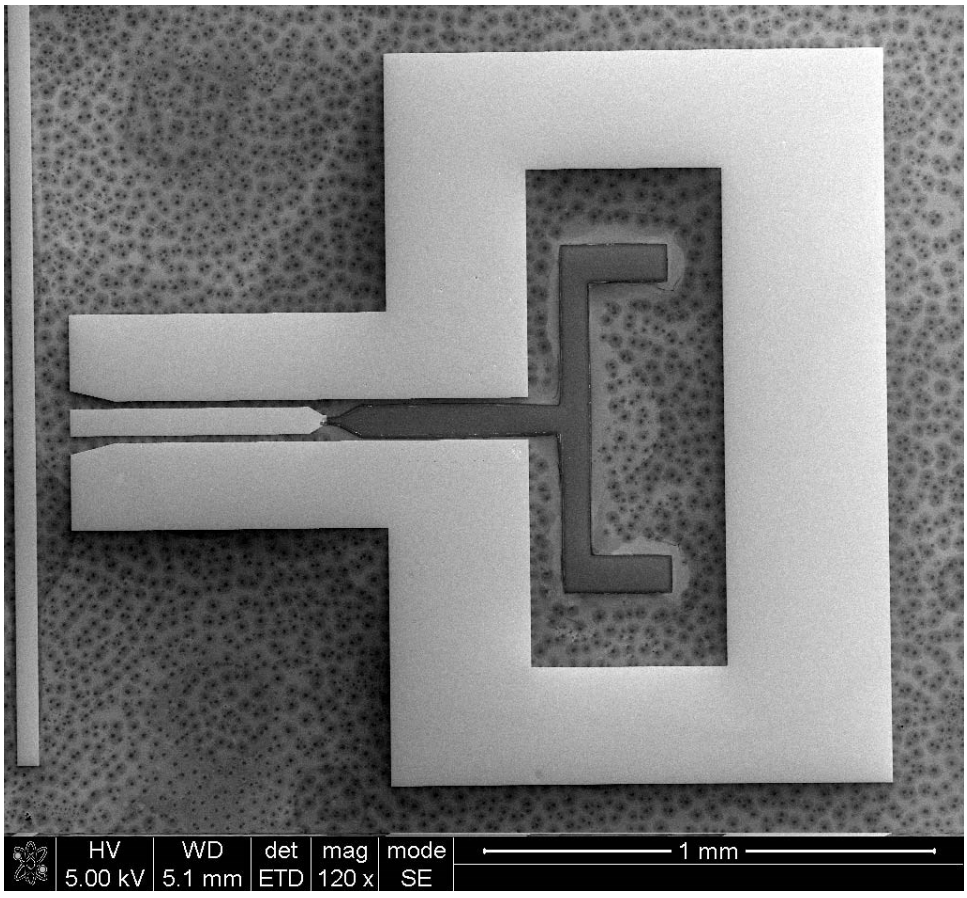

Figure 7.37: An SEM image of a fabricated rectenna device designed to operate at 94GHz. The rectenna grounding surround leads to a CPW (coplanar waveguide) where the rectified power can be measured by a landing probe.

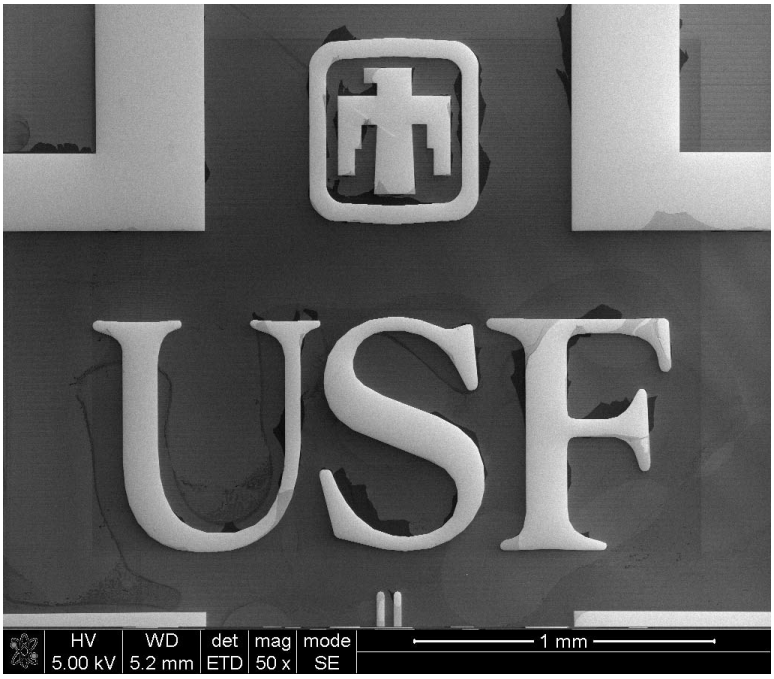

Figure 7.38: An SEM image demonstrating the effects of photo resist scumming. The problem was resolved through a work-up step of O_2 plasma ashing.

7.7 Study of Nanopore Junctions by Focused Ion Beam

Conduction through nanowells (or nanopores) has been reported for some time in literature [272]. They are often used to mill a bulk insulator precisely and make a contact with an underlying thin dielectric. With varied milling sources, contamination can be minimized and not significantly affect electrical measurement. Due to resource limitations, I believed a study was needed to evaluate the rate of gallium contamination for nitride passivated nanopore structures.

7.7.1 Focused Ion Beam

Focused Ion Beam (FIB) is a tool which allows the removal or application of material from a micro-featured surface. The principles behind an FIB are very similar to that of an

electron microscope (SEM). The SEM uses a beam of electrons to generate an image due to backscatter while the FIB uses ions of elements (typically gallium). Because the ions are substantially more massive than electrons, they can be used to mill material by sputtering the surface material. By injecting gasses at the focus site, additional atoms can be deposited or the etch rate can be accelerated. The FIB is commonly used to repair microelectronic circuits by opening and bridging traces as needed. For our application, the high resolution of the FIB is attractive because it can quickly pattern an array of holes only tens of nanometers in diameter. This small contact is precisely what is required to create a THz frequency rectifier with a sufficiently low time constant.

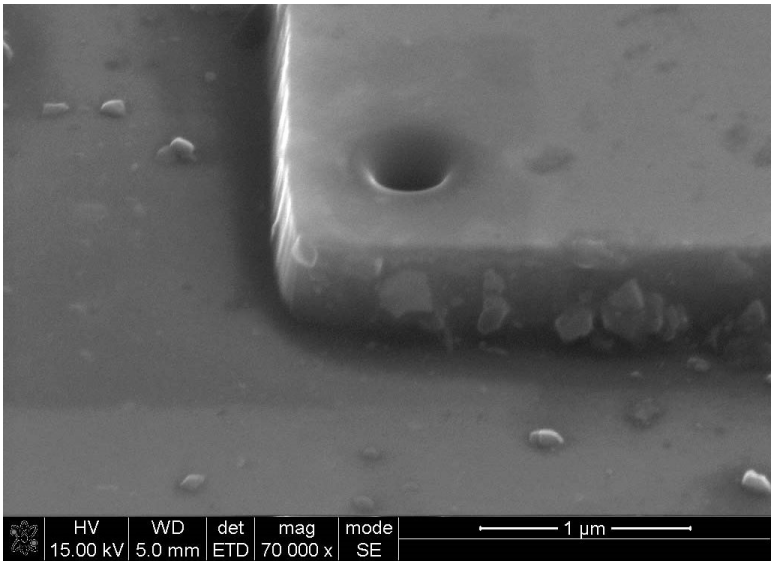

Figure 7.39: An SEM image of a nanowell milled using an FEI FIB (Focused Ion Beam). The nanowell is approximately 250 nm in diameter and is only partially milled. This would require a workup step to ensure no gallium ion contamination in the gold assembly layer.

7.7.2 Surface and Volume Contamination and Solution

The problem often cited with metal milling is contamination by the ablation species. For the case of FIB, this means severe gallium contamination in and on the noble metal assembly

surface. While other ion sources are available, gallium is by far the most common and best characterized. Gallium ions which are accelerated at such high rates implant themselves into the bulk underlying material. This contamination will inhibit and affect the assembly of the monolayer species at the surface. Moreover, the presence of gallium within the bulk material will cause degradation in noble metals as has been studied extensively [273]. The proposed solution is a combination of FIB and RIE milling to achieve the desired nanowell. In Figure 7.39, we see the milling of a small nanowell into silicon nitride using an FIB. The etch will only be carried out partially, leaving a sufficient gap to the next layer and containing contamination. In the following step, a gentile and slow RIE chemical etch will remove the gallium contaminated passivation layer at the expense of slightly enlarging the nanowell diameter. The study was conducted using an ion implantation software called SRIM. The simulations assumed a constant device structure and varying ion acceleration voltages. The extent of contamination was computed and noted. For lower acceleration voltages, the milling process is substantially longer but results in a far smaller contamination zone below the nanowell. For a 15kV acceleration voltage, the gallium contamination was less than 1% at a depth of 20nm and only 0.01% at 25nm. This means a 15nm etch is that is necessary to achieve the well geometry desired. RIE selectivity can be customized to prevent damage to the underlying noble metal surface and prevent erosion and roughening.

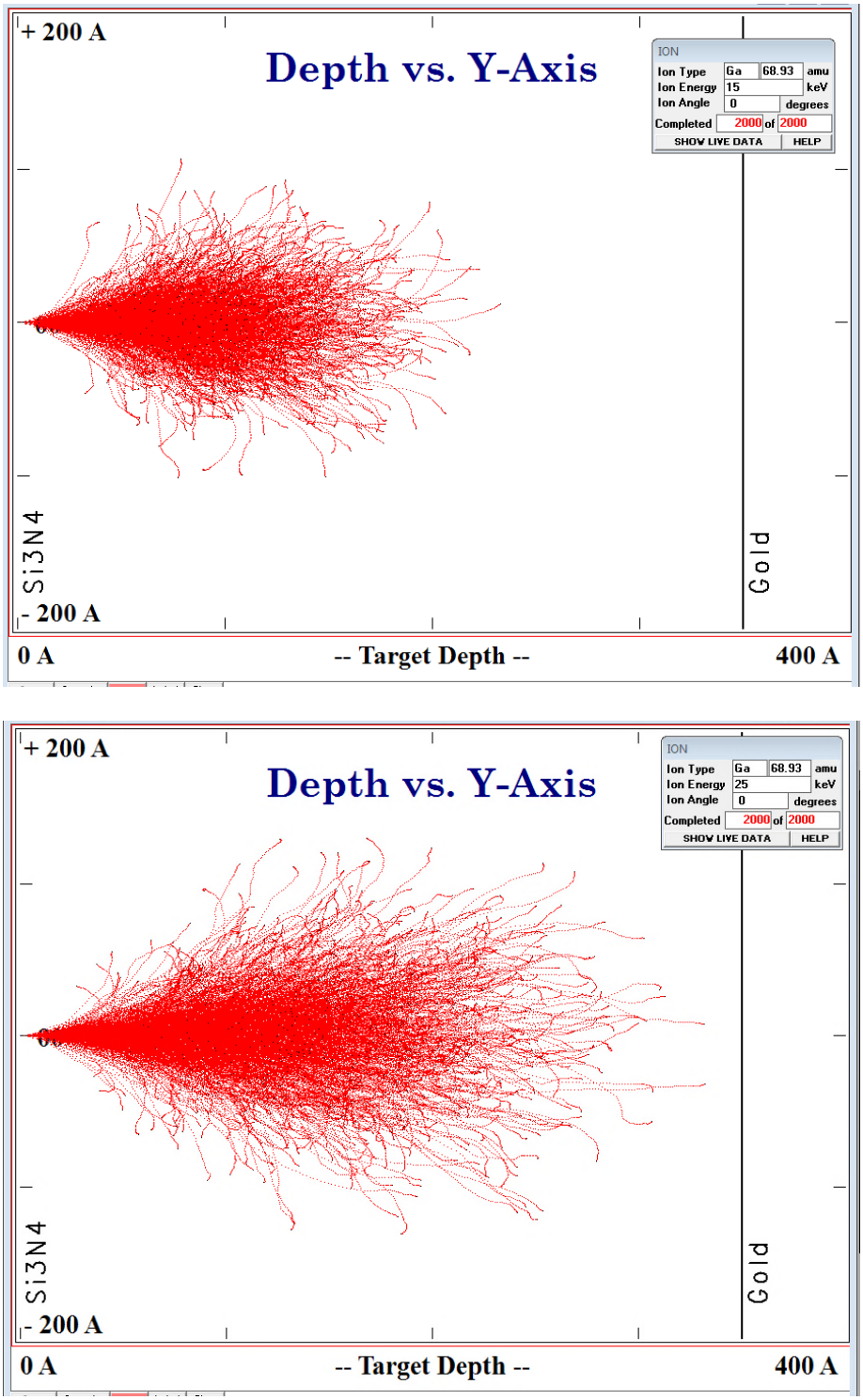

Figure 7.40: A simulation of Gallium ion penetration into silicon nitride during FIB milling. The simulations offer insight into the degree of hold depth possible without risk of gold surface contamination. Acceleration voltage on top figure is 15keV and 25keV on the bottom. Simulations performed on open source software courtesy of James Ziegler (SRIM 2013).

7.8 Top Contact Solutions

The central challenge around the organic MIM will be described by most to be the top metallic contact. Because of the delicate nature of the self-assembled monolayer, a very gentile process must be used to achieve acceptable results (even for experimentation). Here, we explore a variety of techniques including some novel methods never before implemented. All of them center on placement of microscopic metal particles at the SAM surface rather than atomistic evaporation of gaseous metal onto the organic layer.

7.8.1 Electrostatic Nanoparticle Plotting (NEPTUNE)

Collaborative work on the deposition of gold nanoparticles onto non-conductive substrates was carried out and yielded good results [274]. The deposition technique first consisted of the synthesis of gold nanoparticles from auric chloride solution. Size characterization of the nanoparticles found they exhibited a very uniform distribution with very rare cases of particles larger than 70 nm.

While the utility of applying a conformal or macroscopically directed conductive coating on an insulator is good, it was more desirable to have dynamic and higher resolution control over the deposition. One of the challenges noted in the aforementioned study was the low resolution due to electrical transport around the insulating substrate. To overcome this, a conductive sample was used for initial tests. At a basic level, the idea was to direct a probe in solution to specific points above the surface of our sample substrate and apply some type of electrical field which would cause nanoparticles in the liquid to deposit at the specific site. The system was dubbed “NEPTUNE” or Nanoparticle Electrostatic Plotting by Transient Uniform Numeric Excitation. (For the sake of brevity, the acronym “NEPTUNE” will be written as “Neptune” and

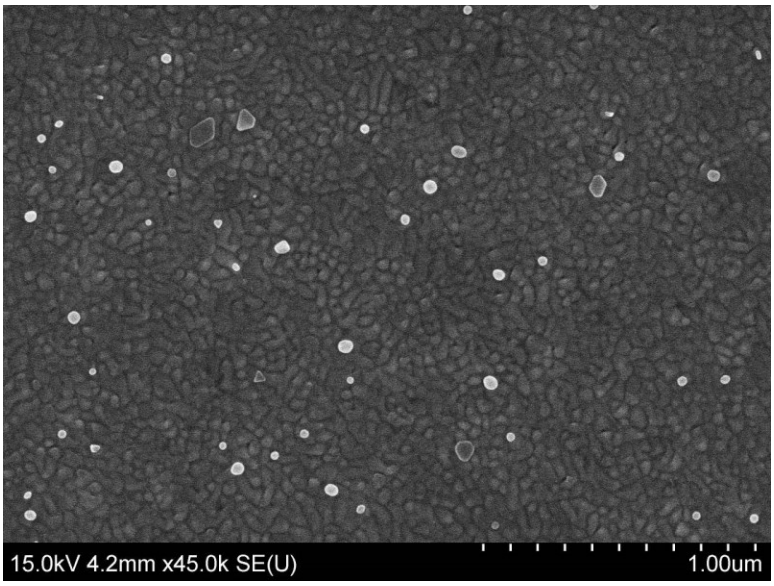

Figure 7.41: An SEM image of the size distribution of gold nanoparticles fabricated for the purpose of electrostatic plotting and deposition. Gold particles are seen in bright white with a textured, thermally evaporated gold surface below.

should be understood to only refer to the aforementioned nanoparticle plotting system and not the astronomical ice planet.) The method by which Neptune deposits nanoparticles is by introducing a biased or asymmetrical AC field across the conductive sample substrate, nanoparticle loaded liquid medium, and excitation electrode. A rough idea of this phenomenon

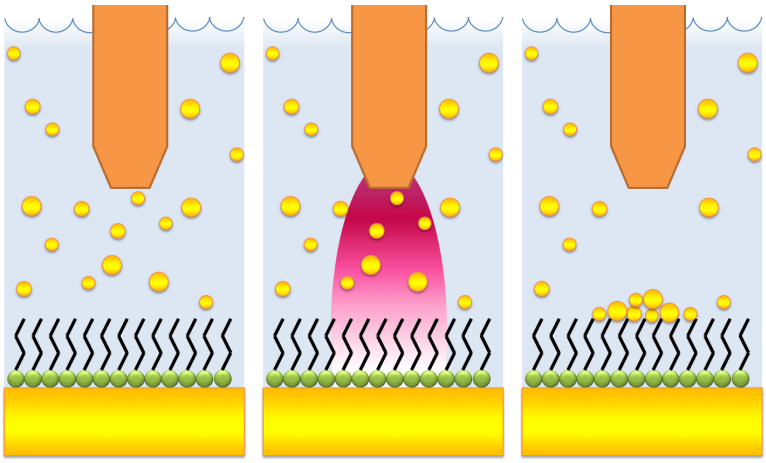

Figure 7.42: An illustration of the electrostatic plotting field depositing nanoparticles onto a SAM decorated substrate.

is depicted in Figure 7.42. What we will discuss is how the system was implemented and how costs were kept low, a discussion of the programming and computer interface behind the system, and a study of the resultant metal films.

7.8.1.1 Refitting An Existing Motion Solution

To expedite the development of this system while also keeping the cost down, a retrofit of existing motion control solutions was employed. What was needed to achieve positioning of the excitation field was a simple X-Y positioning system. Since the Z axis was basically field modulation, we are able to design a system which employs a manual controlled electrode standoff distance for simplicity.

Mechanical motion of the system was implemented through the reuse of consumer electronics subsystems in everyday devices. The x-axis translation was implemented on a disused Epson™ Perfection 1250 flatbed scanner. Inside, was found a unipolar (5 lead) stepper motor which was gear reduced and moved the optical sled by belt-drive. The sled was constructed from fiber reinforced plastic and exceptionally rigid. A solid smooth (precision) steel rod provided the linear motion path while plastic linear slide bearings lubricated with white lithium grease kept the system on track. The Y-axis motion was taken from an optical DVD drive which employed a bipolar (4 lead) stepper motor driving a linear feed screw. This system, which normally positioned the read/write laser, was ideal for this application since it was high precision, compact, and lightweight. Two LDPE motion trackers were spring pressed to the lead screw of the y-axis which permitted linear motion. In addition, this axis employed two steel rods and associated linear slide bearings which allowed adjustment of off-axis tilt. The entire Y-axis assembly was spring-screw mounted at four points to permit fine adjustment of z-height (semi-

static), x-axis tilt, and y-axis tilt. With these 3 degrees of static freedom and 2 degrees of dynamic freedom, the print head can be positioned planar to the patterning surface and freely moved for writing.

Thermal management of all motor drive systems is a concern. Both hardware and software management solutions are implemented here for the sake of simplicity and cost reduction. Transistors selected for the x-axis stepper motor feature TO-220 package. These devices are passively capable of dissipating the anticipated current load. The Y-axis employs an Allegro MicroSystems A3967 stepper motor driver IC which has been tuned to a current limited regime where the supplied current is just above the minimum required to achieve reliable and repeatable motion. Due to the screw drive nature of this axis, fairly low current is required to achieve stable motion. A small black anodized aluminium heat sink was attached to this IC with thermal paste. To avoid wasting power during times of idle, an automatic power-down of all drive circuits is employed in software using an interrupt timer. Timer0 was selected for this application due to the simplicity and versatility of 16-bit counting. A prescaler divides the $F_{osc}/4$ (frequency of oscillation - currently 8 MHz) down by some preset base 2 value in the range of 1 to 256 (i.e. 2, 4, 8, etc.). At the conclusion of any motion or input, the counter present value is reset to 0000_{hex} (16-bit zero). Following the overflow of the counter from $FFFF_{hex}$ to 0000_{hex}, an interrupt is generated which pauses current operation and executes the interrupt procedure. The procedure, in this case, simply sets the ENABLE pin of the A3967 IC to high (normally: active low) and sets the base pin of each of the MH8100c (NPN) amplifiers to low. When a movement event is triggered, the prior state of each of the drivers is restored seamlessly. An initial concern was the drift of the sleds from being unpowered. In the case of the X-axis, only half-stepping is employed and thus relaxed position will be fairly close to the desired position. For the Y-axis

mechanical system, the screw design lends itself to a fairly high amount of stiction due to the two linear slide bearings and mass of the payload. Furthermore, this type of driver system is not readily back drivable and so little load is placed on the stepper. While the relaxed position will surely vary slightly due to the eighth step regime of driving, energizing coils have been seen to pull the screw into the correct position.

To improve ease of alignment of print head to the sample, a game controller is employed for sled movement. The print head, as described earlier, is driven to the desired location using two stepper motors. Thanks to the bidirectional communications, the locally variable position can be shared with a computer for storage or further processing. A Playstation2™ controller was used because of the flexibility of having two X/Y analog joysticks along with a plethora of digital buttons. While implementation of a custom design would likely be more modest, the ergonomic and reliability analysis the Sony Corporation put forth in their design would surely be unmatched.

7.8.1.2 Embedded Software and Interface Protocols

Bi-directional serial communication with the microcontroller is required for the purpose of downloading print image blocks. Print command generation is performed by the microcontroller but can also be sent on a per event basis from the PC. The PC link was created by the use of a USB to serial TTL (Transistor-Transistor Logic, 5V/Ground) bridge. The primary interface IC is a Silicon Labs CP2102 USB to UART Bridge. It enables a virtual com port which can then be used by any compatible application (i.e. Labview™, MATLAB™, Hyperterminal, etc.).

Table 7.2: Communication baud rates and the resultant error. Despite the error value being high, this does not translate into a high BER. The UART module in the microcontroller and USB bridge oversample the communications resulting in reliable data transfer.

Baud Rate	Application	Actual Baud	Baud Error
2400	Debug	2404	0.17%
19200	Standard Speed	19231	0.16%
38400	High Speed	38462	0.16%
57600	Ultra Speed	55556	3.5%

Values represent idealized error rate which does not factor in real world noise conditions.

The data is transferred in 8-bit frames using no parity and 1 STOP bit. The asynchronous nature of the communication also means no Flow Control is used (no CTS, DTR, XON). Because the baud rate generated by the microcontroller is a multiple of the clock speed (8MHz for this particular application), there is some disparity between this baud and the desired rate. This difference is what is referred to in the Table 7.2 above as baud error.

It is important to emphasize that the baud error is not equivalent or synonymous to the Bit Error Rate (BER). The BER describes the actual errors transmitted thus resulting in unusable data packets. Because no Error Correction Code (ECC) is transmitted along with the data, there is no way for either side to correctly decode error laden data. The implemented CRC (Cyclic Redundancy Check) will most effectively detect single bit errors in addition to burst errors. It should be noted that random and periodic errors resulting in opposite glitches at single byte intervals can permit corrupt data to pass the CRC. A small baud error is compensated on both the local device and the interface bridge on PC by super-sampling the incoming transmissions. That said, errors in excess of approximately 5% typically experience unacceptably high BER and poor noise immunity. This degradation in data integrity is due to RF effects at higher frequencies, capacitive and inductive parasitics, and decreased signal strength. This combined

strategy to combat errors will prove effect in this application as rare print errors will likely not adversely affect the printed structure functionality.

While the communication rates seem slow, the relatively small amount of print data means communications of a full 1cm x 1cm block at standard resolution takes $1/8^{th}$ of a second. For example, the total transmit time of a full 2 inch (50mm) wafer is around 3 seconds. It is also important to note that the patterning time for the transmitted data can be orders of magnitude longer depending on the desired dwell time. The slower standard speed data rate ensures successful communications despite potential challenges such as long serial wire length, EMF, and electrical noise generated from on board motors.

Clearly, there will be interest in patterning larger areas or similar sized areas at higher resolution. As discussed in the technical packet details, the structure could permit data payloads of 32kbytes which would allow blocks of 360x360 pixels to be patterned at a time. Rather than deal with these variable data payloads, it may be advantageous to leverage the enhanced processing capabilities of a PC to calculate the optimal trajectories and patterning sequences for large but sparsely patterned structures. In this scheme, standard size packets are sent in addition to coordinates as to patterning locations. The result is vastly superior performance with simplified microcontroller code. For the sake of brevity, the full communication protocol is not described here in detail. The Appendix A contains the description of data packet formation and compression details.

7.8.1.3 Evaluation of a Multi-Electrode Print Head

Printing time using the Neptune system can be slow for large jobs. The most straightforward solution was to pattern multiple points simultaneously. Because the same

excitation signal could simply be switched into the necessary electrodes, all that was needed to enable this upgrade was a switching scheme. After evaluation of electromechanical switches and solid state solutions, the final design selected a solid state switching IC from Analog Devices. The ADG714 is a MUX IC and was selected for its low operating current, serial data connectivity, low cross talk between channels, size, and low on resistance. Its performance was very similar to that which could have been achieved with mechanical relays but implementation was far more straightforward. A PCB was fabricated with the IC which plugged into the existing print head. The firmware on the microcontroller which stages all operation on the Neptune printer was updated with software to allow multi-electrode operation.

To better understand exactly how multiple electrodes are used, Figure 7.44 depicts patterning with a simplified 4 electrode array. Because the X-Y stage stepping size is much finer than the pitch of the electrodes (which do not necessarily need to be spaced very close), printing speed can be improved without compromising resolution. A distinction should be made between systems which merely duplicate images across multiple writing points. Each electrode is simultaneously patterning a different region of a single print design. The multi-electrode print head contains 8 electrodes for patterning and 2 electrodes for surface gap determination. Despite being attached to a very accurate X-Y stage with good tilt correction, it may be desirable to perform active measurements on fluid conductivity or surface proximity.

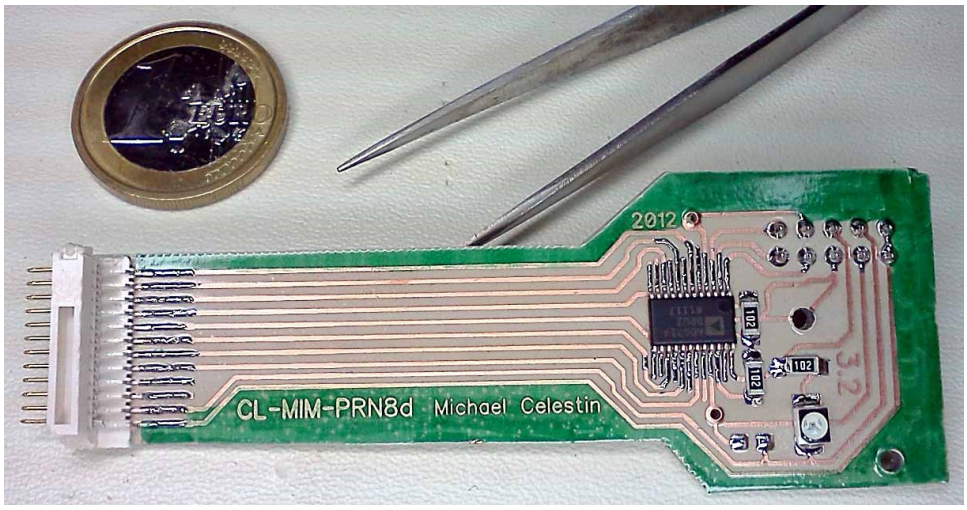

Figure 7.43: A photograph of the fabricated multi-electrode, electrostatic nanoparticle write head. This PCB contains an Analog Devices ADG714 MUX IC which directs excitation signal to 8 electrodes greatly increasing patterning speed. Gap from substrate is determined through impedance and resistivity measurements from the lowest two electrodes. A Euro coin is present for scale.

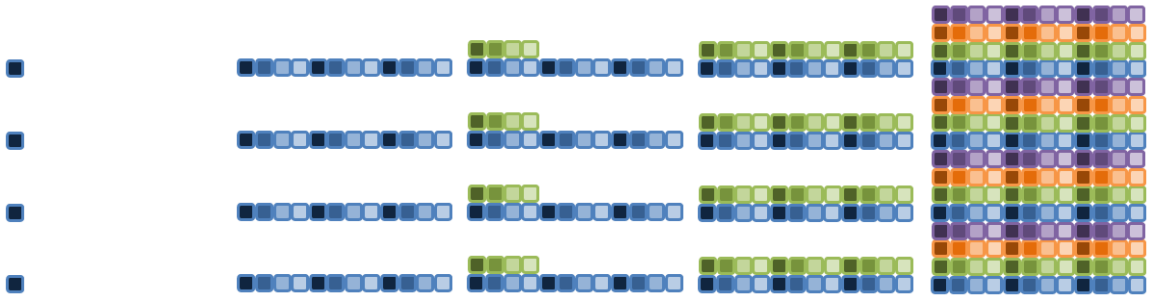

Figure 7.44: An illustration of a multi-electrode electrostatic printing technique for enhanced resolution and speed. Fixed space electrodes in the first image are plotted and the array is moved in sub-step increments towards the next write location. The array can then be moved in high precision in the Y direction leveraging microstepping on the stepper motor drives to result in 16 times the resolution versus conventional plotting.

7.8.1.4 Depositing Nanoparticles

Characterization of the nanoparticle deposits answer a lot of key questions and shape the design applications for this technology. At first, Figure 7.45 depicts the active plotting of an array of nanoparticle points with a single-electrode setup. The deposited nanoparticles are visible as deep purple dots through the small volume of colloidal gold solution.

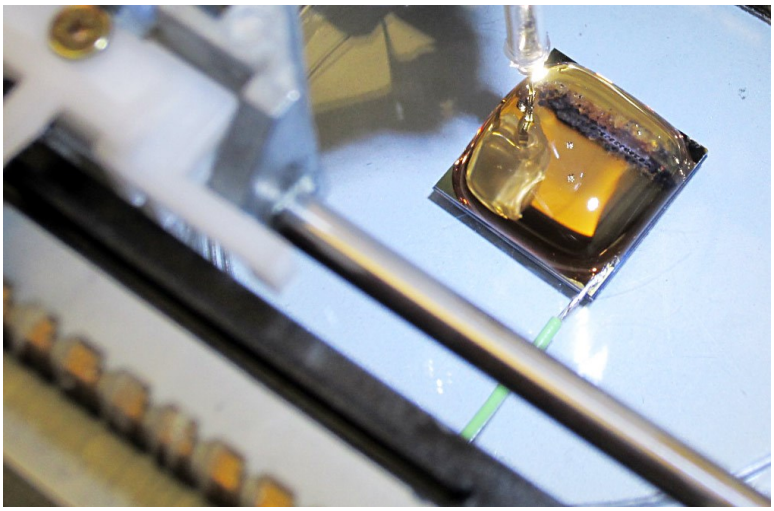

Figure 7.45: A photo of electrostatic nanoparticle plotting in progress revealing a deep purple line on gold surface. At bottom left, a drive screw is visible which a stepper motor actuates to control the X-Y positioning of the excitation electrode.

The grounding electrode is seen soldered to the gold coated sample at the lower right portion of the picture. Following deposition, the morphology of the nanoparticle agglomerations was studied by AFM, SEM, and optical profiler. It was discovered that a fairly thick coating of nanoparticles could be patterned in just a few seconds. Thick film formation or highly dense patterning will require a non-static fluid medium. Nanoparticles cannot be dispersed in high concentration and so depletion of nanoparticles can be a problem for small liquid volumes. In addition, evaporation and area field attraction can reduce the precision of patterned features when small volumes of colloidal liquid are used. It is proposed that a low flow rate laminar fluid

bed be implemented where higher resolution and consistent patterning are needed. Colloidal solutions with a lower incidence of gold particles tend to produce higher resolution patterns at the expense of being very faint to the naked eye. In Figure 7.46, we see the 3D reconstructed profile of a deposited dot of nanoparticles.

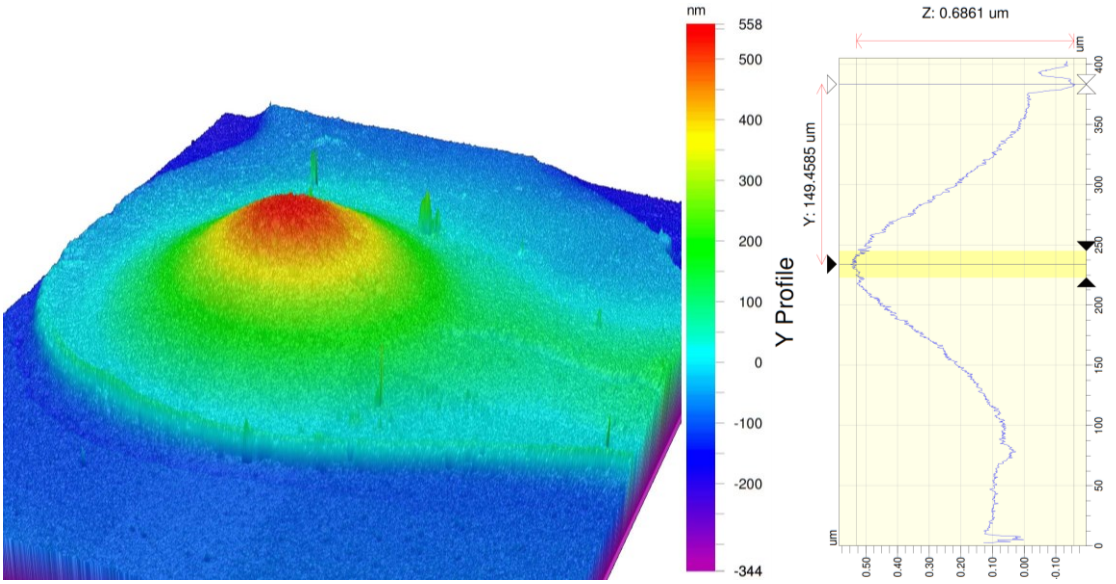

Figure 7.46: Optical profile of electrostatically plotted gold nanoparticle dot with profile slice graphed.

The profiler reveals the central peak as just over 0.5 μm in thickness and sloping to a base that is 250 μm wide. Higher and lower resolution dots are possible and depend on fluid electrode shape and size, excitation voltage, excitation waveform, electrode gap, loading of liquid medium with nanoparticles, and dwell time. Study by SEM revealed that 50 μm spots are possible when using sharpened electrodes and a biased AC sine wave. Using the same electrode and same gap but increasing the voltage and dwell time (Figure 7.47 right) produced a significantly thicker but more irregular coverage spot.

One potential application became quickly clear during AFM study of the resultant film. In Figure 7.48, we see a very rough surface with a very high surface area. Not only is the surface

relatively rough but there are many pores and voids throughout the film which can be leveraged for some sensing application. The film is surprisingly abrasion resistant but can be further strengthened by addition of linking dithiol molecules as will be seen.

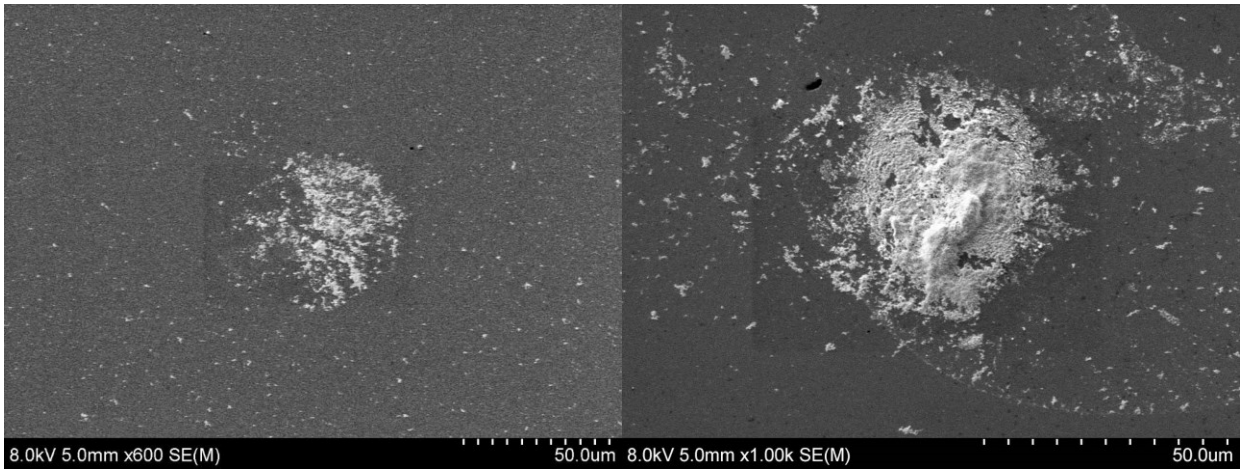

Figure 7.47: An SEM image showing an electrostatically printed cluster of gold nanoparticles. The degree of printing can be controlled by adjusting the voltage, frequency, dwell time, and electrode gap in solution. At left, we see a light spot approximately 50µm in diameter. At right, a large agglomeration is made possible by higher voltages with the disadvantage of spurious depositions in the adjacent region.

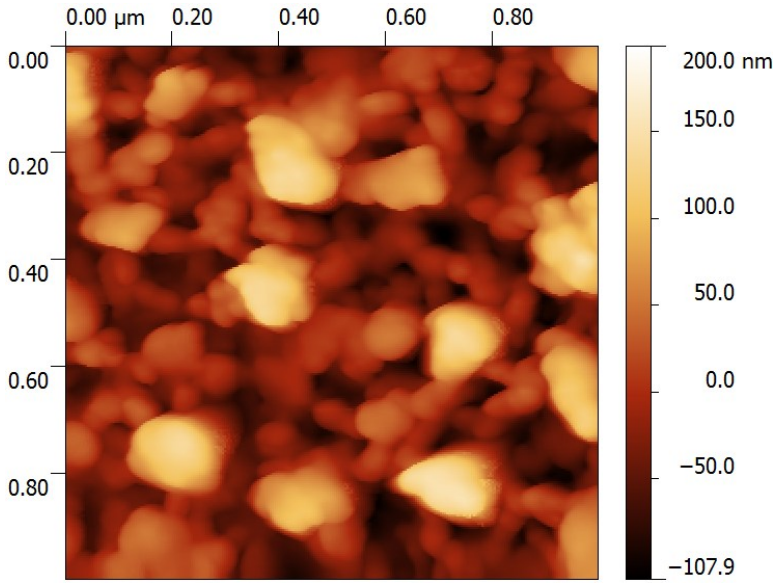

Figure 7.48: A detailed AFM image of electrostatically plotted nanoparticles on a surface. The high surface area film can be used for a variety of sensing and circuit building applications.

Characterization of electrical conduction through these films was carried out by an interdigitated electrode test coupon. Repurposing an existing design fabricated by fellow lab workers, a gold interdigitated electrode set was used as a deposition substrate and nanoparticles were deposited onto the test site. In Figure 7.49, we see a photograph of the spot of nanoparticles on the electrodes as well as an optical profiler reconstruction of the clean interdigitated surface. Testing revealed through electrode resistances as low as 15Ω for a 1mm spot.

Low voltage electrostatic assembly onto monolayer decorated metal surfaces was carried out successfully. The assembly was successful on SAM coated silver, gold, platinum, and palladium films. The use of higher voltage electrostatic fields accelerates the writing time but introduces a number of problems. Starting with the solution around the electrodes, excitation voltages in excess of 1.229 V will begin causing localized electrolysis. As the liquid carrier separates into gasses, small bubbles inhibit proper nanoparticle transport onto the surface and complicate electrostatic field lines. Resolution was witnessed to be diminished and non-circular artifact formation increased. At higher voltages still, the formation of metallic crystallites was visible which can potentially puncture the delicate organic films which they are in contact with (Figure 7.50). At the highest excitation voltages of above 3V, damage to the underlying evaporated metal coating is possible. Site damage has been seen on a number of occasions which results in no conductive surfaces under the electric field (Figure 7.51).

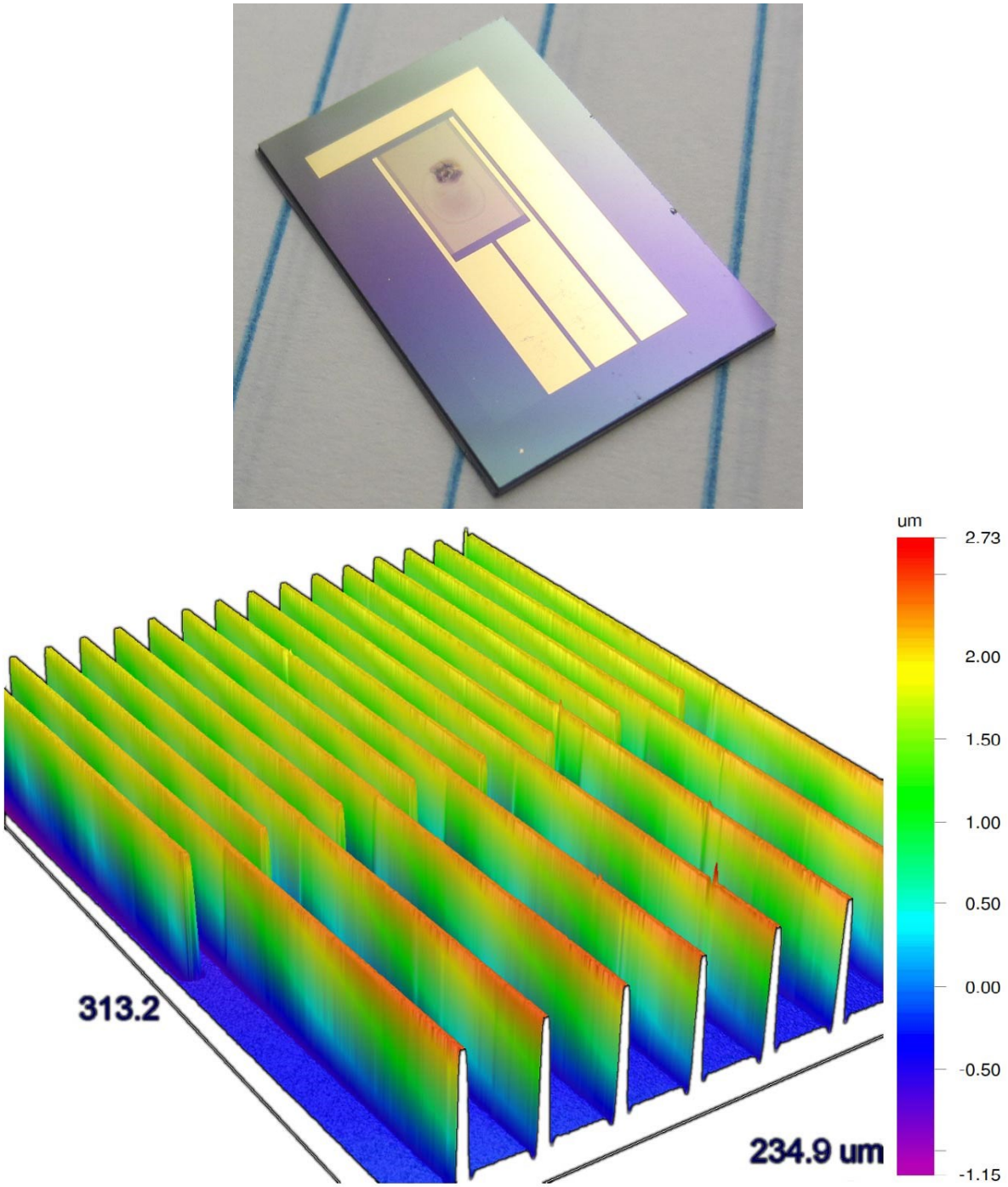

Figure 7.49: A photograph of an interdigitated electrode sample with a spot of nanoparticles deposited for conductivity tests (top). Below, is a 3D white light interferometer reconstruction of the interdigitated electrode surface used for measurements. The electrostatically deposited gold nanoparticles land between the electrodes and resistivity is determined.

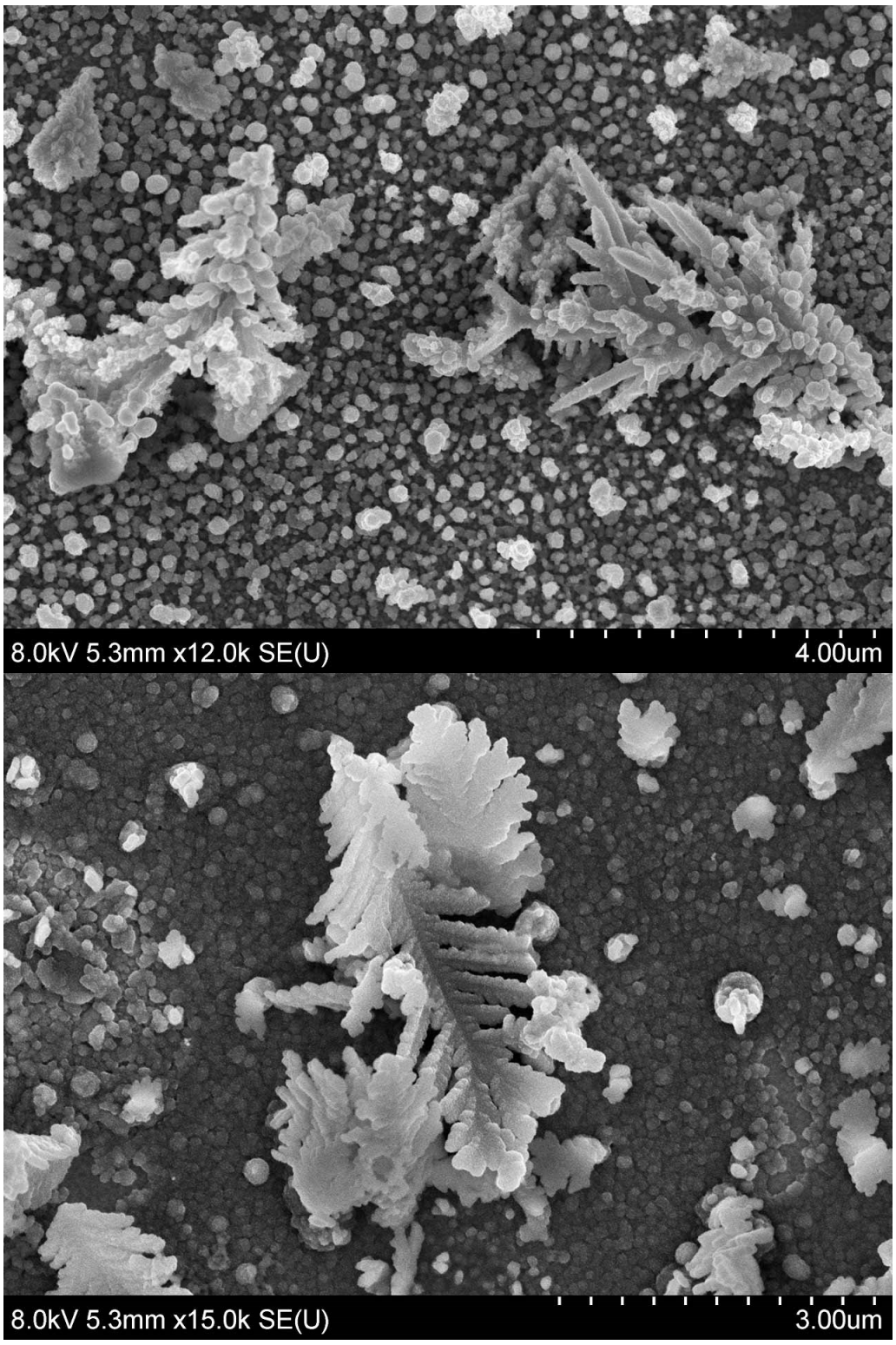

Figure 7.50: A set of SEM images depicting various electrically formed crystallites of gold during electrostatic deposition. It is believe these formed due to the presence of some gold salts which remained in solution after nanoparticle synthesis.

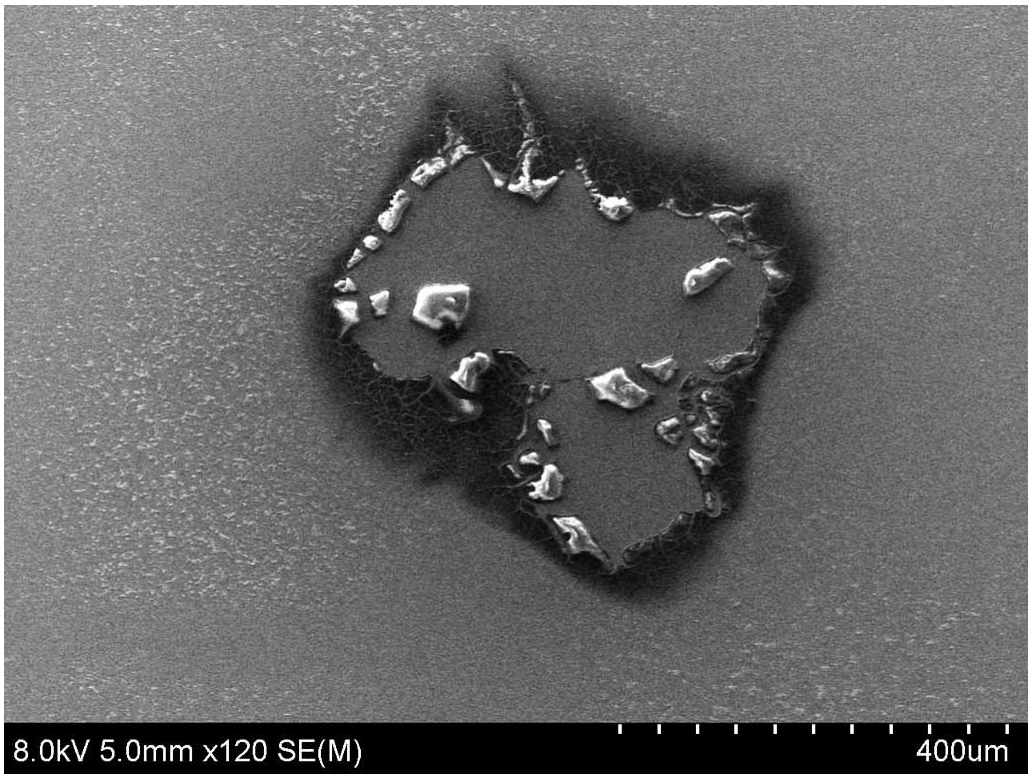

Figure 7.51: An SEM image of the result of excessive voltage when attempting electrostatic printing of gold nanoparticles. Here the voltage accelerated deposition but also delaminated the underlying conductive film from the substrate.

While the surface particles exhibited stability, a more stable lower resistance contact was desired. Experimentation was carried out on methods to "glue" the nanoparticles together both during and after deposition. A solution was found in the use of a di-thiol SAM species. The monomer, 1, 6-Hexanedithiol, was obtained from Sigma-Aldrich and used as is without modification. Initial tests began with the fresh cleaving of V-1 grade Muscovite mica to provide an ultra-smooth surface for AFM study. The dithiol was added to a gold nanoparticle laden solution in a concentration of 1 mM. The solution was mixed by mild agitation and allowed to sit for 5 minutes. Using a micropipette, a small volume of the liquid was dispensed onto the freshly cleaved mica surface and allowed to dry in a clean environment. Study by AFM (Figure 7.52) revealed significant agglomerations of the nanoparticles had resulted.

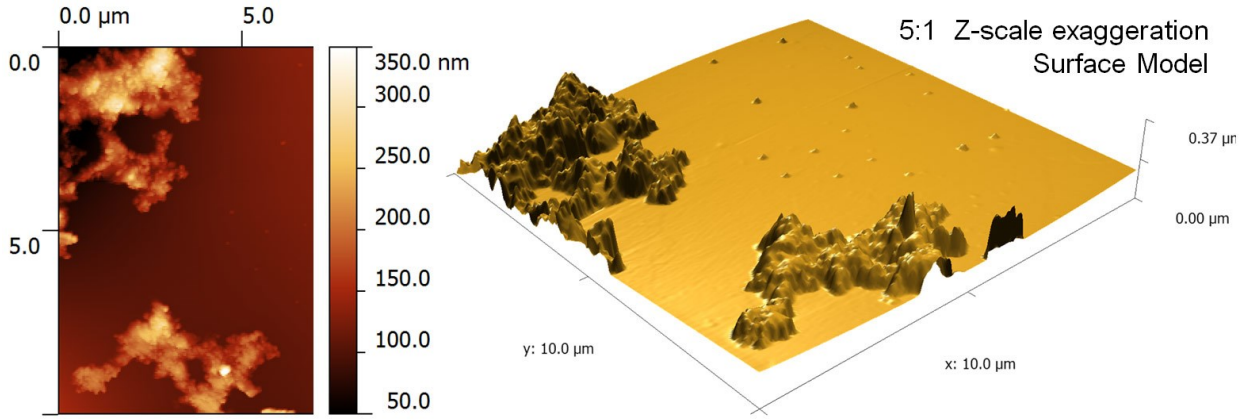

Figure 7.52: An AFM image (left) of nanoparticle agglomerations following surface reordering in solution with a 3D reconstruction (right). These images were taken on gold evaporated cleaved mica for maximum flatness.

A further experiment was performed to understand if a dithiol coated planar surface would uptake a smooth layer of gold nanoparticles. A gold evaporated silicon sample was immersed in 1 mM solution of 1, 6-Hexanedithiol in ethanol for 24 hours. The sample was removed, rinsed with pure ethanol, and dried in an N_2 stream. Following this, the sample was immersed in a nanoparticle loaded solution. After 24 hours, the sample was removed and inspected by SEM. The surface looked very similar to the mica surface in the prior experiment. A proposed mechanism for the agglomeration, rather than even distribution, of nanoparticles is presented in Figure 7.53. A literature review of nanoparticle dynamic response in dithiol environments seems to confirm that given room temperature conditions, reordering and releasing of thiols will result in reorganization such that minimum strain is placed on the thiol bonds. This same bond tightening could also be performed after the nanoparticles were deposited electrostatically. A repeat of the interdigitated electrode test saw a 20-30% reduction in contact resistance after treatment with a dithiol SAM and drying.

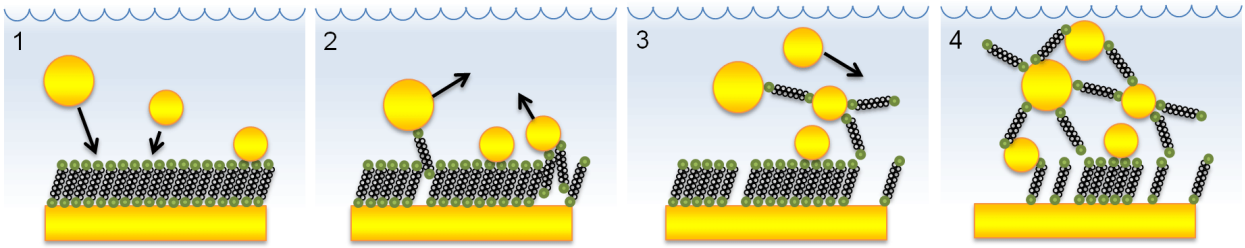

Figure 7.53: An illustration theorizing the agglomeration mechanism for gold nanoparticles on dithiol decorated surfaces.

7.8.1.5 Nanoparticles on Insulators

A collaborative project was undertaken to evaluate if nanoparticles could be deposited in a controlled manner on flexible, dielectric substrates. The nanoparticle loaded solution was created by refluxing a 1mM solution of $HAuCl_4$ with trisodium citrate. The PET (polyethylene terephthalate) film was solvent cleaned in preparation for the deposition. A platinum mesh was placed in close proximity to the PET film and a frequency sweep of 60 Hz to 1 MHz was use to direct the deposition. The voltage between the substrate and mesh was read back on an oscilloscope and the amplitude adjusted such that the V_{pp} = 1.5V. An illustration of the full experimental setup is seen in Figure 7.54.

The film was analyzed by Raman spectroscopy, SEM, and AFM studies. Coverage of the gold nanoparticles was sufficient to allow surface conduction across the insulating substrate. The AFM studies revealed a uniform, thick coating of nanoparticles approximately 120 nm thick (Figure 7.55). While directed deposition was possible, the insulating qualities of the assembly substrate made resolution very poor. The deposition could only be directed to within a 3-5 mm boundary. Further experimentation using a glass capillary array demonstrated that localized nanoparticle solution sources which were excited in a similar manner as described above could also be used for the coating of nanoparticles onto insulating substrates. This technique has

applications in the formation of a top contact for SAM studies, static control in plastics, and an alternative substrate to ITO for a relatively clear substrate.

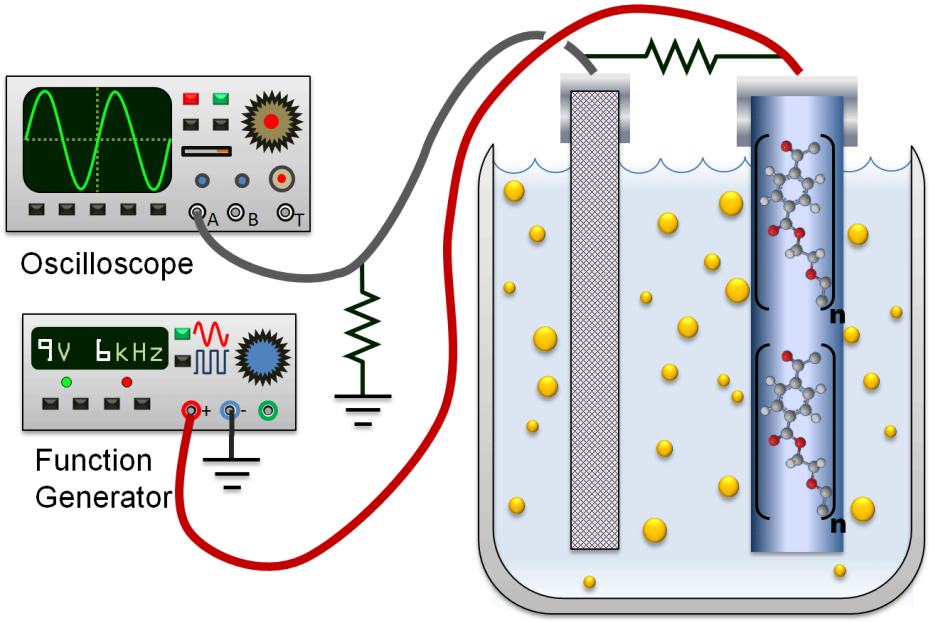

Figure 7.54: An illustration depicting the setup for depositing gold nanoparticles on flexible PET film. (Adapted from Koiry [274], Copyright 2013, John Wiley and Sons.)

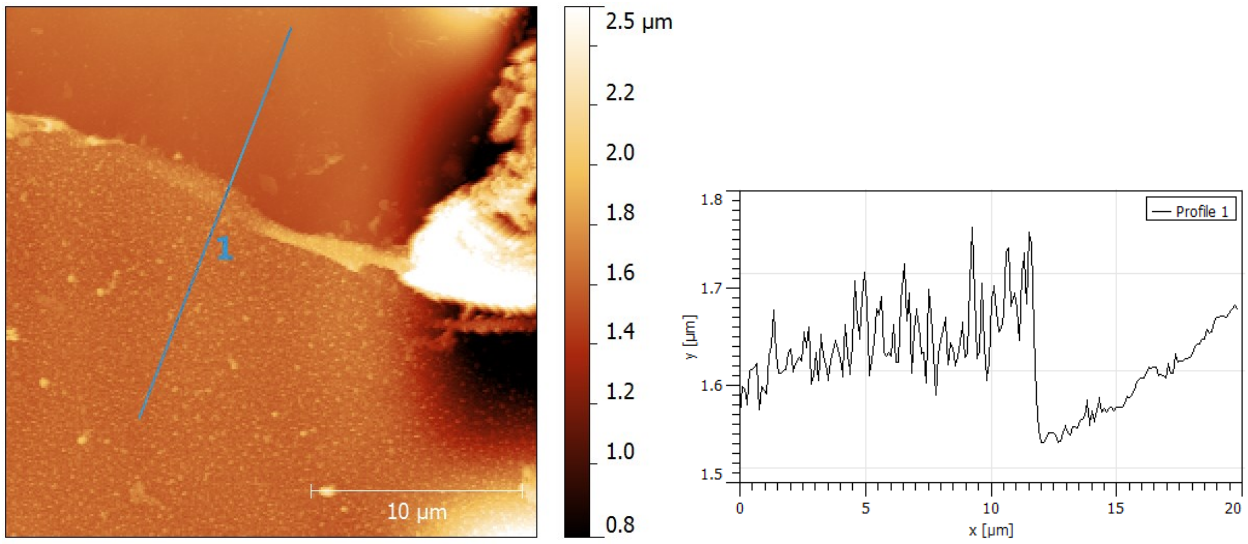

Figure 7.55: AFM image of a smooth electrostatic nanoparticle deposition on flexible PET film depicting step height. The film was scratched using stainless steel tweezers resulting in an agglomeration (at right) and a step to determine deposition thickness. At right, we see the profile of the blue line at left.

7.8.2 Inkjet Printed Insulator

The most elegant solution proposed towards the problem of the fabrication of a top contact was to directly print it using inkjet technology. The possibility of printing conductors, insulators, and semiconductors is possible through directing printing. This is especially appealing for contacting delicate organic monolayers since it is done in atmosphere with no heating. A review of existing inkjet printing solutions revealed numerous solutions for conductive traces but far fewer for the printing of insulators. The few demonstrated examples typically involved a workup step (annealing) which would damage the underlying monolayer and had to be ruled out. Here a unique solution needed to be created in an industry where trade secrets are the status quo.

7.8.2.1 Inkjet Technology Overview

It is important to first review the different types of inkjet technology and rationalize some of the selections of equipment and materials for this project. For this project to be successful, it needed to employ low cost, COTS parts. There are two major categories of inkjet printing systems. Continuous inkjet systems (CIJ) are employed in commercial products where very high speed printing with high duty cycles is required. In these systems, the ink is continuously squeezed through the nozzles and deflected by magnetic or electrostatic fields. The deflections control whether the ink hits the target print area or a gutter which either discards or recycles the unused ink. While these systems are very technologically mature, they often trade precision for speed and are rarely seen in consumer products.

Inkjet printers built for home and office use are almost entirely of the drop-on-demand (DOD) type. These systems modulate ink flow such that nozzles only squirt ink during “data

dark" sections of the print. The system requires a far smaller total volume of ink due to the modulated printing technique. One of the disadvantages of this system is clogging of the nozzles while the print head is at rest for extended periods of time. The two major sub-categories within the DOD-type printers are thermal and piezoelectric print heads. Most manufacturers opt to use thermal inkjet heads which are often disposable and replace along with the ink tanks. The thermal print technology would then logically need to be very inexpensive to permit such use. In Figure 7.56 we see the basic components of the thermal print nozzle.

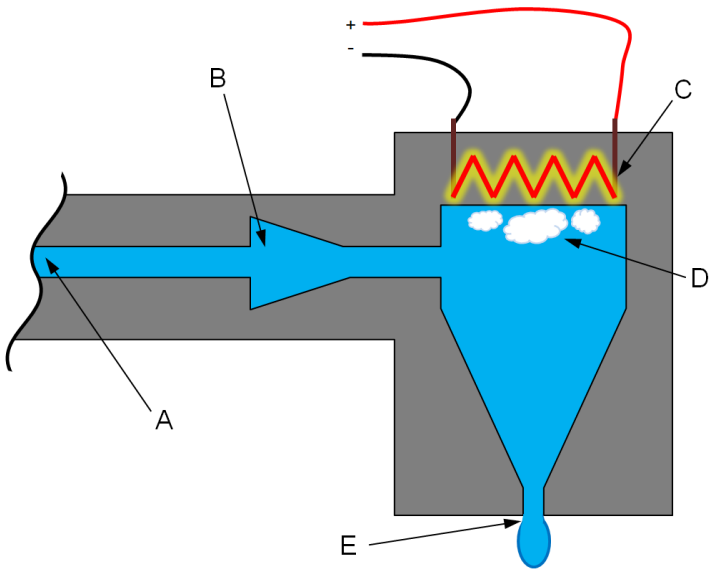

Figure 7.56: An illustration of the operation of a thermal print head element. A heating element (C) is heated with pulsed current which boils the liquid below (D). The cavitation forces liquid out of the nozzle (E) and cooling draws additional fluid from reservoir (A).

The nozzle functions by boiling a small volume of liquid within a microfluidic channel which rapidly increases the volume in the specially shaped reservoir. This boiling forces a small quantity of ink out of the nozzle. After the heating pulse has ceased, the gas bubble quickly collapses and draws in addition fluid from the source. The main disadvantage of this printing technique is the high process temperature and (typically) short service life of the print head.

Reliable thermal heads have been manufactured and employed in a fixed head designs. The boiling excludes the use of thermally cured inks and solvent-based inks which are too volatile to be subjected to the additional heat.

Piezo inkjet technology effectively pumps the ink to force it out of the nozzle. Figure 7.57 shows the cross section of a typical piezoelectric head.

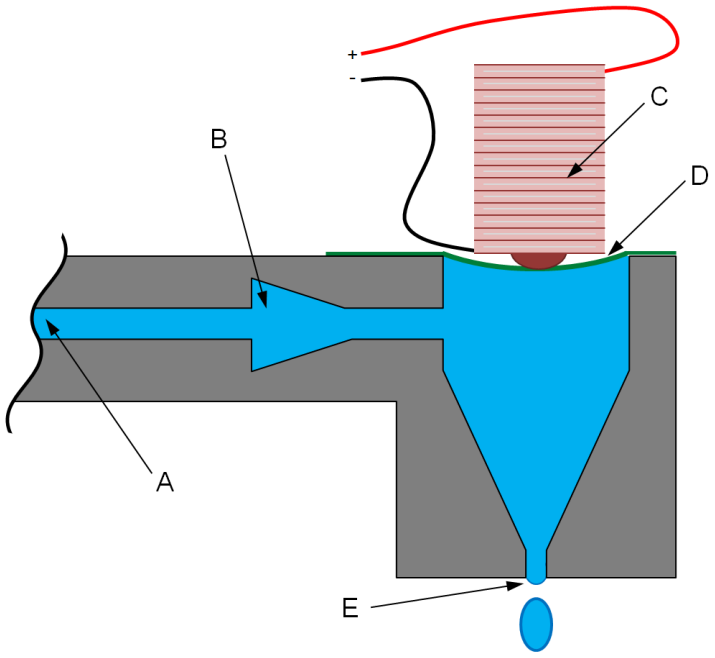

Figure 7.57: An illustration of the operation of a piezo print head element. The piezo stack (C) atop the nozzle body actuates a flexible membrane (D) forcing liquid out of the nozzle (E). One way flow of liquid from the reservoir (A) is ensured by a simple check valve (B).

A piezo stack is excited and bends a flexible membrane over the nozzle. The sudden downwards force causes the ink to flow from the nozzle and a slower return pace allows surface tension to preferentially draw ink from the ink supply rather than withdrawing the ink line at the nozzle. The piezo technology is much more expensive than the competing technology but allows for much greater flexibility in terms of ink formulations. This is an ideal quality for a research printer.

7.8.2.2 Modification of Print Platform

The printer selected for modification is an Epson Stylus Photo R300. It was selected for its relatively low cost, high print resolution, ability to accept rigid media such as compact discs (CDs), and the 6 color printing technology. Each color tank can represent a different ink formulation allowing for the single process deposition of insulators, conductors, semiconductors, and surface modifiers. The printer is capable of producing an ink droplet as small as 3 picoliters and plotting 1440 dpi (dots per inch). The first step was a complete breakdown of all the components and a thorough cleaning to remove existing ink from the system. The print head cleaning process consisted of injecting pressurized cleaning solution through a syringe into the ink tank connection port. The cleaning fluid consisted of 5:1 (v/v) DI water and isopropanol which was heated to 45°C. The process was repeated for each color until the nozzles all flowed freely as in Figure 7.58.

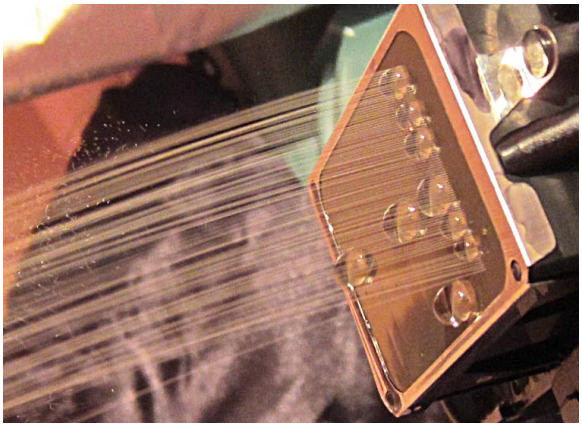

Figure 7.58: An image of the inkjet nozzle cleaning process where DI water is forced through the nozzles.

Part of the plastic casing was permanent removed and interlocks defeated such that dry air can be directly forced over the print area to minimize smearing. Replacement ink tanks lacking the conventional sponge media were commercially acquired in addition to an ink chip resetter.

Because inkjet technologies tend to be loss leaders, manufacturers go to great lengths to ensure that tanks cannot be simply refilled and reused. Each tank contains a small microcontroller which stores the estimated remaining ink level and a lockout which prevents the printer from using the tank once it has been exhausted. This protection is circumvented by the chip resetter which reprograms the resident EEPROM to reflect that of a new ink cartridge. The last hardware requirement was the fabrication of a carrier for the various samples which would be printed. Since the printer system was already designed to print on CDs, it was decided that this would be the basis for the ideal carrier. Various shaped holes were drilled and alignment keys created such that a sample could be loaded, added, removed, and reprinted with an alignment error of less than 150 μm.

7.8.2.3 Formulation of Custom Insulators

The next major challenge was the formulation of a single step insulator which would be reliable printed through the piezo inkjet head. Polyvinylpyrrolidone (PVP) and Polyvinyl Alcohol (PVOH) were selected as insulator candidates for their unique and flexible properties. The primary reason for their selection is they are both readily soluble in water. PVOH can be crosslinked following UV exposure turning this very hydrophilic polymer into a stable surface coating [275]. As currently understood, the crosslinking requires the presence of a sensitizer, typically boric acid, sodium benzoate, or formaldehyde. Studies have demonstrated successful UV hydrogel crosslinking both alone and in the presence of a sensitizer such as hydrogen peroxide. It has been reported that the peroxide serves to increase the rate of crosslinking through hydroxyl radical generation. In either case, cross-linked polymer chains improve the dielectric properties of the insulator and reduce leakage current. For organic and inorganic

printable insulators, the typical setting process involves thermal annealing [276]. Because this research seeks to develop a single-step insulator with no work-up step, these attractive qualities will not be utilized. Compatibility with self-assembled monolayers (SAMs) and Langmuir-Blodgett (LB) films generally require gentler handling. Because these monolayers are very well controlled and of very small geometry, it is foreseeable that simplified incorporation into inkjet printable circuits will 1) improve the quality and consistency of inkjet electronic designs 2) provide a pathway for increased switching speed in circuits 3) facilitate further and more streamlined research in permanent self-assembled structures and detectors.

The polymers selected were all chosen with the lowest molecular weights possible. Because the inkjet nozzle used to print them is on the order of 20 μm, it is recommended that the largest particle be a few orders of magnitude smaller to prevent clogging in the print mechanism. In addition, a clean droplet break is facilitated by the lower molecular weight solutions which generally have lower viscosity and surface tension. These properties not only improve printed resolution but reduce the incidence of clogged print nozzles and improper wetting of the microchannels in the print head.

After studying commercial inks, it was observed that they do not dry completely when deposited in thick layers. The presence of a humectant (most likely a glycol) was sufficiently hygroscopic and allowed the ink to dry to a "cream" state. Because the goal of this ink formulation is to produce a hard, stable insulting layer, less humectant would have to be used. Ink drying times are typically kept as trade secrets in addition to general formulations. Some basic formulation data was discovered and an ink recipe was derived through this, trial and error, and reverse engineering of existing inks. Studies included viscosity, foaming properties, drying time, and surface tension. The primary solvent used is DI water; the co-solvent selected was

isopropanol. The alcohol served to (1) reduce the surface tension, (2) increase the evaporation rate and drying time, (3) prevent clogging, and (4) modify the viscosity. Some of these properties interact in complex ways with all the additional components of the ink. Triton X-100 was chosen as the surfactant which reduced the surface tension while increasing the incidence of foaming. Because these tiny bubbles can act as blockages in the print head, it is desirable to minimize these effects. In an attempt to reduce the number of ingredients and the complexity of number of optimization experiments, diethylene glycol (DEG) would be used as both a humectant and an anti-foaming agent.

Polyvinylpyrrolidone (PVP) (10 000 average molecular weight) was obtained from Sigma Aldrich and used without further purification. As the polymer is somewhat hygroscopic, care was taken to minimize air contact/exposure. The polymer was dissolved on a percentage weight basis of 2, 5, and 10%. Even under room temperature (22°C) conditions with little agitation, the 2% weight loading dissolved in water in a matter of seconds. Unless heating or sonication was applied, the remaining solutions would require on the order of 15-30 minutes to fully dissolve.

Polyvinyl Alcohol (PVOH) (9000 – 10 000 average molecular weight) was obtained from Sigma Aldrich and used without further purification. The polymer was dissolved on a percentage weight basis of 2 and 4%. PVOH is less hygroscopic than the PVP which was observed to greatly accelerate drying time of deposited solution. Films tended to maintain shape very well through drying and were very consistent in thickness. PVOH has the additional benefit of offering a very low surface tension with minimal modification at concentrations of less than 2% in water. Because of this, less surfactant was added to these solutions. A limited amount of DEG was still employed to reduce the natural foaming tendencies of the solvated polymer.

Precise ink formulation was obtained by performing iterative experiments to improve the print quality, film consistency, and drying speed while minimizing nozzle clogging and microchannel wetting problems. It was observed that an exceptionally fast evaporation rate makes printer reliability unacceptably low for practical purposes. The loading of high weight fractions of polymer in water results in a surface tension too high to permit reliable flow into the microchannels of the piezo print head. For this reason, the surfactant Triton X-100 was added in 0.005%-0.010% w/w loading. The humectants diethylene glycol (DEG) and propylene glycol (PG) were added to reduce the rate of clogging in the print head and also act as an anti-foaming agent. Because the glycol also greatly reduces the vapor pressure of the ink, it is recommended as little as possible is used to achieve acceptable foam reduction. It was found that <2% DEG tends to be ineffective at combating the foaming from the surfactant.

The deposited polymer was thick, dense, and clear. While loadings of 2-4% came to dry rather quickly, 10% loading was very slow to dry. In addition, the film resultant from the 10% loading was very rough. Convective deposition ("coffee ring" effect) was much more pronounced in the samples with PVP exhibiting poor consistency through feature cross section. In addition, due to reduced bonding with the silicon surface, small features became distorted more easily. While not necessary for production, it was difficult to determine the location of printing on certain substrates. For this reason, inkjet dye was added in 0.4 – 1.0% v/v levels to assist in visual identification of print boundaries. This had the additional benefit of including all trace ingredients such as anti-fungal and stabilizers which were not present in the custom formulation. Finally, the entire formulation was filtered under vacuum through a 0.22 μm cellulose acetate membrane.

Once all hardware and chemical setups are completed, there are still numerous challenges in achieving quality prints. The surface tension of the printed liquid tends to distort sharp and long features. In Figure 7.59A, we see an example of a challenging shape to print. Here a large contact pad is attached to a thin via.

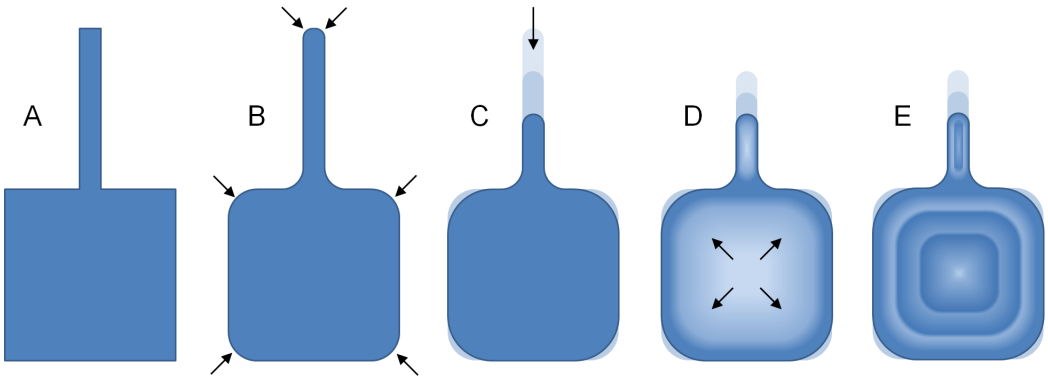

Figure 7.59: An illustration of inkjet fluid migration phenomena affecting print quality. The intended feature (A) is affected by surface tension and printer artifacts resulting in rounded corners (B). After a short time, surface tension draws fluid towards central pool (C). During drying, convective deposition (D) results in a "coffee ring" effect which can be worked around through successively smaller feature printing (E) to compensate for central thinning.

The surface tension of the ink will draw fluid towards the largest pools of liquid. The via is shortened and the edges are all slightly rounded as a result of the surface tension. The viscosity, surface tension, density, evaporation rate, and surface roughness and interaction (hydrophobic/hydrophilic) all play a role in how the ink will react. This is the subject of much modeling research and was largely ignored until recently [277]. The reaction can typically be calculated by determining the minimal surface constrained by the aforementioned conditions. As a general rule, the printed shape will want to transform into a perfectly formed circle. A simple workaround is to print a different shape than what is desired as a final result. This may include numerous extra features or dimensional differences which resolve by the time the ink dries. This is especially important when attempting to achieve very small geometry features. For the scope

of this research, some modifications were made but they were largely done by trial and error—printing a representative shape and modifying as needed to achieve the desired result.

In addition to the edge deformation, there were concerns of convective deposition "coffee ring" effect. This is a phenomenon has been well studied and is the result of capillary flow in the evaporating droplet of liquid [278]. Liquid which evaporates near the edge of the drop is replaced by liquid from the interior of the drop which carries any dispersed species to the edge with it. This is somewhat undesirable for the application of printing because it results in uneven profile thickness. This may result in situations where an insulator is sufficiently thick at the edge but becomes significantly thinned towards the middle. This thinning may be enough to result in a short circuit. Ink formula optimization can correct some of these problems but typically introduces deposition problems due to the modified ink properties. One proposed solution is the successive printing of smaller edge constrained features to fill in these areas. This is illustrated in the last panel of Figure 7.59. Testing with large sized droplets showed that reliable multi-layering of rings was limited to about 3-4. At or above this, even small volumes of liquid centrally located tended to spread to the ring boundary due to surface attraction. While reprinting generally produced sharp features and did not distort the original dried boundary, the creation of symmetric concentric prints can be challenging. Even in the case that the subsequent edge boundaries are pulled to the original print limits, the central region does benefit from additional deposition and thickening. It was also noted that during testing, additional deposited layers benefit from expedited drying time. Because the underlying deposition is still very hydrophilic, it readily wicks away liquid from the fresh deposition which increases drying surface area despite the smaller deposited volume.

Several patterns were developed to achieve an MIM test structure using inkjet printing as the final steps. As previously mentioned, this technique applies to not only SAM films but also those by the LB deposition method. A substrate is prepared and an appropriate electrode material is coated with the monolayer of interest. The insulator allows traces and contact pads to exist in close proximity to the test junction without shorting to the assembly electrode. More importantly, it cushions the next printed contact metal to allow low land force contact probes to directly measure over the monolayer surface (Figure 7.60).

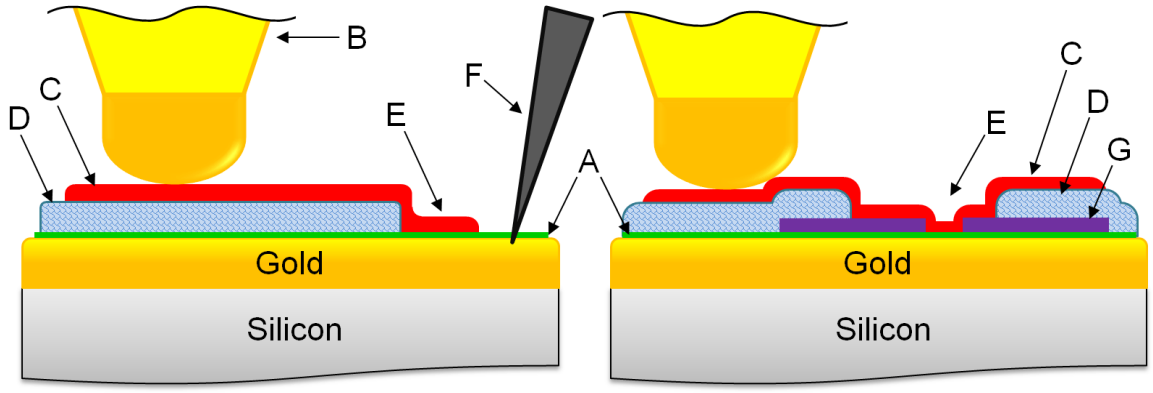

Figure 7.60: An illustration of the cross-section of an inkjet-printed top contact. At left, the contact geometry (E) is entirely dependent on the printer accuracy and precision by the deposition of the water soluble insulator (D) and conductive ink (C). The monolayer (A) is protected from damage resulting during probing (B). Alternatively (at right), the contact can be defined more accurately by photoresist (G) prior to inkjet printing.

7.8.2.4 Surface Cross-linking of Printed Polymer

To further enhance the stability of the printed insulator, the idea of crosslinking at the surface was considered. Polymers are readily cross-linked by either UV exposure or chemical catalysis/reaction. PVP has been demonstrated to be cross-linkable in the presence of a catalyst by UV exposure [279]. Because the SAM film is sensitive to high energy photons, this method and polymer were less desired. Polyvinyl alcohol can be chemically cross-linked using boric

acid. Spot applied, chemically directed crosslinking of the printed polymer insulator has the advantage of improving insulator characteristics without degrading or contaminating the surrounding areas. Chemically, the crosslinking is simple. We start with high purity sodium borate, Na_3BO_3, and dissolve in DI water to form boric acid. This weak acid remains in buffer equilibrium with the surrounding water dynamically converting into the desired tetrahydroxyborate anion required to initialize catalysis.

$$Na_3BO_3 + H_2O \longleftrightarrow B(OH)_3 + 3\ NaOH$$

$$B(OH)_3 + 2\ H_2O \longleftrightarrow B(OH)_4^- + H_3O^+$$

Free alcohol groups on the polymer will have their hydrogen stripped off by the surplus OH^- groups of the borate and a bond formed in their place. The borate will accommodate up to four bonds linking up to four different polymer chains together.

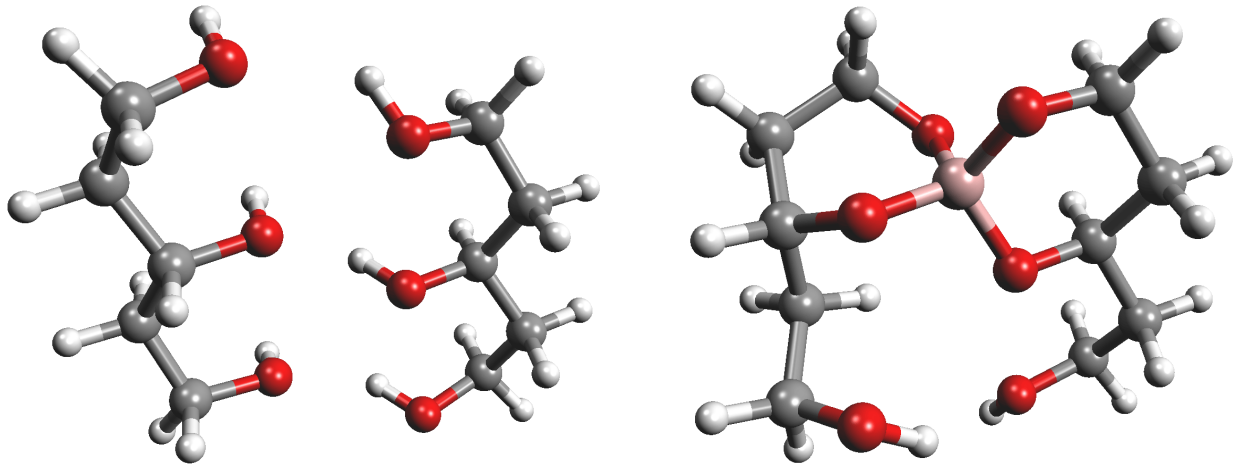

Figure 7.61: A molecular model of polyvinyl alcohol undergoing crosslinking after being exposed to tetrahydroxyborate. The system, dubbed SACHET (Spot Applied Chemically Hardened Electric Terminator), works by crosslinking the printed insulator on the printed surface either in a wet-wet or dry-wet configuration. Left two polyvinyl alcohol molecules are linked at right by (pink) boron atom in tetrahedral configuration.

7.8.3 Inkjet Printed Metal Particles

Connected to the prior research of electrostatically plotting metal nanoparticles, I wanted to evaluate whether or not nanoparticle laden liquids could be printed on an inkjet printer. Various gold colloid samples were attempted in test printers only to result in clogging. Print head conditions almost always resulted in the settling of metal load and clogging of the nozzles. After doing some research, a COTS solution was found to be very compatible with the Epson line of piezoelectric printers. The selected product was the Novacentrix JS-B25P silver nanoparticle ink. This ink has an impressively low sheet resistance of 60 mΩ/square. It is a somewhat viscous water-based liquid at 5 cP with 25% (by weight) silver content. Thermal annealing (described as low temperature oven processing) can be used to result in reduced resistivity but allowing prints to dry overnight seem to result in nearly identical improvements without subjecting the sample to damaging heat. Unlike conventional inks, these require very regular use and are very damaging to the print system. For the duration of experimentation, the printer was operated at least once a day, 6 days a week to ensure clearing of clogs.

7.9 Stability and Packaging

For the same reasons as in commercial microelectronic development, it is desirable to package devices for testing. Packaged devices can be hermetically sealed resulting in greatly reduced effects of oxidation, contamination, and reduced chance of damage. Inert gas backfilling of the packaging is recommended for the application of organic diode storage. As described earlier, organic monolayer suffer from oxidation damage due to the presence of highly reactive oxidation species. Unfortunately, most commercially available packages, Figure 7.63, are not designed to provide these exotic environments.

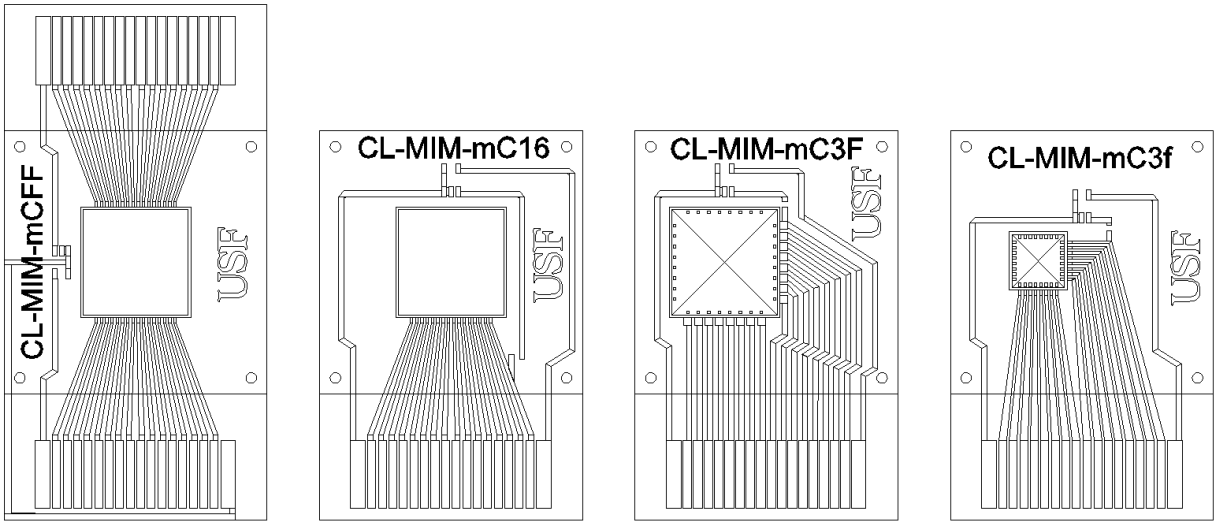

Figure 7.62: CAD renderings of sample carriers based on the xD memory card pinout. These cards allow simple hermetic sealing to prevent oxidation or chemical degradation of the fabricated sample. In addition, simple plug-and-play testing is possible after wire bonding electrical contacts from the sample die to the carrier traces. In addition to testing ease, the carriers contain traces to house a precision temperature sensor making additional experimentation possible.

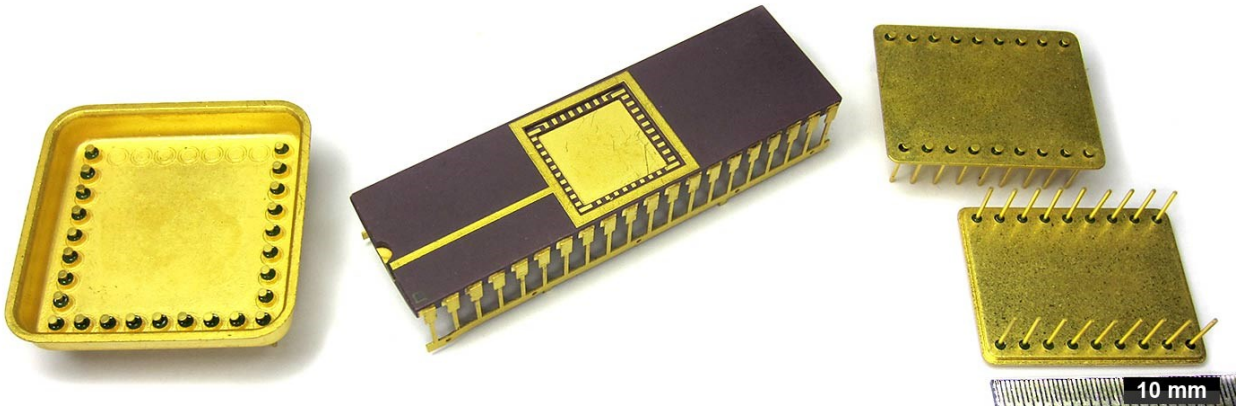

Figure 7.63: Various ceramic and metal chip carriers. These carriers permit the formation of a hermetic seal and provide a more rugged form factor for testing, transport, and storage.

For the sake of a complete study, a glass chip carrier was designed. In Figure 7.64, we see photos of an older generation of FR-4 PCB chip carriers and a rendering of the suggested improved design. Figure 7.62 shows a number of variations of this design which interface with the xD memory card pinout. The xD memory card was chosen as a contact standard because of

the high pin count of the device, ready availability of reader slots, and easily manufactured metal interface. Because multiple pin connections enable more test devices per die, efficient automated testing is possible through the use of a switchbox. Connections between the test die and the carrier are best made by wire bonding. While flip-chip bonding may be an attractive option, the conditions required to achieve the melting of the contact balls are not favorable for the organic films.

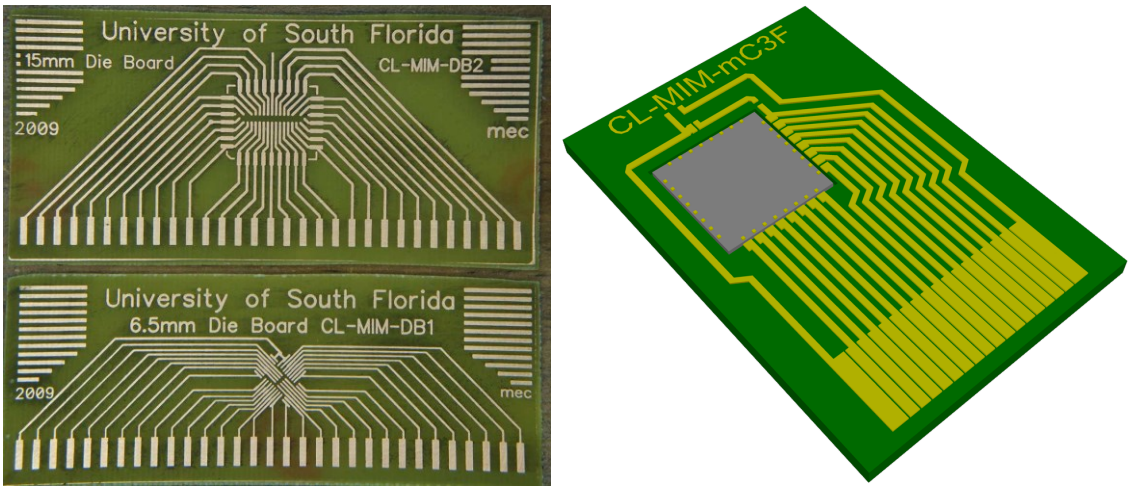

Figure 7.64: Images of fabricated and proposed chip carriers for expedited sample testing. Initial fabricated carriers on FR-4 PCB interfaced with existing experimental setups (left). The proposed design employs very low loss leads with a commercially available socket (right).

The final evolution of this design study is seen in Figure 7.65, in the form of a hermetically sealed glass capped carrier which can be assembled in a glove box filled with the desired inert atmosphere. This design is easily assembled from diced microscope slide fragments and optical epoxy adhesive. Electrical contacts are defined by conventional photolithography and simply evaporated onto the base glass or ceramic substrate. One very attractive benefit to a fully enclosed sample is the ability to test outside of normal ambient parameters. With fear of condensation onto the sample removed, cooling with liquid nitrogen or a Peltier plate is possible.

Temperature variation in measurement can be used to verify measured current is indeed due to quantum tunneling and not thermionic emission.

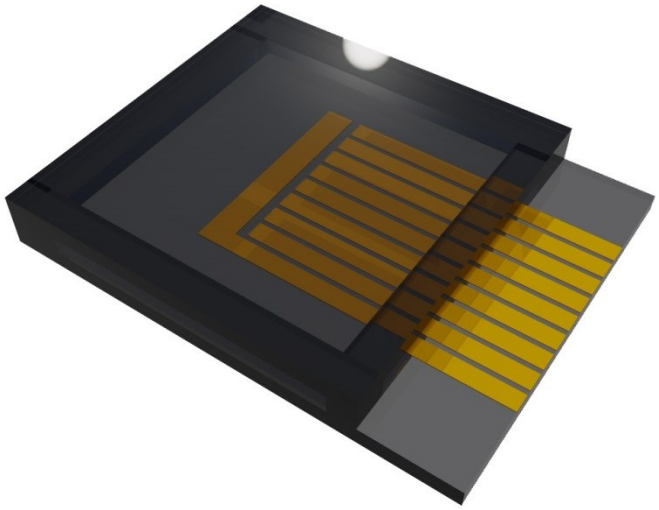

Figure 7.65: A rendering of a simple environmental enclosure for fabricated MIM structure. The structure is constructed from diced glass slides which measure 25 x 75 mm which is epoxied to form a transparent but hermetic seal with electrical feed-through.

CHAPTER 8:

CHARACTERIZATION OF PERFORMANCE

Characterization of this remarkably thin, self-assembled monolayer can prove quite challenging. A set of techniques will be presented which can provide data on binding energy, film thickness, and surface coverage. Perhaps one of the most relevant measurements one can make with these films is directly measuring their potential for rectification in DC and AC systems.

8.1 Film Measurements

We will start this discussion with a review of the most common methods used in analysis for alkanethiol films. These largely center on the surface morphology and binding energy of the samples. While this research group does not have access to all desired equipment, XPS (X-Ray Photoelectron Spectroscopy) studies have been used to glean much useful data on aging, surface coverage, application technique comparison, and more [78, 166, 280, 281].

8.1.1 Atomic Force Microscopy

The atomic force microscope (AFM) is a tool used in metrology labs which is capable of achieving atomic resolution. The AFM is a relatively new tool which compact and inexpensive compared to instruments like SEMs and TEMs. An image is generated by scanning a nano-sharpened probe over the sample surface. Besides imaging surface imaging, the AFM can be

used to measure magnetic fields, determine material hardness, perform electrical measurements, and much more.

At the heart of the microscope is a complex piezo scan head which is used to scan the tip across the sample. The piezo was chosen for this application because with accurate digital to analog converters, it can be controlled with great precision. The AFM tip is a micromachined slab of silicon which has a sharpened tip on the end of a thin cantilever (Figure 8.1). These tips are sometimes adorned with carbon nanotubes or sharpened in an FIB to achieve even greater resolution.

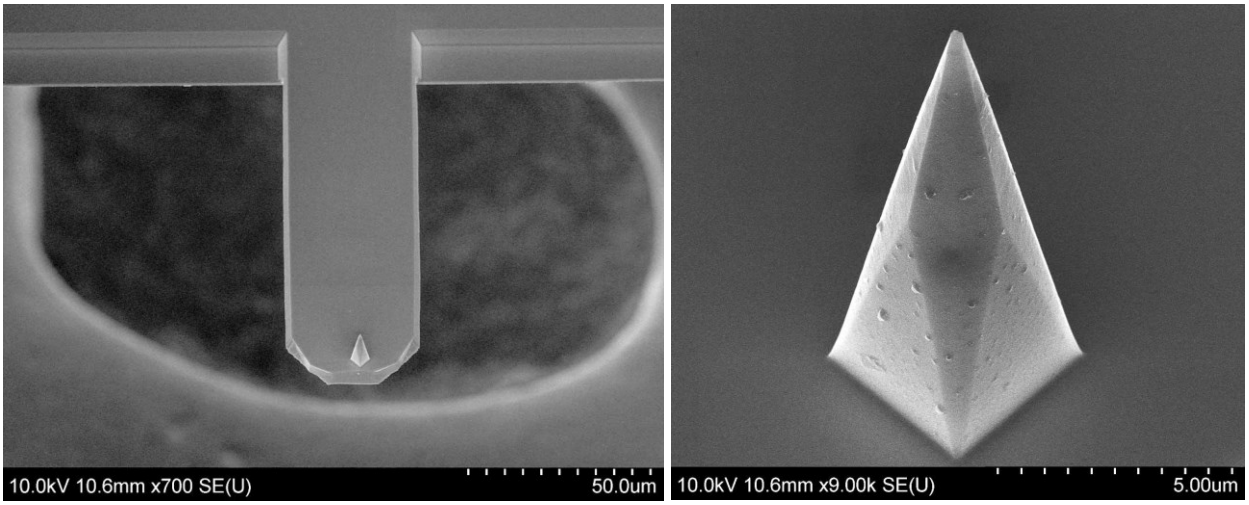

Figure 8.1: A set of SEM images depicting an AFM cantilever and tip. The AFM tip seen at the right is visibly dulled due to collisions with the sample.

While the tip is scanned across the surface, a laser is bounced off the back of the cantilever which bends according to the contour of the sample. A detector captures the returned laser signal and software processes this along with the piezo state to compose an image. Because the degree of flexure in the AFM cantilever is measured, very accurate z-direction measurements can be made in addition to scan plane, X-Y measurements. The AFM is prized for this data-rich image output as most software packages are able to produce a 3D reconstruction of the scanned

surface. The principle of operation just described is called contact mode. An alternative mode which is less damaging to the surface is called tapping mode. In tapping mode, the AFM cantilever is vibrated using the piezo and brought near the sample surface. Before the AFM tip comes into contact with the sample, the electrons of both the tip and the sample begin to interact and the characteristic vibration frequency is detuned slightly. This change in vibrational frequency is measured and the sample location is inferred. In theory, this scanning method is able to resolve the surface features without ever coming in contact with the sample. It is the experience of all operators that the tip does indeed strike the surface and dulls over time even when used in tapping mode.

8.1.2 Impedance Spectroscopy

Impedance spectroscopy (also known as dielectric spectroscopy) is the study of electrical signals through a dielectric in the frequency domain. With several decades of frequency sweep, a good characterization of the film can be made. For the purposes of film thickness measurements, Cui et Al. [173] have described a technique which was followed as described for SAM film analysis. Others have also described similar methods for dielectric measurement which can be employed for varying situations [282].

Below in Figure 8.2, we see the Cole-Cole plot (left) which varying concentrations of Ferrocyanide solution. From the cyclic scans, we are able to use the model presented:

$$m = \left((nF)^2 \frac{k_s}{RT}\right) \mathrm{c} \cdot \exp(-\beta d) \tag{8.1}$$

where m is the slope of the line from Figure 8.2 (right), F is Faraday's constant, T is ambient temperature in Kelvin, n = 1, d is the film thickness, k_s is the electron transfer ratio for the substrate (0.026), c is the concentration of the redox species, and β is the electronic tunneling

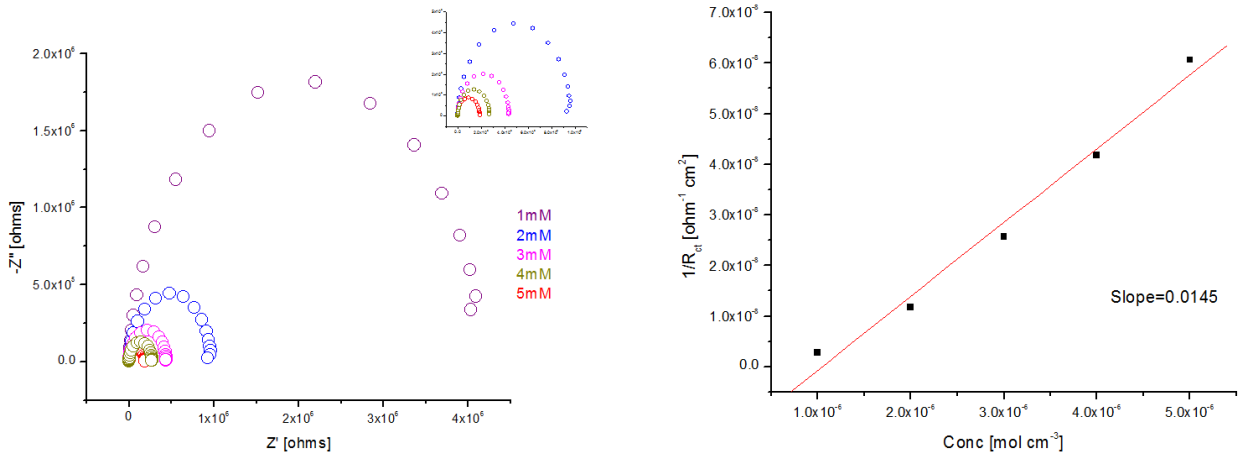

Figure 8.2: A Cole-Cole and slope plot resulting from impedance spectroscopy to determine SAM film thickness.

coefficient (1.02/CH_2). Plugging in these values, we get a film thickness for dodecanethiol of 1.54 nm. Using an open source molecular modeling software called ArgusLab, a simulation predicted a chain length for the dodecanethiol molecule of 1.72 nm. Investigators have established a non-zero contact angle for this SAM on gold substrate. From literature, the contact angle is 28° [103]. A simple cosine transformation results in a bulk film thickness (measured normal to the surface) of 1.52 nm. The experimental value varies only 1.3% from the expected value. Small variations due to film imperfections and measurement error are the likely sources of the small variance. A close match in experimental and simulated film thickness validates the SAM assembly process and demonstrates that a well packed film is being formed. Since impedance spectroscopy measures apparent film thickness, it is a good measure of SAM quality and surface coverage.

8.1.3 Contact Angle

Contact angle measurement is a fast optical analysis performed to determine the wettability of a surface. The setup is relatively straightforward and consists of a macro camera,

syringe, adjustable stage, and analysis software. After calibration with a standardized SiC ball bearing, the camera is capable of recording the shape of the water droplet on the surface of the unknown sample. Through software processing, the volume of water, surface tension of the liquid, and contact angle with respect to the surface can be calculated. A high contact angle implies a hydrophobic material where the minimum liquid contact area is desired. Superhydrophobic materials have been demonstrated using SAMs and highly roughened assembly surface [283]. The shape of the droplet on the surface under the force of gravity can be modeled by Young's Equation. Because the contact angle depends on two interface energies (that of gas to liquid and liquid to solid), very pure liquids should be utilized. The equation is:

$$\gamma_{sg} - \gamma_{sl} - \gamma_{lg}Cos(\theta) = 0 \tag{8.2}$$

where γ is the interfacial energy of solid-gas (sg), solid liquid (sl), and liquid-gas (lg) [284].

Contact angle measurements can confirm the presence of surface contamination on an assembly surface. Adventitious hydrocarbons are ubiquitous in our atmosphere and will coat almost all free surfaces [262]. In figure 8.3, we can see that even the relatively short 24-hour period following deposition resulted in hydrocarbon surface contamination. The problem is especially present in highly humid environments (such as those found in Florida) and where samples are carried in between the climate conditioned environments of buildings. Contact angle responds by increasing due to hydrocarbons being more hydrophobic than the bare metal surface. As touched upon earlier, the remedy for this problem is surface cleaning just prior to SAM assembly. A harsh treatment by liquid chemical processing (such as a short piranha etch) will work but can damage the assembly surface. Instead, most opt to perform an O_2 plasma ashing. Where possible, this treatment was performed at 50W for 300s. The flowrate of O_2 in the Tegal Plasmaline 415 asher was 200 sccm at a pressure of 90 mTorr. For situations where this more

expensive equipment is not available, a UVO cleaner functions similarly albeit much slower. A full description of critical surface cleaning is presented in Section 7.3.1. The minor PVD portion of the cleaning process can roughen the surface at higher RF power. Studies have demonstrated significant surface morphology changes for more corrosive materials [285]. Despite not being as subject for surface reordering, the minimum exposure possible time should be used for cleaning. Binding energy of the thiolate species onto a noble metal surface is very high. This preferential surface species will displace most contamination left on the assembly surface [286]. Prior cleaning ensures faster assembly with fewer grain boundaries causes by assembly redirection.

In Figure 8.4, we can see the varying hydrophobicity of different SAMs assembled onto gold surfaces. The fluorinated tail of 1H, 1H, 2H, 2H-Perfluorodecanethiol (PFDT) responds to surface water in a manner similar to that of bulk Teflon. This coating can be used to reduce friction in MEMS components or reduce the rate of corrosion of the underlying metal (if the metal is not intrinsically chemical resistant). For cases where wetting is desired, an alcohol or acid terminated SAM will offer superior wetting.

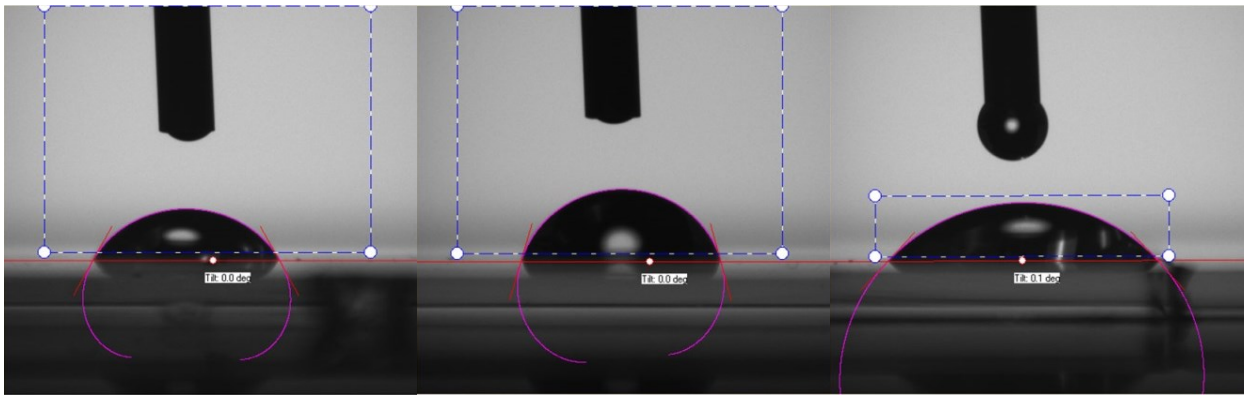

Figure 8.3: A software processed photograph depicting the contact angle of a gold surface over time and after cleaning. The first image was captured less than 24 hours after an e-beam evaporated gold deposition revealing a contact angle of 61.21°. The second image was captured after 1 month being stored in a wafer carrier in a laboratory environment: 74.56° contact angle. The last image in the panel was captured less than 100s after 10 minutes of UVO treatment: 47.19° contact angle.

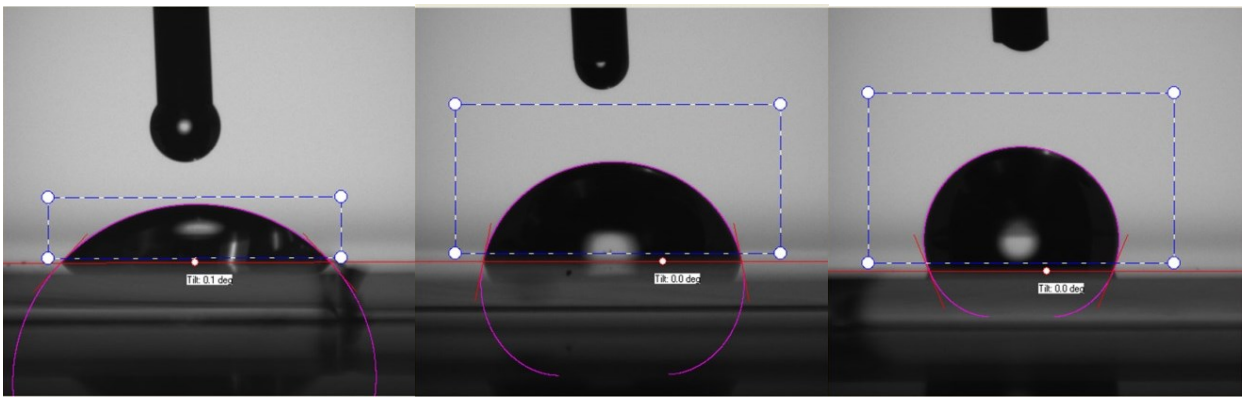

Figure 8.4: A software processed photograph of the contact angles of freshly cleaned bare gold, 1,6-hexanethiol, and 1H, 1H, 2H, 2H-Perfluorodecanethiol (PFDT). The contact angles measured are 47.19°, 78.45°, and 111.84°, respectively.

8.2 DC Electrical Characterization

A basic test often reported as a real-world characteristic is the IV sweep. In this research, we have used this method of characterization extensively because it involves a relatively easy setup and can be carried out quickly. Despite the easy setup, there are a number of concerns which make acquisition of meaningful and quality data challenging. Guidelines have been developed for an optimized probing setup and are described in the following section.

8.2.1 Small Signal Noise Mitigation

Due to the small contact areas and relative inefficiency of quantum tunneling (as compared to silicon-based rectifiers), measured current during testing is often very low. Most devices produce IV current ranging from 10^{-10} to 10^{-6}A. At this range, measurement is occurring close to the noise floor of the instrument and signals are easily perturbed. Unshielded wires couple signal from radio waves readily and nearby transmitters can results in a measurement being swamped. The importance of low noise measurements should be clear: not only does

lower noise produce more reliable and quality data, it also unlocks details which could have previously been masked.

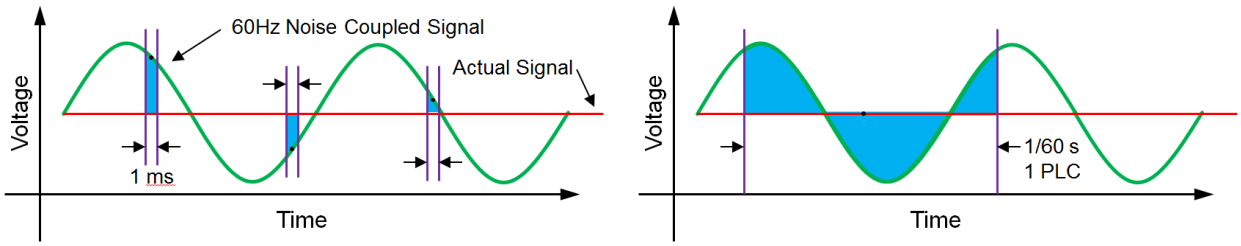

Figure 8.5: An illustration of measurement instrument integration and how accuracy is impacted. At left, short integration times result in capture of line AC coupled noise. At right, by choosing an integration time of greater than or equal to 1 power line cycle (PLC), the cyclic noise is averaged and the correct value is recorded.

The following guidelines were developed to improve signal quality. (1) Install RFI filters on test equipment in use. Ground noise is a common problem on test benches. Many lower-end test pieces have references directly tied to ground which causes traces of any noise which might be found on this line. (2) When acquiring data points slowly such as on a parameter analyzer or source meter, be sure the number of integrations is above unity. Many manufacturers list these integration values as NPLC (Number of Power Line Cycles). In the US, this means that a 1 NPLC measurement will take $1/60^{th}$ of a second—thus allowing the full AC power sine wave to pass and hopefully average out repetitive cycle noise. Integrations at this scale can only hope to filter repetitive noise while higher values can suppress transients and other power anomalies. (3) Reduce vibration in your test setup. Vibrations affect test setup and instruments in a number of ways. Test equipment contains many parts, mainly capacitors, whose performance are greatly affected by vibration. Dampening chassis noise generated by nearby equipment or a case fan can be as simple as installing the equipment on rubber mounts or on a padded conductive foam board. If probing is occurring, a vibration isolation table or similar high

mass on floating mount setup is highly recommended. Unstable contacts were discovered to be the root cause of an entire batch of devices being deemed flawed. The source of the vibration was a nearby fume hood whose fan motor was off balance. (4) Use shielded wire lengths where possible. There are many exotic sense-correct insulation setups which can be employed to reduce noise for work into the lower nanoamp-range. Insulation of the leads prevents radio wave coupling and is usually satisfactory for basic testing. Where possible, a heavy metal hood/box can be sourced to enclose the entire setup. (5) Turn off as many nearby electronic devices. We often forget that we carry radio transmitters in our pockets which can generate up to 0.6W of transmitted RF power [287]. Fluorescent lights, especially those powered by older magnetic ballasts, can be the source of tremendous noise and interference. (6) Accommodate for test leads in basic circuit model design. Test leads can contribute significant impedance, capacitance, and resistance to a test setup. It is important to consider these parasitic elements in formulation of a small-signal circuit model. (7) Select appropriate test leads, equipment, and complementary components. A detailed analysis of a curious device response is presented in Appendix C. This analysis outlines the true origin of a "clipper" effect which was previously reported as an intrinsic device characteristic. Below (Table 8.1) is a table outlining the basic selection parameters of an appropriate current sense diode.

Table 8.1: A comparison of sense resistor values and the resultant performance in test.

	Low Resistor Value	**High Resistor Value**
DUT Current	Diode limited current	Supply limited current
Voltage Output	Low signal to measure	High signal to measure
Noise Immunity	Moderate	Low
Parasitic Immunity	High	Low
Tightness of Traced Curve	Good	Poor
Frequency Limits	Low	High

8.2.2 Current-Voltage Performance

Curve tracing was carried out on one of two instruments: a Keithley Model 2400 SourceMeter and an HP 4145 Semiconductor Parameter Analyzer. This test equipment sourced a particular voltage and read back the voltage and current (amperage) across the DUT (Device Under Test). The software used to acquire the data on the Keithley 2400 was either the vendor distributed "LabTracer" or a custom LabView written script which offers additional flexibility. Analysis and plotting was done in Matlab and Microsoft Excel. The Keithley has a current measurement granularity of 10 pA with an accuracy of 0.029%. Where possible, the measurements were made a minimum of 3 orders of magnitude above this noise floor. As described in the fabrication section, all inorganic MIM diodes fabricated were of Ni-NiO_x-Cr composition. The I(V) performance was improved from prior fabricated devices primarily through the reduction of contact dimensions and the conditioning of metal side-walls.

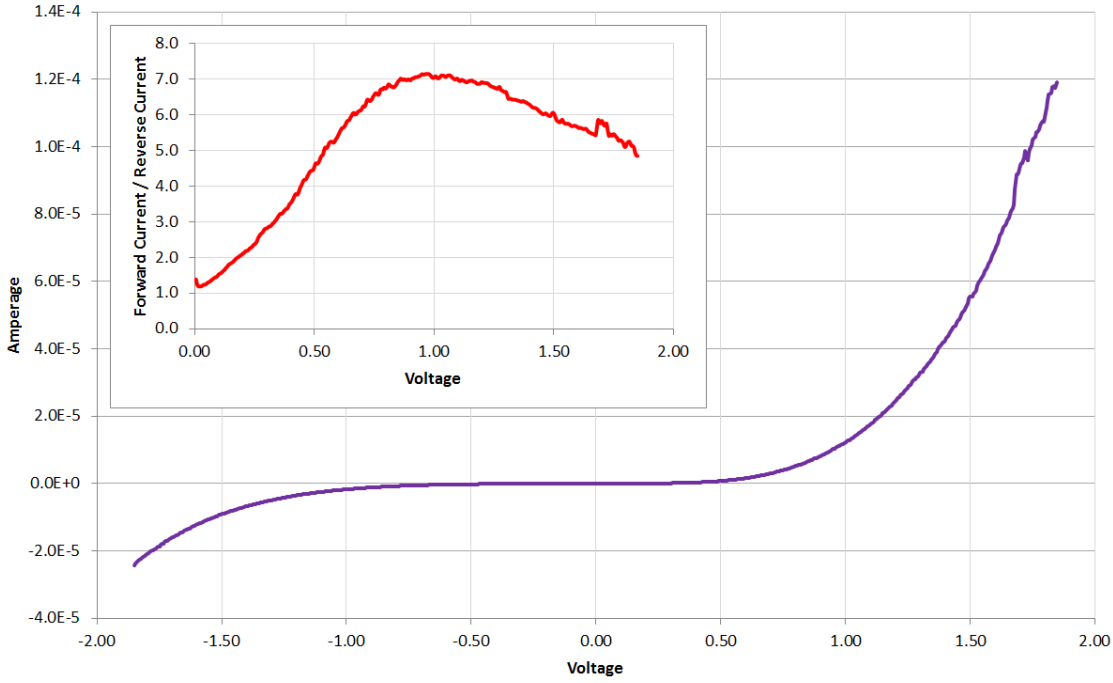

Figure 8.6: The I(V) characteristics and rectification ratio (inset) of a 0.25 μm^2 Ni-NiOx-Cr diode tested to near breakdown. Optimal operating voltage should not exceed 1 V.

Figure 8.6 plots the rectification ratio of a 500 x 500nm diode with a peak value of 7:1 occurring at around 0.95V. It is important to note the very soft inflection present on this I(V) curve. A small AC amplitude signal, even if biased, would not be well rectified by this type of diode. This performance was not typical of junctions. Due to process variation, the curve depicted in Figure 8.7 more accurately depicts the challenges of the inorganic diode junction.

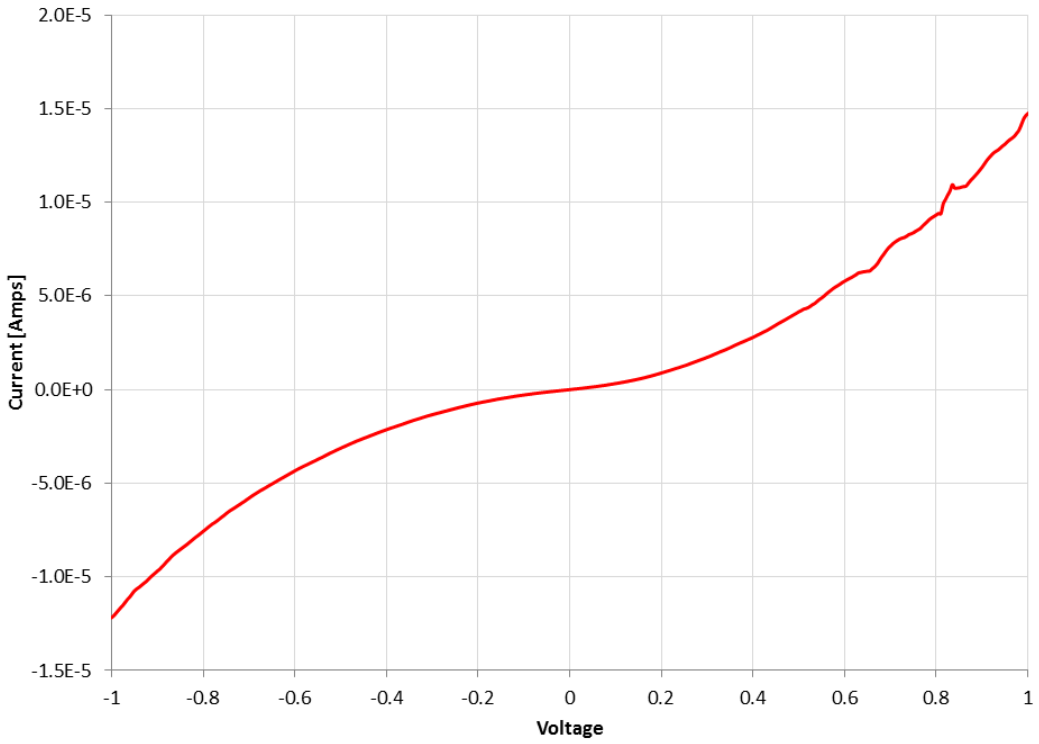

Figure 8.7: The I(V) characteristics of a typical Ni-NiOx-Cr diode tested to 1 V. Performance variations are largely due to process inconsistencies during sputtering.

Below in Figure 8.8, we see a similar diode being tested to failure. The plot begins at the center and expands until the device begins to experience breakdown. The relatively high current flux results in an open circuit failure due to electromigration at the junction edge sites. This was demonstrated in an SEM study seen in Figure 7.4B. Artifacts in the negative region of the plot are due to a lack of sweep delays being programmed in between cycles.

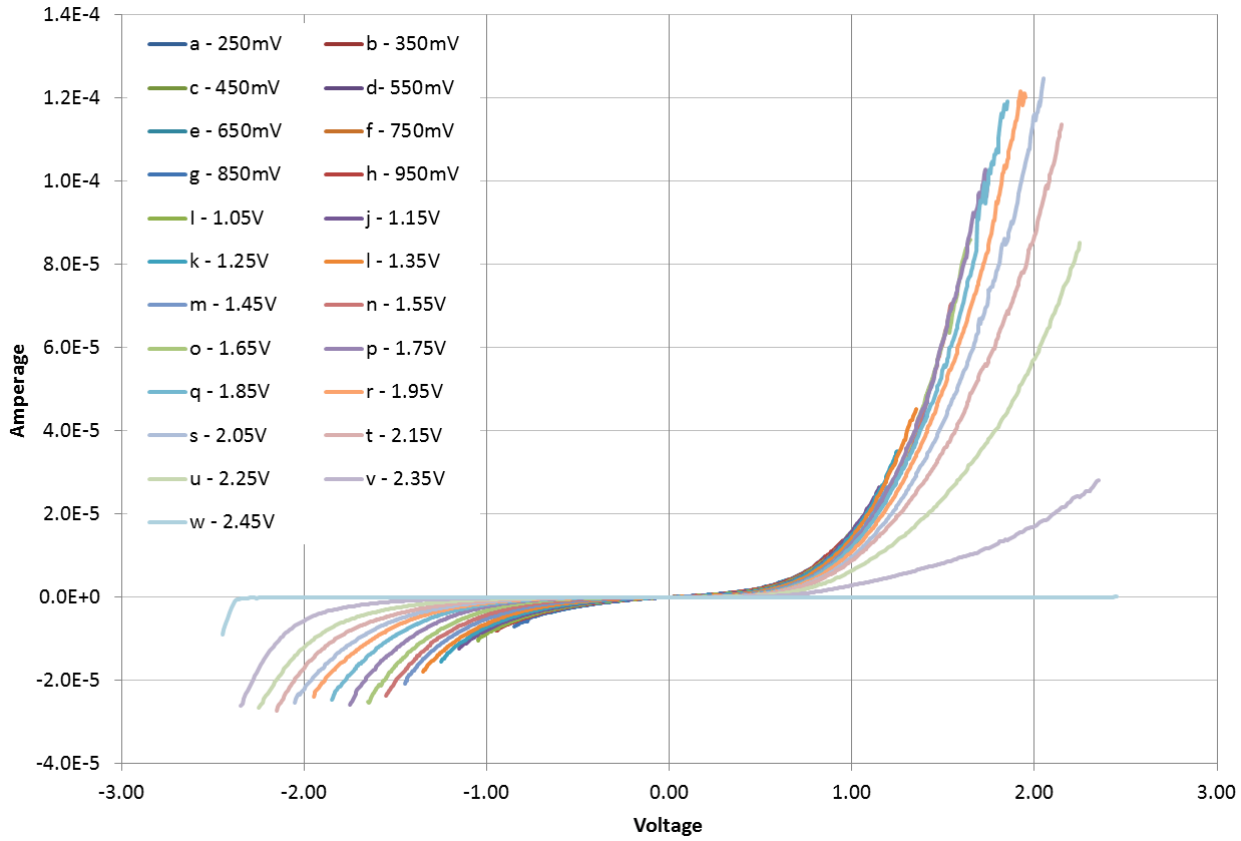

Figure 8.8: A parametric voltage study of 0.25 μm2 Ni-NiOx-Cr diodes tested to breakdown. Voltage sweeps begin at 250 mV and increase in 100 mV increments until breakdown begins to occur—here starting at 1.85V. As further voltage is applied, current handling is reduced until an open circuit failure occurs.

The primary thrust of this work focused on the performance of MIM tunnel junctions through organic self-assembled monolayers. Many of the monolayers were first experimentally probed by the liquid metal contact system described above. This gallium metal contact has a native oxide layer which varies in thickness depending on environmental conditions and exposure time to the atmosphere. Characterization of the baseline effects of the inorganic insulator were the first order of business. In Figure 8.9, we see that the dissimilar metals, gallium and gold, surrounding the GaO_x insulator and result in a mild asymmetry in the I(V) characteristics. The rectification ratio (RR) of these junctions varies between 2 and 4 at 1 V. For

further measurements presented, this baseline is not subtracted from the presented results. One should bear in mind that any results on the order or single digit RR may be insignificant.

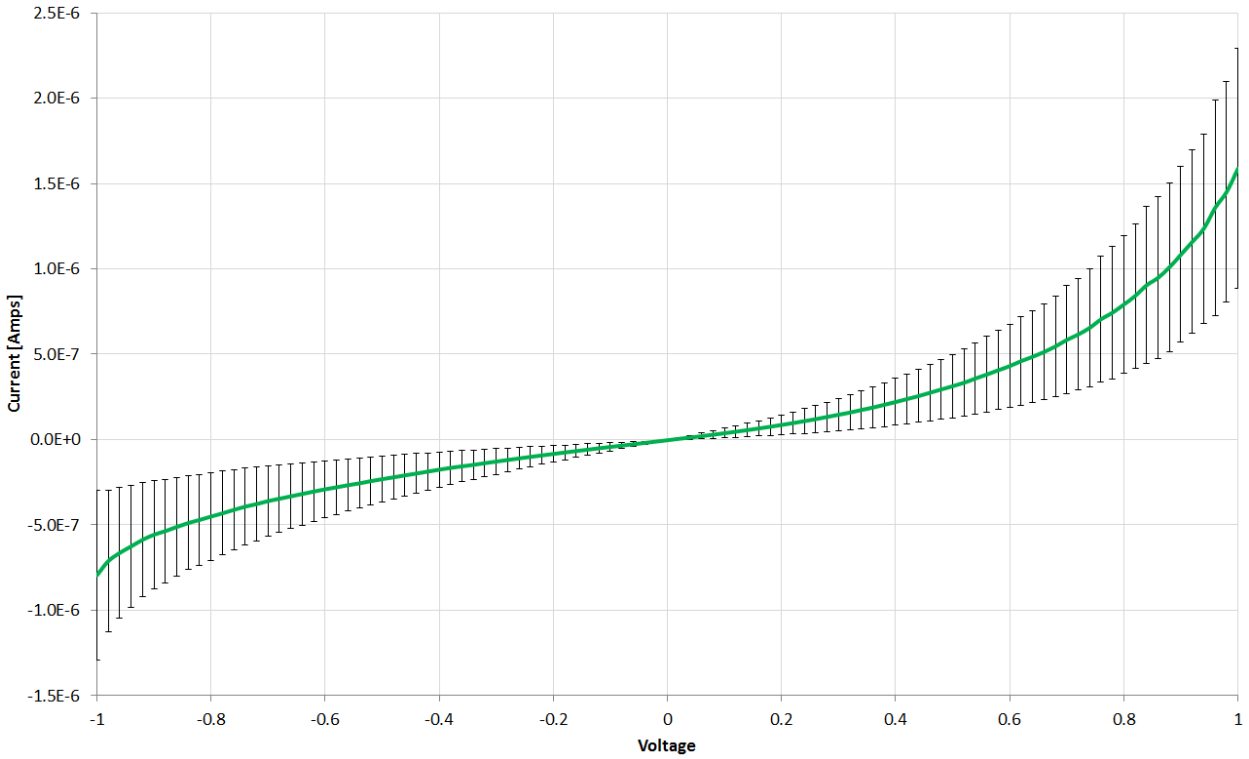

Figure 8.9: A plot depicting the variance of IV characteristics from Au-GaOx-Ga junctions during gallium probing. Data depicts average current normalized to correct for slight variations in contact area. The native oxide thickness variation is the source of the large variability and results in a baseline rectification ratio of 2 to 4 at 1 Vac.

The first monolayers tested were straight chain aliphatic molecules which resulted in tunneling performance very similar to that of the inorganic diodes seen above. A commonly reported molecule is dodecanehtiol. This molecule was well characterized by impedance spectroscopy and electrical measurement using inkjet top contact yielded a very symmetrical I(V) response (Figure 8.10). The diodes which formed the most consistent junctions which were sufficiently asymmetric for rectification applications were those with a 1H, 1H, 2H, 2H-Perfluorodecanethiol monolayer. This monolayer is highly polarized due to the strong

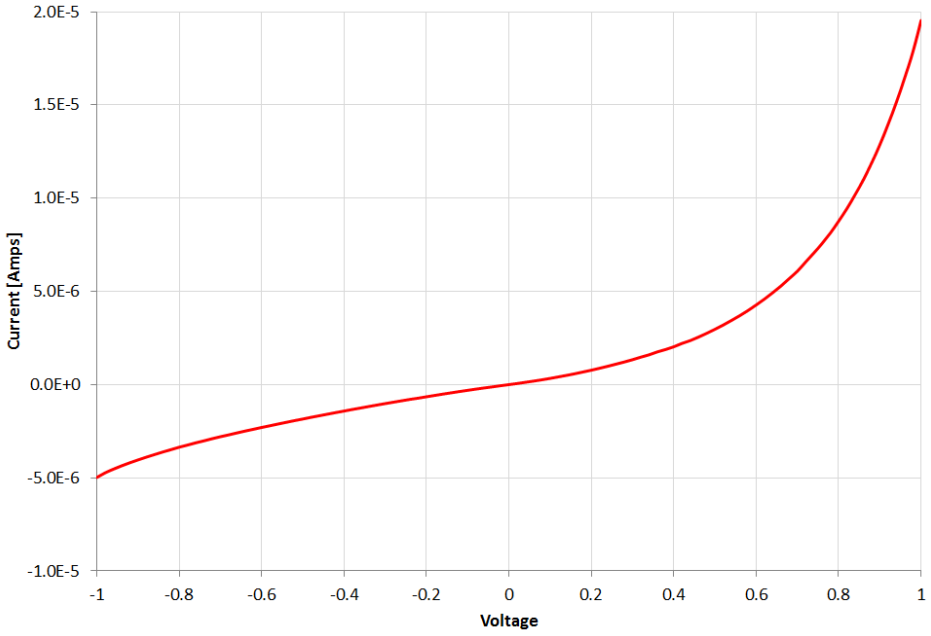

Figure 8.10: A graph of the I(V) characteristics of a Dodecanethiol MIM junction probed by printed conductive traces.

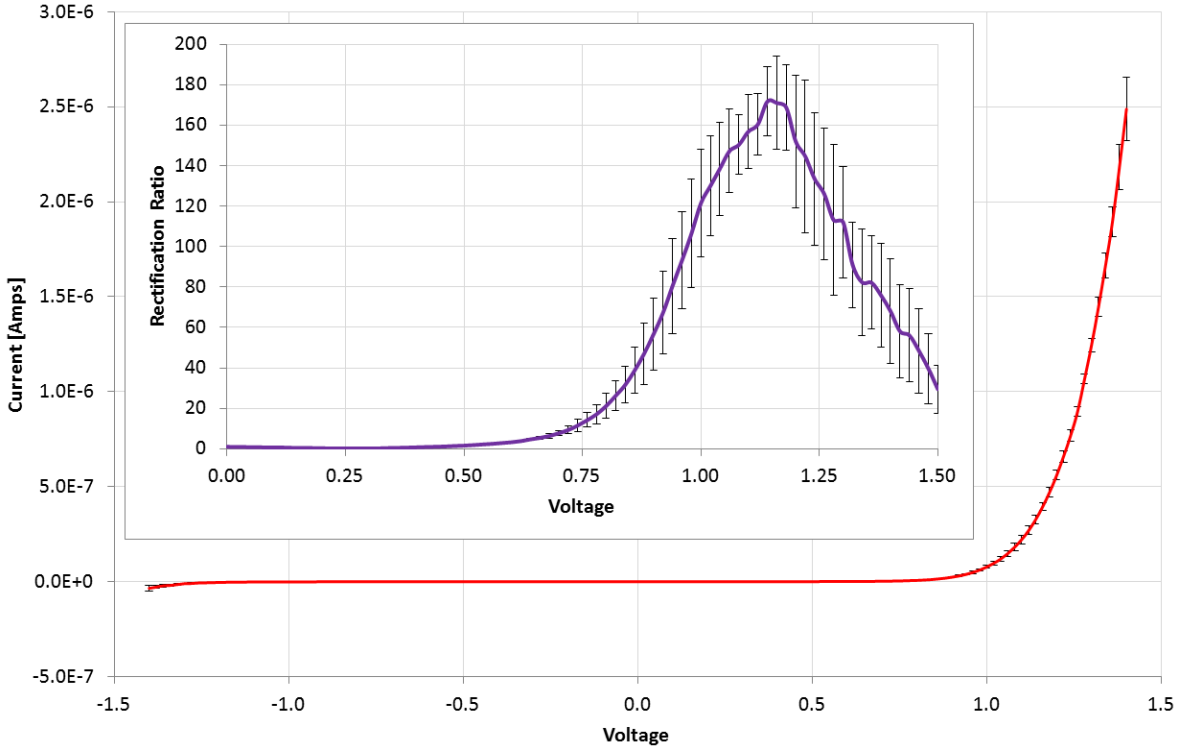

Figure 8.11: A graph of the rectification ratio (inset) and I(V) characteristics of a PFDT-Gallium Oxide junction. This combination resulted in stable, high asymmetry with moderate current handling.

presence of fluorine in the tail section. This electronegative atom affects the Fermi level of the adjoining metal and co-insulator, gallium oxide. For the best performance devices, rectification ratios in excess of 170 were observed at an optimal operating voltage of 1.12 V (Figure 8.11). Also of interest was the very tight consistency of the I(V) sweeps. There is clearly a change in operating regime as the diode is biased to above 1.12 V when noise and inconsistency are recorded in the measurement. Despite these impressive characteristics, the diode still requires a fairly high forward operating voltage to exhibit good conduction. The resistance is still high due to MIIM structure.

A direct comparison was desired between organic and inorganic dielectric-based tunnel diodes. In Figure 8.12, we clearly see more diodic behavior in the organic diode. Reverse current leakage is significantly lower and "turn-on" inflection is sharper. These measurements on the PFDT SAM were made directly using a soft contact measurement technique and represent a more realist performance characteristic than that demonstrated in the temporary junction of Figure 8.9.

Diodes utilizing THPP as insulators performed very well in terms of asymmetry. The molecule and performance characteristics are seen in Figure 8.13. The film casting method produced an exceptionally thick film and therefore resistance was very high and the point of inflection "the knee" occurred at a very high voltage (around 2.1V). A rectification ratio of 54:1 was realized at the peak applied voltage of 3.0V. Spin casting resulted in greater inconsistencies than organic self-assembly methods and so film thickness and breakdown voltage varied. This high voltage operation is most certainly in the Fowler-Nordheim tunneling regime. The diodes, when connected in the same manner as other test structures, demonstrated a reverse current conduction rather than a forward current conduction.

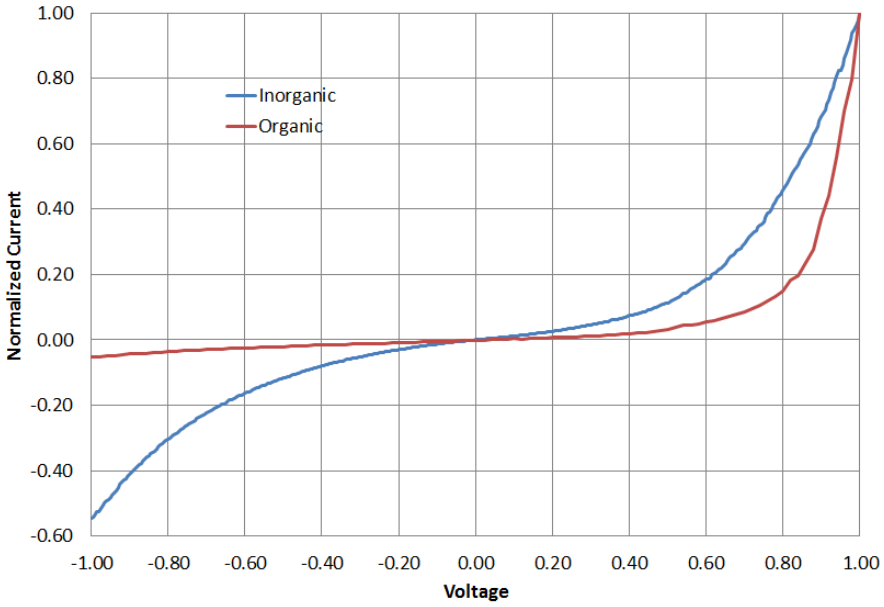

Figure 8.12: A comparison of IV performance between an organic (PFDT) and inorganic (Ni-NiOx-Cr) diodes with normalized current.

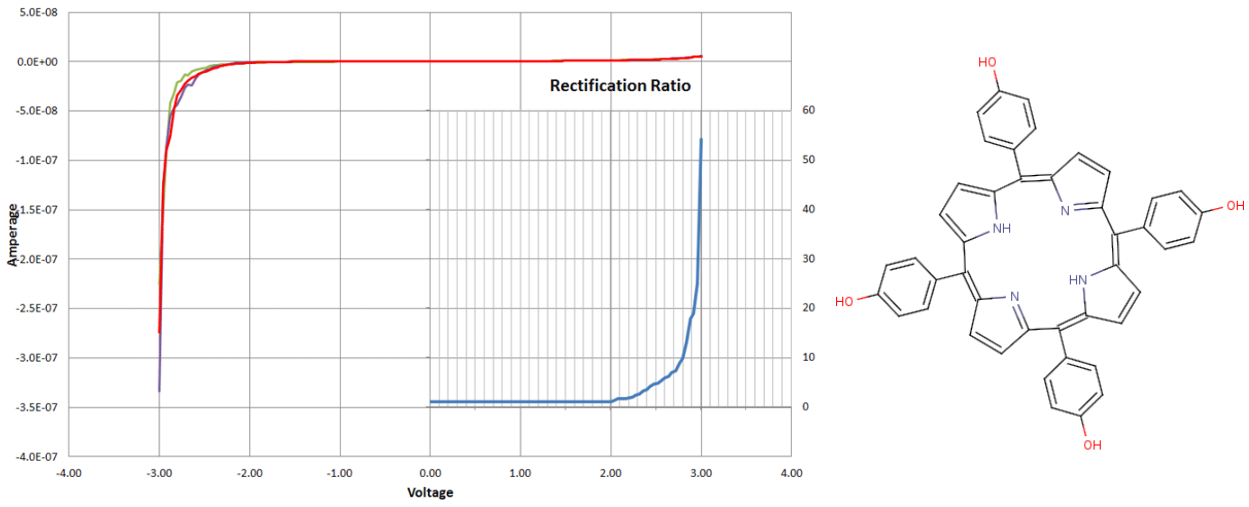

Figure 8.13: An IV curve demonstrating highly asymmetric, diodic response in Porphyrin insulators.

In further experiments using THPP, C_{60} Fullerene was dispersed in the polymer solution to be cast. The same procedure used to produce the above film was carried out. The result was the formation of a light sensitive junction where photon assisted tunneling (PAT) occurs.

Photoconduction has been demonstrated in C_{60} films but it was not known whether or not these properties could be mixed with the asymmetric rectification characteristics of baseline THPP [288]. In Figure 8.14, the gain is computed as the quotient of the two I(V) traces. A significant photoconduction activation event is occurring at 750mV. Because of the intrinsic asymmetry of the THPP molecule, this is largely masked in the forward conduction sweep but clearly seen as a spike in the reverse current sweep. If we use the photon voltage Equation 2.8 originally presented in Section 2.3.3, we find this voltage to correspond to a frequency of 1.139×10^{15} Hz. This frequency corresponds to the UV spectrum at 263.1 nm. Curiously, this is very close to the mercury emission lines present in many fluorescent lighting installations around that wavelength (intensities of 1000, 25, and 40 at 253.6, 265.2, and 265.3nm, respectively). Furthermore, if we examine the UV spectra of C_{60} Fullerene, we find that there is a very strong absorption peak around 262 to 265nm.

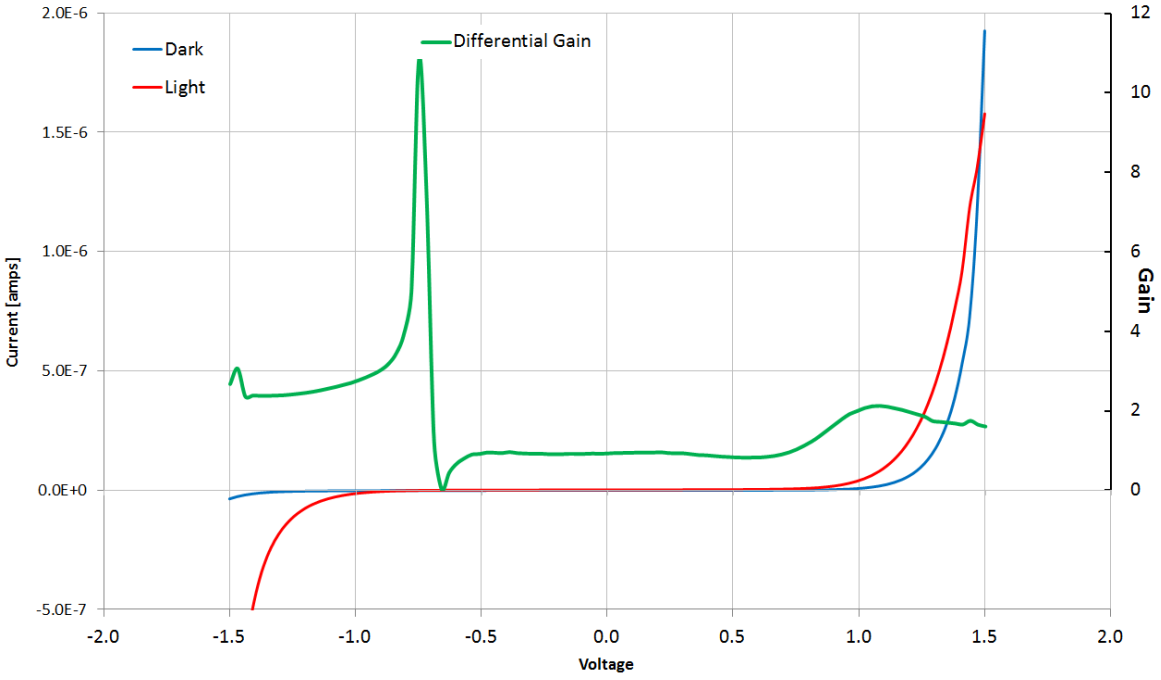

Figure 8.14: A plot highlighting hybrid photoconduction and rectification in Poly-THPP insulator with C60 dispersion.

The curcumin-based junction was created using a relatively thick, spun-on film. The films conducted very suddenly and strongly at 0.32 V forward current (Figure 8.15). At this relatively low voltage, the physical structure of the diode changed and the response changed from insulator-like to resistor-like. Testing multiple junctions revealed very reliable breakdown in this voltage range. While not applicable for rectification, this junction has many applications in ROM and perhaps other memory devices. The attractive quality of this ROM memory cell is the very low read and write voltage necessary for operation.

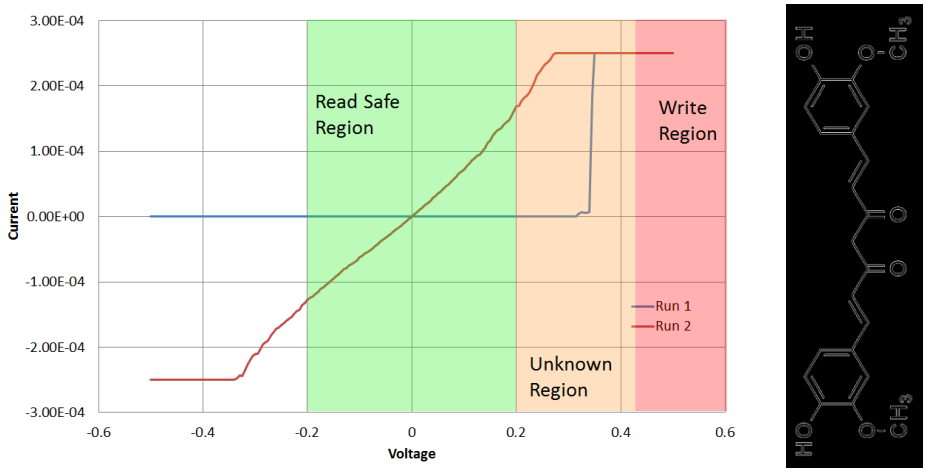

Figure 8.15: The two cycle IV plot of a ROM element based on a curcumin natural organic film diode. The data storage element is remarkably low-power exhibiting high isolation until a breakdown event just over 320mV.

8.3 AC and RF Performance

Testing in the AC domain presents a number of challenges for the more bulky junction setups seen in the body of this work. Frequency limitations of test setups and measurement artifacts are covered in Appendix C. AC measurements were carried out using a function generator and digital storage oscilloscope. The applied AC voltage was split with one terminal being monitored with the oscilloscope while the other was wired to the diode. On the low-side of the diode connection to ground, a current sense resistor was added per the guidelines

described in Section 8.2.1. Assuming an infinitesimally low turn-on voltage, the effect of reverse current leakage on efficiency is depicted in Figure 8.16. Voltage was gradually ramped and constant frequency to witness the turn-on effect of the sine wave from a state of non-conduction (Figure 8.17). Also, variable frequencies studies were performed (Figure 8.18) up to 20MHz. At the upper frequency, only certain types of junctions could be probed—specifically, those with very small contact areas on the order of single microns in size. In the later subsets of Figure 8.18, we see the beginning of distortion on the measured waveform.

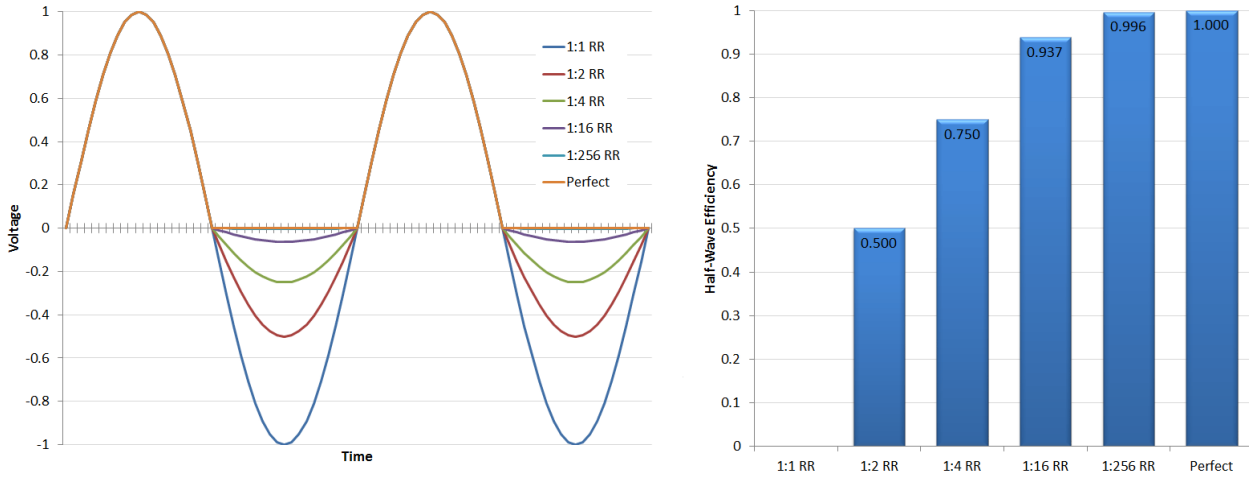

Figure 8.16: An illustration of the effect of reverse current leakage on rectification efficiency for a half-wave rectifier.

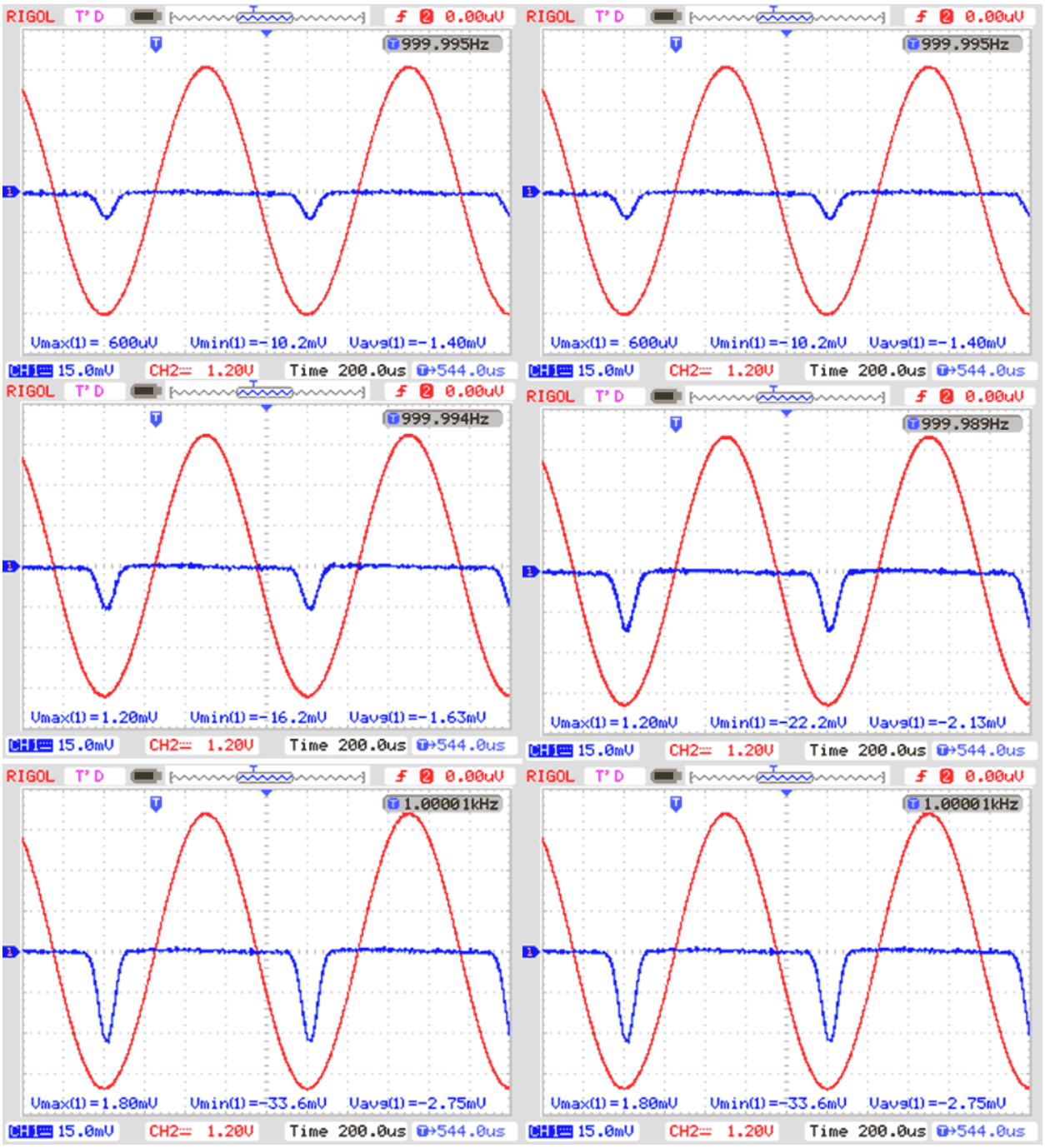

Figure 8.17: A parametric AC study of organic diode turn-on response under constant frequency while ramping amplitude.

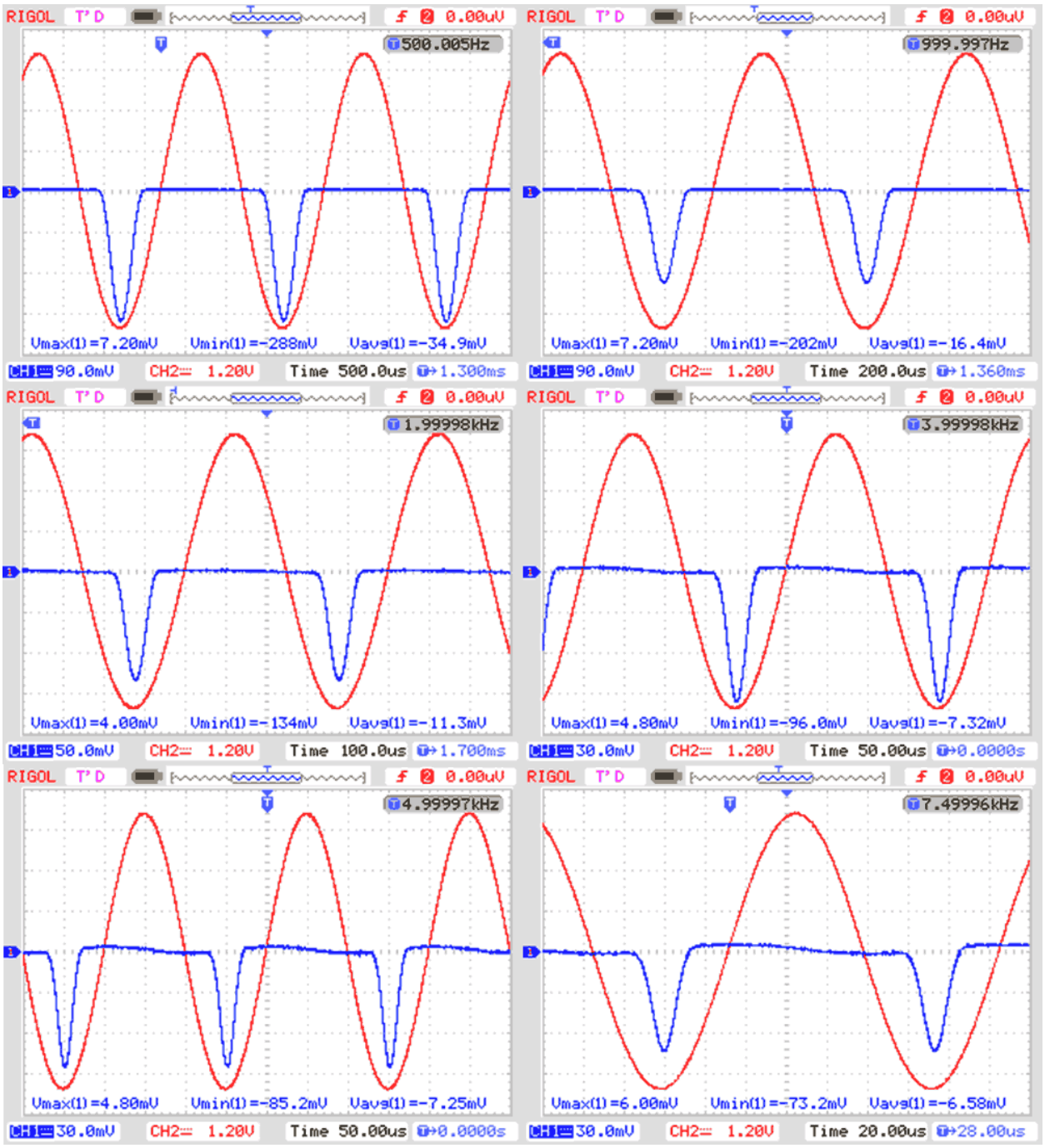

Figure 8.18: A parametric AC study of organic diode response to constant amplitude, sweeping frequency. Higher frequency testing was plagued by parasitics in the test setup.

8.4 Discussion of Experiments

It is clear that organic dielectric diodes provide better performance and greater design flexibility as compared to their inorganic counterparts. The best performance was seen for hybrid (organic-inorganic) MIIM diodes with PFDT as the organic dielectric. With the relatively high turn-on voltages seen in many of the most successful rectifiers, we should clearly explain the limitations of using such a device in a harvesting application. In Figure 8.19, we see the incident wave (blue) and response signal (red). The shaded blue region represents energy lost due the forward or reverse conduction not being significant. This contributes greatly to diode resistance. Furthermore, the red shaded region represents reverse leakage. To determine rectifier efficiency, we must subtract the area of the red shaded region from the green shaded region. This value over the integral of one incident wave cycle is the rectifier efficiency.

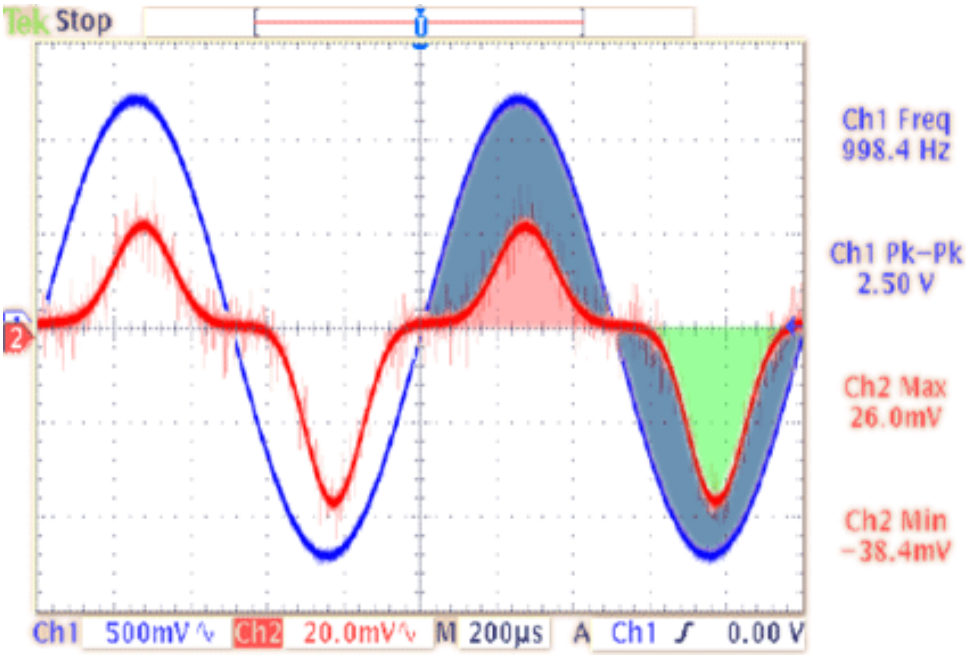

Figure 8.19: The AC frequency response of a somewhat symmetrical MIM diode. The region shaded dark blue represents energy lost due to high turn-on voltage. The region shaded in red is energy drained due to reverse bias leakage. The green shaded region is forward current energy transmitted.

CHAPTER 9:

APPLICATIONS

The applications pertaining to this research can be broken up into two major subheadings of basic science and end product. It is important to first delineate these as it does not feel appropriate to describe a fabrication benefit next to a human benefit. That said, the applications for this research pertain strongly to the master project application of a rectifier. Because the detailed basic science applications of monolayer was described in context as appropriate throughout the body of this work, here, we will focus primarily on the end-consumer applications of monolayers incorporated into systems.

9.1 Energy Harvesting

In many industrial scenarios, it is desirable to harvest power from ambient heat or stray RF energy rather than mechanical sources. There has been work carried out in thermoelectric power (TEP) at the micro [289] and nano [290] scales. Rectenna (rectifying antenna) arrays [291] have been proposed for broad band energy harvesting as well, however, the efficiency of these systems still trails behind competing TEP technologies [36, 292]. Systems have been implemented which successfully coupled RF energy with an antenna, matched impedance, rectified signal and performed final signal conditioning [293, 294]. These on-chip solutions are still limited to just over the single gigahertz frequencies. Parasitic capacitance and resistance in the THF-range hinder easy improvements. A successful rectenna system requires a very high

speed rectifier (diode) to minimize losses. When first demonstrated by Brown [12], a Schottky diode was used to rectify microwave energy in a functional demo. While the Schottky diode is free of carrier recombination delays, there are still real-world frequency limitations which prevent its use in the desired THz range. It is for this reason that quantum tunneling is such an attractive phenomenon to exploit for rectification. One option to improve efficiency is the use of a radiation collector-emitter which absorbs high frequency solar energy and reradiates the energy onto the rectenna at a lower frequency (Figure 9.1).

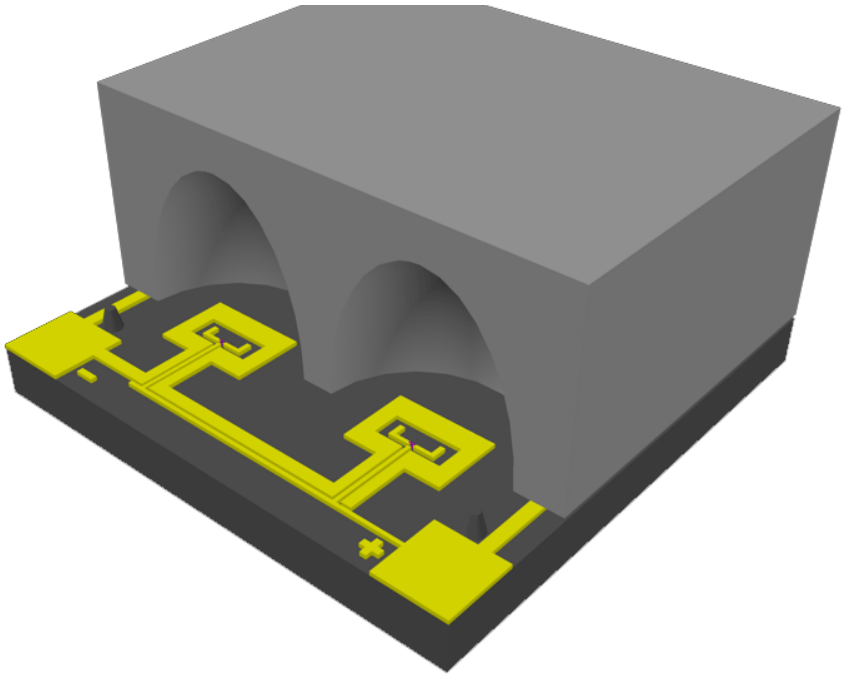

Figure 9.1: A conceptual rendering of an emitter-concentrator atop a rectenna array. This setup improves the efficiency of the rectenna array by re-emitting a more monochromatic energy which is concentrated.

At much lower frequencies, this system is well proven and has been demonstrated for efficient wireless energy transmission and harvesting [295, 296]. The transition to frequencies much above the single GHz proves non-trivial as dielectric dispersion and atomic interactions with the incident wave consumes harvestable energy. Ultimately, the dimensions of the rectifier

play a huge role in the performance at these frequencies; it follows that tunneling devices on the order of single molecules could be a possible solution.

9.2 Infrared Detectors and Imaging

Material identification from a standoff distance is desired for identification of security threats in sensitive areas. The ability to perform spectroscopic analysis through layers of concealment allows law enforcement to detect the presence of non-metallic materials which may not appear in metal detectors or millimeter wave (MMW) detectors [297]. The characteristic transmission and reflection spectra of many explosives are in the 0.5 – 10 THz range [298]. THz spectroscopy can also detect the presence of certain drugs which are commonly carried undetected by travelers due to their non-metallic, small, and flexible nature. In applications of long range imaging, the long IR region permits visibility through smoke, fog, and dust where visible light would be blocked. The microbolometer is a popular and well proven technology for detection. Bolometers respond to incident radiation by absorbing it, converting the energy into heat, and measuring the change in resistance of the warmed sensor element [299]. Limitations such as slow response time and wide spectrum sensitivity limit their use in high-speed and multi-spectral imaging systems [299, 300].

Terahertz sensing at discreet frequencies can also be accomplished by photonic [301] or rectenna systems [302]. Electro-optic imaging shifts the THz frequency energy into that which can be detected by conventional camera sensors [303]. This technique is capable of high speed response but has a lower dynamic range and sensitivity making study of naturally illuminated subjects (passive detection) difficult. Another popular approach is the use of antenna-coupled diodes (rectennas) for direct conversion of the electromagnetic energy for readout [302]. These

systems add additional capabilities such as directional detection, narrow frequency response, and nearly instantaneous speeds. The antenna coupled diode directly rectifies the incident signal and produces a DC output which can be read directly by support electronics. For long standoff range detection (a desirable quality for security applications), the attenuation due to water vapor continues to pose a challenge and requires illumination by specialized narrow-band sources [304]. These limitations currently prevent the creation of portable or handheld sensors based on this technology.

9.3 Medical and Diagnostic Imaging

In a similar manner to detection of concealed weapons, THz imaging can serve as an imaging technique for medical applications. The use of this frequency region serves a number of purposes and perhaps most appealing is the interaction of the waves with specific proteins of similar scale [305] and its non-ionizing, non-destructive nature [306, 307]. Tissue analysis can occur by transmission and tomography techniques (akin to X-Ray CT scanning) or reflectance techniques [306]. Studies have reported on the detection of cancerous tissue both ex vivo [308] and in vivo non-invasive [309, 310].

CHAPTER 10:

CONCLUSION AND FUTURE WORK

In this work, the goal of establishing a "toolkit" of techniques for fabrication and characterization of self-assembled monolayers for high frequency rectification has been completed. An extensive study was completed describing the feasibility and approach to the creation of a near-IR rectifier coupled rectenna.

10.1 Demonstrated Innovations

Through the course of this research, many innovations were required to achieve the desired goal of a reliable organic monolayer-based device. These innovations include the development of formulas of unique, work-up free insulating inkjet inks for the creation of low-temperature printable circuits. Because these inks require no work-up step, they can be processed simply and in one COTS (commercial, off-the-shelf) printer in one session. In addition, the problem of substrate roughness of the assembly layer was tacked in a number of manners. One of the techniques was the development of a low-cost, open-air annealing system. This system employs a PID controller and forces inert gas over the sample to reflow the surface structure in a controlled manner, minimizing vaporization of the thin film. By being open to air, cost savings were realized without compromising contamination resistance. In addition, future iterations of this system may be able to employ an optical roughness validation method which would allow live end-point measurements for this technique. Lastly, much work was done in the

development of directed nanoparticle deposition. Because nanoparticles offer a simple and non-damaging contact solution, they were highly sought after for the application of top contact on self-assembled monolayers. A process was developed which allowed metallic nanoparticles to plotted with low resolution onto insulting, flexible PET films [274]. This technique unlocks a low cost method of applying a conductive coating onto an insulating substrate of variable geometry. A shortcoming of this technique was plotting resolution and accuracy due to the insulating nature of the substrate. A more complex system was created from various disused consumer electronics which was capable of plotting thick nanoparticle films onto conductive substrates in any pattern. This was accomplished through an X-Y microcontroller driven stepper motor drive system which scanned a print electrode over the surface of the substrate which was submersed in a nanoparticle loaded solution.

10.2 Novel Studies and Structures

This project required an extensive review to be conducted on the current state-of-the-art in organic self-assembled monolayer-based rectifier structures. This was completed and unique conclusions were drawn which were published and will help lead the future research directions in this field. In the field of microfabrication, a variety of designs were evaluated, constructed, and tested for the purpose of efficient rectifier fabrication. A photolithographic process was developed which was compatible for use with self-assembled monolayer-patterned systems—typically, the UV exposure from photoresist processing causes extensive damage to the delicate monolayers. In addition, e-beam lithography and focus ion beam structures were devised and tested. Each of these techniques offered various advantages typically at the expense of increased cost of processing time. Extensive simulation of the efficacy of these techniques and possibility

of damage to the monolayers was presented. For data collection, a reliable and low-cost temporary top contact was desired to perform electrical tests on the monolayers. Unique experimentation using sub-cooled liquid gallium metal has never been reported in literature and has allowed for useful work-function calculations to be performed which relate the macroscopically observed IV performance to the theoretical quantum tunneling simulations.

10.3 Direction of Continued Work

Due to the deeply interdisciplinary nature of the master project, a successful rectenna system will likely be the result of many generations of graduate students each tackling specific areas of interest. Good modeling work has been done on emissivity and coatings for the emitter concentrator block of the proposed rectenna system [311]. Continuing down the process stack, the antenna element has been explored with both 2D and 3D solutions[36]. Work has been done on the development of 3D RF integration solutions which can permit greatly flexibility in rectenna design [312]. The rectifier element itself remains a challenging area of study. Further exploration into hybrid organic/inorganic insulating layers should yield improved rectification characteristics and reliability. Current experimentation employing the Langmuir-Blodgett (LB) film deposition method seems to hold promising results regarding reliability. Using the LB method, some of the same challenges of films stability and process suitability apply and much of the work done in this research will be applicable at that time of experimentation. Outside the scope of tunnel diodes as rectifiers, there is new promising work in the field of structural, geometric diodes. These geometric diodes exhibit asymmetry from the shape of the structure [313]. The areas which need the most exploration are those of the development of high frequency testing techniques. There is a large gap between DC and RF testing methods and

literature seems to suggest live rectenna testing as the only suitable method for evaluating rectifiers in these tremendously high frequency regimes. The development of standardized coplanar test structures, test die sizes, and automated switching systems will greatly streamline this area of research and should yield a wealth of information which is missing in literature. It is the author's belief that the future of research should follow a path of minimal expenditures and desk-top experimentation. The open-source initiative seen in today's innovation community has begun to up-end the conventional designers of the past. Through the use of low-cost fabrication methods and repurposed existing technology, it is now possible to achieve comparable to equipment orders of magnitude more costly.

LIST OF REFERENCES

[1] Sathyajith M. Wind Energy: Fundamentals, Resource Analysis and Economics: Springer; 2006.

[2] Priya S, Inman DJ. Energy harvesting technologies Springer; 2008.

[3] Parida B, Iniyan S, Goic R. A review of solar photovoltaic technologies. Renewable and Sustainable Energy Reviews. 2011;15:1625-36.

[4] Shockley W, Queisser HJ. Detailed Balance Limit of Efficiency of p‐n Junction Solar Cells. Journal of Applied Physics. 1961;32:510-9.

[5] McConnell R, Symko-Davies M. Multijunction Photovoltaic Technologies for High-Performance Concentrators. Photovoltaic Energy Conversion, Conference Record of the 2006 IEEE 4th World Conference on2006. p. 733-6.

[6] Green MA, Emery K, Hishikawa Y, Warta W, Dunlop ED. Solar cell efficiency tables (version 41). Progress in Photovoltaics: Research and Applications. 2013;21:1-11.

[7] Bell LE. Cooling, Heating, Generating Power, and Recovering Waste Heat with Thermoelectric Systems. Science. 2008;321:1457-61.

[8] Kongtragool B, Wongwises S. A review of solar-powered Stirling engines and low temperature differential Stirling engines. Renewable and Sustainable Energy Reviews. 2003;7:131-54.

[9] Strasser M, Aigner R, Franosch M, Wachutka G. Miniaturized thermoelectric generators based on poly-Si and poly-SiGe surface micromachining. Sensors and Actuators A: Physical. 2002;97–98:535-42.

[10] Binggeli C. Building Systems for Interior Designers. 2nd ed: Wiley; 2009.

[11] Sacco JJ, Botten J, Macbeth F, Bagust A, Clark P. The average body surface area of adult cancer patients in the UK: a multicentre retrospective study. PloS one. 2010;5:e8933.

[12] Brown WC. THE HISTORY OF POWER TRANSMISSION BY RADIO-WAVES. Ieee Transactions on Microwave Theory and Techniques. 1984;32:1230-42.

[13] Bailey RL. A proposed new concept for a solar-energy converter. Journal of Engineering for Power. 1972;94:73.

[14] Mashaal H, Gordon JM. Fundamental bounds for antenna harvesting of sunlight. Opt Lett. 2011;36:900-2.

[15] Robel I, Bunker BA, Kamat PV. Single-Walled Carbon Nanotube–CdS Nanocomposites as Light-Harvesting Assemblies: Photoinduced Charge-Transfer Interactions. Advanced Materials. 2005;17:2458-63.

[16] Novotny L, van Hulst N. Antennas for light. Nature Photonics. 2011;5:83-90.

[17] Hasegawa H, Furukawa M, Yanai H. Properties of Microstrip Line on Si-SiO₂ System. Microwave Theory and Techniques, IEEE Transactions on. 1971;19:869-81.

[18] Berland B, Simpson L, Nuebel G, Collins T, Lanning B. Optical rectenna for direct conversion of sunlight to electricity. Proceedings of the National Center for Photovoltaics Program Review Meeting (NREL, 2001)2001. p. 323-4.

[19] Huang W-X, Lee S-H, Sung HJ, Lee T-M, Kim D-S. Simulation of liquid transfer between separating walls for modeling micro-gravure-offset printing. International Journal of Heat and Fluid Flow. 2008;29:1436-46.

[20] Drexler H, Scott JS, Allen SJ, Campman KL, Gossard AC. Photon assisted tunneling in a resonant tunneling diode: Stimulated emission and absorption in the THz range. Applied Physics Letters. 1995;67:2816-8.

[21] Alù A, Engheta N. Input Impedance, Nanocircuit Loading, and Radiation Tuning of Optical Nanoantennas. Physical Review Letters. 2008;101:043901.

[22] Bean JA, Weeks A, Boreman GD. Performance optimization of antenna-coupled Al/AlOX/Pt tunnel diode infrared detectors. IEEE J Quantum Electron. 2011;47:126-35.

[23] Werner DH, Ganguly S. An overview of fractal antenna engineering research. Antennas and Propagation Magazine, IEEE. 2003;45:38-57.

[24] Dutoit NE, Wardle BL, Kim S-G. DESIGN CONSIDERATIONS FOR MEMS-SCALE PIEZOELECTRIC MECHANICAL VIBRATION ENERGY HARVESTERS. Integrated Ferroelectrics. 2005;71:121-60.

[25] Abdelkefi A, Nayfeh AH, Hajj MR. Design of piezoaeroelastic energy harvesters. Nonlinear Dyn. 2012;68:519-30.

[26] Beeby SP, Torah RN, Tudor MJ, Glynne-Jones P, Donnell TO, Saha CR, et al. A micro electromagnetic generator for vibration energy harvesting. Journal of Micromechanics and Microengineering. 2007;17:1257.

[27] Basset P, Galayko D, Paracha AM, Marty F, Dudka A, Bourouina T. A batch-fabricated and electret-free silicon electrostatic vibration energy harvester. Journal of Micromechanics and Microengineering. 2009;19:115025.

[28] Low M. From Einstein to Shirakawa: the Nobel Prize in Japan. Minerva. 2001;39:445-60.

[29] Lüth H. Particle-Wave Duality. Quantum Physics in the Nanoworld: Springer Berlin Heidelberg; 2013. p. 27-78.

[30] Schouten HF, Kuzmin N, Dubois G, Visser TD, Gbur G, Alkemade PFA, et al. Plasmon-Assisted Two-Slit Transmission: Young's Experiment Revisited. Physical Review Letters. 2005;94:053901.

[31] Donati O, Missiroli GP, Pozzi G. An Experiment on Electron Interference. American Journal of Physics. 1973;41:639-44.

[32] Arndt M, Nairz O, Vos-Andreae J, Keller C, Van der Zouw G, Zeilinger A. Wave–particle duality of C60 molecules. nature. 1999;401:680-2.

[33] Razavy M. Quantum Theory of Tunneling. 1st ed. River Edge, NJ: World Scientific; 2003.

[34] Sanchez A, Davis CF, Liu KC, Javan A. The MOM tunneling diode: Theoretical estimate of its performance at microwave and infrared frequencies. Journal of Applied Physics. 1978;49:5270-7.

[35] DiBenedetto SA, Facchetti A, Ratner MA, Marks TJ. Molecular Self-Assembled Monolayers and Multilayers for Organic and Unconventional Inorganic Thin-Film Transistor Applications. Advanced Materials. 2009;21:1407-33.

[36] Krishnan S, La Rosa H, Stefanakos E, Bhansali S, Buckle K. Design and development of batch fabricatable metal-insulator-metal diode and microstrip slot antenna as rectenna elements. Sensors and Actuators a-Physical. 2008;142:40-7.

[37] Heisenberg W. Über den anschaulichen Inhalt der quantentheoretischen Kinematik und Mechanik. Z Physik. 1927;43:172-98.

[38] Dunham JL. The Wentzel-Brillouin-Kramers Method of Solving the Wave Equation. Physical Review. 1932;41:713-20.

[39] Simmons JG. Generalized Formula for the Electric Tunnel Effect between Similar Electrodes Separated by a Thin Insulating Film. Journal of Applied Physics. 1963;34:1793-803.

[40] Simmons JG. Conduction in thin dielectric films. Journal of Physics D: Applied Physics. 1971;4:613-58.

[41] Beebe JM, Kim B, Gadzuk JW, Daniel Frisbie C, Kushmerick JG. Transition from Direct Tunneling to Field Emission in Metal-Molecule-Metal Junctions. Physical Review Letters. 2006;97:026801.

[42] Brinkman WF, Dynes RC, Rowell JM. Tunneling Conductance of Asymmetrical Barriers. Journal of Applied Physics. 1970;41:1915-&.

[43] Miller CW, Belyea DD. The impact of barrier height distributions in tunnel junctions. Journal of Applied Physics. 2009;105:094505--5.

[44] DiBenedetto SA, Facchetti A, Ratner MA, Marks TJ. Charge Conduction and Breakdown Mechanisms in Self-Assembled Nanodielectrics. Journal of the American Chemical Society. 2009;131:7158-68.

[45] Zehner RW, Parsons BF, Hsung RP, Sita LR. Tuning the work function of gold with self-assembled monolayers derived from X- C6H4-C C- (n)C6H4-SH (n = 0, 1, 2; X = H, F, CH3, CF3, and OCH3). Langmuir. 1999;15:1121-7.

[46] Nijhuis CA, Reus WF, Barber JR, Dickey MD, Whitesides GM. Charge Transport and Rectification in Arrays of SAM-Based Tunneling Junctions. Nano Letters. 2010;10:3611-9.

[47] Kasap S, Capper P. Springer handbook of electronic and photonic materials: Springer; 2006.

[48] Nuzzo RG, Allara DL. Adsorption of bifunctional organic disulfides on gold surfaces. Journal of the American Chemical Society. 1983;105:4481-3.

[49] Porter MD, Bright TB, L. AD, Chidsey CED. Spontaneously organized molecular assemblies. 4. structural characterization of n -alkyl thiol monolayers on gold by optical ellipsometry, infrared spectroscopy, and electrochemistry. J Am Chem Soc. 1987;109:3559.

[50] Bain CD, Whitesides GM. Molecular-Level Control over Surface Order in Self-Assembled Monolayer Films of Thiols on Gold. Science. 1988;240:62-3.

[51] Leung TYB, Gerstenberg MC, Lavrich DJ, Scoles G. 1,6-hexanedithiol monolayers on Au(111): a multi-technique structural study. Langmuir. 2000;16:549.

[52] Vericat C, Vela ME, Benitez GA, Gago JAM, Torrelles X, Salvarezza RC. Surface characterization of sulfur and alkanethiol self-assembled monolayers on Au(111). Journal of Physics: Condensed Matter. 2006;18:R867.

[53] Laibinis PE, Whitesides GM, Allara DL, Tao YT, Parikh AN, Nuzzo RG. Comparison of the structures and wetting properties of self-assembled monolayers of n-alkanethiols on the coinage metal surfaces, copper, silver, and gold. Journal of the American Chemical Society. 1991;113:7152-67.

[54] Rusu PC, Giovannetti G, Brocks G. Dipole Formation at Interfaces of Alkanethiolate Self-assembled Monolayers and Ag(111). The Journal of Physical Chemistry C. 2007;111:14448-56.

[55] Weiss EA, Chiechi RC, Kaufman GK, Kriebel JK, Li Z, Duati M, et al. Influence of Defects on the Electrical Characteristics of Mercury-Drop Junctions: Self-Assembled Monolayers of n-Alkanethiolates on Rough and Smooth Silver. Journal of the American Chemical Society. 2007;129:4336-49.

[56] Laibinis PE, Whitesides GM, Allara DL, Tao YT, Parikh AN, Nuzzo RG. Comparison of the structures and wetting properties of self-assembled monolayers of n -alkanethiol on the coinage metal surfaces, Cu, Ag, Au. J Am Chem Soc. 1991;113:7152.

[57] Walczak MM, Chung C, Stole SM, Widrig CA, Porter MD. Structure and interfacial properties of spontaneously adsorbed n-alkanethiolate monolayers on evaporated silver surfaces. Journal of the American Chemical Society. 1991;113:2370-8.

[58] Chang S-C, Li Z, Lau CN, Larade B, Williams RS. Investigation of a model molecular-electronic rectifier with an evaporated Ti--metal top contact. Applied Physics Letters. 2003;83:3198-200.

[59] Lee M H SG, Sankey OF. Electron transport through single alkane molecules with different contact geometries on gold. Phys Status Solidi. 2006;243:2021.

[60] Noguchi H, Ito M, Uosaki K. Molecular Orientation of Self-assembled Monolayer of Octadecanethiol on Platinum Surface Studied by Femtosecond Broad-bandwidth Sum Frequency Generation Spectroscopy. Chemistry Letters. 2005;34:950-1.

[61] Li Z, Chang S-C, Williams RS. Self-Assembly of Alkanethiol Molecules onto Platinum and Platinum Oxide Surfaces. Langmuir. 2003;19:6744-9.

[62] Stapleton JJ, Daniel TA, Uppili S, Cabarcos OM, Naciri J, Shashidhar R, et al. Self-Assembly, Characterization, and Chemical Stability of Isocyanide-Bound Molecular Wire Monolayers on Gold and Palladium Surfaces. Langmuir. 2005;21:11061-70.

[63] Carvalho A, Geissler M, Schmid H, Michel B, Delamarche E. Self-Assembled Monolayers of Eicosanethiol on Palladium and Their Use in Microcontact Printing. Langmuir. 2002;18:2406-12.

[64] Lukas S, Vollmer S, Witte G, Woll C. Adsorption of acenes on flat and vicinal Cu(111) surfaces: Step induced formation of lateral order. The Journal of Chemical Physics. 2001;114:10123-30.

[65] Jennings GK, Yong T-H, Munro JC, Laibinis PE. Structural Effects on the Barrier Properties of Self-Assembled Monolayers Formed from Long-Chain ω-Alkoxy-n-alkanethiols on Copper. Journal of the American Chemical Society. 2003;125:2950-7.

[66] Colvin VL, Goldstein AN, Alivisatos AP. Semiconductor nanocrystals covalently bound to metal surfaces with self-assembled monolayers. Journal of the American Chemical Society. 1992;114:5221-30.

[67] McGuiness CL, Shaporenko A, Mars CK, Uppili S, Zharnikov M, Allara DL. Molecular Self-Assembly at Bare Semiconductor Surfaces: Preparation and Characterization of Highly Organized Octadecanethiolate Monolayers on GaAs(001). Journal of the American Chemical Society. 2006;128:5231-43.

[68] Zerulla D, Chassé T. Structure and self-assembly of alkanethiols on III–V semiconductor (1 1 0) surfaces. Journal of Electron Spectroscopy and Related Phenomena. 2009;172:78-87.

[69] Muskal N, Turyan I, Mandler D. Self-assembled monolayers on mercury surfaces. J Electroanal Chem. 1996;409:131-6.

[70] Mann B, Kuhn H, Szentpály Lv. Tunnelling through fatty acid monolayers and its relevance to photographic sensitization. Chemical Physics Letters. 1971;8:82-4.

[71] Slowinski K, Chamberlain RV, Miller CJ, Majda M. Through-bond and chain-to-chain coupling. Two pathways in electron tunneling through liquid alkanethiol monolayers on mercury electrodes. J Am Chem Soc. 1997;119:11910.

[72] Haag R, Rampi MA, Holmlin RE, Whitesides GM. Electrical breakdown of aliphatic and aromatic self-assembled monolayers used as nanometer-thick organic dielectrics. J Am Chem Soc. 1999;121:7895.

[73] Muskal N, Mandler D. Thiol self-assembled monolayers on mercury surfaces: the adsorption and electrochemistry of [omega]-mercaptoalkanoic acids. Electrochimica Acta. 1999;45:537-48.

[74] Madou MJ. Fundamentals of Microfabrication. 2nd ed. New York: CRC Press; 2002.

[75] Senturia SD. Microsystem Design. 1st ed. New York: Springer; 2000.

[76] Moon DW, Kurokawa A, Ichimura S, Lee HW, Jeon IC. Ultraviolet-ozone jet cleaning process of organic surface contamination layers. Journal of Vacuum Science & Technology A: Vacuum, Surfaces, and Films. 1999;17:150-4.

[77] Adamson AW, Gast AP. Physical Chemistry of Surfaces. 6th ed. New York: John Wiley & Sons, Inc.; 1997.

[78] Crist BV. Handbook of Monochromatic XPS Spectra, Semiconductors: Wiley; 2000.

[79] Love JC, Wolfe DB, Haasch R, Chabinyc ML, Paul KE, Whitesides GM, et al. Formation and Structure of Self-Assembled Monolayers of Alkanethiolates on Palladium. Journal of the American Chemical Society. 2003;125:2597-609.

[80] Skaife JJ, Brake JM, Abbott NL. Influence of Nanometer-Scale Topography of Surfaces on the Orientational Response of Liquid Crystals to Proteins Specifically Bound to Surface-Immobilized Receptors. Langmuir. 2001;17:5448-57.

[81] Wang D, Thomas SG, Wang KL, Xia Y, Whitesides GM. Nanometer scale patterning and pattern transfer on amorphous Si, crystalline Si, and SiO[sub 2] surfaces using self-assembled monolayers. Applied Physics Letters. 1997;70:1593-5.

[82] Choi-Yim H, Johnson WL. Bulk metallic glass matrix composites. Applied Physics Letters. 1997;71:3808-10.

[83] Das J, Tang MB, Kim KB, Theissmann R, Baier F, Wang WH, et al. "Work-Hardenable" Ductile Bulk Metallic Glass. Physical Review Letters. 2005;94:205501.

[84] Strong L, Whitesides GM. Structures of self-assembled monolayer films of organosulfur compounds adsorbed on gold single crystals: electron diffraction studies. Langmuir. 1988;4:546-58.

[85] Luedtke WD, Landman U. Structure and Thermodynamics of Self-Assembled Monolayers on Gold Nanocrystallites. The Journal of Physical Chemistry B. 1998;102:6566-72.

[86] Weisbecker CS, Merritt MV, Whitesides GM. Molecular Self-Assembly of Aliphatic Thiols on Gold Colloids. Langmuir. 1996;12:3763-72.

[87] Terrill RH, Postlethwaite TA, Chen C-h, Poon C-D, Terzis A, Chen A, et al. Monolayers in Three Dimensions: NMR, SAXS, Thermal, and Electron Hopping Studies of Alkanethiol Stabilized Gold Clusters. Journal of the American Chemical Society. 1995;117:12537-48.

[88] Hostetler MJ, Wingate JE, Zhong CJ, Harris JE, Vachet RW, Clark MR, et al. Langmuir. 1998;14:17.

[89] Sato Y, Frey BL, Corn RM, Uosaki K. Polarization Modulation Fourier Transform Infrared Studies of the Effects of Self-Assembly Time on the Order and Orientation of 11-Ferrocenyl-1-undecanethiol Monolayers on Gold. Bulletin of the Chemical Society of Japan. 1994;67:21-5.

[90] Rijal K, Mutharasan R. Method for Measuring the Self-Assembly of Alkanethiols on Gold at Femtomolar Concentrations. Langmuir. 2007;23:6856-63.

[91] Bain CD, Troughton EB, Tao YT, Evall J, Whitesides GM, Nuzzo RG. Formation of monolayer films by the spontaneous assembly of organic thiols from solution onto gold. Journal of the American Chemical Society. 1989;111:321-35.

[92] Ulman A. Formation and Structure of Self-Assembled Monolayers. Chemical Reviews. 1996;96:1533-54.

[93] Katz HE. Multilayer Deposition of Novel Organophosphonates with Zirconium(IV). Chemistry of Materials. 1994;6:2227-32.

[94] Schilling ML, Katz HE, Stein SM, Shane SF, Wilson WL, Ungashe SB, et al. Structural studies of zirconium alkylphosphonate monolayers and multilayer assemblies. Langmuir. 1993;9:2156-60.

[95] Nuzzo RG, Zegarski BR, Dubois LH. Fundamental studies of the chemisorption of organosulfur compounds on gold(111). Implications for molecular self-assembly on gold surfaces. Journal of the American Chemical Society. 1987;109:733-40.

[96] Bareman JP, Klein ML. Collective tilt behavior in dense, substrate-supported monolayers of long-chain molecules: a molecular dynamics study. The Journal of Physical Chemistry. 1990;94:5202-5.

[97] Camillone III N, Chidsey CED, Eisenberger P, Fenter P, Li J, K S, et al. Structural defects in self-assembled organic monolayers via combined atomic beam and x-ray diffraction. The Journal of Chemical Physics. 1993;99:744-7.

[98] Love JC, Estroff LA, Kriebel JK, Nuzzo RG, Whitesides GM. Self-assembled monolayers of thiolates on metals as a form of nanotechnology. Chemical Reviews. 2005;105:1103-69.

[99] Schreiber F. Structure and growth of self-assembling monolayers. Progress in Surface Science. 2000;65:151-257.

[100] Sheen CW, Shi JX, Maartensson J, Parikh AN, Allara DL. A new class of organized self-assembled monolayers: alkane thiols on gallium arsenide(100). Journal of the American Chemical Society. 1992;114:1514-5.

[101] Magnussen OM, Ocko BM, Deutsch M, Regan MJ, Pershan PS, Abernathy D, et al. Self-assembly of organic films on a liquid metal. Nature. 1996;384:250-2.

[102] Fenter P, Schreiber F, Zhou L, Eisenberger P, Forrest SR. In situ studies of morphology, strain, and growth modes of a molecular organic thin film. Physical Review B. 1997;56:3046.

[103] Dubois LH, Nuzzo RG. Synthesis, Structure, and Properties of Model Organic Surfaces. Annu Rev Phys Chem. 1992;43:437.

[104] Yamamoto H, Waldeck DH. Effect of Tilt-Angle on Electron Tunneling through Organic Monolayer Films. The Journal of Physical Chemistry B. 2002;106:7469-73.

[105] Poirier GE, Tarlov MJ. The c(4X2) Superlattice of n-Alkanethiol Monolayers Self-Assembled on Au(111). Langmuir. 1994;10:2853-6.

[106] Gottschalck J, Hammer B. A density functional theory study of the adsorption of sulfur, mercapto, and methylthiolate on Au(111). The Journal of Chemical Physics. 2002;116:784-90.

[107] Tachibana M, Yoshizawa K, Ogawa A, Fujimoto H, Hoffmann R. Sulfur−Gold Orbital Interactions which Determine the Structure of Alkanethiolate/Au(111) Self-Assembled Monolayer Systems. The Journal of Physical Chemistry B. 2002;106:12727-36.

[108] Pensa E, Vericat C, Grumelli D, Salvarezza RC, Park SH, Longo GS, et al. New insight into the electrochemical desorption of alkanethiol SAMs on gold. Physical Chemistry Chemical Physics. 2012;14:12355-67.

[109] Vericat C, Vela ME, Benitez G, Carro P, Salvarezza RC. Self-assembled monolayers of thiols and dithiols on gold: new challenges for a well-known system. Chemical Society Reviews. 2010;39:1805-34.

[110] Petty MC. Langmuir-blodgett films. Endeavour. 1983;7:65-9.

[111] Thomas RC, Sun L, Crooks RM, Ricco AJ. Real-time measurements of the gas-phase adsorption of n-alkylthiol mono- and multilayers on gold. Langmuir. 1991;7:620-2.

[112] Mekhalif Z, Laffineur F, Couturier N, Delhalle J. Elaboration of Self-Assembled Monolayers of n-Alkanethiols on Nickel Polycrystalline Substrates: Time, Concentration, and Solvent Effects. Langmuir. 2003;19:637-45.

[113] Dannenberger O BM, Grunze M. Self-Assembly of n -alkanethiols: a kinetic study by second harmonic generation. J Phys Chem. 1999;103:2202.

[114] Schwartz DK. MECHANISMS AND KINETICS OF SELF-ASSEMBLED MONOLAYER FORMATION. Annual Review of Physical Chemistry. 2001;52:107-37.

[115] Karpovich DS, Blanchard GJ. Direct Measurement of the Adsorption Kinetics of Alkanethiolate Self-Assembled Monolayers on a Microcrystalline Gold Surface. Langmuir. 1994;10:3315-22.

[116] Bertilsson L, Liedberg B. Infrared study of thiol monolayer assemblies on gold: preparation, characterization, and functionalization of mixed monolayers. Langmuir. 1993;9:141-9.

[117] Poirier GE. Mechanism of Formation of Au Vacancy Islands in Alkanethiol Monolayers on Au(111). Langmuir. 1997;13:2019-26.

[118] Maoz R, Cohen SR, Sagiv J. Nanoelectrochemical Patterning of Monolayer Surfaces: Toward Spatially Defined Self-Assembly of Nanostructures. Advanced Materials. 1999;11:55-61.

[119] Camillone N, Leung TYB, Schwartz P, Eisenberger P, Scoles G. Chain Length Dependence of the Striped Phases of Alkanethiol Monolayers Self-Assembled on Au(111): An Atomic Beam Diffraction Study. Langmuir. 1996;12:2737-46.

[120] Leopold MC, Bowden EF. Influence of Gold Substrate Topography on the Voltammetry of Cytochrome c Adsorbed on Carboxylic Acid Terminated Self-Assembled Monolayers. Langmuir. 2002;18:2239-45.

[121] Gun J, Sagiv J. On the formation and structure of self-assembling monolayers : III. Time of formation, solvent retention, and release. Journal of Colloid and Interface Science. 1986;112:457-72.

[122] Keller H, Schrepp W, Fuchs H. Self-assembled organic films on gold and silver. Thin Solid Films. 1992;210-211:799-802.

[123] Yamada R, Wano H, Uosaki K. Effect of Temperature on Structure of the Self-Assembled Monolayer of Decanethiol on Au(111) Surface. Langmuir. 2000;16:5523-5.

[124] Bensebaa F, Voicu R, Huron L, Ellis TH, Kruus E. Kinetics of Formation of Long-Chain n-Alkanethiolate Monolayers on Polycrystalline Gold. Langmuir. 1997;13:5335-40.

[125] Smith RK, Lewis PA, Weiss PS. Patterning self-assembled monolayers. Progress in Surface Science. 2004;75:1-68.

[126] Weck M, Jackiw JJ, Rossi RR, Weiss PS, Grubbs RH. Ring-Opening Metathesis Polymerization from Surfaces. Journal of the American Chemical Society. 1999;121:4088-9.

[127] Haes AJ, Chang L, Klein WL, Van Duyne RP. Detection of a Biomarker for Alzheimer's Disease from Synthetic and Clinical Samples Using a Nanoscale Optical Biosensor. Journal of the American Chemical Society. 2005;127:2264-71.

[128] Camarero JA. Recent developments in the site-specific immobilization of proteins onto solid supports. Peptide Science. 2008;90:450-8.

[129] Sullivan TP, Huck WTS. Reactions on Monolayers: Organic Synthesis in Two Dimensions. European Journal of Organic Chemistry. 2003;2003:17-29.

[130] Pirrung MC. How to Make a DNA Chip. Angewandte Chemie International Edition. 2002;41:1276-89.

[131] Rozsnyai LF, Wrighton MS. Controlling the Adhesion of Conducting Polymer Films with Patterned Self-Assembled Monolayers. Chemistry of Materials. 1996;8:309-11.

[132] Ruckenstein E, Li ZF. Surface modification and functionalization through the self-assembled monolayer and graft polymerization. Advances in Colloid and Interface Science. 2005;113:43-63.

[133] Bumm LA, Arnold JJ, Charles LF, Dunbar TD, Allara DL, Weiss PS. Directed Self-Assembly to Create Molecular Terraces with Molecularly Sharp Boundaries in Organic Monolayers. Journal of the American Chemical Society. 1999;121:8017-21.

[134] Kautz NA, Kandel SA. Alkanethiol/Au(111) Self-Assembled Monolayers Contain Gold Adatoms: Scanning Tunneling Microscopy before and after Reaction with Atomic Hydrogen. Journal of the American Chemical Society. 2008;130:6908-9.

[135] Schoenenberger C, Sondag-Huethorst JAM, Jorritsma J, Fokkink LGJ. What Are the "Holes" in Self-Assembled Monolayers of Alkanethiols on Gold? Langmuir. 1994;10:611-4.

[136] Kautz NA, Kandel SA. Alkanethiol Monolayers Contain Gold Adatoms, and Adatom Coverage Is Independent of Chain Length. The Journal of Physical Chemistry C. 2009;113:19286-91.

[137] Huang J, Hemminger JC. Photooxidation of thiols in self-assembled monolayers on gold. Journal of the American Chemical Society. 1993;115:3342-3.

[138] Lewis M, Tarlov M, Carron K. Study of the Photooxidation Process of Self-Assembled Alkanethiol Monolayers. Journal of the American Chemical Society. 1995;117:9574-5.

[139] Zhou C, Walker AV. UV Photooxidation and Photopatterning of Alkanethiolate Self-Assembled Monolayers (SAMs) on GaAs (001). Langmuir. 2007;23:8876-81.

[140] Zhou C, Walker AV. UV Photooxidation of a Homologous Series of n-Alkanethiolate Monolayers on GaAs(001): A Static SIMS Investigation. The Journal of Physical Chemistry C. 2008;112:797-805.

[141] Cooper E, Wiggs R, A. Hutt D, Parker L, Leggett GJ, L. Parker T. Rates of attachment of fibroblasts to self-assembled monolayers formed by the adsorption of alkylthiols onto gold surfaces. Journal of Materials Chemistry. 1997;7:435-41.

[142] Hutt DA, Cooper E, Leggett GJ. Structure and Mechanism of Photooxidation of Self-assembled Monolayers of Alkylthiols on Silver Studied by XPS and Static SIMS. The Journal of Physical Chemistry B. 1998;102:174-84.

[143] Zhang Y, Terrill RH, Tanzer TA, Bohn PW. Ozonolysis Is the Primary Cause of UV Photooxidation of Alkanethiolate Monolayers at Low Irradiance. Journal of the American Chemical Society. 1998;120:2654-5.

[144] Shadnam MR, Kirkwood SE, Fedosejevs R, Amirfazli A. Direct Patterning of Self-Assembled Monolayers on Gold Using a Laser Beam. Langmuir. 2004;20:2667-76.

[145] Xia Y, Zhao X-M, Whitesides GM. Pattern transfer: Self-assembled monolayers as ultrathin resists. Microelectronic Engineering. 1996;32:255-68.

[146] Chan KC, Kim T, Schoer JK, Crooks RM. Polymeric Self-Assembled Monolayers. 3. Pattern Transfer by Use of Photolithography, Electrochemical Methods, and an Ultrathin, Self-Assembled Diacetylenic Resist. Journal of the American Chemical Society. 1995;117:5875-6.

[147] Gillen G, Wight S, Bennett J, Tarlov MJ. Patterning of self-assembled alkanethiol monolayers on silver by microfocus ion and electron beam bombardment. Applied Physics Letters. 1994;65:534-6.

[148] Ballav N, Schilp S, Zharnikov M. Electron-Beam Chemical Lithography with Aliphatic Self-Assembled Monolayers. Angewandte Chemie. 2008;120:1443-6.

[149] Berggren K, Bard A, Wilbur J, Gillaspy J, Helg A, McClelland J, et al. Microlithography by using neutral metastable atoms and self-assembled monolayers. Science. 1995;269:1255-7.

[150] Klauser R, Hong IH, Wang SC, Zharnikov M, Paul A, Gölzhäuser A, et al. Imaging and Patterning of Monomolecular Resists by Zone-Plate-Focused X-ray Microprobe. The Journal of Physical Chemistry B. 2003;107:13133-42.

[151] Zharnikov M, Grunze M. Modification of thiol-derived self-assembling monolayers by electron and x-ray irradiation: Scientific and lithographic aspects. Journal of Vacuum Science & Technology B: Microelectronics and Nanometer Structures. 2002;20:1793-807.

[152] Younkin R, Berggren KK, Johnson KS, Prentiss M, Ralph DC, Whitesides GM. Nanostructure fabrication in silicon using cesium to pattern a self-assembled monolayer. Applied Physics Letters. 1997;71:1261-3.

[153] Delamarche E, Schmid H, Bietsch A, Larsen NB, Rothuizen H, Michel B, et al. Transport Mechanisms of Alkanethiols during Microcontact Printing on Gold. The Journal of Physical Chemistry B. 1998;102:3324-34.

[154] Biebuyck HA, Larsen NB, Delamarche E, Michel B. Lithography beyond light: Microcontact printing with monolayer resists. IBM Journal of Research and Development. 1997;41:159-70.

[155] Sirringhaus H, Kawase T, Friend RH, Shimoda T, Inbasekaran M, Wu W, et al. High-Resolution Inkjet Printing of All-Polymer Transistor Circuits. Science. 2000;290:2123-6.

[156] Bietsch A, Hegner M, Lang HP, Gerber C. Inkjet Deposition of Alkanethiolate Monolayers and DNA Oligonucleotides on Gold: Evaluation of Spot Uniformity by Wet Etching. Langmuir. 2004;20:5119-22.

[157] Wang JZ, Zheng ZH, Li HW, Huck WTS, Sirringhaus H. Dewetting of conducting polymer inkjet droplets on patterned surfaces. Nat Mater. 2004;3:171-6.

[158] Salaita K, Wang Y, Mirkin CA. Applications of dip-pen nanolithography. Nat Nano. 2007;2:145-55.

[159] Salaita K, Amarnath A, Higgins TB, Mirkin CA. The effects of organic vapor on alkanethiol deposition via Dip-pen nanolithography. Scanning. 2010;32:9-14.

[160] Piner RD, Zhu J, Xu F, Hong S, Mirkin CA. "Dip-Pen" Nanolithography. Science. 1999;283:661-3.

[161] Salaita K, Wang Y, Fragala J, Vega RA, Liu C, Mirkin CA. Massively Parallel Dip–Pen Nanolithography with 55 000-Pen Two-Dimensional Arrays. Angewandte Chemie. 2006;118:7378-81.

[162] Tobias PA, Trindade DC. Applied Reliability. 2nd ed. New York: CRC Press; 1995.

[163] Lee S-H, Lin W-C, Kuo C-H, Karakachian M, Lin Y-C, Yu B-Y, et al. Photooxidation of Amine-Terminated Self-Assembled Monolayers on Gold. The Journal of Physical Chemistry C. 2010;114:10512-9.

[164] Hutt DA, Leggett GJ. Functionalization of Hydroxyl and Carboxylic Acid Terminated Self-Assembled Monolayers. Langmuir. 1997;13:2740-8.

[165] Schoenfisch MH, Pemberton JE. Air Stability of Alkanethiol Self-Assembled Monolayers on Silver and Gold Surfaces. Journal of the American Chemical Society. 1998;120:4502-13.

[166] Aqua T, Cohen H, Vilan A, Naaman R. Long-Range Substrate Effects on the Stability and Reactivity of Thiolated Self-Assembled Monolayers. The Journal of Physical Chemistry C. 2007;111:16313-8.

[167] Bucher J-P, Santesson L, Kern K. Thermal Healing of Self-Assembled Organic Monolayers: Hexane- and Octadecanethiol on Au(111) and Ag(111). Langmuir. 1994;10:979-83.

[168] Chandekar A, Sengupta SK, Whitten JE. Thermal stability of thiol and silane monolayers: A comparative study. Applied Surface Science. 2010;256:2742-9.

[169] Schlenoff JB, Li M, Ly H. Stability and Self-Exchange in Alkanethiol Monolayers. Journal of the American Chemical Society. 1995;117:12528-36.

[170] Yang G, Amro NA, Starkewolfe ZB, Liu G-y. Molecular-Level Approach To Inhibit Degradations of Alkanethiol Self-Assembled Monolayers in Aqueous Media. Langmuir. 2004;20:3995-4003.

[171] Akkerman HB, Blom PWM, de Leeuw DM, de Boer B. Towards molecular electronics with large-area molecular junctions. Nature. 2006;441:69-72.

[172] Williams KR, Gupta K, Wasilik M. Etch rates for micromachining processing - Part II. Journal of Microelectromechanical Systems. 2003;12:761-78.

[173] Cui XL, Jiang DL, Diao P, Li JX, Tong RT, Wang XK. Assessing the apparent effective thickness of alkanethiol self-assembled monolayers in different concentrations of Fe(CN)(6)(3-)/Fe(CN)(6)(4-) by ac impedance spectroscopy. Journal of Electroanalytical Chemistry. 1999;470:9-13.

[174] Cras JJ, Rowe-Taitt CA, Nivens DA, Ligler FS. Comparison of chemical cleaning methods of glass in preparation for silanization. Biosensors and Bioelectronics. 1999;14:683-8.

[175] Campina JM, Martins A, Silva F. A new cleaning methodology for efficient Au-SAM removal. Electrochimica Acta. 2008;53:7681-9.

[176] Holmlin RE, Haag R, Chabinyc ML, Ismagilov RF, Cohen AE, Terfort A, et al. Electron transport through thin organic films in metal-insulator-metal junctions based on self-assembled monolayers. Journal of the American Chemical Society. 2001;123:5075-85.

[177] Rampi MA, Schueller OJA, Whitesides GM. Alkanethiol self-assembled monolayers as the dielectric of capacitors with nanoscale thickness. Applied Physics Letters. 1998;72:1781-3.

[178] Rampi MA, Whitesides GM. Chemical and electrical properties of metal-SAM/SAM-metal junctions. Abstracts of Papers of the American Chemical Society. 1998;216:166-COLL.

[179] Slowinski K, Chamberlain RV, Miller CJ, Majda M. Through-Bond and Chain-to-Chain Coupling. Two Pathways in Electron Tunneling through Liquid Alkanethiol Monolayers on Mercury Electrodes. Journal of the American Chemical Society. 1997;119:11910-9.

[180] Watson CM, Dwyer DJ, Andle JC, Bruce AE, Bruce MRM. Stripping analysis of mercury using gold electrodes: irreversible adsorption of mercury. Anal Chem. 1999;71:3181.

[181] Vasjari M, Shirshov YM, Samoylov AV, Mirsky VM. SPR investigation of mercury reduction and oxidation on thin gold electrodes. J Electroanal Chem. 2007;605:73.

[182] Davis JR. Corrosion of Aluminum and Aluminum Alloys: ASM International; 1999.

[183] Mangum BW, Thornton DD. Determination of the Triple-Point Temperature of Gallium. Metrologia. 1979;15:201.

[184] Surmann P, Zeyat H. Voltammetric analysis using a self-renewable non-mercury electrode. Analytical and Bioanalytical Chemistry. 2005;383:1009-13.

[185] Chiechi RC, Weiss EA, Dickey MD, Whitesides GM. Eutectic Gallium–Indium (EGaIn): A Moldable Liquid Metal for Electrical Characterization of Self-Assembled Monolayers. Angewandte Chemie. 2008;120:148-50.

[186] Borisov B, Charnaya E, Gartvik A, Tien C, Kumzerov Y, Lavrentev V. Peculiarities of gallium crystallization in confined geometry. Physics of the Solid State. 2004;46:2286-91.

[187] Michel B, Bernard A, Bietsch A, Delamarche E, Geissler M, Juncker D, et al. IBM J Res Dev. 2001;45:697.

[188] Nijhuis CA, Reus WF, Whitesides GM. Molecular Rectification in Metal-SAM-Metal Oxide-Metal Junctions. Journal of the American Chemical Society. 2009;131:17814-27.

[189] Wold DJ, Frisbie CD. Fabrication and Characterization of Metal−Molecule−Metal Junctions by Conducting Probe Atomic Force Microscopy. Journal of the American Chemical Society. 2001;123:5549-56.

[190] Li X HJHJXBLSM, Tao N. Conductance of single alkanedithiols: conduction mechanism and effect of molecule-electrode contacts. J Am Chem Soc. 2006;128:2135.

[191] Sakaguchi H, Hirai A, Iwata F, Sasaki A, Nagamura T, Kawata E, et al. Determination of performance on tunnel conduction through molecular wire using a conductive atomic force microscope. Appl Phys Lett. 2001;79:3708.

[192] Wold JD, Frisbie CD. Formation of metal-molecule-metal junctions: microcontacts to alkanethiol monolayers with a conducting AFM tip. J Am Chem Soc. 2000;122:2970.

[193] Song H LH, Lee T. Intermolecular chain-to-chain tunneling in metal-alkanethiol-metal junctions. J Am Chem Soc. 2007;129:3806.

[194] Binnig G, Rohrer H, Gerber C, Weibel E. Tunneling through a controllable vacuum gap. Appl Phys Lett. 1982;40:178.

[195] Xu B, Tao NJ. Measurement of single-molecule resistance by repeated formation of molecular junctions. Science. 2003;301:1221.

[196] Cygan MT, et al. Insertion, conductivity and structures of conjugated organic oligomers in self-assembled alkanethiol monolayers on Au(111). J Am Chem Soc. 1998;120:2721.

[197] Muller CJ, van Ruitenbeek JM, de Jongh LJ. Experimental observation of the transition from weak link to tunnel junction. Physica. 1992;191:485.

[198] Reed MA, Zhou C, Muller CJ, Burgin TP, Tour JM. Conductance of a molecular junction. Science. 1997;278:252-4.

[199] van Ruitenbeek JM, Alvarez A, Piñero I, Grahmann C, Joyez P, Devoret H, et al. Adjustable nanofabricated atomic size contacts. Rev Sci Instrum. 1995;67:108.

[200] Agraït N, Yeyati AL, van Ruitenbeek JM. Quantum properties of atomic-sized conductors. Phys Rep. 2003;377:81.

[201] Vrouwe SAG, van der Giessen E, van der Molen SJ, Dulic D, Trouwborst ML, van Wees BJ. Mechanics of lithographically defined break junctions. Phys Rev. 2005;71:035313.

[202] Park H, Lim AKL, Alivisatos AP, Park J, McEuen PL. Fabrication of metallic electrodes with nanometer separation by electromigration. Applied Physics Letters. 1999;75:301-3.

[203] Liang W, Shores MP, Bockrath M, Long JR, Park H. Kondo resonance in a single-molecule transistor. Nature. 2002;417:725.

[204] Heersche HB, Lientschnig G, O'Neill K, J. vdZHS, Zandbergen HW. In situ imaging of electromigration-induced nanogap formation by transmission electron microscopy. Appl Phys Lett. 2007;91:072107.

[205] Kushmerick JG, Holt DB, Pollack SK, Ratner MA, Yang JC, Schull TL, et al. Effect of Bond-Length Alternation in Molecular Wires. Journal of the American Chemical Society. 2002;124:10654-5.

[206] Blum AS, Kushmerick JG, Pollack SK, Yang JC, Moore M, Naciri J, et al. Charge Transport and Scaling in Molecular Wires. The Journal of Physical Chemistry B. 2004;108:18124-8.

[207] Akkerman HB, Boer Bd. Electrical conduction through single molecules and self-assembled monolayers. Journal of Physics: Condensed Matter. 2008;20:013001.

[208] Lindsay SM, Ratner MA. Molecular Transport Junctions: Clearing Mists. Advanced Materials. 2007;19:23-31.

[209] McCreery RL. Molecular Electronic Junctions. Chemistry of Materials. 2004;16:4477-96.

[210] Haynie B C WAVTTBAD, Winograd N. Adventures in molecular electronics: how to attach wires to molecules. Appl Surf Sci. 2003;203-204:433.

[211] Bang GS, Chang H, Koo J-R, Lee T, Advincula RC, Lee H. High-Fidelity Formation of a Molecular-Junction Device Using a Thickness-Controlled Bilayer Architecture. Small. 2008;4:1399-405.

[212] Lee J-O, Lientschnig G, Wiertz F, Struijk M, Janssen RAJ, Egberink R, et al. Absence of Strong Gate Effects in Electrical Measurements on Phenylene-Based Conjugated Molecules. Nano Letters. 2003;3:113-7.

[213] Haick H, Niitsoo O, Ghabboun J, Cahen D. Electrical Contacts to Organic Molecular Films by Metal Evaporation: Effect of Contacting Details. The Journal of Physical Chemistry C. 2007;111:2318-29.

[214] Haick H, Cahen D. Making contact: Connecting molecules electrically to the macroscopic world. Progress in Surface Science. 2008;83:217-61.

[215] Haick H, Cahen D. Contacting Organic Molecules by Soft Methods: Towards Molecule-Based Electronic Devices. Accounts of Chemical Research. 2008;41:359-66.

[216] de Boer B FMMCYJJWGE, Bao Z. Metallic contact formation for molecular electronics: interactions between vapor-deposited metals and self-assembled monolayers of conjugated mono- and dithiols. Langmuir. 2004;20:1539.

[217] Walker AV, Tighe TB, Cabarcos OM, Reinard MD, Haynie BC, Uppili S, et al. The Dynamics of Noble Metal Atom Penetration through Methoxy-Terminated Alkanethiolate Monolayers. Journal of the American Chemical Society. 2004;126:3954-63.

[218] Metzger RM, Xu T, Peterson IR. Electrical Rectification by a Monolayer of Hexadecylquinolinium Tricyanoquinodimethanide Measured between Macroscopic Gold Electrodes. The Journal of Physical Chemistry B. 2001;105:7280-90.

[219] Zhou C, Deshpande MR, Reed MA, Jones L, Tour JM. Nanoscale metal self-assembled monolayer metal heterostructures. Applied Physics Letters. 1997;71:611-3.

[220] Majumdar N, Gergel N, Routenberg D, Bean JC, Harriott LR, Li B, et al. Nanowell device for the electrical characterization of metal--molecule--metal junctions. Journal of Vacuum Science & Technology B: Microelectronics and Nanometer Structures. 2005;23:1417-21.

[221] Wang WY, Lee T, Reed MA. Mechanism of electron conduction in self-assembled alkanethiol monolayer devices. Physical Review B. 2003;68.

[222] Kim JY, Jung JH, Lee DE, Joo J. Enhancement of electrical conductivity of poly(3,4-ethylenedioxythiophene)/poly(4-styrenesulfonate) by a change of solvents. Synthetic Metals. 2002;126:311-6.

[223] Akkerman HB, Naber RCG, Jongbloed B, van Hal PA, Blom PWM, de Leeuw DM, et al. Electron tunneling through alkanedithiol self-assembled monolayers in large-area molecular junctions. Proceedings of the National Academy of Sciences. 2007;104:11161-6.

[224] Milani F, Grave C, Ferri V, Samorì P, Rampi MA. Ultrathin π-Conjugated Polymer Films for Simple Fabrication of Large-Area Molecular Junctions. ChemPhysChem. 2007;8:515-8.

[225] Kaiser AB. Electronic transport properties of conducting polymers and carbon nanotubes. Reports on Progress in Physics. 2001;64:1.

[226] Moons E, Bruening M, Shanzer A, Beier J, Cahen D. Electron transfer in hybrid molecular solid-state devices. Synthetic Metals. 1996;76:245-8.

[227] Vilan A, Cahen D. Soft contact deposition onto molecularly modified GaAs. Thin metal film flotation: Principles and electrical effects. Advanced Functional Materials. 2002;12:795-807.

[228] Shimizu KT, Fabbri JD, Jelincic JJ, Melosh NA. Soft Deposition of Large-Area Metal Contacts for Molecular Electronics. Advanced Materials. 2006;18:1499-504.

[229] Stein N, Korobko R, Yaffe O, Har Lavan R, Shpaisman H, Tirosh E, et al. Nondestructive Contact Deposition for Molecular Electronics: Si-Alkyl//Au Junctions. The Journal of Physical Chemistry C. 2010;114:12769-76.

[230] Xia Y, Rogers JA, Paul KE, Whitesides GM. Unconventional Methods for Fabricating and Patterning Nanostructures. Chemical Reviews. 1999;99:1823-48.

[231] Kumar A, Whitesides GM. Features of gold having micrometer to centimeter dimensions can be formed through a combination of stamping with an elastomeric stamp and an alkanethiol ‘ink’ followed by chemical etching. Appl Phys Lett. 1993;63:2002.

[232] Xia Y, Whitesides GM. Soft lithography. Angew Chem Int Edn. 1998;37:550.

[233] Loo Y-L, Lang DV, Rogers JA, Hsu JWP. Electrical Contacts to Molecular Layers by Nanotransfer Printing. Nano Letters. 2003;3:913-7.

[234] Bolotin KI, Kuemmeth F, Pasupathy AN, Ralph DC. Metal-nanoparticle single-electron transistors fabricated using electromigration. Applied Physics Letters. 2004;84:3154-6.

[235] Chu C, Na J-S, Parsons GN. Conductivity in Alkylamine/Gold and Alkanethiol/Gold Molecular Junctions Measured in Molecule/Nanoparticle/Molecule Bridges and Conducting Probe Structures. Journal of the American Chemical Society. 2007;129:2287-96.

[236] Tivanski AV, He Y, Borguet E, Liu H, Walker GC, Waldeck DH. Conjugated Thiol Linker for Enhanced Electrical Conduction of Gold−Molecule Contacts. The Journal of Physical Chemistry B. 2005;109:5398-402.

[237] Long DP, Patterson CH, Moore MH, Seferos DS, Bazan GC, Kushmerick JG. Magnetic directed assembly of molecular junctions. Applied Physics Letters. 2005;86:153105.

[238] Liao J, Bernard L, Langer M, Schönenberger C, Calame M. Reversible Formation of Molecular Junctions in 2D Nanoparticle Arrays. Advanced Materials. 2006;18:2444-7.

[239] Schneeweiss MA, Kolb DM. The Initial Stages of Copper Deposition on Bare and Chemically Modified Gold Electrodes. physica status solidi (a). 1999;173:51-71.

[240] Sondag-Huethorst JAM, Fokkink LGJ. Galvanic Copper Deposition on Thiol-Modified Gold Electrodes. Langmuir. 1995;11:4823-31.

[241] Maisch S, Buckel F, Effenberger F. Preparation of high quality electrical insulator self-assembled monolayers on gold. Experimental investigation of the conduction mechanism through organic thin films. Journal of the American Chemical Society. 2005;127:17315-22.

[242] Azuma Y, Yasutake Y, Kono K, Kanehara M, Teranishi T, Majima Y. Single-Electron Transistor Fabricated by Two Bottom-Up Processes of Electroless Au Plating and Chemisorption of Au Nanoparticle. Japanese Journal of Applied Physics. 2010;49:090206.

[243] Charbonnier M, Alami M, Romand M. Plasma Treatment Process for Palladium Chemisorption onto Polymers before Electroless Deposition. Journal of The Electrochemical Society. 1996;143:472-80.

[244] Kobayashi Y, Salgueiriño-Maceira V, Liz-Marzán LM. Deposition of Silver Nanoparticles on Silica Spheres by Pretreatment Steps in Electroless Plating. Chemistry of Materials. 2001;13:1630-3.

[245] Garno JC, Zangmeister CD, Batteas JD. Directed Electroless Growth of Metal Nanostructures on Patterned Self-Assembled Monolayers. Langmuir. 2007;23:7874-9.

[246] Mbindyo JKN, Mallouk TE, Mattzela JB, Kratochvilova I, Razavi B, Jackson TN, et al. Template Synthesis of Metal Nanowires Containing Monolayer Molecular Junctions. Journal of the American Chemical Society. 2002;124:4020-6.

[247] Rampi MA, Whitesides GM. A versatile experimental approach for understanding electron transport through organic materials. Chemical Physics. 2002;281:373-91.

[248] Engelkes V B BJM, Frisbie CD. Length-dependent transport in molecular junctions based on SAMS of alkanethiols and alkanedithiols: effect of metal work function and applied bias on tunneling efficiency and contact resistance. J Am Chem Soc. 2004;126:14287.

[249] Chen F LXHJHZ, Tao N. Effect of anchoring groups on single-molecule conductance: comparative study of thiol-, amine, and carboxylic-acid-terminated molecules. J Am Chem Soc. 2006;128:15874.

[250] Kim T-W, Wang G, Lee H, Lee T. Statistical analysis of electronic properties of alkanethiols in metal–molecule–metal junctions. Nanotechnology. 2007;18:315204.

[251] Morita T, Lindsay S. Determination of single molecule conductances of alkanedithiols by conducting-atomic force microscopy with large gold nanoparticles. J Am Chem Soc. 2007;129:7262.

[252] Whitfield WJ. Ultra-Clean Room. United States: USPTO; 1964.

[253] Xu T. Characterization of minienvironments in a clean room: Design characteristics and environmental performance. Building and Environment. 2007;42:2993-3000.

[254] Park J-H, Sudarshan T. Chemical vapor deposition: ASM International; 2001.

[255] Jenkins FA, White HE. Fundamentals of optics 4th edition. Fundamentals of Optics 4th edition by Francis A Jenkins, Harvey E White New York, NY: McGraw-Hill Book Company, 1976. 1976;1.

[256] Williams DB, Carter CB. The Transmission Electron Microscope: Springer; 1996.

[257] Miller CW, Li Z-P, Akerman J, Schuller IK. Impact of interfacial roughness on tunneling conductance and extracted barrier parameters. Applied Physics Letters. 2007;90:043513--3.

[258] Clavilier J, Faure R, Guinet G, Durand R. Preparation of monocrystalline Pt microelectrodes and electrochemical study of the plane surfaces cut in the direction of the {111} and {110} planes. Journal of Electroanalytical Chemistry and Interfacial Electrochemistry. 1979;107:205-9.

[259] Wilcox WR, Lachapelle TJ. Mechanism of Gold Diffusion into Silicon. Journal of Applied Physics. 1964;35:240-6.

[260] Frey W, Woods CK, Chilkoti A. Ultraflat Nanosphere Lithography: A New Method to Fabricate Flat Nanostructures. Advanced Materials. 2000;12:1515-9.

[261] Thuo MM, Reus WF, Nijhuis CA, Barber JR, Kim C, Schulz MD, et al. Odd−Even Effects in Charge Transport across Self-Assembled Monolayers. Journal of the American Chemical Society. 2011;133:2962-75.

[262] Sherman R, Whitlock W. The removal of hydrocarbons and silicone grease stains from silicon wafers. Journal of Vacuum Science & Technology B: Microelectronics and Nanometer Structures. 1990;8:563-7.

[263] Vig JR. UV/ozone cleaning of surfaces. Journal of Vacuum Science & Technology A: Vacuum, Surfaces, and Films. 1985;3:1027-34.

[264] Huynh CK, Mitchener JC. Plasma versus ozone photoresist ashing: Temperature effects on process‐induced mobile ion contamination. Journal of Vacuum Science & Technology B: Microelectronics and Nanometer Structures. 1991;9:353-6.

[265] Yonekura K, Sakamori S, Goto K, Matsuura M, Fujiwara N, Yoneda M. Investigation of ash damage to ultralow-<equation>k</equation> inorganic materials. Journal of Vacuum Science & Technology B: Microelectronics and Nanometer Structures. 2004;22:548-53.

[266] Mino N, Tamura H, Ogawa K. Photoreactivity of 10,12-pentacosadiynoic acid monolayers and color transitions of the polymerized monolayers on an aqueous subphase. Langmuir. 1992;8:594-8.

[267] Slowinski K FHKY, Majda M. Mercury-mercury tunneling junctions. 1. Electron tunneling across symmetric and asymmetric alkanethiolate bilayers. J Am Chem Soc. 1999;121:7257.

[268] Hou Z, Abbott NL, Stroeve P. Electroless Gold as a Substrate for Self-Assembled Monolayers. Langmuir. 1998;14:3287-97.

[269] Selikson B, Longo TA. A study of purple plague and its role in integrated circuits. Proceedings of the IEEE. 1964;52:1638-41.

[270] Horsting CW. Purple Plague and Gold Purity. Reliability Physics Symposium, 1972 10th Annual1972. p. 155-8.

[271] Ziegler JF, Ziegler MD, Biersack JP. SRIM – The stopping and range of ions in matter (2010). Nuclear Instruments and Methods in Physics Research Section B: Beam Interactions with Materials and Atoms. 2010;268:1818-23.

[272] Nakayama M, Yanagisawa J, Wakaya F, Gamo K. Focused ion beam process for a formation of metal/insulator/metal double tunnel junctions. Microprocesses and Nanotechnology Conference, 1999 Digest of Papers Microprocesses and Nanotechnology '99 1999 International1999. p. 26-7.

[273] Rubanov S, Munroe PR. The effect of the gold sputter-coated films in minimising damage in FIB-produced TEM specimens. Materials Letters. 2003;57:2238-41.

[274] Koiry SP, Celestin ME, Ratnadurai R, Veerender P, Krishnan S, Aswal DK, et al. One pot, single step, room temperature dielectrophoretic deposition of gold nanoparticles clusters on polyethylene terephthalate substrate. ELECTROPHORESIS. 2013;34:1182-8.

[275] Chen Y, Sun Z, Yang Y, Ke Q. Heterogeneous photocatalytic oxidation of polyvinyl alcohol in water. Journal of Photochemistry and Photobiology A: Chemistry. 2001;142:85-9.

[276] Sanchez-Romaguera V, Madec M-B, Yeates SG. Inkjet printing of 3D metal–insulator–metal crossovers. Reactive and Functional Polymers. 2008;68:1052-8.

[277] Kim CS, Park S-J, Sim W, Kim Y-J, Yoo Y. Modeling and characterization of an industrial inkjet head for micro-patterning on printed circuit boards. Computers & Fluids. 2009;38:602-12.

[278] Deegan RD, Bakajin O, Dupont TF, Huber G, Nagel SR, Witten TA. Capillary flow as the cause of ring stains from dried liquid drops. Nature. 1997;389:827-9.

[279] Lopérgolo LC, Lugão AB, Catalani LH. Direct UV photocrosslinking of poly(N-vinyl-2-pyrrolidone) (PVP) to produce hydrogels. Polymer. 2003;44:6217-22.

[280] Floridia Addato MaA, Rubert AA, Benítez GA, Fonticelli MH, Carrasco J, Carro P, et al. Alkanethiol Adsorption on Platinum: Chain Length Effects on the Quality of Self-Assembled Monolayers. The Journal of Physical Chemistry C. 2011;115:17788-98.

[281] Shaporenko A, Brunnbauer M, Terfort A, Grunze M, Zharnikov M. Structural Forces in Self-Assembled Monolayers: Terphenyl-Substituted Alkanethiols on Noble Metal Substrates†. The Journal of Physical Chemistry B. 2004;108:14462-9.

[282] Janek RP, Fawcett WR, Ulman A. Impedance Spectroscopy of Self-Assembled Monolayers on Au(111): Sodium Ferrocyanide Charge Transfer at Modified Electrodes. Langmuir. 1998;14:3011-8.

[283] Sun C, Ge L-Q, Gu Z-Z. Fabrication of super-hydrophobic film with dual-size roughness by silica sphere assembly. Thin Solid Films. 2007;515:4686-90.

[284] Zisman WA. Relation of the Equilibrium Contact Angle to Liquid and Solid Constitution. Contact Angle, Wettability, and Adhesion: AMERICAN CHEMICAL SOCIETY; 1964. p. 1-51.

[285] Kim SH, Na SW, Lee NE, Nam YW, Kim Y-H. Effect of surface roughness on the adhesion properties of Cu/Cr films on polyimide substrate treated by inductively coupled oxygen plasma. Surface and Coatings Technology. 2005;200:2072-9.

[286] Love J C ELAKJKNRG, Whitesides GM. Self-assembled monolayers of thiolates on metals as a form of nanotechnology. Chem Rev. 2005;105:1103.

[287] Marino AA, Nilsen E, Frilot C. Nonlinear changes in brain electrical activity due to cell phone radiation. Bioelectromagnetics. 2003;24:339-46.

[288] Kalinowski J, Giro G, Camaioni N, Fattori V, Di Marco P. Photoconduction in solid films of C60. Synthetic Metals. 1996;77:181-8.

[289] Huesgen T, Woias P, Kockmann N. Design and fabrication of MEMS thermoelectric generators with high temperature efficiency. Sens Actuator A-Phys. 2008;145:423-9.

[290] Dragoman D, Dragoman M. Giant thermoelectric effect in graphene. Applied Physics Letters. 2007;91.

[291] Goswami DY, Vijayaraghavan S, Lu S, Tamm G. New and emerging developments in solar energy. Solar Energy. 2004;76:33-43.

[292] Corkish R, Green MA, Puzzer T. Solar energy collection by antennas. Sol Energy. 2002;73:395-401.

[293] Paing T, Falkenstein E, Zane R, Popovic Z. Custom IC for Ultra-low Power RF Energy Harvesting. Applied Power Electronics Conference and Exposition, 2009 APEC 2009 Twenty-Fourth Annual IEEE2009. p. 1239-45.

[294] Hagerty JA, Zhao T, Zane R, Popovic Z. Efficient Broadband RF Energy Harvesting for Wireless Sensors. 2005.

[295] Hagerty JA, Helmbrecht FB, McCalpin WH, Zane R, Popovic ZB. Recycling ambient microwave energy with broad-band rectenna arrays. Ieee Transactions on Microwave Theory and Techniques. 2004;52:1014-24.

[296] Harb A. Energy harvesting: State-of-the-art. Renew Energy. 2011;36:2641-54.

[297] Chen HM, Varshney PK. Automatic two-stage IR and MMW image registration algorithm for concealed weapons detection. IEE Proc-Vis Image Signal Process. 2001;148:209-16.

[298] Federici JF, Schulkin B, Huang F, Gary D, Barat R, Oliveira F, et al. THz imaging and sensing for security applications - explosives, weapons and drugs. Semicond Sci Technol. 2005;20:S266-S80.

[299] Richards PL. Bolometers For Infrared And Millimeter Waves. Journal of Applied Physics. 1994;76:1-24.

[300] Grover S, Dmitriyeva O, Estes MJ, Moddel G. Traveling-Wave Metal/Insulator/Metal Diodes for Improved Infrared Bandwidth and Efficiency of Antenna-Coupled Rectifiers. IEEE Trans Nanotechnol. 2010;9:716-22.

[301] Siebert KJ, Quast H, Leonhardt R, Loffler T, Thomson M, Bauer T, et al. Continuous-wave all-optoelectronic terahertz imaging. Applied Physics Letters. 2002;80:3003-5.

[302] Tiwari B, Bean JA, Szakmany G, Bernstein GH, Fay P, Porod W. Controlled etching and regrowth of tunnel oxide for antenna-coupled metal-oxide-metal diodes. Journal of Vacuum Science & Technology B. 2009;27:2153-60.

[303] Wu Q, Hewitt TD, Zhang XC. Two-dimensional electro-optic imaging of THz beams. Applied Physics Letters. 1996;69:1026-8.

[304] Lee AWM, Qin Q, Kumar S, Williams BS, Hu Q. Real-time terahertz imaging over a standoff distance (> 25 meters). Applied Physics Letters. 2006;89.

[305] Mickan SP, Menikh A, Liu HB, Mannella CA, MacColl R, Abbott D, et al. Label-free bioaffinity detection using terahertz technology. Phys Med Biol. 2002;47:3789-95.

[306] Huang SY, Wang YXJ, Wyeung DK, Ahuja AT, Zhang YT, Pickwell-MacPherson E. Tissue characterization using terahertz pulsed imaging in reflection geometry. Phys Med Biol. 2009;54:149-60.

[307] Yasuda T, Yasui T, Araki T, Abraham E. Real-time two-dimensional terahertz tomography of moving objects. Opt Commun. 2006;267:128-36.

[308] Reid CB, Fitzgerald A, Reese G, Goldin R, Tekkis P, O'Kelly PS, et al. Terahertz pulsed imaging of freshly excised human colonic tissues. Phys Med Biol. 2011;56:4333-53.

[309] Dabiri A, Motamedi M. Method for non-invasive cancerous tissue diagnosis and tomography using terahertz imaging. 2011.

[310] Wallace VP, Taday PF, Fitzgerald AJ, Woodward RM, Cluff J, Pye RJ, et al. Terahertz pulsed imaging and spectroscopy for biomedical and pharmaceutical applications. Faraday Discussions. 2004;126:255-63.

[311] Wijewardane S, Goswami Y. Exergy of partially coherent thermal radiation. Energy. 2012;42:497-502.

[312] Boone J, Krishnan S, Bhansali S. Development of a through wafer 3D vertical micro-coaxial probe. Journal of Micromechanics and Microengineering. 2013;23:075029.

[313] Moddel G, Zhu Z, Grover S, Joshi S. Ultrahigh speed graphene diode with reversible polarity. Solid State Communications. 2012;152:1842-5.

APPENDICES

Appendix A: Copyright Permissions

Below is a copyright permission screenshot for modified use of Figure 7.54.

Copyright Clearance Center RightsLink®

Home | Account Info | Help

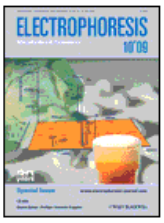

Title: One pot, single step, room temperature dielectrophoretic deposition of gold nanoparticles clusters on polyethylene terephthalate substrate

Author: Shankar P. Koiry,Michael E. Celestin,Rudraskandan Ratnadurai,Putta Veerender,Subramanian Krishnan,Dinesh K. Aswal,Shekhar Bhansali

Publication: Electrophoresis

Publisher: John Wiley and Sons

Date: Apr 8, 2013

Logged in as:
Michael Celestin
Account #:
3000401884

LOGOUT

Order Completed

Thank you very much for your order.

This is a License Agreement between Michael E Celestin ("You") and John Wiley and Sons ("John Wiley and Sons"). The license consists of your order details, the terms and conditions provided by John Wiley and Sons, and the payment terms and conditions.

Get the printable license.

License Number	3262361260472
License date	Nov 05, 2013
Licensed content publisher	John Wiley and Sons
Licensed content publication	Electrophoresis
Licensed content title	One pot, single step, room temperature dielectrophoretic deposition of gold nanoparticles clusters on polyethylene terephthalate substrate
Licensed copyright line	© 2013 WILEY-VCH Verlag GmbH & Co. KGaA, Weinheim
Licensed content author	Shankar P. Koiry,Michael E. Celestin,Rudraskandan Ratnadurai,Putta Veerender,Subramanian Krishnan,Dinesh K. Aswal,Shekhar Bhansali
Licensed content date	Apr 8, 2013
Start page	1182
End page	1188
Type of use	Dissertation/Thesis
Requestor type	University/Academic
Format	Electronic
Portion	Figure/table
Number of figures/tables	1
Original Wiley figure/table number(s)	Figure 1
Will you be translating?	No
Total	0.00 USD

ORDER MORE... | CLOSE WINDOW

Below is a copyright permission screenshot for modified use of Figure 7.54.

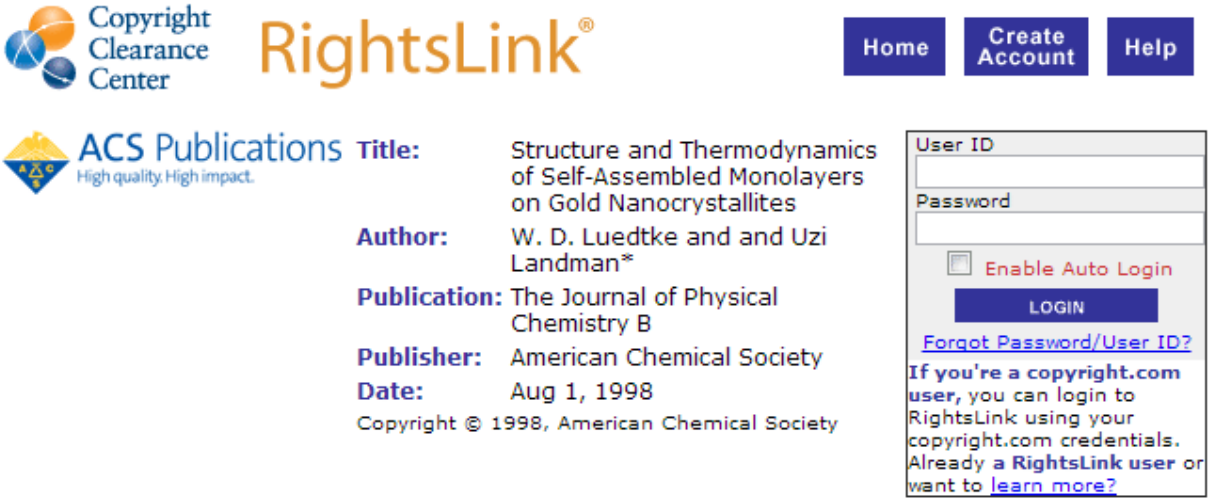

PERMISSION/LICENSE IS GRANTED FOR YOUR ORDER AT NO CHARGE

This type of permission/license, instead of the standard Terms & Conditions, is sent to you because no fee is being charged for your order. Please note the following:

- Permission is granted for your request in both print and electronic formats, and translations.
- If figures and/or tables were requested, they may be adapted or used in part.
- Please print this page for your records and send a copy of it to your publisher/graduate school.
- Appropriate credit for the requested material should be given as follows: "Reprinted (adapted) with permission from (COMPLETE REFERENCE CITATION). Copyright (YEAR) American Chemical Society." Insert appropriate information in place of the capitalized words.
- One-time permission is granted only for the use specified in your request. No additional uses are granted (such as derivative works or other editions). For any other uses, please submit a new request.

If credit is given to another source for the material you requested, permission must be obtained from that source.

BACK CLOSE WINDOW

Below is an emailed permission screenshot from author for use of Figure 4.1.

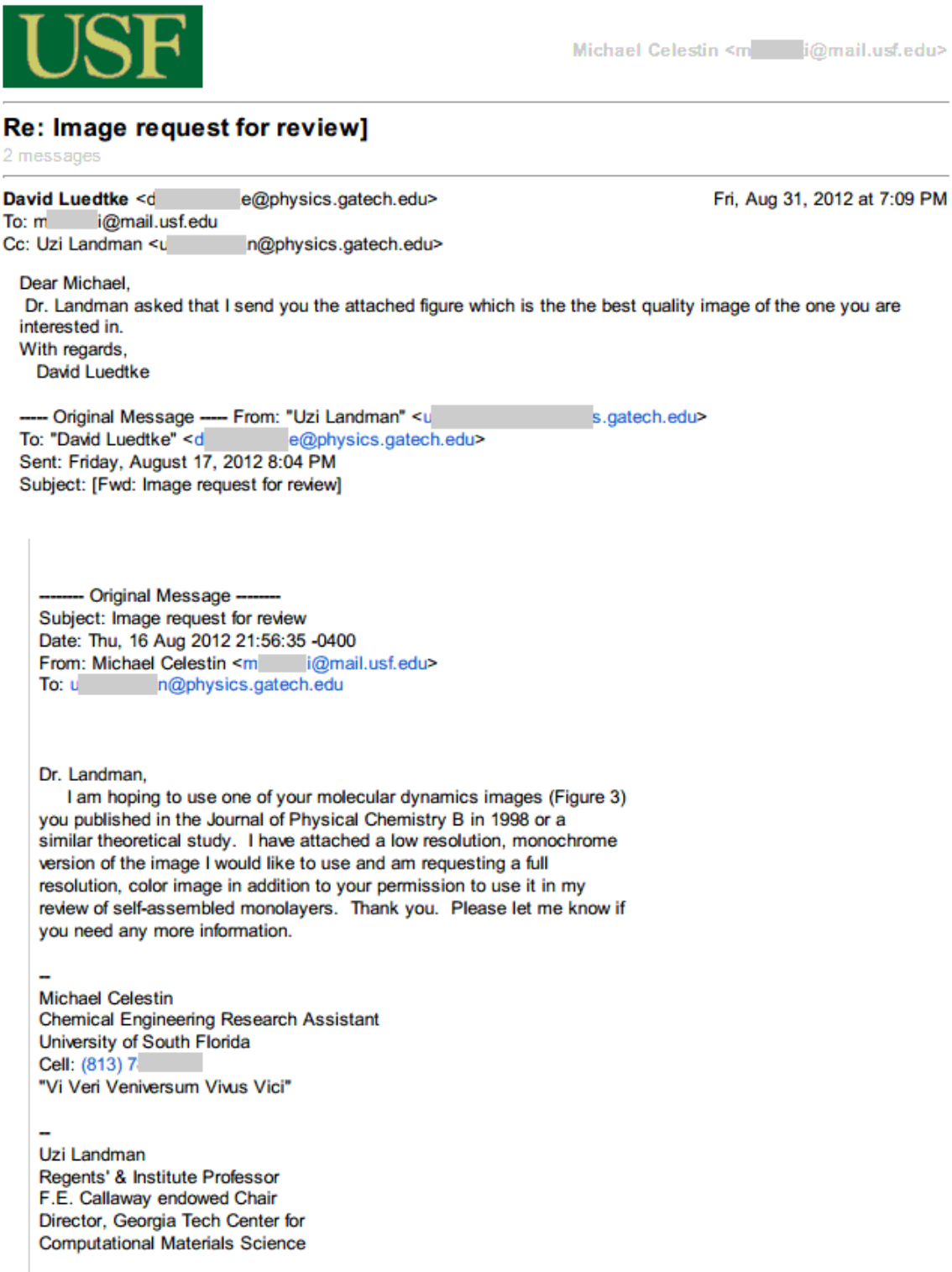

USF

Michael Celestin <m[redacted]i@mail.usf.edu>

Re: Image request for review]

2 messages

David Luedtke <d[redacted]e@physics.gatech.edu> Fri, Aug 31, 2012 at 7:09 PM
To: m[redacted]i@mail.usf.edu
Cc: Uzi Landman <u[redacted]n@physics.gatech.edu>

Dear Michael,
Dr. Landman asked that I send you the attached figure which is the the best quality image of the one you are interested in.
With regards,
David Luedtke

----- Original Message ----- From: "Uzi Landman" <u[redacted]s.gatech.edu>
To: "David Luedtke" <d[redacted]e@physics.gatech.edu>
Sent: Friday, August 17, 2012 8:04 PM
Subject: [Fwd: Image request for review]

-------- Original Message --------
Subject: Image request for review
Date: Thu, 16 Aug 2012 21:56:35 -0400
From: Michael Celestin <m[redacted]i@mail.usf.edu>
To: u[redacted]n@physics.gatech.edu

Dr. Landman,
I am hoping to use one of your molecular dynamics images (Figure 3) you published in the Journal of Physical Chemistry B in 1998 or a similar theoretical study. I have attached a low resolution, monochrome version of the image I would like to use and am requesting a full resolution, color image in addition to your permission to use it in my review of self-assembled monolayers. Thank you. Please let me know if you need any more information.

--
Michael Celestin
Chemical Engineering Research Assistant
University of South Florida
Cell: (813) 7[redacted]
"Vi Veri Veniversum Vivus Vici"

--
Uzi Landman
Regents' & Institute Professor
F.E. Callaway endowed Chair
Director, Georgia Tech Center for
Computational Materials Science

Appendix B: Table and Figures Pertaining to Neptune Data Formatting

To achieve reliable communications between the nanoparticle plotting system and PC, a data communication protocol needed to be developed. The primary goals of the protocol were that it be very simple, require low computational intensity (such to reduce embedded side processing requirements), and efficiently and reliably transmit print data to the remote device. The standard is dubbed the Celestin Packet Communication Protocol (CP)2 and consists of a packet described as follows:

Table B.1: Summary of data payload elements arranged by packet address.

Address	Symbol	Format	Description and Use
$00\text{-}03_{hex}$	U*::	ASCII	Packet Header denotes the start of a valid packet
$04\text{-}0B_{hex}$	FILENAME	ASCII	8 characters for description and communication
$0C\text{-}0D_{hex}$	TT	BINARY	Patterning time (Max) per pixel in deci-seconds (10^{-1}s)
$0E_{hex}$	X	BINARY	Number of steps in between data columns
$0F_{hex}$	Y	BINARY	Number of steps in between data rows
$10\text{-}11_{hex}$	CC	BINARY	Cyclic Redundancy CheckSum: an INT16 of DATA
$12\text{-}13_{hex}$	MN	BINARY	Packet sequence M of N packets transmitted
$14\text{-}17_{hex}$	CMND	ASCII	String which directs system to perform actions
$18\text{-}19_{hex}$	::	ASCII	Colon symbols are simply visual spaces
$1A\text{-}99_{hex}$	DATADA	BINARY	128 bytes of print payload data (optional)
$9A\text{-}9F_{hex}$	::U*ND	ASCII	Packet Delimiter is present at the end of useful data

ASCII format denotes use of the user printable character set (i.e. 7, Q, r, %) as opposed to BINARY which denotes the hexadecimal raw value which can take on non-printable forms.

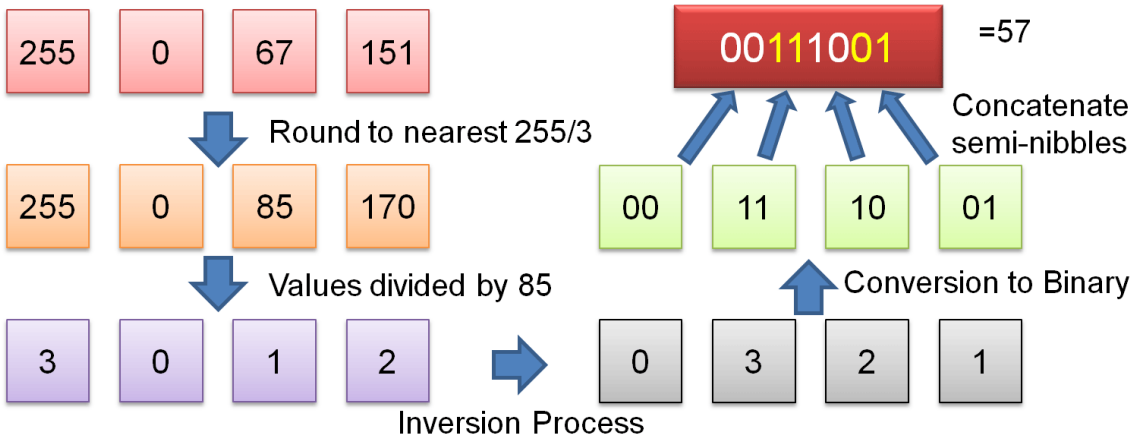

Figure B.1: Flow chart illustration of data preparation and compression processes for printing. Data from a 4 pixel cluster is taken, reduced to 2-bit representation and concatenated to permit higher speed data transfer and reduce microcontroller processing.

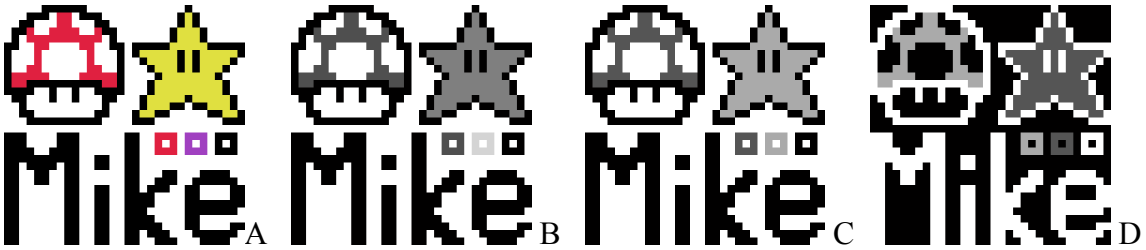

Figure B.2: Visual representation of data conversion in MATLAB in preparation of printing. The data can be imported as a color bitmap image (A). From there, it is converted to grayscale (B) and down-sampled to 2 bits (C). The final step is a polarity inversion (D). (Mushroom and Starman are fair-use images which may be subject to copyright by Nintendo Co., Ltd.)

Appendix C: Detailed Study on Parasitics in Measurement

Conventional wisdom for the testing of diodes generally suggests a setup which employs a current sense resistor in series with the Device Under Test (DUT). This resistor is actually a very important part of the electrical measurement—affecting both the accuracy of measurement and stability of the diode. In the case of our measurement, we are performing a "low side" current sensing where the load is on the positive side and the current sense resistor is tied to ground at one end (Figure C.1b). This permits simplistic oscilloscope analysis of the voltage measured which is easily referenced to earth ground. In addition, it permits a more simple power supply design for the system.

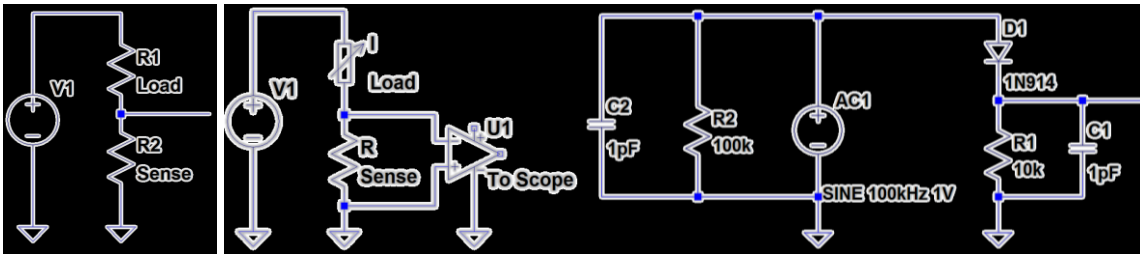

Figure C.1: Three small-signal model circuits describing parasites. At left (a) a voltage divider, center (b) full DUT test setup, and right (c) parasitic model.

A more complete view of any test setup will include consideration for parasitics present in the measurement setup. In this case, there is parasitic resistance, capacitance, and inductance caused by the wiring and component orientation. As it follows, the lowest interference and parasitic effects are noticed with the shortest leads, best RF isolation, and fewest discreet components. Sadly, this is not always possible when a complete setup is desired.

One of the challenges is the selection of the current sense resistor. While seemly a straightforward, trivial choice, the resistor value should take into account the parasitic values present in the system, the diode, the operating voltage, desired current (supply current limited of

diode limited regime), test signal frequency, and interference and noise immunity. For optimum balance, the resistor should be on the order of the equivalent resistance expected from the DUT. When the sense resistor is a very low value as compared to the equivalent resistance of the load, the measured signal will be very low as compared to the input voltage. In addition, the diode will be the current limiter in this scenario. For a simple approximation, we can visualize this system as a 2 component voltage divider (Figure C.1a). As one can now clearly see, for values of R1 >> R2, the voltage between the two devices will approach 0. (Example, R1 = 100Ω, R2 = 1Ω, V1 = 1V; output is 9.9mV) While the current holding this value is high, the low voltage will eventually approach the noise table to the measurement device. In addition to this, the low value of resistor will permit higher current through the resistor which can lead to heating and reduced linearity unless precautions are taken.

One might then be motivated to select a very high resistor value for to make the measurement. As an example, we can select R1 as a 50Ω load with a 10kΩ current sense resistor. When powered under 1V, the signal output would be 0.995V. While this permits a measurement to be made very easily, there are a number of shortcomings. First, the current through the load is now externally limited to 100μA. As this current goes lower and lower, the immunity to electromagnetic and RF interference coupled into the test leads increases dramatically. Minor, low current noise sources begin to appear on the order of desired data making traces noisy. In addition, the more serious problem of parasitic capacitance (inductance as well but this will be omitted for the time being) prevents accurate tracing an AC waveform. In Figure C.1c, we have the model used to study parasitic capacitance in the test setup.

Here a parasitic capacitor, C1, is present around the current sense resistor, R1. For this study, a 1N914 silicon diode was chosen as the active element in the model. While the

characteristics of this diode more closely mimic an idea diode than a tunnel diode, it will be used initially for simplicity. A parametric study was performed by sweeping resistance value R1 to study the effects on the waveform. The truest trace is seen in uses a 100ohm resistor to pull down the voltage on the test lead trace on the order of the sine wave slew. (Points of focus are lower blue and green traces noting symmetry on the positive cycles of the sine wave.) As this resistor value progressively increases, the resistor is not able to discharge the parasitic capacitance and the test lead voltage floats for longer and longer until it is not able to return to 0V before the start of the next positive phase input cycle.

Coming to a final point, we must be very careful when making measurements because reported results always account for all components in the system (desired and undesired). The reduction of parasitics can ensure a more easy to analyze result but one can remove effects of parasitics through model to deduce the nature of the original signal of interest. Take for instance the "clipper" behavior seen in recent reports. While this study is not to imply that the behavior is a function of parasitic coupled diodic behavior, it does suggest that this is a pathway to produce these types of results. Surely there may be a different mechanism at play which permits this clipping functionality. However, if there is no clear understanding of the mechanics, one should be cautiously pessimistic and report that this may be source of the phenomenon. In Figure C.2, we see the circuit diagram inset on the waveform traces. The small signal model for the tunnel diode here is approximated as an anti-parallel arrangement of diodes with dissimilar resistance values. Though the clipped waveform is out of phase with the incident waveform, this can be corrected with additional capacitive and inductive components.

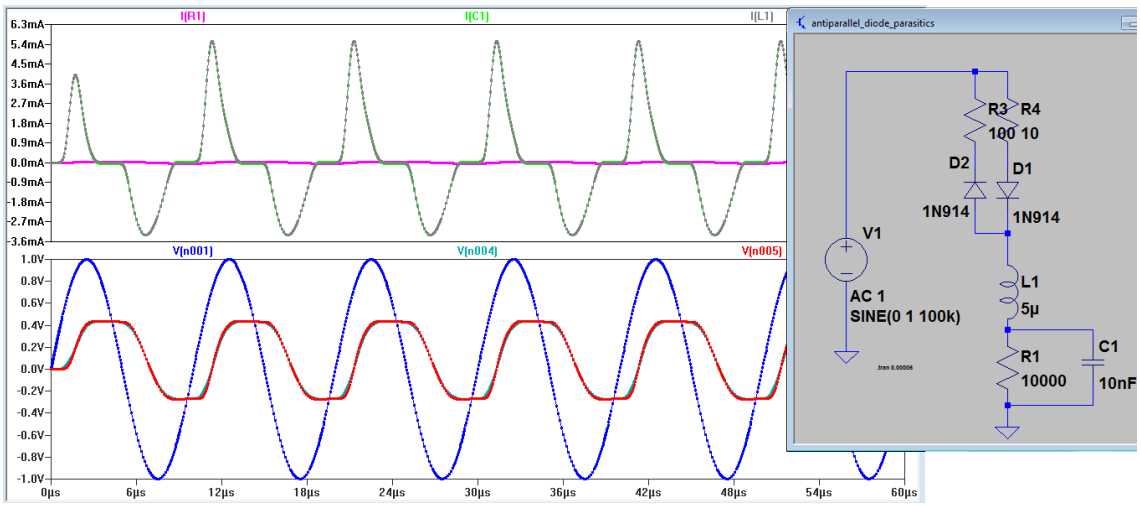

Figure C.2: An LT Spice simulation of a sine wave corrupted to produce a clipper effect due to parasitics.

Appendix D: Detailed Photo Lithography Process Steps With Descriptions

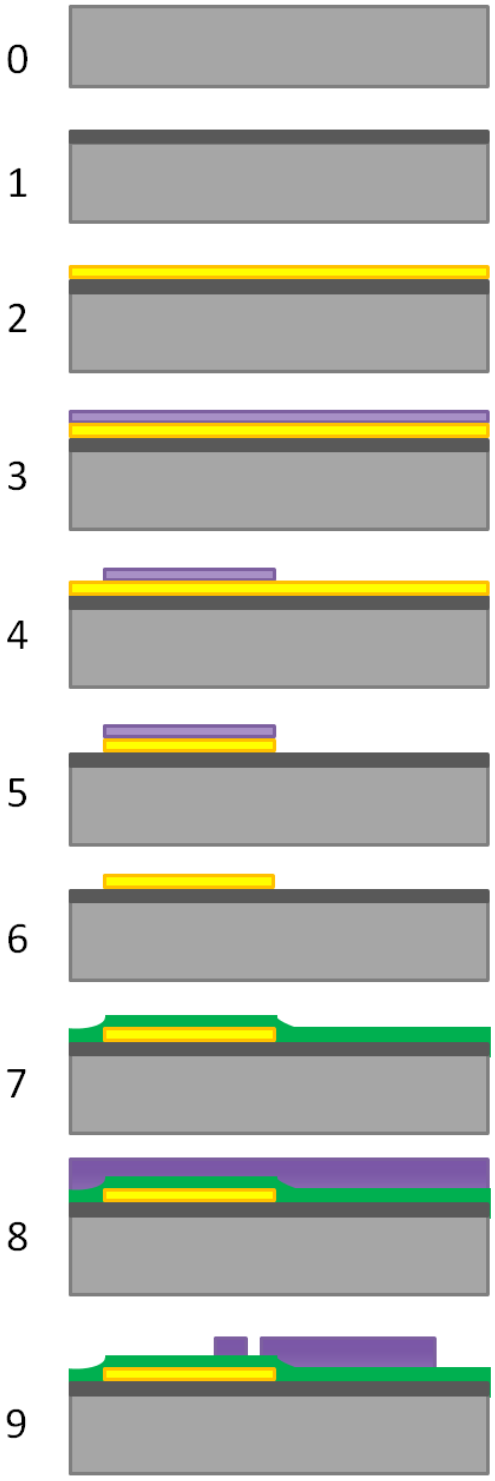

0 — Test grade silicon with unknown native oxide

1 — Substrate prepared (RCA Clean, oxidation, and characterization

2 — Base metal coated (noble metal for assemble) (Optional: Template Stripped Metal)

3 — Photo resist coated on base metal (positive tone)

4 — Photo resist is patterned and developed (lightfield mask)

5 — Base metal is etched (Transene TFA gold etch)

6 — Photo resist is stripped away

7 — Chemical Vapor Deposition of insulator layer (Si_3N_4)

8 — Photo resist is coated on nitride layer

9 — Photo resist is exposed, developed, and an O_2 plasma descum is performed to improve quality

Figure D.1: Cross-section process flow diagram illustrating the first nine steps of the photo lithography process for SAM-based MIM junctions.

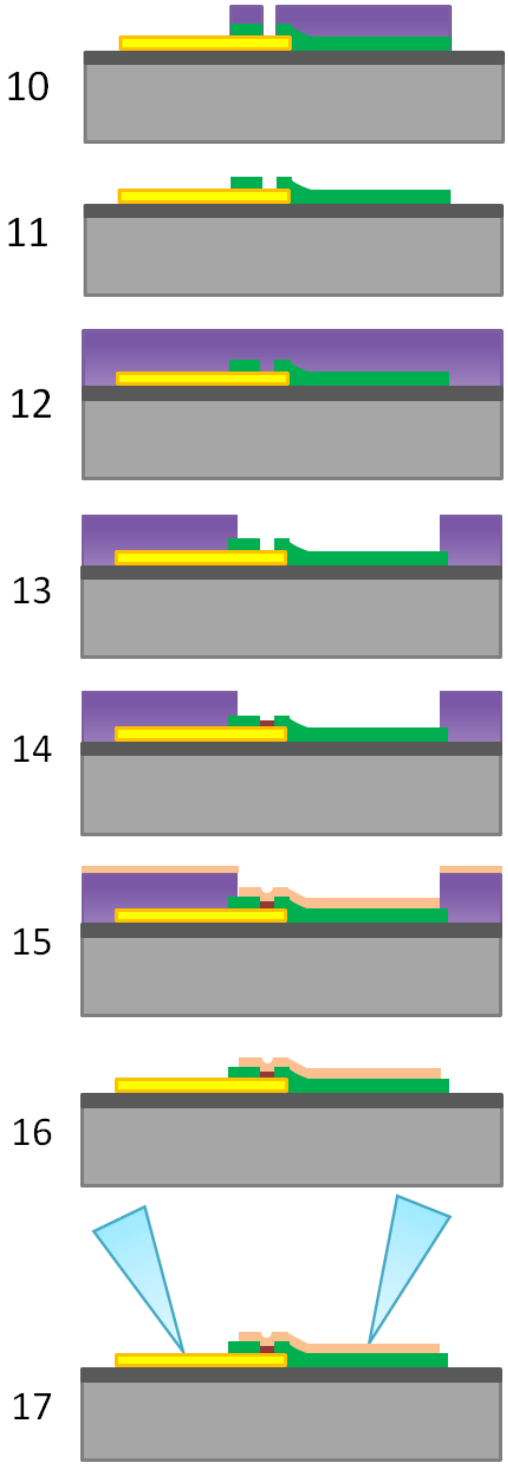

Reactive ion etch in custom recipe CF_4 diluted in Ar to control reaction rate

Photo resist is stripped away

Spin coat a solvent tolerant photo resist (Negative tone) with OmniCoat to assist release

Photo resist is exposed, developed and cleaned in an O_2 plasma descum

SAM Immersion (done immediately after plasma cleaning from prior step)

Ultra-low rate top metal e-beam evaporation (also done in short succession with prior step)

Lift-off top metal mechanically with tweezers

Probe test of finished device(s) (testing performed shortly after fabrication to minimized effects of oxidation)

Figure D.2: Cross-section process flow diagram illustrating the final seven steps of the photo lithography process for SAM-based MIM junctions.

Appendix E: Example Calculation and Table of SAM Dosing For Assembly

Below is an example calculation of SAM solution formulation. Here, it is desired to create a 1mM solution of 1-Dodecanethiol in 25mL ethanol. The calculations are as follows:

$$1mM = 0.001M\ [moles/L] \tag{E.1}$$

$$0.001\ M\ [moles/L] \times 0.025\text{L} = 2.5\ \times 10^{-5}\text{moles} \tag{E.2}$$

$$2.5\ \times 10^{-5}\text{moles}\ \times 202.40\ [g/mole] = 5.06\ \times\ 10^{-3}g \tag{E.3}$$

$$\left(\frac{5.06\ \times\ 10^{-3}g}{0.845\ [g/mL]}\right) \times\ 1000\ \mu L/mL = 5.988\,\mu L \tag{E.4}$$

Table E.1: A table of experimentally used SAM molecules and their dosing in solution.

SAM Molecules	Molecular wt. [g/mole]	Density [g/mL] (at 25°C)	Volume [µL] for 1mM in 10mL
1-Hexanethiol	118.24	0.832	1.42
1,6-Hexanedithiol	150.31	0.983	1.53
1-Decanethiol	174.35	0.824	2.12
1H, 1H, 2,H, 2H-Perfuorodecanethiol	480.18	1.678	2.86
1-Dodecanethiol	202.40	0.845	2.40
1-Tetradecanethiol	230.45	0.846	2.72
1-Octadecanethiol	286.56	0.847	3.38
1, 8-Octadecanedithiol	178.36	0.970	1.84
11-Mercaptoundecanoic Acid	218.36	Granular solid	2.184 mg
4, 4'-Bis(mercaptomethyl)biphenyl	246.39	Granular solid	2.464 mg
6-(Ferrocenyl)hexanethiol	302.26	Granular solid	3.023 mg

All properties from Sigma-Aldrich chemical MSDS and Technical Data sheets

Appendix F: A Glossary of the Acronyms and Abbreviations Used

AC – Alternating Current
AFM – Atomic Force Microscopy
BDR – Brinkman, Dynes, Rowell [model]
BER – Bit Error Rate
BSA – Body Surface Area
CAD – Computer Aided Design
CD – Compact Disc OR Critical Dimension
CIJ – Continuous InkJet [printing technology]
CMOS – Complementary Metal Oxide Semiconductor
CMP – Chemical Mechanical Polishing
CP-AFM – Conducting Probe Atomic Force Microscopy
CPW – Coplanar Waveguide
CRC – Cyclic Redundancy Check
CT – X-Ray Computed Tomography
CVD – Chemical Vapor Deposition
DC – Direct Current
DDT – Dodecanethiol
DEG – Diethylene Glycol
DI – DeIonized [water]
DNA – Deoxyribonucleic Acid
DOD – Drop-On-Demand [printing technology]
DPN – Dip-Pen Nanolithography
DRIE – Deep Reactive Ion Etching
DVD – Digital Versatile Disc (Optical Disc)
ECC – Error Correction Code
EEPROM – Electronically Erasable Programmable Read Only Memory
ESD – Electrostatic Discharge
FCC – Face Centered Cubic
FN – Fowler-Nordheim [model]
GHz – 10^9 Hertz
GPIB – General Purpose Interface Bus (IEEE-488)
HEPA – High-Efficiency Particulate Air [Filter]
HOMO – Highest Occupied Molecular Orbital
HTF – Heat Transfer Fluid
IC – Integrated Circuit
IC – Integrated Circuit
IPA – Isopropyl Alcohol
IR – InfraRed
ITO – Indium-Tin Oxide (transparent conductive film)
kHz – 10^3 Hertz
LB – Langmuir-Blodgett Films
LDPE – Low Density Polyethylene
LOFO – Lift-off-float-on
LUMO – Lowest unoccupied molecular orbital

MATLAB – (portmanteau) MATrix LABoratory – a high level programming language
MCB – Mechanically Controllable Break [Junction]
MD – Molecular Dynamics
MEMS – Micro-Electronic Mechanical Systems
MHz – 10^6 Hertz
MIBK – Methyl Isobutyl Ketone
MIM – Metal-Insulator-Metal device structure
MMW – Millimeter Wave
MSDS – Material Safety Data Sheet
MUX – MUltipleXer
NEPTUNE – Nanoparticle Electrostatic Plotting by Transient Uniform Numeric Excitation
NMR – Nuclear Magnetic Resonance
NP – Nanoparticle
NPGS – Nanometer Pattern Generation System
NPN – Negative-Positive-Negative referring to a type of BJT Transistor
ODE – Ordinary Differential Equations
PALO – Polymer Assisted Lift-off
PANI – Polyaniline Polymer
PAT – Photon Assisted Tunneling
PC – Personal Computer
PCB – Printed Circuit Board
PDE – Partial Differential Equations
PDMS – Polydimethylsiloxane
PEDOT:PSS – poly(3,4-ethylenedioxythiophene poly(styrenesulfonate)
PET – Polyethylene Terephthalate [polymer]
PFDT – 1H, 1H, 2H, 2H-Perfluorodecanethiol
PG – Propylene Glycol
PMMA – Poly(methyl methacrylate)
PmPV – poly[(m-phenylenevinylene)-co-(2,5-dioctoxy-p-phenylenevinylene)]
PROM – Programmable Read Only Memory
PTFE – Polytetrafluoroethylene known by its trade name, Teflon™
PV – Photovoltaic
PVD – Physical Vapor Deposition
PVOH – Polyvinyl Alcohol
PVP – Polyvinylpyrrolidone
QM – Quantum Mechanics
RF – Radio Frequency
RFID – Radio Frequency IDentification
RIE – Reactive Ion Etching
ROM – Read Only Memory
SAM – Self-assembled Monolayer
SC – SuperCapacitor
SCCM – Standard Cubic Centimeters per Minute
SEM – Scanning Electron Microscope
SRIM – Stopping Range of Ions in Matter (Simulation software)
STM – Scanning Tunneling Microscope

TEM – Transmission Electron Microscope
TEP – Thermoelectric Power
THPP – 5, 10, 15, 20 tetra(4-hydroxyphenyl)-porphyrin
THz – 10^{12} Hertz
TSG – Template Stripped Gold
TSP – Titanium Sublimation Pump
TTL – Transistor-Transistor Logic
TUNA – Tunneling Atomic Force Microscopy
UART – Universal Asynchronous Receiver/Transmitter
USB – Universal Serial Bus
UV – Ultraviolet
UVO – Ultra Violet Ozone [Cleaning]
VLS – Vapor-Liquid-Solid
XPS – X-Ray Photoelectron Spectroscopy
XRD – X-Ray Diffraction

ABOUT THE AUTHOR

Michael E. Celestin was born in North Bergen, NJ. He moved to Florida to attend the University of South Florida where he earned a B.S. Degree in Chemical Engineering and a B.A. Degree in Chemistry. After working in the environmental industry, he returned to the University of South Florida where he completed a Masters in Chemical Engineering Degree. While working towards his Ph.D., he participated in a summer technical internship at Sandia National Laboratories under NSF sponsorship. Michael's research interests include microfabrication, self-assembled monolayers, process science, and materials characterization. In his spare time, Michael develops human interface devices and small consumer electronics projects which typically seek to improve quality of life in some way. In all work done, he has considered the environmental impact on the land, air, and water.